Solar Origin of Space Weather

A thesis submitted in partial fulfillment of
the requirements for the degree of

Doctor of Philosophy

by

Ranadeep Sarkar

(Roll No. 15330018)

Under the guidance of

Dr. Nandita Srivastava
Senior Professor
Udaipur Solar Observatory
Physical Research Laboratory, Udaipur, India.

DEPARTMENT OF PHYSICS

INDIAN INSTITUTE OF TECHNOLOGY GANDHINAGAR

2020

to

my parents

&

teachers

Declaration

I declare that this written submission represents my ideas in my own words and where others' ideas or words have been included, I have adequately cited and referenced the original sources. I also declare that I have adhered to all principles of academic honesty and integrity and have not misrepresented or fabricated or falsified any idea/data/fact/source in my submission. I understand that any violation of the above will be cause for disciplinary action by the Institute and can also evoke penal action from the sources which have thus not been properly cited or from whom proper permission has not been taken when needed.

Ranadeep Sarkar

30/06/2020 (Signature)

(Name: Ranadeep Sarkar)

(Roll No: 15330018)

CERTIFICATE

It is certified that the work contained in the thesis titled **"Solar Origin of Space Weather"** by **Ranadeep Sarkar** (Roll no: 15330018), has been carried out under my supervision and that this work has not been submitted elsewhere for degree.

I have read this dissertation and in my opinion, it is fully adequate in scope and quality as a dissertation for the degree of Doctor of Philosophy.

N. Srivastava 30/6/2020

Prof. Nandita Srivastava
(Thesis Supervisor)
Senior Professor
Udaipur Solar Observatory
Physical Research Laboratory
Badi Road, Udaipur 313001, India

Thesis Approval

The thesis entitled

Solar Origin of Space Weather

by

Ranadeep Sarkar
(Roll No. 15330018)

is approved for the degree of

Doctor of Philosophy

Examiner	Examiner
Supervisor	Chairman

Date: ____________________

Place: ____________________

Acknowledgements

This thesis would not have come to reality without the help, support and guidance of many people. I would like to express my gratitude towards all of them in this opportunity.

First and foremost I wish to express my sincere thanks to my Ph.D. supervisor, Prof. Nandita Srivastava for her help all the way to the stage of writing this thesis. It was a great experience to work under her supervision. Her continuous support and constant encouragement throughout my tenure in PRL mould me as an independent researcher.

I convey my sincere thanks to Dr. Nat Gopalswamy for giving me opportunity to carry out a part of my Ph.D. project in NASA/GSFC under his guidance which helped me to accomplish my thesis goal. I also thank my collaborators Dr. Astrid Veronig, Dr. Marilena Mierla, Dr. Matthew J West and Dr. Elke D'Huys for their invaluable support in my research work.

I take this opportunity to thank my Doctoral Studies Committee, Prof. Shibu K Mathew and Dr. Brajesh Kumar for evaluating my work in a regular basis. Their valuable comments helped me to improve scientific outcomes. Also I am grateful to them for the examination of this thesis.

I express my gratitude to Prof. Anil Bhardwaj, Director, Physical Research Laboratory (PRL) for providing necessary facilities to carry out my research work. I heartily thank all the faculty and staff members of Udaipur Solar Observatory (USO) for providing me a nice research environment which I always enjoyed.

It would have been impossible to pass the five years without the joyful company of my dear batch mates, all the seniors and juniors in PRL. I convey my sincere thanks to them for an enjoyable stay in USO/PRL. I would like to specially thank my beloved seniors Sajal da, Avijeet da and Sanjay bhaiya for always motivating and supporting me during the highs and lows of my Ph.D. years.

I am grateful to Indian Institute of Technology, Gandhinagar (IIT Gn) for my Ph.D. registration.

I would like to express my deepest appreciation to the entire family of PRL.

Finally, I would like to thank my family, above all my parents, for all their unconditional love and lifelong support. I feel immense pleasure to dedicate this thesis to them. I must say, that being away from home, I have missed many opportunities to be with my family members. But, they have always been by my *side all the time. Last and foremost, I would like to thank my wife Emon for being my best friend and always believing in me that I can reach this goal. Completion of my Ph.D. was a dream cherished by both of us, which would not have come true without her love and support.*

(Ranadeep Sarkar)

Abstract

Coronal mass ejections (CMEs), the most violent eruptive phenomena occurring in the heliosphere, are recognized as one of the major solar origins of space weather disturbances. CMEs erupt in the form of gigantic clouds of magnetized plasma from the Sun and can reach Earth within several hours to days. If the magnetic field inside an Earth-directed CME or its associated sheath region has southward directed component (Bz), then it interacts with the Earth's magnetosphere, leading to severe geomagnetic storms. Therefore, it is crucial to predict the strength of Bz inside an Earth impacting interplanetary CME (ICME) in order to forecast the intensity of the resulting geomagnetic storms. Forecasting the strength and orientation of CME magnetic field at 1 AU requires advance knowledge of near-Sun CME properties and its nature of evolution in the heliosphere. The source region characteristics of CMEs may help to acquire knowledge about the CME properties close to the Sun as well as the conditions leading to CME initiation. However, the understanding of CME initiation and its nature of evolution close to Sun are limited due to lack of continuous observations which can capture the CME evolution starting from its initiation to post-eruptive phase. Moreover, in absence of any direct measurement of vector magnetic field in solar corona, it becomes quite challenging to estimate the magnetic field strength of CMEs close to the Sun. Apart from the above mentioned challenges, further complexities arise in modeling the CME parameters from Sun to Earth in order to predict its strength and orientation of magnetic field at 1 AU. In spite of several numerical and analytical modeling efforts, to date there is no such model yet which is capable of giving reliable prediction of Bz at 1 AU.

In backdrop of the above scenario, in the thesis, we first explore the conditions leading to CME eruptions from its source active regions (ARs) by studying the source region characteristics of the largest AR (NOAA 12192) of the solar cycle 24. This active region is a unique representative case, as it gave rise to several non-eruptive X-class flares as well as an eruptive M-class flare, giving an excellent opportunity to compare the photospheric magnetic environments of confined and eruptive events originated from a same AR. Comparing the magnetic characteris-

tics associated with both the confined and eruptive flares, we found that, although the flare-related permanent and abrupt changes in photospheric magnetic field and Lorentz forces are a common feature in large flares, the magnitude of those changes is smaller in the case of confined flares compared to the eruptive ones. In order to shed light on the physical scenario behind the confined nature of the high energetic flares originated from AR 12192, we have examined the magnetic environment over the source locations of both the confined and eruptive flares occurred in the AR. From the study of the extrapolated magnetic field, we have found that the critical decay index (1.5) for the onset of torus instability was achieved at a higher height (52 Mm) over the non-eruptive core region of AR 12192, whereas this critical height was comparatively lower (35 Mm) over the eruptive part of the AR. This is an important finding which suggests that the decay rate of the overlying magnetic-field strength can be used as a key parameter to determine whether a flare productive active region will result in a CME eruption or not.

Further, we extend the studies of source region characteristics to the active regions leading to recurrent large eruptive flares in order to unveil the conditions leading to successive eruptive events. A longstanding unsolved problem in flare physics is that, whether these events occur due to the continuous supply of free magnetic energy to the solar corona or because not all of the available free magnetic energy is released during a single major flaring event. In order to address this question, we study the evolution of photospheric magnetic field and the associated Lorentz force changes in NOAA ARs 11261 and 11283, each of which gave rise to recurrent eruptive M- and X-class flares. The distinct rebuild-up of net Lorentz force in between the successive flares and its abrupt downward changes during each flare in ARs 11261 and 11283 as obtained in our study, are the first observational evidences found in the evolution of any non-potential parameter of solar ARs, that confirms the build-up and release scenario for magnetic energy storage in the solar corona. We conclude that the recurrent large flares reported in our study occurred due to the newly supplied energy to the AR, instead of consuming the available residual energy. In the context of space weather predictions, the evolutionary pattern of the net Lorentz force changes reported in our study has significant implications, in particular, for the forecasting of recurrent large eruptive flares from the same AR and hence the chances of interaction between the associated CMEs.

Addressing the source region characteristics of CMEs, next, we have studied the CME initiation and its nature of evolution close to Sun. Since the morphological and magnetic properties of coronal cavities hold critical clues to triggering mechanism behind the CME initiation, we have tracked the evolution of a solar coronal cavity from a quasi-static equilibrium in the lower corona to its eruption into the interplanetary space using the multiple vantage point observations from SDO, STEREO (A & B), PROBA2 and LASCO. Importantly, by comparing the cavity centroid height during different stages of its evolution from quiescent to pre-eruptive phases, we have found that the eruption of the CME is triggered when the cavity centroid height reached a critical height for the onset of torus instability. Therefore, we have concluded that monitoring the cavity centroid height can be a useful forecasting tool to predict the cavity eruption in the form of CMEs.

Utilizing the large field-of-view of SWAP EUV imager and combining the EUV observations with the white-light images obtained from LASCO coronagraph, we have captured the complete evolution of the erupting cavity by filling the observational gap between 1 to 2 $R_\odot$. By applying successive geometrical fits to the cavity morphology, we have found that the nature of expansion of the coronal cavity was not selfsimilar in the lower corona, below a critical height (2.2 ± 0.2 $R_\odot$). However, above that critical height the nature of expansion remained self similar throughout the rest of the observed propagation path. Our observations also revealed that the cavity exhibited a strong deflection at 1.3 $R_\odot$ and after that, the direction of propagation remains approximately constant. The above mentioned results provide important observational constraints on both the nature of expansion and direction of propagation of CMEs, which are useful to model the CME properties from Sun to Earth in order to forecast its space weather impact at near-Earth space.

Combining the knowledge of CME source region characteristics and the nature of evolution of its near-Sun properties as developed in the thesis, finally, we have attempted to model the CME magnetic field from Sun to Earth in order to forecast the strength of Bz at 1 AU. Using the near-Sun CME properties as initial inputs, we developed an observationally constrained analytical model, the INterplanetary Flux ROpe Simulator (INFROS), to predict the magnetic field vectors of the associated ICMEs at any heliocentric distance. As a proof of concept, we validate the model for a test case of an Earth-impacting CME which occurred on 2013 April 11. The predicted magnetic field-vectors of the ICME obtained from INFROS show good agreement with those observed by the WIND spacecraft at 1 AU. This shows promising results in forecasting of Bz in near real time. It may be highlighted that INFROS is advantageous in many aspects compared to the existing Bz forecasting models, as it uses the realistic inputs and is capable of predicting the time-varying axial field strength and the expanding nature of the ICME without involving any free parameters. Therefore, the model (INFROS) developed and described in this thesis could prove to be a promising space-weather forecasting tool for advance prediction of magnetic field vectors of ICMEs.

In short, exploiting both the observational and modeling efforts, this thesis provides novel techniques to predict the magnetic field vectors of ICMEs which build the stepping stones towards the forecasting of intensity of the associated geomagnetic storms at near-Earth space.

Keywords: Solar active regions, Solar magnetic fields, Solar flares, Solar coronal mass ejections, Solar-terrestrial relations, Space weather

List of Publications

I. Research Papers in Refereed Journals:

1. **Sarkar, R.**, Gopalswamy, N. & Srivastava, N. 2020, *"An Observationally Constrained Analytical Model for Predicting Magnetic Field Vectors of ICMEs at 1 AU"*, **Astrophysical Journal**, 888, 121.

2. **Sarkar, R.**, Srivastava, N., & Veronig, A. M. 2019, *"Lorentz Force Evolution Reveals the Energy Build-up Processes during Recurrent Eruptive Solar Flares"*, **Astrophysical Journal Letters**, 885, L17.

3. **Sarkar, R.**, Srivastava, N., Mierla, M., et al. 2019, *"Evolution of the Coronal Cavity From the Quiescent to Eruptive Phase Associated with Coronal Mass Ejection"*, **Astrophysical Journal**, 875, 101.

4. **Sarkar, R.**, Srivastava, N.: 2018, *"A Comparative Study of the Eruptive and Non-Eruptive Flares Produced by the Largest Active Region of Solar Cycle 24."* **Solar Physics**, 293, 16.

II. Research Papers in Proceedings:

1. **Sarkar, R.** and Srivastava, N.: 2018, *"Geometric and magnetic properties of coronal flux ropes associated with CMEs leading to geomagnetic storms"* In: Banerjee, D., Jiang, J., Kusano, K., Solanki, S. (eds.) **Proceedings of the International Astronomical Union**, 13(S340), 191-192.

2. **Sarkar, R.**, Srivastava, N., Dhara, S. K.: 2017, *"On the dynamics of the largest active region of the solar cycle 24."* In: Foullon, C., Malandraki, O. (eds.) **Proceedings of the International Astronomical Union**, 13 (S335), 32-35.

Contents

Acknowledgements **i**

Abstract **iii**

List of Publications **vii**

Contents **ix**

List of Figures **xv**

List of Tables **xxvii**

1 Introduction **1**

- 1.1 Space Weather 1
- 1.2 Solar Origin of Space Weather Disturbances 2
- 1.3 Sun and Heliosphere 4
  - 1.3.1 Solar interior 4
  - 1.3.2 Solar atmosphere 6
  - 1.3.3 Solar wind and heliosphere 8
- 1.4 Space Weather Drivers 10
  - 1.4.1 Solar flares 10
  - 1.4.2 Coronal mass ejections 13
    - 1.4.2.1 Remote sensing observations 13
    - 1.4.2.2 In-situ observations 17
  - 1.4.3 Co-rotating interaction regions 21
- 1.5 Origin and Initiation Mechanism of CMEs 22

1.5.1 Association of CMEs with solar flares 23

1.5.2 Association of CMEs with prominence eruptions 24

1.5.3 Low coronal signatures of CME eruption 25

1.5.4 Triggering mechanism of CMEs 26

1.5.4.1 Tether-cutting mechanism 26

1.5.4.2 Flux cancellation model 28

1.5.4.3 Magnetic breakout model 29

1.5.4.4 MHD instabilities 29

1.6 CME Evolution in Heliosphere 32

1.6.1 Direction of CME propagation 33

1.6.2 Orientation of CME magnetic axis 35

1.6.3 Nature of CME expansion 38

1.7 Space Weather Consequences of CMEs 40

1.8 Forecasting Models to Predict Geo-effectiveness of CMEs 45

1.9 Motivation and Organization of the Thesis 46

2 Observational Data and Processing 53

2.1 Introduction 53

2.2 The Solar Dynamic Observatory (SDO) 54

2.2.1 Atmospheric Imaging Assembly (AIA) 55

2.2.2 The Helioseismic and Magnetic Imager (HMI) 56

2.3 PROBA-2 57

2.4 LASCO Onboard SOHO 57

2.5 STEREO 58

2.5.1 Extreme Ultra Violet Imager (EUVI) 59

2.5.2 COR1 59

2.5.3 COR2 59

2.5.4 Heliospheric Imager (HI) 60

2.6 In Situ Observations from WIND 61

2.7 Summary 61

3 Conditions in Source Active Regions Leading to Confined and Eruptive Events 63
3.1 Introduction 63
3.2 Overview of the Active Region Under Study 68
3.3 Data Analysis 70
3.4 Comparative Study of Confined and Eruptive Events: Results . . 77
  3.4.1 Magnetic-field evolution for the non-eruptive flares 77
  3.4.2 Magnetic-field evolution for the eruptive flare 79
  3.4.3 Morphological evolution of AR 12192 81
  3.4.4 Comparison of overlying magnetic-field strength for both the eruptive and non-eruptive region 85
3.5 Summary and Conclusion 87

4 Conditions in Source Active Regions Leading to Recurrent Eruptive Events 93
4.1 Introduction 93
4.2 Overview of the Recurrent Events and Analysis Methods 95
4.3 Magnetic Field Evolution in Recurrent Eruptive Events 98
  4.3.1 Abrupt changes in magnetic field and Lorentz force 98
    4.3.1.1 Magnetic field evolution in AR 11261 99
    4.3.1.2 Magnetic field evolution in AR 11283 101
  4.3.2 Lorentz force re-build up in between the successive flares in the ARs 102
  4.3.3 Evolution of GOES X-ray flux and the associated Lorentz force during the recurrent flares 105
4.4 Conclusion 105

5 CME Initiation and its Evolution Close to Sun 109
5.1 Introduction 109
5.2 Observations of the Coronal Cavity During Quiescent Phase . . . 114
5.3 Evolution of the Coronal Cavity During Eruptive Phase 122
  5.3.1 Morphological evolution of the cavity 122

5.3.2 Kinematic evolution of the cavity-prominence system . . . 126
5.4 Results 128
5.4.1 Spatial relation between the EUV cavity and the associated prominence 128
5.4.2 Cavity morphology during the quiescent phase 128
5.4.3 Cavity dynamics during the eruptive phase 130
5.4.4 Nature of expansion of the erupting cavity 132
5.4.5 Kinematic evolution of the cavity 133
5.4.6 Eruption mechanism of the coronal cavity in the context of torus instability 135
5.5 Discussion and Conclusions 137

6 An Observationally Constrained Analytical Model for Predicting the Magnetic-field Vectors of ICMEs 143

6.1 Introduction 143
6.2 Near-Sun Observations of Flux Rope Properties 145
6.2.1 Geometrical properties 145
6.2.2 Magnetic properties 147
6.2.2.1 Chirality and the direction of axial magnetic field of the flux rope 147
6.2.2.2 Axial field strength (B_0) 148
6.3 Development of INFROS Model to Estimate the Magnetic Field Vectors of ICMEs 150
6.3.1 Estimating the impact distance 151
6.3.2 Cross-sectional radius of the flux rope when the spacecraft just encounters the arrival of MC 152
6.3.3 Self-similar approach to incorporate the flux rope expansion during its passage through the spacecraft 154
6.3.4 Estimating the final magnetic field profiles of the MC at 1 AU using a cylindrical flux rope solution 157
6.4 Validation of INFROS Model for the CME Event on 2013 April 11 159

6.4.1 Inputs to INFROS model for the CME event on 2013 April 11 160
6.4.1.1 Poloidal flux content of the flux-rope 160
6.4.1.2 Chirality and the direction of the axial-magnetic field of the flux-rope 161
6.4.1.3 Axial field-strength of the flux-rope 164
6.4.1.4 Propagation direction of the CME 165
6.4.2 Sensitivity of the estimated magnetic vectors to the propagation direction and tilt angle of the CME 165
6.4.3 INFROS model outputs 167
6.5 Conclusion 170

7 Summary and Future Work **173**
7.1 Summary 173
7.2 Future Work 177

List of Figures

1.1 An artist's impression that shows how the space and ground-based technological systems can be effected due to the space weather events. Image credit: NASA 2

1.2 An artist's illustration depicting Sun-Earth interactions that influence space weather. Image credit: NASA's Goddard Space Flight Center 3

1.3 Variation of average temperature and density of solar atmosphere as function of height where zero corresponds to the height of solar photosphere 7

1.4 The eclipsed sun during the Great American Eclipse on 21 August 2017 depicting the structure of solar corona. Image credit: The research team that includes Miloslav Druckmüller, Peter Aniol and Shadia Habbal 8

1.5 Observation of Sun in extreme ultraviolet wavelength (193 Å passbands) as captured by the Solar Dynamics Observatory on 13 August 2018. The contoured region marked by the white dashed line denote a coronal hole which is extended from the north pole to the lower latitude of the Sun, spewing high-speed solar wind into space. 9

1.6 Schematic illustration of the heliosphere depicting termination shock, heliosheath, heliopause and bow shock. Image credit: NASA . . . 10

1.7 A two-ribbon H-alpha flare observed by Udaipur Solar Observatory on 3 March 1981 in the neighborhood of a 'S' shaped filament which can be seen as dark thread like structures. 11

1.8 Multi-wavelength observation of a solar flare on 24 February 2014 by the Solar Dynamics Observatory (SDO) in EUV wavelengths. . 12

1.9 A schematic profile of the temporal evolution of flare intensity in different wavelengths. 13

1.10 Observation of a halo CME on 21 June 2015 as captured by the Solar and Heliospheric Observatory (SOHO). Compared to the direct image as shown in left panel, the halo CME can be seen more clearly in the difference image (right panel), which is created by subtracting two consecutive frames. Credit: ESA&NASA/SOHO . 14

1.11 An example of classical three part structure of a CME. 15

1.12 Left panel: A schematic picture of an ICME associated with a fast forward shock (arc), and the sheath region. Right panel: In situ observations of an ICME from the ACE spacecraft located at the Lagrangian point L1. 18

1.13 Six possible tracks of an observing spacecraft through an ICME with (left) and without (right) a leading shock. 19

1.14 Schematic picture of two high-speed streams co-rotating with the Sun, leading to the formation of compressed plasma due to interaction with the slow solar wind. 22

1.15 The different phases of CME kinematics and its relation with the temporal evolution of the associated GOES soft X-ray flux. The initiation, acceleration, and propagation phase of the CME kinematics are associated with the preflare, rise, and decay phase of the associated flare, respectively. 23

1.16 A polar crown filament (PCF) observed on 22 July 2002 in Hα by Big Bear Solar Observatory (BBSO) (top left) and associated coronal cavity (top right) observed in white light by Mauna Loa Solar Observatory (MLSO/Mk4). 25

1.17 Lower coronal signatures of the occurrence of a CME. 26

1.18 The tether-cutting scenario as the triggering mechanism for CMEs. 27

1.19 Flux cancellation in a sheared magnetic field. 28

1.20 A schematic picture of magnetic field evolution in the breakout model. 29

1.21 Top: the MHD simulation of the kink instability of a strongly-twisted flux tube emerging from the subsurface to the corona, where the pre-existing magnetic field declines slowly with height. Bottom: the MHD simulation of the torus instability of a weakly-twisted flux tube emerging into the corona, where the pre-existing magnetic field declines rapidly with height 31

1.22 Panel (a) indicates the locations of the STEREO spacecraft, separated by an angle of 86.7° at the time of a prominence eruption observed in EUVI-B (panel b) at around 03:00 UT, which becomes the inner material of the CME. The multiscale edge detection and corresponding ellipse characterization are overplotted in COR1 (panel b). Panel (c) shows the Earth-directed CME being observed off the east limb in STEREO-A and off the west limb in STEREO-B combining the field-of-view of EUVI, COR and HI 32

1.23 Panel (a) depicts the eruption of a high-latitude prominence on 2 November 2008 seen by STEREO-B EUVI at 304 Å wavelength. The corresponding CME is observed in STEREO-B COR1 (panel b) and STEREO-B COR2 (panel c). The arrows overlaid on the images indicate the equator-ward deflection of the CME 34

1.24 Panel (a) shows the heliospheric positions of various planets and spacecraft on 7 January 2014. The temporal evolution of the modeled CME front is plotted in different colors. Panels (b-g) show the plasma parameters associated with the solar wind observed in near-Earth space by Wind spacecraft during 9 to 11 January 2014 35

1.25 Face-on (left column) and side-view (right column) of the erupting field structure of a left handed flux rope. Different rows depict the temporal evolution of the field structure as obtained from the simulation results. The magenta and green field lines represent the orientation of the azimuthal (poloidal) and axial (toroidal) field during the eruption. The temporal evolution of the axial field orientation clearly depicts a counterclockwise rotation of the left handed flux rope. 36

1.26 CME rotation as a function of time and heliocentric radial distance. The rotation is derived from the GCS fits to SECCHI/COR2-A, B, and LASCO/C2, C3 for heights above 3 $R_\odot$ and GCS fits to SECCHI/COR1-A and B for heights below 3 $R_\odot$. Positive angles correspond to counterclockwise rotation relative to the solar equator. 37

1.27 Magnetic field data at MESSENGER is overlapped with the field data at STEREO-B while normalizing both the temporal and spatial scale 39

1.28 Schematic picture of interplanetary and magnetospheric coupling, showing the reconnection process and energy injection into the night side magnetosphere, which lead to the formation of the storm-time ring current 41

1.29 Aurora borealis seen in the night sky of Canada 42

1.30 The magnetogram for the 1-2 September 1859 magnetic storm . . 43

1.31 IMF Bz and Dst hourly averages are shown for two different types of geomagnetic storms. The left panel shows a normal one-step magnetic storm during 17-20 September 2000. 44

1.32 Evolution of flux rope structure in a simulated CME. 46

2.1 The field-of-view of the HI telescopes and the COR-2 Sun-centred coronagraphs 60

3.1 *Panel a*: HMI continuum intensity-map of AR 12192. *Panel b*: AR 12192 in AIA 1600 Å image. *Panel c*: high resolution Hα image of AR 12192 taken from Multi Application Solar Telescope (MAST) at the Udaipur Solar Observatory. *Panel d*: HMI vector magnetogram of the AR. 66

3.2 Images show the SDO continuum intensity map of AR 12192 (b) in its previous rotation (a), and subsequent rotations (c) and (d), respectively. 69

3.3 The upper panels show the appearance of AR 12192 (indicated by the red circles) in GONG far-side images in between the first and second rotation. The bottom panels show the same in between the second and third rotation. 70

3.4 G-band images of AR 12192 taken from Multi Application Solar Telescope (MAST) at the Udaipur Solar Observatory. 72

3.5 *Left column*: HMI line-of-sight magnetic field during the non-eruptive flares. *Right column*: the post-flare arcade in AIA 94 Å images. 73

3.6 *Top panel*: the cumulative intensity histogram for identifying the umbra–penumbra and penumbra–quiet-Sun boundary. *Bottom panel*: the linearly fitted flattest part of the plot enlarged from the rectangular box shown in the top panel. 75

3.7 Horizontal magnetic-field evolution during the non-eruptive flares. The dashed, solid, and dotted vertical lines denote the flare onset, peak, and decay times respectively. 76

3.8 Temporal evolution of the total and vertical magnetic flux for the non-eruptive flares. The dashed, solid, and dotted vertical lines denote the flare onset, peak, and decay times respectively. 77

3.9 The temporal evolution of positive and negative magnetic flux for the four non-eruptive flares in AR 12192. The dashed, solid, and dotted vertical lines denote the flare onset, peak, and decay times respectively. 78

3.10 The changes in radial component of Lorentz force for the non-eruptive flares. The dashed, solid, and dotted vertical lines denote the flare onset, peak, and decay times respectively. 79

3.11 *Left panel*: HMI line-of-sight magnetic field during the eruptive M4.0-class flare. *Right panel*: the line-of-sight magnetic field enlarged from the selected region shown in the left panel. 80

3.12 Magnetic-field evolution and Lorentz-force changes for the eruptive M4.0-class flare. 80

3.13 Variation of umbral and penumbral area of AR 12192 during its disk passage (upper right panel), previous (upper left panel) and next rotation (lower). Temporal evolution of the area ratio of penumbra to umbra is shown in the second row of each panels. . . 82

3.14 *Top panel*: the temporal profile of GOES X-ray flux during 2014 October 21 - 26. The black arrows in the panel mark the X-class flares. *Bottom panel*: the total area variation of AR 12192 during the same period. 83

3.15 The morphological structure of the penumbral region away from the core region of AR 12192 before (a) and after (b) the eruptive M4.0-class flare respectively. Panels (c) and (d) depict the vector magnetograms of the same region shown in panels (a) and (b). . . 84

3.16 *Lower-panel*: the areal variation of the contoured penumbral region shown in *upper-left* and *upper-right* panels. The dashed, solid, and dotted vertical lines in the *lower-panel* denote the flare onset, peak, and decay times respectively. 85

3.17 The red and blue arrows in panels (a) and (b) mark the source location of the eruption on 2014 October 24 in AIA 1600 Å and 304 Å images respectively. Panel (c) depicts the two decay-index profiles drawn over the HMI line-of-sight magnetogram. The two decay index profiles shown in panel (c) are illustrated separately in panels (d) and (e) respectively. 86

4.1 HMI vector magnetogram of AR 11261 (Left panel) and AR 11283 (Right panel). 96

4.2 Temporal profile of the GOES 1-8 Å X-ray flux during the recurrent flares that occurred in AR 11261 (a). Evolution of the horizontal magnetic field (b) and changes in the radial component of the Lorentz force (c) within the selected regions of AR 11261. 97

4.3 Temporal profile of the GOES 1-8 Å X-ray flux during the recurrent flares that occurred in AR 11283 (a). Evolution of the horizontal magnetic field (b) and changes in the radial component of the Lorentz force (c) within the selected regions (shown by rectangular boxes in Figure 4.1) of AR 11283. 98

4.4 Radial component of HMI vector magnetic field of AR 11261 (upper-left panel) and AR 11283 (lower-left panel). 100

4.5 HMI continuum images of the flare-productive part of AR 11261 (First column) and the radial component of the HMI vector magnetic field (Second column) within the same field-of-view as shown in the first column. HMI continuum images of the flare-productive part of AR 11283 (Third column) and the radial component of the HMI vector magnetic field (Fourth column) within the same field-of-view as shown in the third column. 102

4.6 Relative evolution of GOES 1-8 Å X-ray flux (black solid lines) with that of the associated Lorentz force (red solid lines) during the recurrent flares under study. 103

5.1 Observation of the coronal cavity in the AIA 193 Å channel (a). The associated prominence structure as seen in the AIA 304 Å channel (b). The superimposed images of panels (a) and (b) are shown in panel (c). The green dotted line denotes the outer boundary of the true cavity. The yellow dotted line depicts the approximate outer boundary of the flux-rope. 113

5.2 Positions of STEREO A and B. The red and blue arrows drawn on (a) and (b) denote the direction of the plane-of-sky as viewed by EUVI on 2010 June 4 by STEREO A and on 2010 June 7 by STEREO B. 115

5.3 Observations of the coronal cavity as seen in the 195 Å bandpass of EUVI on STEREO A and B (panels (a) and (d) respectively), the associated prominence structure in 304 Å bandpass (panels (b) and (e)) and a superposition of the 195 Å and 304 Å bandpasses (panels (c) and (f)). 117

5.4 Observations of the coronal cavity as viewed in SWAP composite images (a) and the associated prominence structure as seen in the AIA 304 Å channel (b). The superimposed images of cavity morphology and the prominence structure as depicted in panels (a) and (b) are shown (c). In panel (c), the background image in gray scale represents the cavity morphology as depicted in panel (a) and the foreground image in AIA 304 Å color scale represents the prominence structure as shown in panel (b). 118

5.5 Cavity morphology as seen in SWAP composite images stacked over the period between 00:00 UT to 01:35 UT on 2010 June 13 (a). The daily averaged polarized brightness as imaged by the groundbased coronagraph MK4 on 2010 June 13 (b). The green cross-marks drawn on panel (b) approximately indicate the outer-boundary of the white-light cavity embedded in a coronal streamer. The same green cross-marks shown in panel (b) have been drawn on panel (a). FORWARD-modeled (line-of-sight integrated) EUV emission in 174 Å passband (c) and the white-light polarized brightness (d) using the model density and temperature of the cavity embedded in a coronal streamer. 119

5.6 Cavity morphology as seen in SWAP composite images stacked over the period between 00:00 UT to 01:35 UT on 2010 June 13. . 122

5.7 Cavity morphology as observed in the SWAP EUV images during the eruptive phase. 123

5.8 Morphological evolution of the cavity system within SWAP FOV during the eruptive phase. 124

5.9 Cavity morphology as observed in white-light coronagraphic images of LASCO C2 and C3 observations 125

5.10 The left panel shows the geometrical fit to the cavity morphology observed in the combined FOV of SWAP (green ellipses) and LASCO C2 (yellow ellipses). The right panel shows the geometrical fit to the cavity morphology observed in the combined FOV of SWAP (green dotted ellipses), LASCO C2 (yellow dotted ellipses) and LASCO C3 (red dotted ellipses). The red solid boundary highlights the solar limb. The red asterisks depict the trajectory of the cavity centroid. 126

5.11 The position of the slits superimposed on the SWAP and AIA images (panels (a) and (b) respectively) along with the height-time profiles for the lower-most boundary of the cavity (c) and the top-most part of the prominence (d). 127

5.12 The height-time profiles of the lowermost boundary of the cavity (red) and the leading edge of the filament (blue), as recorded in Figure 5.11. 128

5.13 Hα image of the polar crown filament on 2010 June 6 (a). STEREO-A EUVI 195 Å image on 2010 June 13 (b). 129

5.14 The evolution of the cavity width to centroid height aspect-ratio (top panel). Evoloution of the length along the semi-major axis of the cavity with respect to the cavity centroid height (bottom panel). 133

5.15 Height-time profiles for the cavity top, cavity centroid and cavity bottom (a). Velocity profiles for the cavity top, cavity centroid and cavity bottom (b). Polynomial fit to the cavity centroid height during the time interval 06:40 to 07:30 UT on 2010 June 13 (c). Acceleration profiles for the cavity top, cavity centroid and cavity bottom (d). 134

5.16 Decay index profiles for the different phases of the quiescent cavity. The black solid and dashed lines mark the decay index values at the cavity centroid and the top of the filament respectively. . . . 139

6.1 The face-on (a) and edge-on (b) views of Graduated Cylindrical Shell (GCS) model are shown with several positioning parameters (c). 146

6.2 A schematic picture that shows two flux ropes (FRs) with different chirality. 147

6.3 A schematic picture that shows the formation of a magnetic flux rope (the helical field line as indicated by a black arrow) and underlying post arcade loops (denoted by C) as a result of magnetic reconnection. 149

6.4 *Left panel*: The black solid line denotes the projected CME axis on the solar disc. *Right panel*: Schematic picture of an MC propagating through the interplanetary space in between the Sun and Earth. 150

6.5 Schematic picture of the MC cross-section on the plane (the orange plane as depicted in Figure 6.4) perpendicular to the MC axis. . . 153

6.6 Schematic picture of the cross-section of an expanding FR as it passes over the spacecraft with a propagation speed V_{pro} and expansion speed V_{exp}. 154

6.7 Upper-left panel depicts the flare ribbon in AIA 1600 Å image. The red boundary line in upper-right panel marks the post eruption arcades (PEAs) in AIA 193 Å image. Lower-left and lower-right panel illustrate the HMI line-of-sight magnetic field. 160

6.8 The pre-flare sigmoidal structure observed in the composite images constructed from the AIA 94 Å (red), 335 Å (green) and 193 Å (blue) passband observations (a). The associated HMI line-of-sight magnetic field plotted in gray scale within saturation values ± 500 G (b). The post-eruption arcades (PEAs) observed in AIA 193 Å passbands (c) and the associated HMI line-of-sight magnetic field (d). 162
6.9 Top panels depict the CME morphology observed in COR2-A (top-left), LASCO C2 (top-middle), and COR2-B (top-right), respectively, at 07:54 UT on 2013 April 11. Bottom panels illustrate the overplot of the best-fitted wire frame (green dotted marks) of the FR using the GCS model. 163
6.10 Location of Earth (blue dots) with respect to the magnetic axis (black solid lines) of the CME projected on the solar disk. 165
6.11 Magnetic vectors as detected by the WIND spacecraft for 2013 April 14 ICME event. 167
6.12 Left panel: Cross-section of the flux rope as viewed on the ecliptic plane when the spacecraft at 1 AU just encounters the arrival of the magnetic cloud (MC). Right panel: Cross-section of the expanded flux-rope when the spacecraft completes its passage through the magnetic cloud and reaches to the rear boundary of the MC at 1 AU. 168
6.13 Hodogram plot of the magnetic field vectors within the MC for both observed and modeled data values. 169

List of Tables

2.1 Different channels of AIA centered on specific lines and corresponding regions of solar atmosphere with different characteristic temperatures 56
2.2 System parameters for C1, C2 and C3 58
2.3 System parameters for SECCHI 59

3.1 Major M and X-class flares observed in NOAA 12192 during 2014 October 22 - 25 71
3.2 Comparison between the eruptive and non-eruptive flares produced by AR 12192 88

4.1 Recurrent flares observed in AR 11261 and AR 11283 95

5.1 Cavity morphology throughout the quiescent phase 121
5.2 Temporal evolution of decay index 135

Chapter 1

Introduction

Most of the ancient civilizations on Earth recognized Sun as a source of life and worshiped it as a God or Goddess. From the daily life experience, they have realized that there will be no light, life and warmth on Earth without Sun. Even in this twenty first century, there are many cultures and religions that worship Sun. Indeed, the modern civilization has made a tremendous technological advancements utilizing the solar energy. Despite of the blessings to the human civilization, there is a dark side of the Sun that imposes harmful effects to the human technologies in near-Earth space and ground as well. In modern science, this is popularly known as the space weather effects of the Sun.

1.1 Space Weather

The term space weather refers to the time varying conditions within the solar system, including the solar wind, magnetosphere, ionosphere, and thermosphere that can influence the performance and reliability of space-borne and ground-based technological systems (Figure 1.1) (Schwenn, 2006).

Being a magnetically active and variable star, Sun has profound impacts on the planetary atmosphere. Therefore, the conditions in the near-Earth space is extremely vulnerable to the explosive events on the Sun leading to disturbed space weather. The economic consequences of the extreme space weather events can be enormous (Siscoe, 2000). Importantly, the study of space weather has

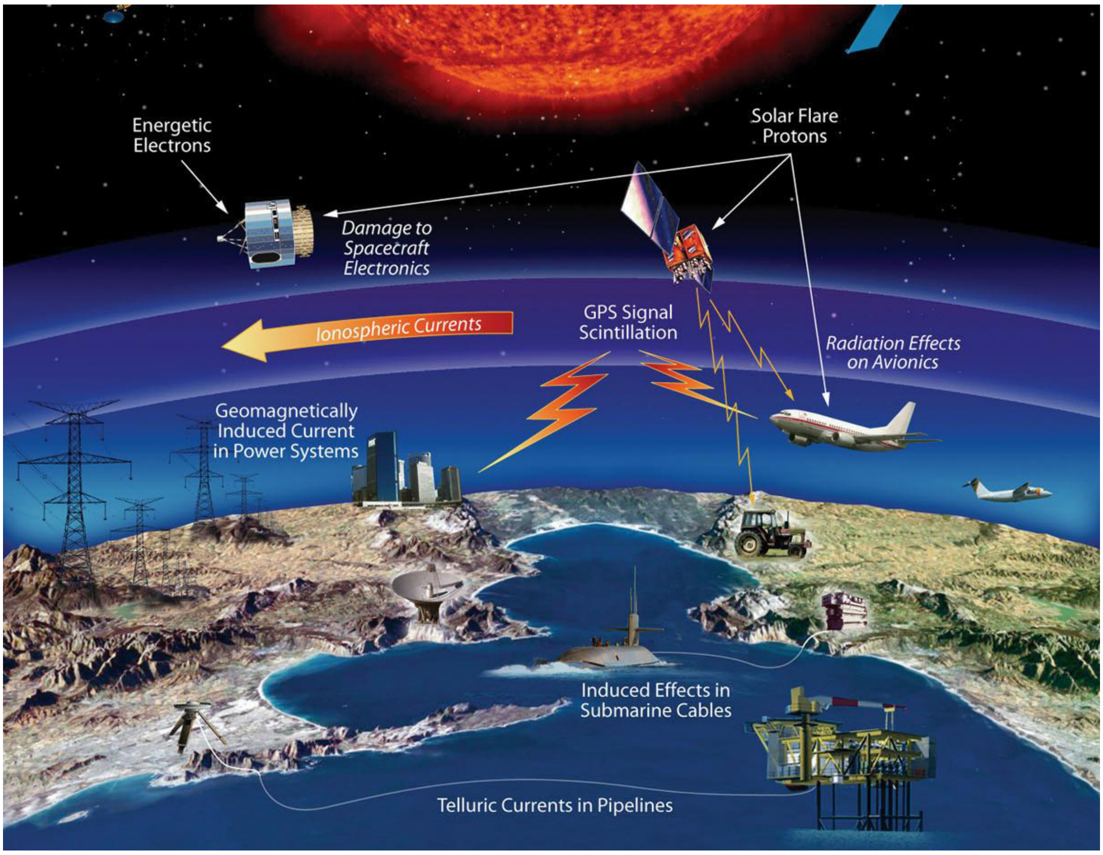
Energetic Electrons
Solar Flare Protons
Damage to Spacecraft Electronics
Ionospheric Currents
GPS Signal Scintillation
Radiation Effects on Avionics
Geomagnetically Induced Current in Power Systems
Induced Effects in Submarine Cables
Telluric Currents in Pipelines

Figure 1.1: An artist's impression that shows how the space and ground-based technological systems can be effected due to the space weather events. Image credit: NASA

become one of the fast-developing scientific discipline, which not only deals with the consequences of the coupling between Sun-Earth system, but also includes fundamental physics of the astrophysical plasma. In a broader sense, understanding the influence of solar variability on the planetary atmosphere lead us to shed light on the chances of planetary habitability in other Sun like exo-solar systems.

1.2 Solar Origin of Space Weather Disturbances

Violent eruptions in the solar atmosphere, categorized as solar flares and coronal mass ejections (CMEs) are the primary drivers of the most dramatic space weather disturbances (Figure 1.2). Solar flares release sudden flashes of energy that can heat up and expand the terrestrial atmosphere, which in turn increases the atmospheric drag so that the satellites are slowed down and drop into lower orbits (Schwenn, 2006). Moreover, the satellites can be exposed to the energetic

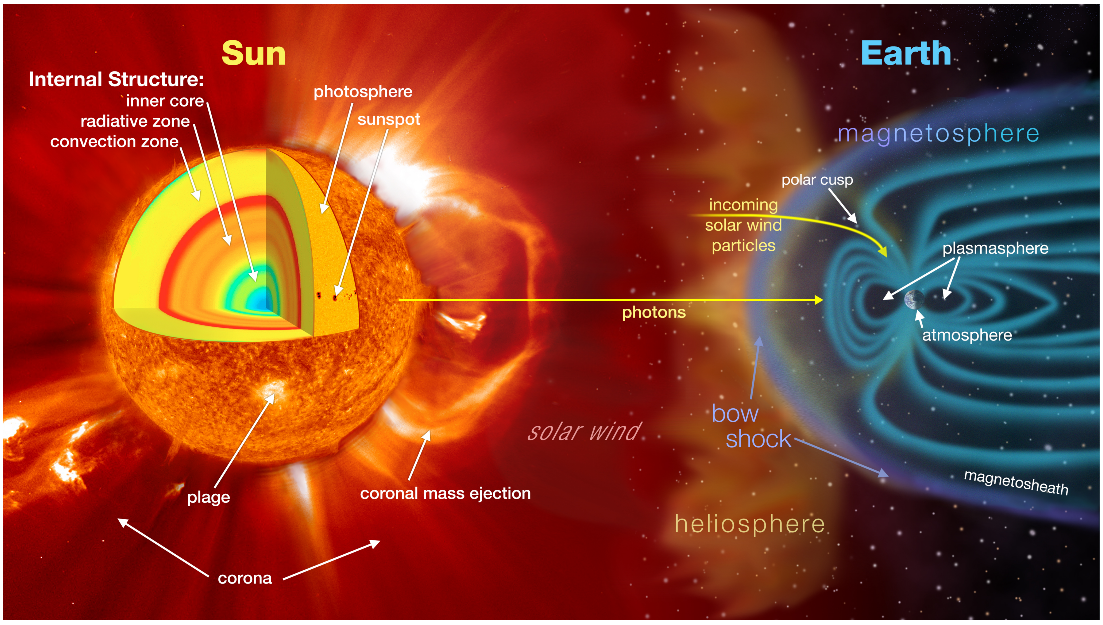
Sun
Internal Structure:
inner core
radiative zone
convection zone
photosphere
sunspot
plage
coronal mass ejection
corona
solar wind
photons
Earth
magnetosphere
polar cusp
incoming solar wind particles
plasmasphere
atmosphere
bow shock
magnetosheath
heliosphere

Figure 1.2: An artist's illustration depicting Sun-Earth interactions that influence space weather. Image credit: NASA's Goddard Space Flight Center

particle radiation emitted from the Sun during the flares, which can cause temporary or permanent failure of the satellite functionality, causing degradation or disruption of communication and navigation system on Earth. The exposure of the high energy particles are also dangerous to the health of astronauts and polar-route airlines crews. On the other hand, CMEs are gigantic clouds of magnetized plasma that are routinely ejected from the Sun into the interplanetary space, and after a few hours or days may hit the Earth's magnetosphere, which may cause severe geomagnetic storms. As a consequence, a geomagnetically induced current is produced which can disrupt the electronic, tele-communication and power-grid systems on Earth. Therefore, it is very important to study the origin and early evolution of the solar eruptive events in order to predict the severity of associated space weather consequences. Apart from the solar explosive events, there is another source of geomagnetic disturbances, which are known as co-rotating interaction regions (CIRs). The fast solar wind originated from the coronal holes on the Sun interacts with the preceding slow speed solar wind in the interplanetary space, giving rise to CIRs that are responsible for recurrent geomagnetic storms (Richardson, 2018 and references therein).

In order to understand the solar origin and the consequences of the space-weather events, an exploratory journey from the solar interior to the inner heliosphere is presented in the following section.

1.3 Sun and Heliosphere

The Sun is a G2 type main-sequence star located in a spiral arm of our galaxy, the Milky Way. Approximately 4.5 billion years ago, Sun was born from the gravitational collapse of a large molecular cloud and is expected to remain in main sequence phase upto next 4.5 billion years before entering into the red giant phase. Currently, it is in hydro-static equilibrium with effective black body temperature $\approx$ 5700 K, mass $\approx 1.98 \times 10^{30}$ kg, radius $\approx 6.96 \times 10^{8}$ m and luminosity $\approx 3.84 \times 10^{26}$ Watt. Being the nearest star to our planet, Sun can be observed with a very high spatial resolution through the modern space and ground-based telescopes, providing a unique opportunity to study the different aspects of a stellar body in detail. Indeed, Sun acts as an astrophysical laboratory where the fundamental theories related to space physics plasma can be tested and verified.

There are various physical environments and processes involved in solar interior, solar atmosphere, solar wind and heliosphere, which are interconnected through different chains of actions.

1.3.1 Solar interior

The visible solar surface that can be observed through the naked eyes is the solar photosphere. More deeper into the solar photosphere and its interior cannot be observed directly. The main contributions to build the modern picture of solar interior came from the standard solar model (SSM) (Bahcall et al., 1982) and the helioseismology i.e. the study of solar oscillation (Leibacher et al., 1985). The SSM is based on the outputs obtained by solving the classical stellar equations and incorporating the knowledge of fundamental physics like nuclear reaction rates, photon interaction and plasma physics. The model outputs are matched with the real observations in an iterative way to build the realistic picture of the solar interior. On the other hand, helioseismology uses the observation of waves on the solar surface which allows to probe the solar interior (Leighton et al., 1962; Ulrich, 1970).

According to the different physical environment, the solar interior is separated into three regions that include the core, the radiation zone and the convection zone (Figure 1.2). From the center of the Sun, the core extends out to about 0.25 $R_\odot$ and contains almost half the mass of the entire Sun. The temperature ($\approx$ 15 million K) and density ($\approx 1.6 \times 10^5$ kg m^{-3}) in the core is so high that it acts as a furnace for thermonuclear fusion which is the source of energy for Sun (Priest, 2014, p. 10). During the processes of thermonuclear fusion, groups of four protons fuse into one helium nucleus, which results in the formation of two high frequency γ-rays (26.2 MeV) and two electron neutrinos (0.5 MeV). These neutrinos escape in an unimpeded way from the core through the rest of the solar interior and serve as the direct diagnostic of the core condition.

Outside the core, the shell that extends from 0.25 to 0.70 $R_\odot$ is known as the radiative zone. This part of the solar interior is characterized by its mode of energy transport, i.e. radiation. The high energy gamma photons generated in core, are absorbed and re-emitted repeatedly by the particles in the radiative zone, as if they make a random walk towards the outer edge of this zone. From the bottom to the top of the radiative zone, the density drops from 2×10^4 kg m^{-3} to 2×10^2 kg m^{-3} and the temperature falls from 7 million K to 2 million K. Due to the random walk motion, an individual photon takes almost millions of year to reach the outer edge of the radiative zone. This implies an interesting fact that if the energy generation processes in solar core suddenly stops then Sun will continue to shine for millions of years.

Due to the increasing opacity the temperature gradient above the radiative zone becomes so high that the convective instability begins. Therefore, extending from 0.70 to 1 $R_\odot$, most of the energy flux is transmitted by convection rather than radiation. This part of the solar interior is known as the convection zone. In this zone, the temperature decreases very rapidly with increasing radial distance and becomes around 5700 K at the solar photosphere. The energy transport is mediated by large convective cells formed in the convection zone, which can be traced on the solar photosphere in the form of granules. The different convective envelops inside the convection zone rotates differentially. The helioseismic studies reveal that at the base of the convection zone, there is a sharp transition between the nearly uniform rotation of radiative interior and the differential rotation of the convective envelope. This transition region at near about 0.7 $R_\odot$ is known as the solar tachocline, which is one of the most important domain in heliophysics. Due to the strong shear in the form of differential rotation, the tachocline region is believed to play a key role in generating and storing the toroidal magnetic flux. Due to magnetic buoyancy, the toroidal flux eventually rises up from the base of the convection zone to the surface of the Sun and senses the solar rotation during this journey. Therefore, the field emerges with a preferential twist on both the hemisphere of Sun and gives rise to the sunspots on the solar surface. The sense of twist appears to be opposite in both the hemisphere with some exceptions due to the interaction with the turbulent convective motions, resulting in a net dipole moment which is the main cause to shape up the heliospheric structure.

1.3.2 Solar atmosphere

The photons that travel through the partially opaque solar interior, encounter transparent atmosphere at the solar surface, which is the lower most atmospheric layer of Sun, called as solar photosphere. Above the photosphere, the other two atmospheric layers are categorized as chromosphere and solar corona.

Solar photosphere is about a 100 km thick layer having the average temperature around 5700 K. Up to about 2000 km above the photosphere the solar atmosphere is known as chromosphere. Within a few thousands of kilometers, the density of the solar atmosphere drops by about seven order of magnitudes. The temperature of the solar atmosphere decreases radially outward from the solar photosphere and reaches to a minimum value of roughly 4400 K at a height about 500 km above the solar surface (Figure 1.3). The temperature further increases slowly and shoots up to about one million K within a less than 100 km thick layer above the chromosphere, known as the transition region. The solar

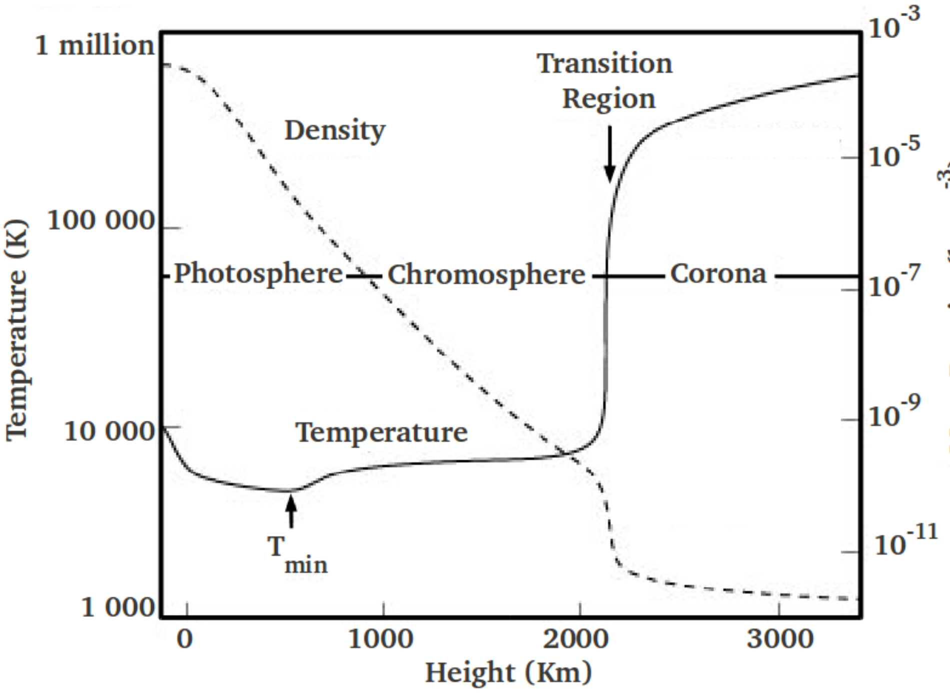

Figure 1.3: Variation of average temperature and density of solar atmosphere as function of height where zero corresponds to the height of solar photosphere (Courtesy of Eugene Avrett, Smithsonian Astrophysical Observatory. Lang 2006, p. 115).

atmosphere with a million K temperature above the transition region is known as the solar corona (Figure 1.4).

The buoyant magnetic field that emerges on the photosphere, expands into the highest layers of the solar atmosphere and entangles all the dynamics occurring at different atmospheric layers of the Sun. At the coronal height, the magnetic pressure becomes so dominant over the plasma pressure that the plasma motions follow the magnetic fields, leading to giant glowing arches like structures called coronal loops. On the other hand, some fraction of field lines temporarily open up into the heliosphere. The regions of solar corona that belong to these open field lines are observed as coronal holes in extreme ultra-violet (EUV), X-ray and He 10830 Å wavelengths as the charge particles can easily escape through the open field lines, causing density depletion in the solar corona. Apart from the large scale quasi-static structures, the solar atmosphere also contains a magnetic structure like flux ropes that range from millions of short lived (only for few minutes) small scale to a very few long lived (for several days or weeks) large scale

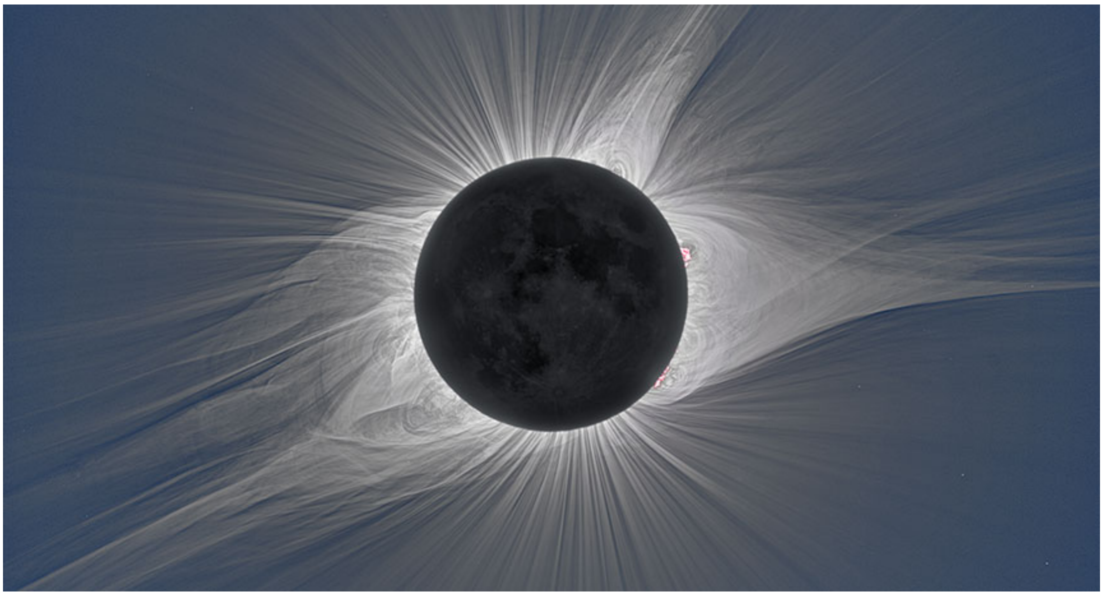

Figure 1.4: The eclipsed sun during the Great American Eclipse on 21 August 2017 depicting the structure of solar corona. Image credit: The research team that includes Miloslav Druckmüller, Peter Aniol and Shadia Habbal

structures. The magnetic flux ropes (MFR) in the solar atmosphere may emerge from the convection zone or can be generated by the sub-surface flows. Further, the MFRs are destabilized due to either ideal or resistive magneto hydrodynamic processes, leading to solar eruptive phenomena that causes the space weather disturbances.

1.3.3 Solar wind and heliosphere

The outer solar corona does not remain in hydrostatic equilibrium, rather continuously expands outwards in the form of out-stream of charged particles, called as solar wind (Parker, 1958). During the early space era, the in situ properties of solar wind were observed at different heliocentric distances by the spacecraft that include Luna 1 (1959), Mariner 2 (1962), Helios 1 (1974) and Helios 2 (1976). The observational properties of solar wind suggest that there are two states of wind; slow and fast solar wind. The bulk speed of slow solar wind ranges between about 300 km s^{-1} and 500 km s^{-1}, whereas the speed of fast solar wind ranges between about 500 km s^{-1} and 800 km s^{-1} (Srivastava & Schwenn, 2000). During the Skylab era in 1973, the coronal holes on the Sun are identified as the sources of fast solar wind (Krieger et al., 1973). In particular, the fast solar wind

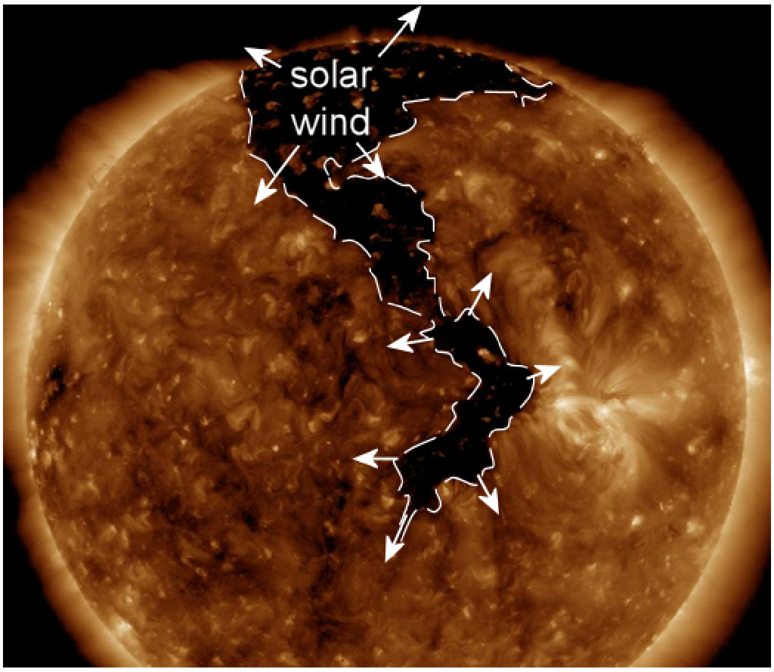

Figure 1.5: Observation of Sun in extreme ultraviolet wavelength (193 Å passbands) as captured by the Solar Dynamics Observatory on 13 August 2018. The contoured region marked by the white dashed line denote a coronal hole which is extended from the north pole to the lower latitude of the Sun, spewing high-speed solar wind into space. The high speed solar wind originated from the low latitude region of the coronal hole, is the potential candidate for the formation of Earth-impacting CIRs that may cause geomagnetic disturbances (`https://spaceweather.com/archive.php?day=14&month=08&year=2018&view=view&PHPSESSID=123o552t3ke5q1uhcjqjnn0r15`).

originated from low latitude coronal holes on the Sun (Figure 1.5), are the potential candidates that can give rise to formation of co-rotating interaction regions (CIRs) which can hit Earth and may cause space-weather disturbances.

As the solar wind propagates out into the interstellar medium (ISM), its speed abruptly slows down from supersonic to sub-sonic at a certain distance from the Sun, known as the termination shock. The twin spacecraft Voyager 1 and Voyager 2, which were launched in 1977, passed through the termination shock at ≈ 94 AU and 84 AU from Sun in 2004 (Stone et al., 2005) and 2007 respectively (Richardson et al., 2008; Burlaga et al., 2008). The region beyond the termination shock is the heliosheath, where the pressure balance occurs between the solar wind and ISM. The outer boundary of the heliosheath where the solar wind can not expand anymore, is the heliopause which is the end boundary of the heliosphere (Figure 1.6). In general, the heliosphere refers to the region dominated by the solar wind

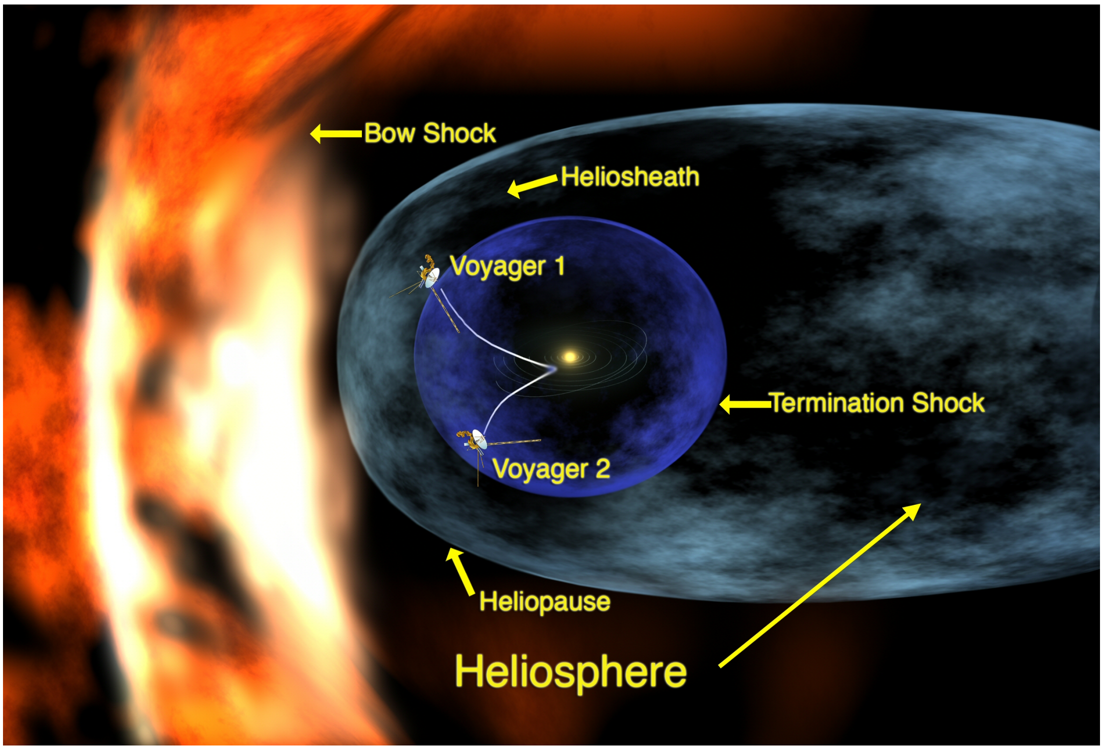

Figure 1.6: Schematic illustration of the heliosphere depicting termination shock, heliosheath, heliopause and bow shock. Image credit: NASA

around Sun. On 25 August 2012, Voyager 1 crossed the heliopause at a distance of 121 AU from the Sun (Cowen, 2012) and became the first spacecraft to enter into the ISM.

1.4 Space Weather Drivers

Solar flares, coronal mass ejections (CMEs) and the co-rotating interaction regions (CIRs) are the main solar origins of the space weather. The consequences of the space weather events associated with the aforementioned solar sources, can be dangerous for space-borne and ground-based technological systems as discussed in Section 1.2. A brief description and observational aspects of these space weather drivers are presented in the following sections.

1.4.1 Solar flares

Solar flares are the one of the most violent explosive phenomena occurs in solar atmosphere. Observationally, it is defined as the sudden brightening of any emis-

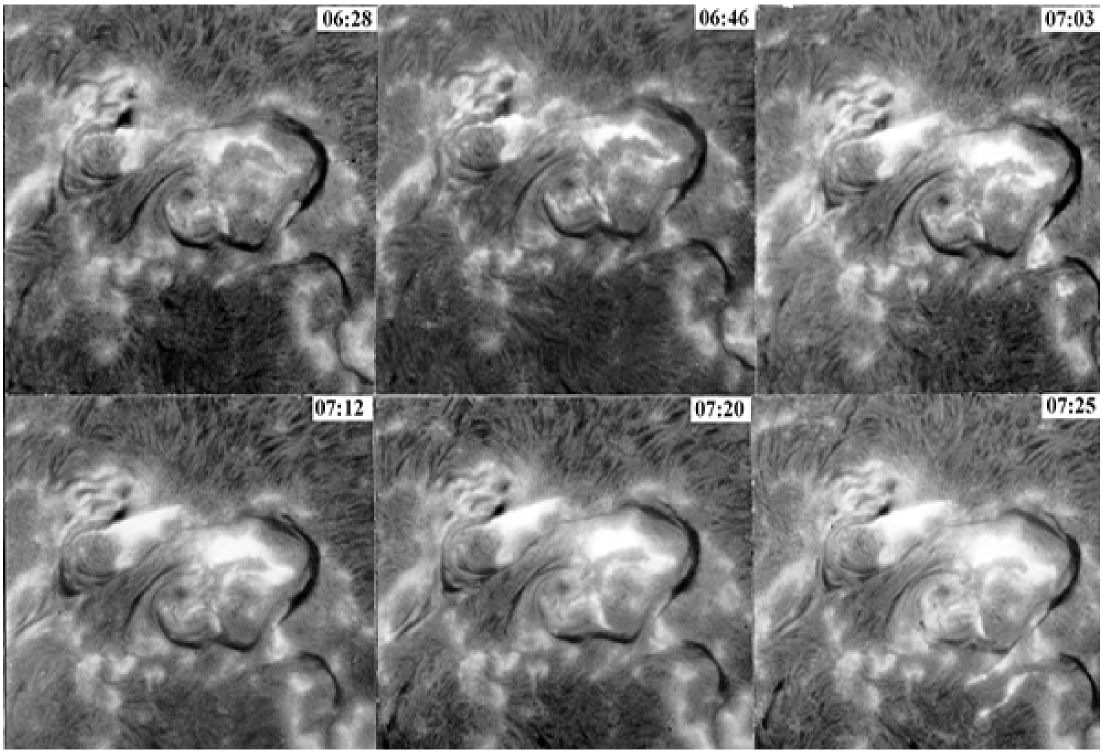

Figure 1.7: A two-ribbon H-alpha flare observed by Udaipur Solar Observatory on 3 March 1981 in the neighborhood of a 'S' shaped filament which can be seen as dark thread like structures.

sion across the electromagnetic spectrum, releasing an energy from 10^{28} to 10^{34} ergs at a time scale of seconds to several tens of minutes (Benz, 2008).

The first observation of solar flare was reported by R.C. Carrington and R. Hodgson on 1 September 1859. They observed localized and minute-long brightenings on the solar photosphere in white light continuum, which is popularly known as the "Carrington white light flare". This event was associated with an extreme space weather consequence as on 2 September 1859, a powerful geomagnetic storm was observed, which is the largest geomagnetic storm ever recorded. Within a few years after the observation of white light flare, the reports of solar flares became much more frequent when the observations were started to study the Sun in the Hα line originating in the solar chromosphere. Figure 1.7 depicts the observation of an Hα flare imaged by the Udaipur Solar Observatory on 3 March 1981. With the advancement in space-based instrumentation, now the multi-wavelength imaging of solar flares are possible with high spatial resolution and high temporal cadence (Figure 1.8).

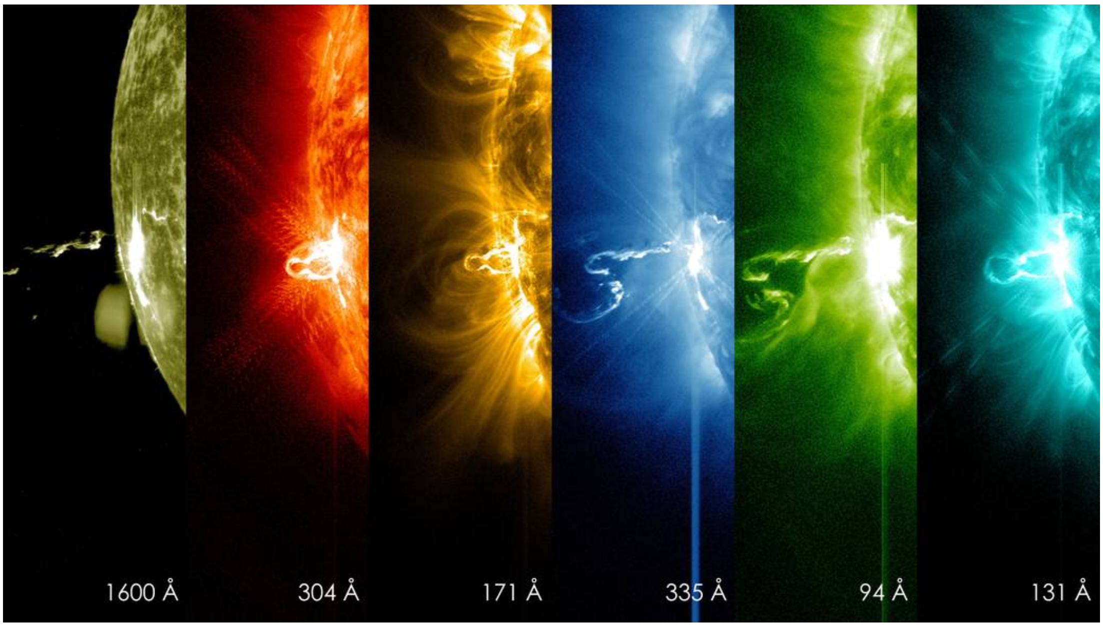

Figure 1.8: Multi-wavelength observation of a solar flare on 24 February 2014 by the Solar Dynamics Observatory (SDO) in EUV wavelengths. The brightening observed on the left limb of the Sun in each panel refers to the location of the flare. Above the flaring location the hot solar material can be seen in eruptive phase. Image credit: NASA/SDO

The different phases of flare energy release are broadly classified as pre-flare, impulsive, flash and decay phases presented schematically in Figure 1.9. During the preflare phase, the coronal plasma in the flaring region slowly heats up and becomes visible in soft X-rays and EUV. A large number of energetic ions and electrons is accelerated during that phase, which hits the thick chromosphere. As a consequence, the hard X-ray footpoint sources appear at the chromospheric altitude (Hoyng et al., 1981). During this process, some high-energy particles are also trapped in the magnetic field which give rise to intensive emissions in the radio band. The thermal soft X-ray and Hα emissions reach their peak after the impulsive phase, when energy is released more gently. The phase of rapid increase in the Hα light curve is known as the flash phase. This phase largely coincides with the impulsive phase, although the Hα emission may peak later. In the decay phase, the lower coronal plasma returns back nearly to its original state. However, in the high corona (> 1.2 R$_\odot$), the particles are continuously accelerated due to the plasma ejections and shock waves. These accelerated particles result in meter wave radio bursts and energetic particle events.

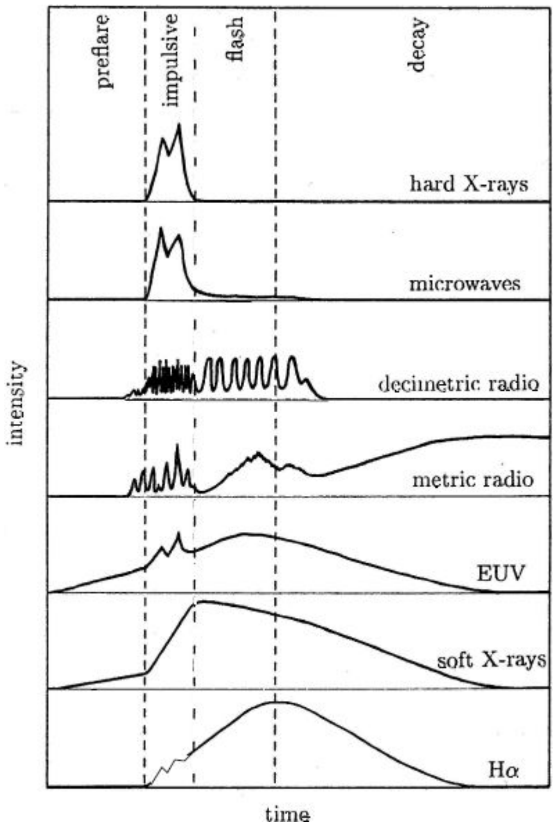

Figure 1.9: A schematic profile of the temporal evolution of flare intensity in different wavelengths. The vertical dashed lines mark the different phases of solar flare (adapted from Benz, 2008).

1.4.2 Coronal mass ejections

Coronal mass ejections (CMEs) are gigantic clouds of magnetized plasma that are routinely expelled from the Sun into the heliosphere and sometimes cause the most extreme space weather effects at Earth (Tsurutani et al., 1988; Gonzalez et al., 1999; Huttunen et al., 2005; Schwenn, 2006; Yurchyshyn et al., 2005; Gopalswamy et al., 2008). In order to understand its origin and space-weather consequences, CMEs are studied extensively through both the remote sensing and in-situ observations.

1.4.2.1 Remote sensing observations

The remote sensing observations reveal the CMEs as the large transient structures in solar corona. As the coronal density is very low with respect to the solar photosphere, the intense light comes from the solar photosphere needs to be blocked by artificial occulter in order to see any feature in the solar corona (Howard, 2011,

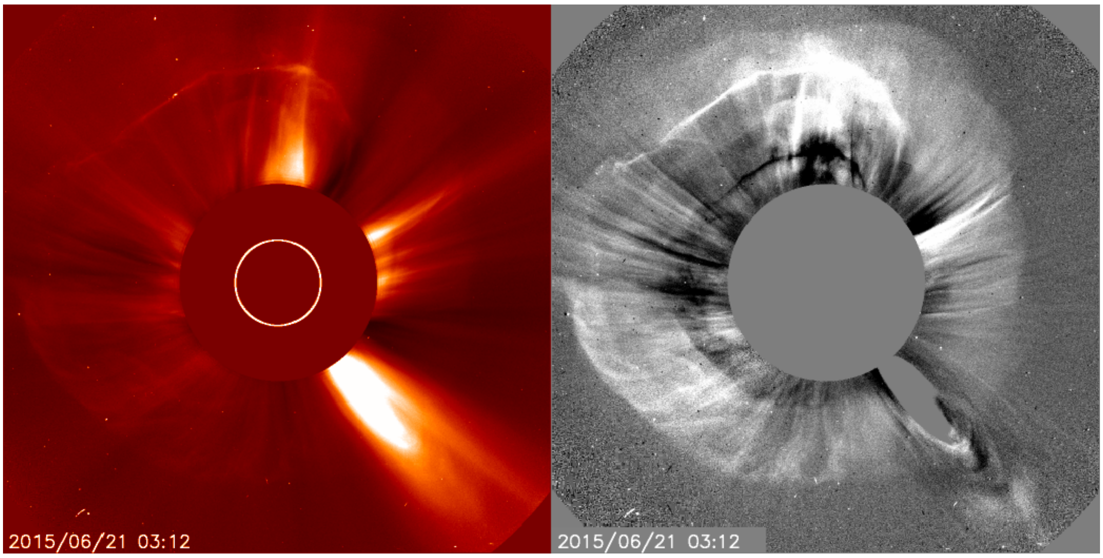

Figure 1.10: Observation of a halo CME on 21 June 2015 as captured by the Solar and Heliospheric Observatory (SOHO). Compared to the direct image as shown in left panel, the halo CME can be seen more clearly in the difference image (right panel), which is created by subtracting two consecutive frames. Credit: ESA&NASA/SOHO

and references therein). The imaging instrument that uses an artificial occulter to block the photospheric light in order to image the solar corona, is called a coronagraph. The light coming from the solar photosphere is Thomson-scattered from the free electrons in coronal and heliospheric plasma, which can be imaged through solar coronagraphs. The density structure of CMEs are relatively faint with respect to background corona, but much more transient. Therefore, CMEs are typically identified by applying some form of suitable background subtractions.

The first space-based observations of CMEs were made in the early 1970s by the OSO-7 coronagraph (Tousey, 1973). Afterwards, the CME observations with a better quality and longer periods, were made by Skylab (1973 – 1974, Gosling et al., 1974), P78-1 (Solwind) (1979-1985, Sheeley et al., 1980), and Solar Maximum Mission (SMM) (1980; 1984 – 1989, House et al., 1981). A major breakthrough in CME observations came in late 1995, when SOHO was launched (Domingo et al., 1995). Two of the three LASCO coronagraphs onboard the SOHO spacecraft continue to take observations. Another major advancement in this field occurred late in 2006, when twin STEREO spacecraft (Howard et al.,

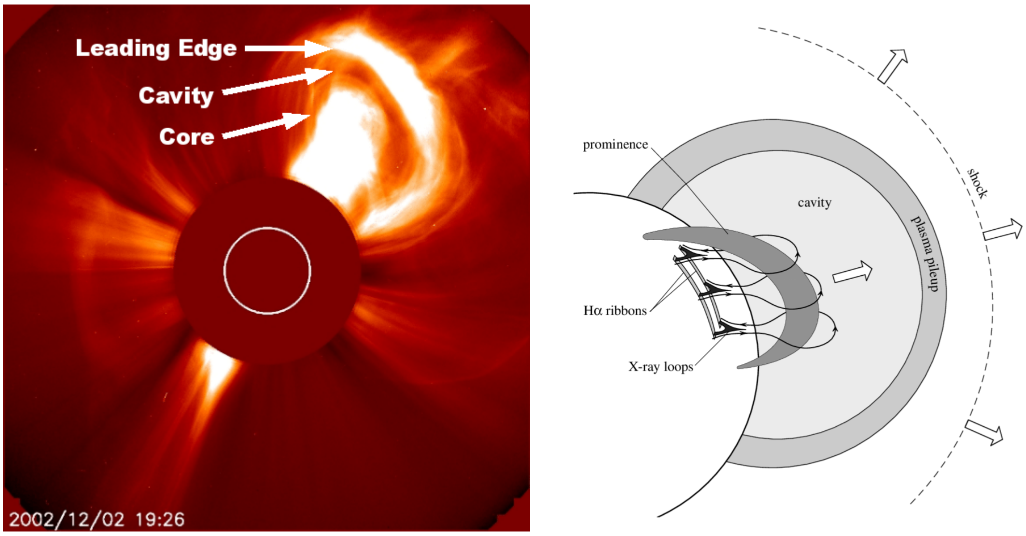

Figure 1.11: Left panel: An example of classical three part structure of a CME. The leading edge, core and cavity are indicated (Riley et al., 2008). Right panel: A standard model for an erupting CME (Forbes, 2000).

2008) started to provide multi-vantage point observations of CMEs. The space-based remote-sensing observations of CMEs were complemented by the ground-based facilities that include the K-coronameter in Mauna Loa Solar Observatory (MLSO) (Fisher et al., 1981; Koomen et al., 1974) and green line observations from the coronagraphs at Sacramento Peak, New Mexico (Demastus et al., 1973) and Norikura, Japan (Hirayama & Nakagomi, 1974). Apart from the white-light coronagraphic imaging, the observations of the CMEs were also made in the interplanetary space using the method of interplanetary radio scintillation (1964 — present, Hewish et al., 1964; Houminer & Hewish, 1974; Vlasov, 1981). However, the white light observations of CMEs are more advantageous over radio, infrared or ultra-violet observations as the Thomson scattering is independent of the wavelength and temperature, and depends only on the observed electron density (Hundhausen, 1993).

The white light coronagraphs capture the two dimensional (2D) plane-of-sky projection of the three dimensional (3D) morphological structure of CMEs. As the brightness of Thomson scattered light attains the maximum when the scattering angle becomes ≈ 90° with respect to the observer, the white light coronagraphic images are mostly sensitive to the features that lie on the plane-of-sky. Therefore the morphology of the CME as seen by the observer depends on the viewing angle subtended by the observer and the propagation direction of the CME. The CMEs that are launched towards or away from the Sun, appear as 'halo' with respect to the observing coronagraph on board the near-Earth spacecraft (Figure 1.10). According to the nomenclature, the CMEs having apparent angular width ≈ 360° are called as 'halo' CMEs, whereas, the CMEs with angular width less than 360° but greater than 120° are known as 'partial halo' (Schwenn, 2006; Webb & Howard, 2012). The CME associated phenomena like flares (Feynman & Hundhausen, 1994), prominence eruptions (Hundhausen, 1999), coronal dimming (Sterling & Hudson, 1997) and arcade formation (Hanaoka et al., 1994) which can be observed on the solar disk, are particularly important to determine whether a 'halo' CME is Earth directed or a backside event. The front side halo CME events are extremely important in space weather perspective as they tend to be more geo-effective than the CMEs that are launched from close to the solar limb. Several front side CME events have also been observed which lack any association with the solar surface activities (Robbrecht et al., 2009; Ma et al., 2010). These CMEs, having no easily identifiable signatures of their source region on the Sun, are known as "problem or stealth CMEs".

The CMEs which are launched from close to the solar limb, are known as 'limb' CMEs. A typical limb CME observed near the Sun often appears as "three-part" structure, which is indicative of the internal magnetic structure of CMEs. The three-part structure comprises of a bright frontal loop known as the 'leading edge', followed by a 'dark cavity' which is embedded with a 'brighter core' at the lower end (Figure 1.11). The magnetic field strength inside the cavity is probably much higher than the background corona, whereas the plasma density inside this region drops down to a much lower value. The internal magnetic structure of the dark cavity is generally considered as the helical magnetic field, called as magnetic flux ropes (MFRs) (Webb & Howard, 2012). If the CME axis approximately aligns along the line-of-sight, one can observe closed density structures inside the dark cavity, indicating winding of the field lines that builds the twisted magnetic structures of the MFRs. The bright frontal part of the CME appears due to the piled up of plasma material swept out by the erupting MFR or the presence of pre-existing plasma material trapped in the overlying magnetic fields (Illing & Hundhausen, 1985; Riley et al., 2008). The bright core embedded at the lower end of the cavity represents the filament material carried by the erupting MFR.

1.4.2.2 In-situ observations

Once the CMEs propagate out into the heliosphere, its interplanetary counterpart is termed as interplanetary coronal mass ejections (ICMEs) (Dryer, 1994; Zhao & Webb, 2003). The in-situ observations of ICMEs reveal that their magnetic and plasma properties are different than that of the ambient solar wind. The identification of ICME signatures in the in situ data can be made using the following observed plasma properties.

Magnetic field signatures of ICMEs

The increased field strength and reduced variability in magnetic field are the main in situ signatures of ICMEs. Figure 1.12 shows a schematic picture and an example of solar wind data during an ICME event. The ICME can be clearly identified from the ambient solar wind by the enhanced magnetic field in the in situ data as shown in Figure 1.12. The region bounded by the two red solid lines in the solar wind data, denotes the observed ICME. The magnetic field vectors of the ICME show coherent rotation, which indicate the three dimensional magnetic structure of the ICME as the helical magnetic flux ropes. However, an ICME identified with magnetic flux rope characteristics may not always associate with a drop in temperature or plasma beta (Rouillard, 2011). A subclass of ICMEs which are detected with the following in situ properties are called as MCs (Burlaga et al., 1981).

1. Enhanced magnetic field with strength > 10 nT
2. Smooth rotation of the magnetic field vectors over a large angle in about one day
3. Low proton temperature and plasma beta (i.e., the ratio of the plasma to magnetic pressure).

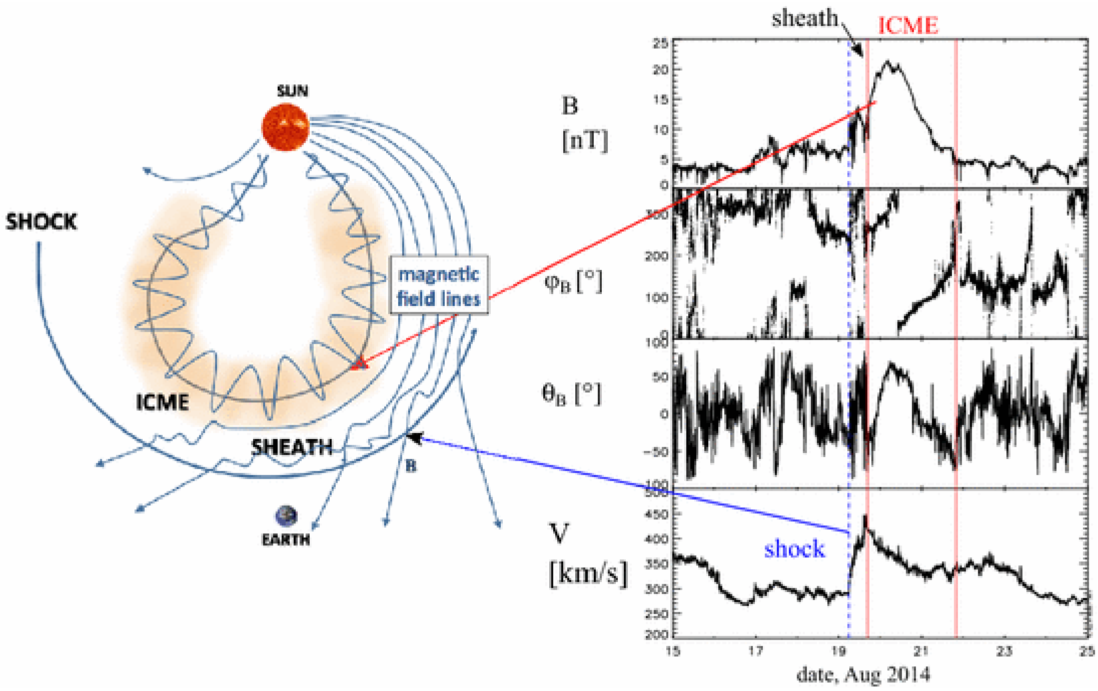

Figure 1.12: Left panel: A schematic picture of an ICME associated with a fast forward shock (arc), and the sheath region. Right panel: In situ observations of an ICME from the ACE spacecraft located at the Lagrangian point L1. The panels show from top to bottom: the magnetic field magnitude, the longitude and latitude angles of the magnetic field in the Geocentric Solar Magnetospheric (GSM) coordinate system, and the solar wind speed. The blue dashed line marks the shock and the ICME is bounded by the pair of red lines (adapted from Kilpua et al., 2017a)

Interestingly, one to one correspondence can be made between the dark cavity observed in the white light CME morphology and the associated ICME if observed as MC in the in situ data, as both represent the same flux rope that evolves from Sun to Earth. If a CME propagates with a speed higher than the characteristic speed of the ambient medium, then it produces a fast forward shock ahead of it. Such shocks are wide and may span over approximate two times the value of angular width of the associated ICME (Richardson & Cane, 1993). A forward shock can be identified in in situ observations, based on a simultaneous enhancement in the temperature, density, speed and magnetic field in the plasma. The shock is usually followed by a sheath region before the leading edge of the ICME/MC. The schematic picture in Figure 1.12 shows the shock and sheath region ahead of the ICME. The blue dashed line drawn on the plot of in-situ data (Figure 1.12), indicates the shock arrival as both the magnetic field

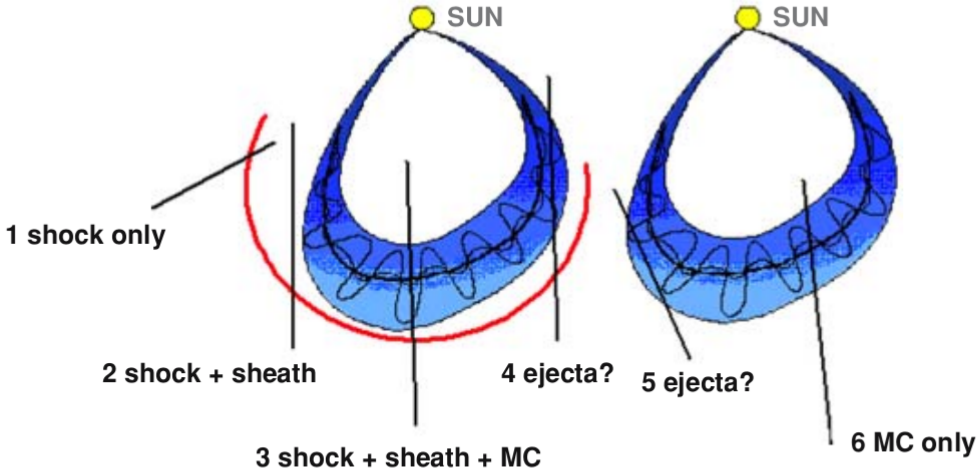

Figure 1.13: Six possible tracks of an observing spacecraft through an ICME with (left) and without (right) a leading shock. Track 1 encounters the shock only, whereas track 2 passes through both the shock and sheath region. Track 3 corresponds to a situation when the CME nose propagates towards the in situ spacecraft. In this case, the spacecraft encounters the shock, sheath, and the magnetic cloud. Trajectory 4 passes through the shock, sheath, and through the edge of the MC. Therefore, the spacecraft in track 4 may not encounter the flux rope signature in the ICME. Tracks 5 and 6 are similar to 4 and 3, respectively, where there is no shock ahead of the CME possibly due to the slow speed of the CME. (adapted from Gopalswamy, 2006)

and the velocity field shows sudden discontinuity at this point. The region in between the blue dashed line and the red solid line, is the sheath region identified as turbulent and compressed regions of solar wind having strong fluctuations in magnetic fields which last for several hours (Zurbuchen & Richardson, 2006, and references therein). The sheath regions provide a unique natural plasma laboratory to study many important plasma properties such as turbulence and magnetic reconnection. Both the sheath and ICMEs may drive space weather disturbances. In particular, sheaths and ICMEs are the only interplanetary structures that can cause extreme geomagnetic storms (Kilpua et al., 2017a).

It is important to note that all the ICMEs may not show flux rope signatures in their in situ observations, and therefore cannot be categorized as MC. These ICMEs which lack the MC signatures are known as non-cloud ejecta. Importantly, all ICMEs may have the flux rope structures, but their in-situ observations may lack that coherent magnetic structure depending on the path of the observing spacecraft as shown in Figure 1.13 (Kim et al., 2013; Gopalswamy, 2006).

Temperature characteristics of ICMEs

As the ICMEs evolve in the interplanetary space it continue to expand. Due to expansion, the proton temperature inside the ICME decreases with respect to the ambient solar wind. The expansion phase of the ICME during its passage over the spacecraft is also reflected in its in situ velocity profile. The ICME leading edge shows higher speed compared to its trailing edge and the speed monotonically decreases in between the two edges (Klein & Burlaga, 1982). The average speed of the leading and trailing edge gives the expansion speed of the ICME. It is also observed that the electron temperature (T_e) inside the ICME is greater than proton temperature (T_p). (Richardson et al., 1997) reported that the ratio of electron to proton temperature, i.e. $T_e/T_p > 2$ is a good indicator of an ICME.

Compositional signatures of ICMEs

The compositional signatures of an ICME as obtained from the in situ observations, is different than the ambient solar wind medium. The alpha to proton ratio (He^{+2}/H^{+}) inside an ICME has been found to be higher ($> 6\%$) than that in normal solar wind. This indicates that an ICME also contains material from the solar atmosphere below corona (Hirshberg et al., 1971; Zurbuchen et al., 2003). The in situ observations also suggest that an ICME is associated with an enhanced value of $^{3}He^{+2}/^{4}He^{+2}$ and heavy ion abundances (especially iron) with enhanced charge states (Lepri et al., 2001; Lepri & Zurbuchen, 2004). Importantly, the enhanced charge states of iron observed in ICME plasma, suggest that the solar origin of CMEs is different from that of the ambient solar wind. During the initiation phase of CMEs, the high energy release due to the magnetic reconnection in solar atmosphere only can result in those high charge states of iron carried by the ICMEs, connecting the ICMEs to its solar origin (Bemporad et al., 2006; Ko et al., 2013; SONG et al., 2015). It is also observed that the ICMEs show relative enhancement of O^{+7}/O^{+6} (Hundhausen et al., 1968; Henke et al., 1998; Richardson & Cane, 2004). However, ICMEs can also be observed with unusual low ion charge states, e.g., the abundances of singly-charged helium well above the normal values observed in the solar wind (Schwenn et al., 1980; Burlaga et al., 1998; Skoug et al., 1999). Such low charge states suggest that the plasma inside those ICMEs is possibly associated with the cool and dense prominence material (Gopalswamy et al., 1998; Lepri & Zurbuchen, 2010; Sharma & Srivastava, 2012).

1.4.3 Co-rotating interaction regions

Co-rotating interaction regions (CIRs) are one of the space weather drivers that may enhance the geomagnetic activity (Kilpua et al., 2017b, and references therein). The stream of high speed solar wind originating from a coronal hole at the Sun interacts with the preceding solar wind, forming a region of compressed plasma. As the solar wind plasma is frozen into the solar magnetic field, this interaction region is twisted approximately into an Archimedean spiral due to the solar rotation. Since the coronal holes persist for a long duration up to several months, the high-speed streams and the interaction region tend to sweep past an observer at regular intervals of approximately the solar rotation period ($\approx$ 27 days). Hence, the interaction regions are popularly known as corotating interaction regions (CIRs).

Figure 1.14 depicts a schematic picture of two high speed streams co-rotating with the Sun, as viewed on the ecliptic plane and the associated temporal variation in the solar wind parameters at 1 AU. The enhancement in plasma density and magnetic field strength observed in the solar wind parameters are indicative of compressed plasma in the vicinity of the positive gradient in the solar wind speed (Belcher & Davis, 1971). This enhancement in the plasma parameters corresponds to the leading edge of the interaction region. The whole structure follows an approximately an Archimedean-spiral like configuration.

Compression of the solar wind flow in CIRs may result in an enhanced out-of-ecliptic field components, which may generate southward pointing IMF, causing geomagnetic disturbances at Earth. Due to the co-rotating nature with the long lived coronal holes, CIRs are also responsible for recurrent geomagnetic storms (Richardson, 2018).

This thesis mainly focuses on the CMEs as the major solar origin of space weather disturbances. In this regard, a brief introduction to the current under-

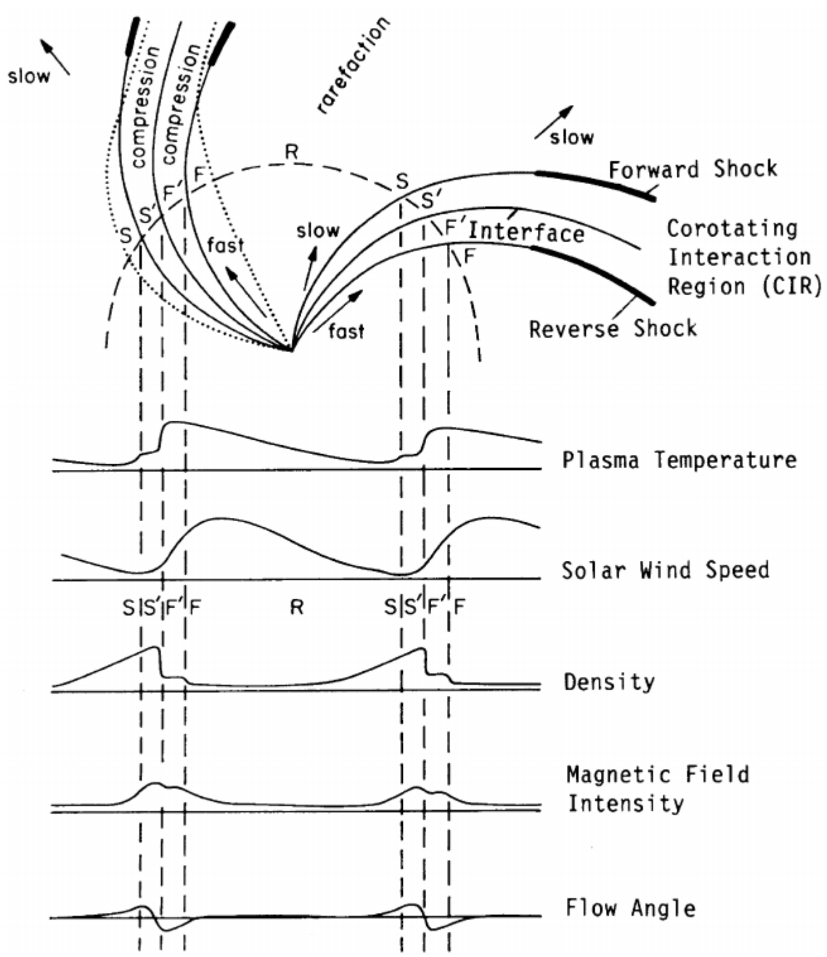
slow
compression
compression
rarefaction
R
slow
Forward Shock
S
S′
F′
F
S′
S
fast
slow
F′ Interface
F
Corotating
Interaction
Region (CIR)
fast
Reverse Shock
Plasma Temperature
Solar Wind Speed
S S′ F′ F R S S′ F′ F
Density
Magnetic Field
Intensity
Flow Angle

Figure 1.14: Schematic picture of two high-speed streams co-rotating with the Sun, leading to the formation of compressed plasma due to interaction with the slow solar wind. The flow streamlines/magnetic field lines in the slow and fast solar wind are represented by the dotted lines. The associated changes in solar wind parameters observed at 1 AU are also shown. The different regions are indicated by S (ambient slow solar wind), S′ (compressed and accelerated slow solar wind), F (compressed and decelerated fast-stream plasma) and F′ (ambient undisturbed fast-stream plasma). Beyond 1 AU, the trailing and leading edges of the expanding CIRs typically steepen into reverse and forward shocks respectively (adapted from Belcher & Davis, 1971).

standing of origin, evolution and space weather consequences of CMEs has been discussed in the following sections.

1.5 Origin and Initiation Mechanism of CMEs

Understanding the origin and initiation mechanism of CMEs is crucial for space weather forecasting. CMEs can be accompanied by solar flares occurring on the complex active regions on the Sun or the prominence eruptions. The physical properties of CMEs, like the initial speed, direction, width, mass, orientation and strength of magnetic field, are the key parameters to forecast the severity of geomagnetic storms (Srivastava & Venkatakrishnan, 2002; Gopalswamy et al., 2010; Dumbović et al., 2015, and references therein). Importantly, the initial physical properties of CMEs depends on its association with flares or prominence eruptions.

1.5.1 Association of CMEs with solar flares

The observations of flare associated CMEs reveal that flares and CMEs can be considered as two different manifestations of the same energy release process (Harrison, 1995; Zhang et al., 2001; Harrison, 2003). Zhang et al. (2001) reported that

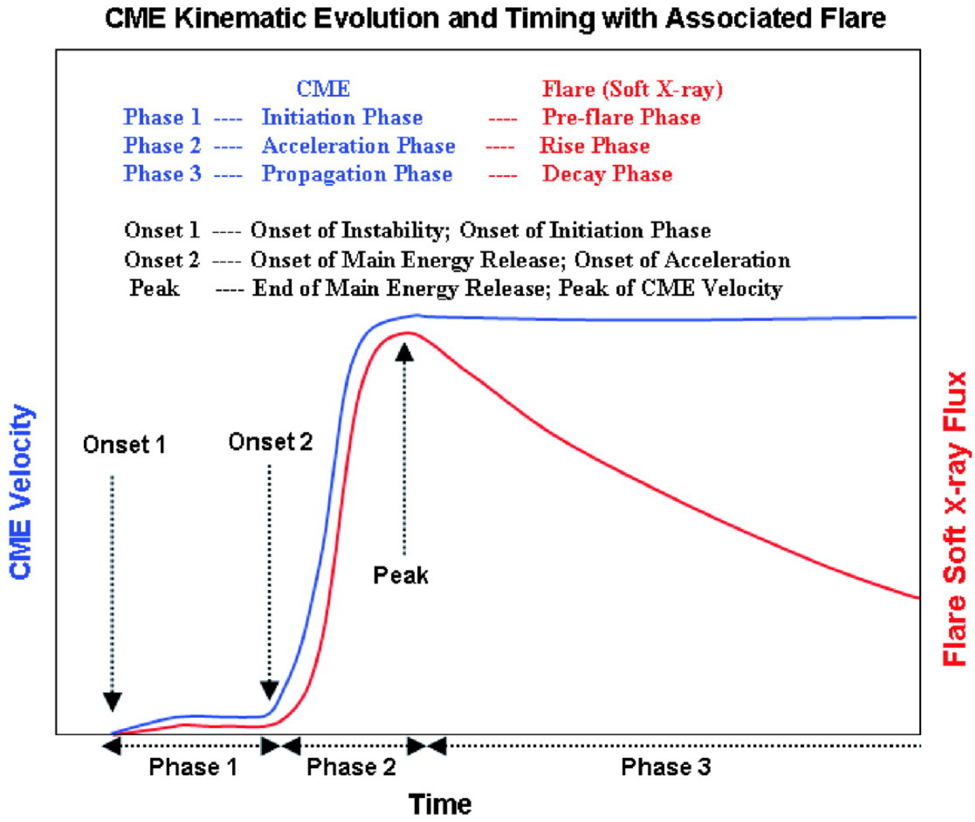
CME Kinematic Evolution and Timing with Associated Flare
CME
Flare (Soft X-ray)
Phase 1 ---- Initiation Phase ---- Pre-flare Phase
Phase 2 ---- Acceleration Phase ---- Rise Phase
Phase 3 ---- Propagation Phase ---- Decay Phase
Onset 1 ---- Onset of Instability; Onset of Initiation Phase
Onset 2 ---- Onset of Main Energy Release; Onset of Acceleration
Peak ---- End of Main Energy Release; Peak of CME Velocity
Onset 1
Onset 2
Peak
CME Velocity
Flare Soft X-ray Flux
Phase 1
Phase 2
Phase 3
Time

Figure 1.15: The different phases of CME kinematics and its relation with the temporal evolution of the associated GOES soft X-ray flux. The initiation, acceleration, and propagation phase of the CME kinematics are associated with the preflare, rise, and decay phase of the associated flare, respectively (reproduced from Zhang & Dere, 2006).

the fast acceleration phase of CMEs in the inner corona is temporally correlated with the rise time of the associated soft X-ray flares (Figure 1.15). Temmer et al. (2008) also reported that the peak of CME acceleration profile and the hard x-ray emission occurs simultaneously within 5 minutes. These results suggest that both of the phenomena to be connected through the same physical process, possibly via magnetic reconnection (Lin & Forbes, 2000; Priest & Forbes, 2002). Notably, CMEs may also occur without any association with solar flares. However, it is important to note that for some cases, the flare association may not be observed if the source region is behind the solar limb or the associated soft X-ray brightening is very weak (Hiei et al., 1993; Wu et al., 2002; Zhou et al., 2003). On the other hand, many flares can occur without any CMEs. Statistical studies show that, ≈ 70 % of C-class, ≈ 44 % of M-class, and ≈ 10 % of X-class flares have no association with CMEs (Yashiro et al., 2006; Wang & Zhang, 2007).

1.5.2 Association of CMEs with prominence eruptions

CMEs can be also associated with solar filament/prominence eruptions, sometimes without showing any prominent soft x-ray emissions that can be registered as flares. Prominences are cool and dense plasma material suspended in the corona and appear as bright in emission at the limb. The same structure, when observed on the solar disk in Hα, appear as dark meandering ribbon like structures called filaments. Solar filaments can remain in quiescent phase for several hours to days. It is believed that either the highly sheared magnetic field or the twisted magnetic flux ropes are key magnetic structures within which the prominence plasma can be supported (Martin, 1998; Wang & Muglach, 2007; Gaizauskas, 2008). When the axis of the filament carrying flux ropes aligns along the line of sight at the solar limb, the inner void part of the flux rope appears as dark cavity. These cavities are ubiquitous in both white light (Waldmeier, 1970), soft X-ray (SXR) (Vaiana et al., 1973) and extreme ultraviolet (EUV) (Schmahl, 1979) observations (Figure 1.16). During the eruption, the low coronal cavities form the dark cavity structure in white light observations and the prominence material lying at the lower end of the cavity becomes the bright core

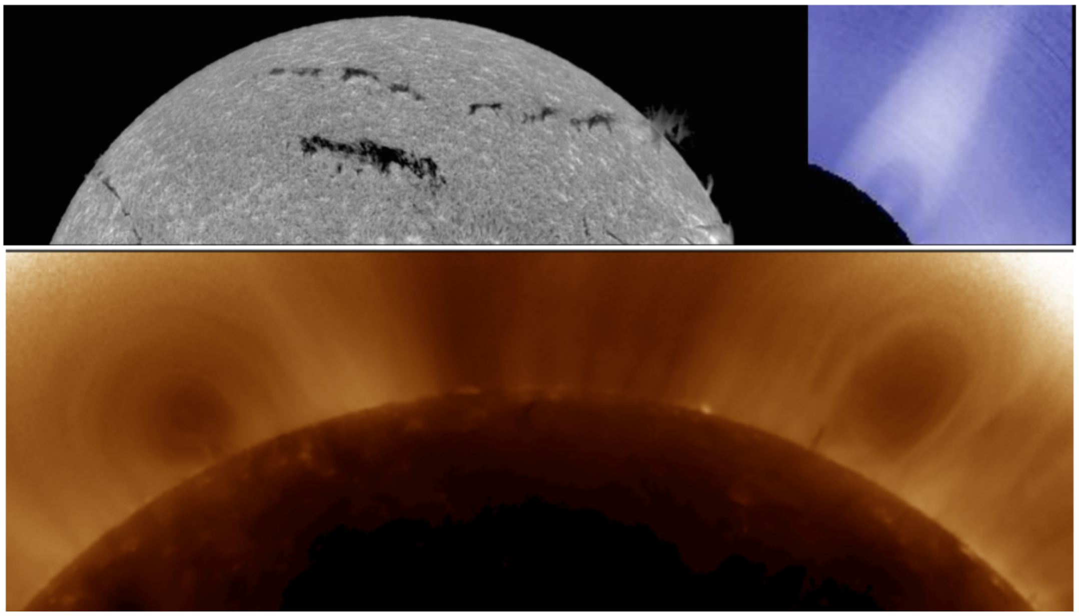

Figure 1.16: A polar crown filament (PCF) observed on 22 July 2002 in Hα by Big Bear Solar Observatory (BBSO) (top left) and associated coronal cavity (top right) observed in white light by Mauna Loa Solar Observatory (MLSO/Mk4). An example of EUV cavity associated with PCF can be seen on both the limb as observed by Solar Dynamics Observatory/Atmospheric Imaging Assembly (SDO/AIA) in 193 Å passbands (reproduced from Gibson, 2015).

of the CME, manifesting two of the three part structure of CMEs (Gibson & Fan, 2006; Vourlidas et al., 2013; Howard et al., 2017).

1.5.3 Low coronal signatures of CME eruption

Although CMEs are generally observed by occulting the entire solar disk, it may leave spectacular low coronal signatures that can be observed from solar disk observations. The lower coronal observations reveal that the source region of the CMEs may show slowly evolving pre-eruptive plasma structures in the form of ‘S’ shaped hot channels seen at EUV and/or soft X-ray wavelengths. These ‘S’ shaped hot channels are known as the sigmoids which have been studied extensively using observations obtained by Yohkoh/SXT (Moore et al., 2011; Green & Kliem, 2014), SDO/AIA channels (Liu et al., 2010; Zharkov et al., 2011) and STEREO/EUVI data (Bein et al., 2011; Patsourakos et al., 2013). In the wake of a CME eruption, the sigmoidal structure is reconfigured and results in unsheared magnetic loops, which is known as post flare arcades or

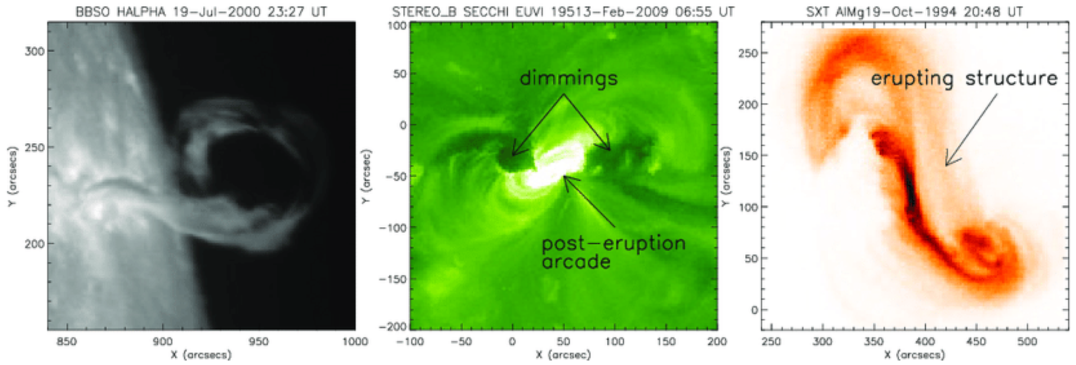
BBSO HALPHA 19-Jul-2000 23:27 UT
Y (arcsecs)
300
250
200
850
900
950
1000
X (arcsecs)
STEREO_B SECCHI EUVI 19513-Feb-2009 06:55 UT
Y (arcsec)
100
50
0
-50
-100
-150
-200
-100
-50
0
50
100
150
200
X (arcsec)
dimmings
post-eruption arcade
SXT AlMg19-Oct-1994 20:48 UT
Y (arcsecs)
250
200
150
100
50
0
250
300
350
400
450
500
X (arcsecs)
erupting structure

Figure 1.17: Lower coronal signatures of the occurrence of a CME. There are a variety of observational manifestations of CMEs including filament eruptions (left panel), post-eruption arcades (also called flare arcades, middle panel), dimming regions (middle panel) and rising EUV/soft X-ray structures (right panel) (reproduced from Green et al., 2018)

post-eruption arcade. Once the eruption is well underway, the EUV or soft X-ray observations reveal dimming regions around the source location of the CMEs due to the reduction in plasma density. These dimming regions are believed to be the footpoints of the expanding and erupting magnetic flux ropes associated with the CME eruption (Rust & Hildner, 1976; Sterling & Hudson, 1997; Zarro et al., 1999). Another interesting feature associated with CME eruptions are the EUV waves, which are best seen in running difference images at 195 Å passbands. These EUV waves are interpreted as fast mode MHD waves (Thompson et al., 1998). Figure 1.17 shows examples of various lower corona signatures that indicate the occurrence of a CME eruption.

1.5.4 Triggering mechanism of CMEs

Several studies have been carried out to understand the genesis of CMEs. However, the CME initiation mechanism still remains an elusive topic in solar physics. The current well accepted possible triggering mechanisms of CMEs are illustrated as follows.

1.5.4.1 Tether-cutting mechanism

Moore & Labonte (1980) proposed the tether cutting mechanism as one of the triggering mechanism of CMEs. The detail of this mechanism can be understood with the help of a schematic picture as depicted in Figure 1.18. The left panel shows the initial phase where a filament is suspended over highly sheared magnetic field lines, e.g., the field lines AB and CD, which probably form the sigmoids visible in soft x-rays. The lower lying highly sheared field lines are also accompanied with less sheared overlying field lines. Before the eruptive phase, all the field lines around the filament are in force free state, except those field lines that hold the filament material. As the magnetic shear increases, the positive leg of the field line CD comes close to the negative leg of the field line AB, forming a configuration of closed by anti-parallel field lines that generate a strong current sheet in between. As a result magnetic reconnection commences. Consequently, the field lines AB and CD reconnects to form a long field AD and a short lower lying loop CB. In this process, the field lines AB and CD, which act like tethers to support the filament material, are cut from being tied to the photosphere. Due to the reconnection outflow, the long loop AD further expands upward, and the small loop CB shrinks downwards. As the localized reconnection continues, the core field near AD pulls the filament upward and thereby stretching up the overlying magnetic field lines which lead to the formation of a elongated current sheet. This newly formed current sheet speeds up the reconnection further, which

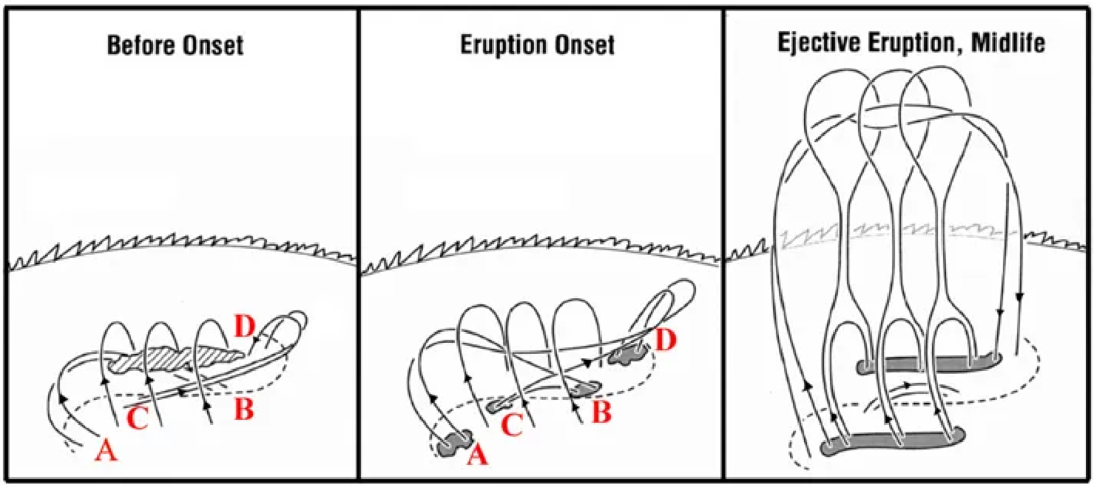

Figure 1.18: The tether-cutting scenario as the triggering mechanism for CMEs. Left panel: strongly sheared core field is accompanied by the less-sheared overlying field; Middle panel: The reconnection between field lines AB and CD triggers the core field to rise; Right panel: The rising core field stretches up the overlying field, forming a current sheet below the core field (adapted from Moore et al., 2001).

results in the filament eruption leading to form a CME. The filament eruption and the two-ribbon flare, preceded by precursor activities in the form of small Hα brightenings are the observational signatures that support the tether-cutting mechanism.

1.5.4.2 Flux cancellation model

Flux cancellation is a similar mechanism like tether-cutting, as proposed by van Ballegooijen & Martens (1989). They pointed out that the flux cancellation near the magnetic polarity inversion line of sheared arcades would give rise to the formation of helical field lines, i.e., a flux rope, which can support a filament structure. As a consequence of further flux cancellation, the previously formed filament erupts as depicted in Figure 1.19. Although the flux-cancellation and tether-cutting models are almost similar, the main difference between them is that the flux-cancellation mechanism refers to more gradual evolution, whereas the tether cutting mechanism is a relatively more impulsive process.

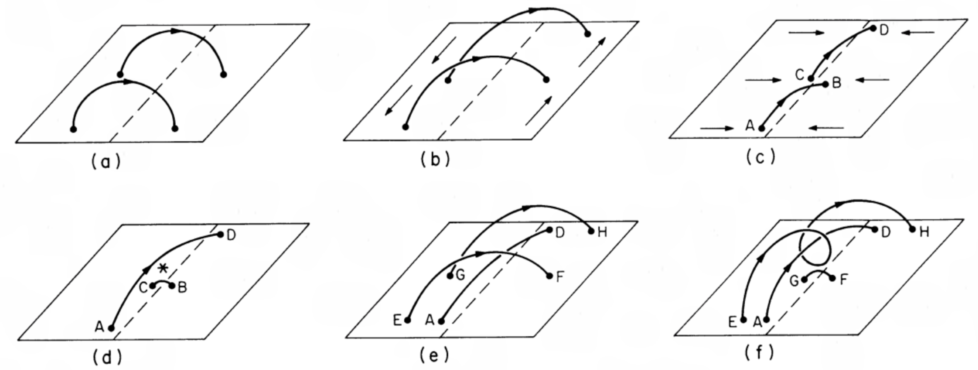

Figure 1.19: Flux cancellation in a sheared magnetic field. The rectangle represents the solar photosphere, and the dashed line is the neutral line separating two regions of opposite magnetic polarity, (a) Initial potential field; (b) sheared magnetic field produced by flows along the neutral line; (c) magnetic shear is increased further due to flows toward the neutral line; (d) reconnection produces long loop AD and a shorter loop CB which subsequently submerges; (e) overlying loops EF and GH are pushed to the neutral line; (f) reconnection produces the helical loop EH and a shorter loop GF which again submerges (adapted from van Ballegooijen & Martens, 1989).

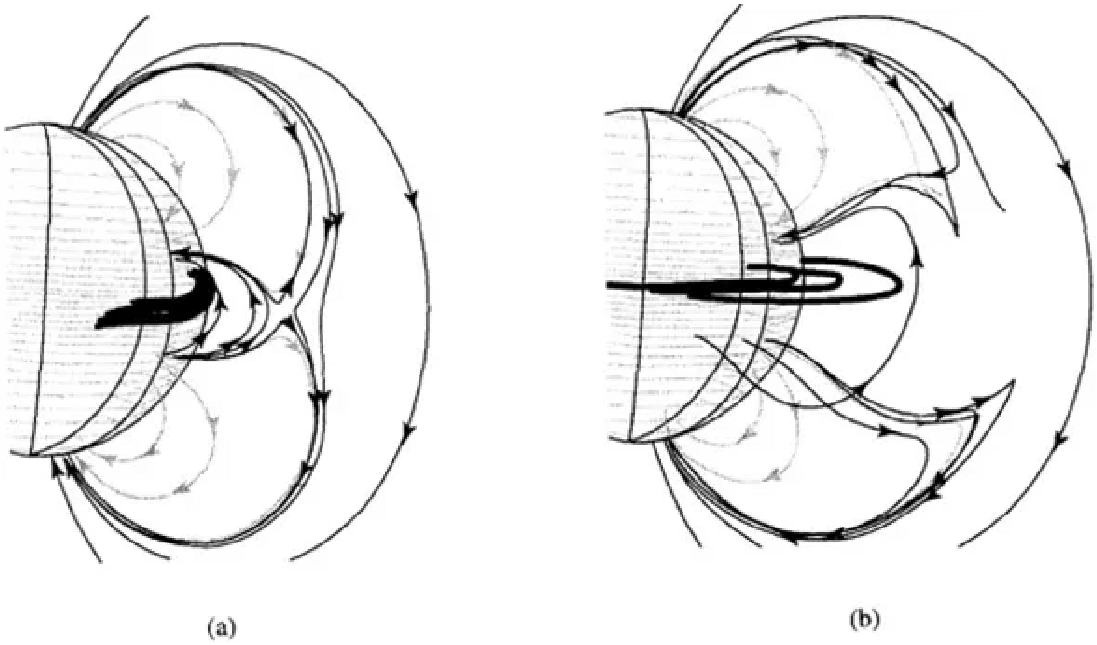

Figure 1.20: A schematic picture of magnetic field evolution in the breakout model. Magnetic reconnection above the central flux system removes the overlying field and results in the eruption of the core field as depicted by the thick lines (adapted from Antiochos et al., 1999).

1.5.4.3 Magnetic breakout model

Antiochos et al. (1999) proposed the magnetic breakout model, as shown in Figure 1.20. The initial magnetic configuration involves in this model consist of a quadrupolar topology, with a magnetic null point located above the central flux system. As the shearing motion goes on, the enhanced magnetic pressure causes the central flux system to inflate. As a result, the magnetic X-point above the central flux system distorts and becomes an elongated horizontal layer to form enhanced electric current. Once the stress is sufficiently large and the current layer is sufficiently thin, magnetic reconnection commences. Such a reconnection process removes the higher magnetic loops, which in turn triggers the eruption of the core field as depicted by the thick lines in Figure 1.20.

1.5.4.4 MHD instabilities

Since the time scale of the energy accumulation in coronal magnetic field is very long, whereas the flare and filament eruptions occur in a very short time scale, it was proposed that the triggering mechanism behind such energy release processes should be related to some kind of instabilities (Gold & Hoyle, 1960). Forbes (2000) describes various mechanisms of such instability processes. The photospheric motions and flux emergence govern the evolution of coronal magnetic field in a quasi-statical way, which may reach to a critical stage where the instability commences, resulting in an eruption. The well known instability mechanisms that are proposed to play an important role behind the CME initiation, are described as follows.

Kink instability

Kink instability is one of the ideal MHD instabilities, which can be developed in a twisted magnetic flux tube as observed through the numerical experiments by Sakurai (1976). Considering the line-tying effect of the solar photosphere, Hood & Priest (1979) found that there is a critical limit for twist (2π to π), above which the flux tube becomes unstable. Further considering the effect of external magnetic field, Török & Kliem (2005) showed that the kink instability would be suppressed after the initial development, if the overlying magnetic field decays slowly with height, resulting in a failed eruption. On the other hand, if the overlying field decays faster, then the kink instability would lead to an eruptive CME.

Torus instability

Torus instability is also one of the ideal MHD instability that can play a key role in the initiation of CMEs as proposed by Kliem & Török (2006). As the magnetic flux rope consists of helical magnetic structure, it carries an axial current. From the numerical experiments, it was shown that a current carrying ring is unstable against its expansion if the external potential field decays faster with height (Bateman, 1978). Further extending the study, Kliem & Török (2006) found a critical parameter called the decay index [n] which is defined as

$$n = -\frac{\partial \log(B_{\mathrm{ex}})}{\partial \log(h)} \ ,$$

where h is the height above the solar photosphere and B_{ex} is the external magnetic field. They found that if the flux rope rises to a certain height where the decay

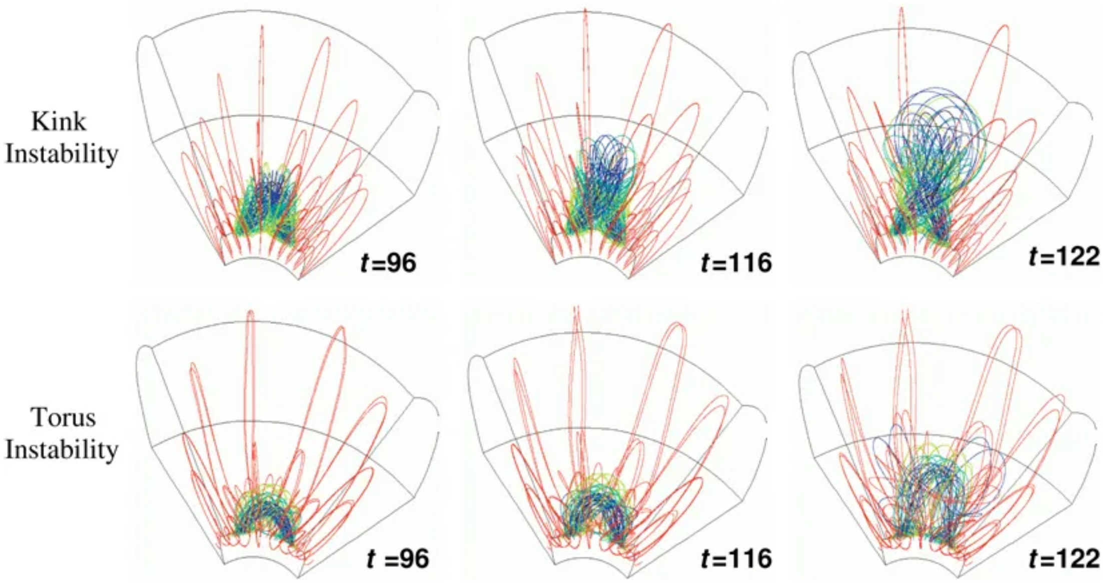

Figure 1.21: Top: the MHD simulation of the kink instability of a strongly-twisted flux tube emerging from the subsurface to the corona, where the pre-existing magnetic field declines slowly with height. Bottom: the MHD simulation of the torus instability of a weakly-twisted flux tube emerging into the corona, where the pre-existing magnetic field declines rapidly with height (adapted from Fan & Gibson, 2007).

index value reaches a critical limit (≈ 1.5), then the flux rope system would give rise to a CME eruption.

Fan & Gibson (2007) performed a 3D MHD simulation of the emergence of a flux rope from the subsurface into the magnetized corona, as depicted in Figure 1.21. They found that, when the background magnetic field decays slowly with height, a strongly twisted emerging flux tube may erupt through the arcade field via kink instability as depicted in top panels. Whereas, when the background magnetic field decays faster with height, a weakly twisted flux tube having twist below the threshold value for kink instability, can still erupt due to the torus instability.

Despite of the current understanding of various possible initiation mechanisms for the genesis of CMEs, it is still not clear whether the magnetic reconnection or ideal MHD instability plays a predominant role behind the eruption.

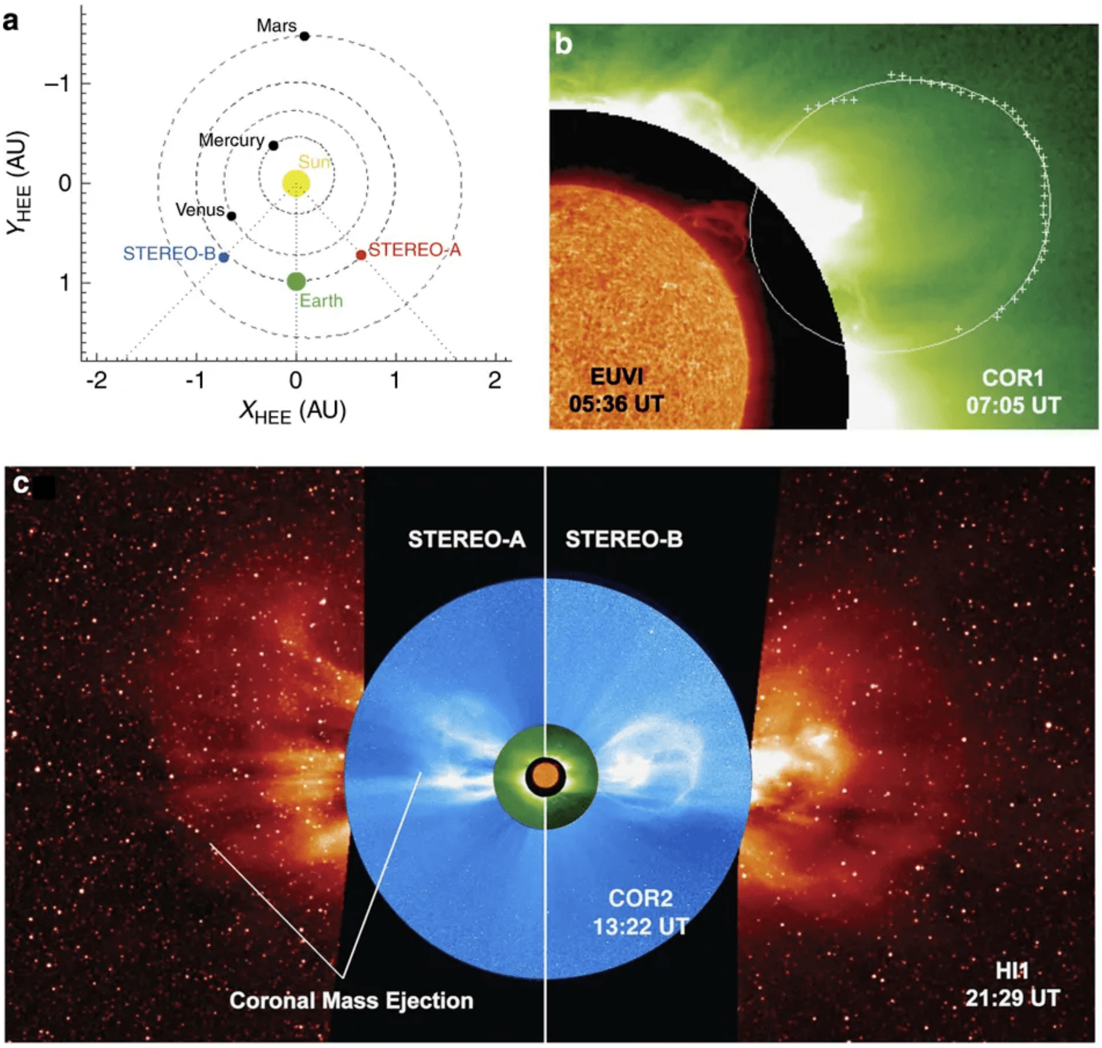
a
Mars
Mercury
Sun
Venus
STEREO-B
STEREO-A
Earth
Y_{HEE} (AU)
X_{HEE} (AU)
–1
0
1
-2
-1
0
1
2
b
EUVI
05:36 UT
COR1
07:05 UT
c
STEREO-A
STEREO-B
COR2
13:22 UT
HI1
21:29 UT
Coronal Mass Ejection

Figure 1.22: Panel (a) indicates the locations of the STEREO spacecraft, separated by an angle of 86.7° at the time of a prominence eruption observed in EUVI-B (panel b) at around 03:00 UT, which becomes the inner material of the CME. The multiscale edge detection and corresponding ellipse characterization are overplotted in COR1 (panel b). Panel (c) shows the Earth-directed CME being observed off the east limb in STEREO-A and off the west limb in STEREO-B combining the field-of-view of EUVI, COR and HI (adapted from Byrne et al., 2010).

1.6 CME Evolution in Heliosphere

One of the key step in space weather forecasting is to understand how the initial properties of CMEs evolve in between Sun and Earth. After the launch of STEREO spacecraft, CMEs can be continuously imaged from its initiation phase in the lower corona out to 1 AU and beyond using the Sun Earth Connection Coronal and Heliospheric Investigation (SECCHI; Howard et al., 2008) coronagraph (COR) and Heliospheric Imager (HI) data (Figure 1.22). The heliospheric white light imaging has been extensively used to predict the arrival time of CMEs at Earth (Möstl et al., 2011; Mishra & Srivastava, 2013; Mishra et al., 2014). However, the main focus of this thesis is to understand the geo-effectiveness of CMEs which involves the knowledge of CME evolution, particularly the evolution of its magnetic properties in the heliosphere. This requires the utilization of the multi-wavelength remote-sensing data as well as in-situ data obtained from multiple spacecraft. In the following sections, we present the evolutionary properties of the important physical parameters of CMEs, which play a key role in determining its geo-effectiveness.

1.6.1 Direction of CME propagation

The direction in which a CME propagates is one of the most important parameter in space weather forecasting. Depending on its direction of propagation, a CME may hit or miss the Earth. Once a CME is launched from its source region on the Sun, the deflection of CMEs that may occur in coronal or interplanetary region, adds complexity in determining its final propagation direction to forecast how the CME will impact on Earth.

The direction obtained from the source location of CMEs on the Sun may not correspond to its actual propagation direction seen in the white light coronagraphic images, as most of the CMEs differ from its radial trajectory and suffer significant deflection in lower corona (Gosling et al., 1987; Vandas et al., 1996; Wang et al., 2004; Gui et al., 2011; Lugaz et al., 2011; Shen et al., 2011; Kay et al., 2013; Möstl et al., 2015). An example shown in Figure 1.23 depicts the deflection of a CME from higher to lower latitude as observed in STEREO-B COR1 to COR2 images on 2 November 2008.

The open magnetic flux system originated from coronal holes is identified as one of the potential candidate that causes the CME deflection (Cremades et al., 2006). Gopalswamy et al. (2009) and Mohamed et al. (2012) reported that the CMEs tend to deflect away from the coronal holes. Therefore, the equator-ward deflection of CMEs (e.g. the event depicted in Figure 1.23) are more ubiquitous

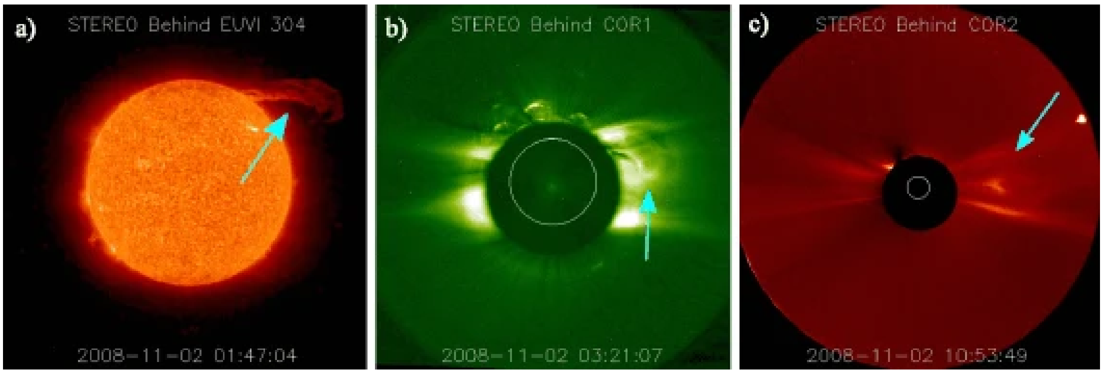

Figure 1.23: Panel (a) depicts the eruption of a high-latitude prominence on 2 November 2008 seen by STEREO-B EUVI at 304 Å wavelength. The corresponding CME is observed in STEREO-B COR1 (panel b) and STEREO-B COR2 (panel c). The arrows overlaid on the images indicate the equator-ward deflection of the CME (adapted from Kilpua et al., 2009)

during the solar minimum due to the presence of polar coronal holes (Cremades et al., 2006; Panasenco et al., 2011). Apart from the influence of coronal holes, several studies have also shown that the CMEs can be deflected by the strong magnetic fields around the source active region (Kay et al., 2015; Möstl et al., 2015; Wang et al., 2015). More precisely, the change in magnetic pressure around the region of strong magnetic field such as coronal holes and active regions exerts magnetic pressure gradient force that effects the direction of CME propagation (Wang et al., 2015).

Example of a CME event on 7 January 2014, as studied by Möstl et al. (2015), emphasizes the role of magnetic pressure gradient force close to Sun that can alter the CME trajectory, thereby changing its geomagnetic effect on Earth. The CME was launched from an active region very close to the solar disk center (S12W08) with a speed $\approx$ 2400 km s^{-1}. Therefore, a significant geomagnetic impact was expected. However, due to the strong coronal channeling, the CME was deflected longitudinally by $37 \pm 10^{\circ}$ away from its source region, leading only to minimal geomagnetic effects. Figure 1.24 depicts that the CME mostly impacted on Mars, whereas it had a merely glancing encounter with Earth. Möstl et al. (2015) reported that the strong magnetic field of a nearby active region and a region of open coronal field were responsible for the large deflection of the aforementioned CME close to the Sun.

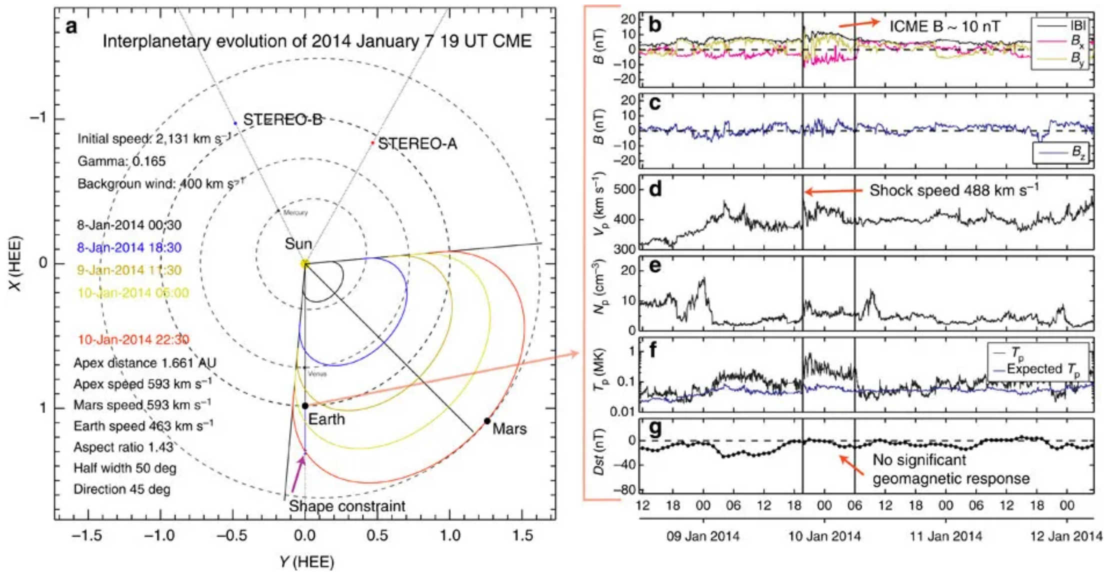

Figure 1.24: Panel (a) shows the heliospheric positions of various planets and spacecraft on 7 January 2014. The temporal evolution of the modeled CME front is plotted in different colors. Panels (b-g) show the plasma parameters associated with the solar wind observed in near-Earth space by Wind spacecraft during 9 to 11 January 2014 (adapted from Möstl et al., 2015).

Apart from the solar sources that influence the CME propagation close to the Sun, CMEs can also suffer longitudinal deflections at larger distances in the corona and heliosphere due to its interaction with the Parker spiral structured solar wind (Gosling et al., 1987; Wang et al., 2014). However, it is important to note that the ambient Parker spiral field may not be able to deflect even a slow ICME by more than a few degrees, as the kinetic energy density of an ICME is atleast two orders of magnitude higher than that of the Parker field (Manchester et al., 2017). Recent studies confirm that most of the dramatic deflection of CMEs occur close to the Sun within 10 $R_\odot$ (Kay et al., 2015). Therefore, the direction of CME propagation estimated beyond 10 $R_\odot$ can be considered as the direction that would be maintained by the CME during the rest of its propagation path. This is an important observational constraint that can be used to model the CME evolution in heliosphere.

1.6.2 Orientation of CME magnetic axis

One of the most important parameters that determines the geo-effectiveness of an ICME, is its orientation of the magnetic axis with respect to the Earth's mag-

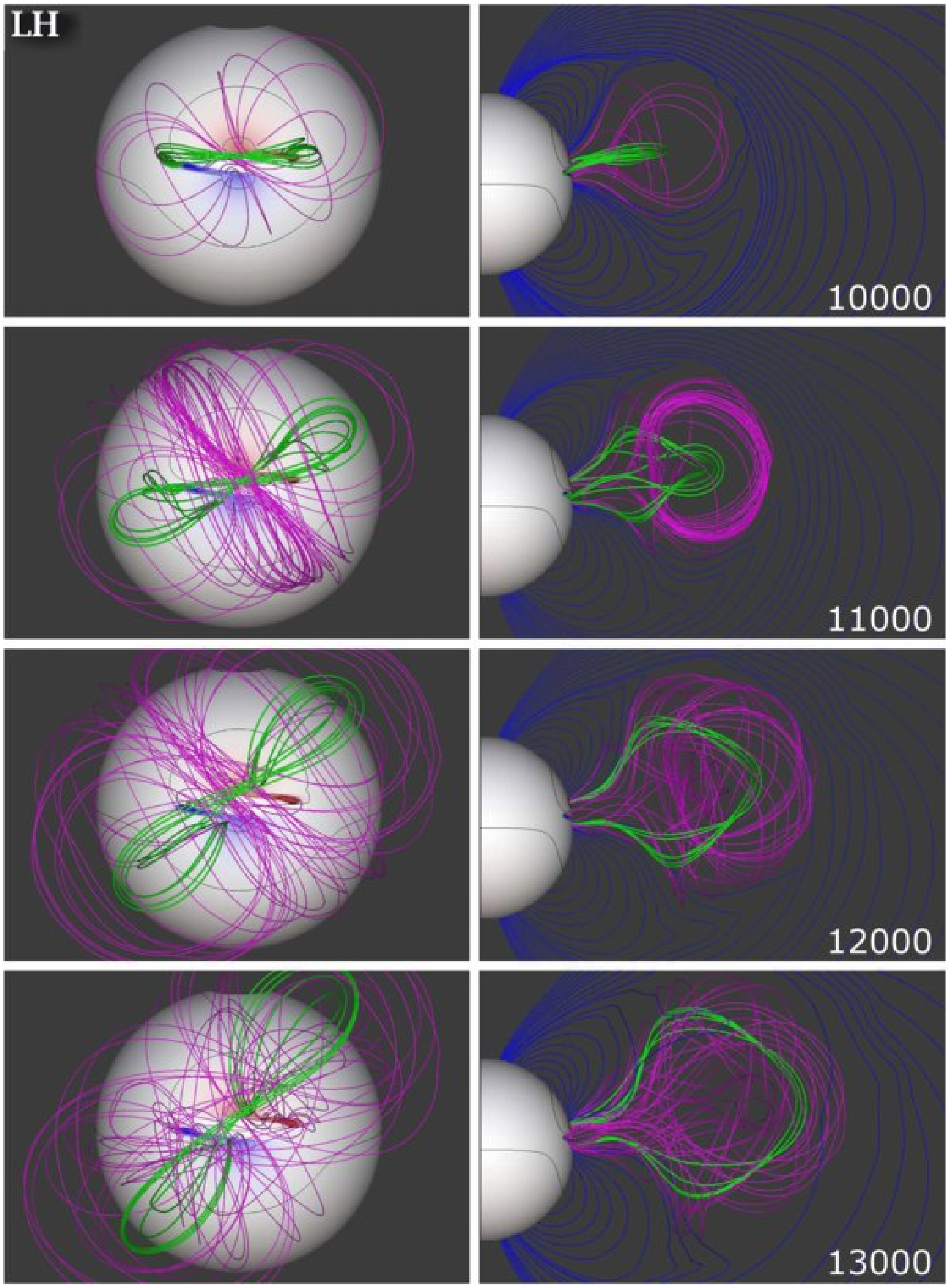

Figure 1.25: Face-on (left column) and side-view (right column) of the erupting field structure of a left handed flux rope. Different rows depict the temporal evolution of the field structure as obtained from the simulation results. The magenta and green field lines represent the orientation of the azimuthal (poloidal) and axial (toroidal) field during the eruption. The temporal evolution of the axial field orientation clearly depicts a counterclockwise rotation of the left handed flux rope (adapted from Lynch et al., 2009).

netic field (Gonzalez et al., 1994; Gopalswamy et al., 2008). The axis orientation of the CME flux ropes close to the Sun can be obtained from its lower coronal signatures such as pre-flare sigmoidal structures (Rust & Kumar, 1996), J-shaped flare ribbons (Janvier et al., 2014), coronal dimmings (Webb et al., 2000; Thompson et al., 2000; Gopalswamy et al., 2018c), coronal cells (Sheeley et al., 1980) or filament orientations (Hanaoka & Sakurai, 2017). However, the CME magnetic axis may undergo significant rotation during its early evolution phase, making the prediction of CME axis orientation at 1 AU a much more challenging task.

Numerical simulations of flux rope eruption using breakout model, shows that the right handed flux rope rotates clockwise and the left-handed flux rope rotates counterclockwise during the eruptive phase in lower corona below 5 $R_\odot$ (Lynch et al., 2009). Their results show that by 3.5 $R_\odot$, an erupting flux rope may exhibit an average rotation angle of $\approx 50°$. Their study also reveals that the rotation angle of the flux rope depends on the amount of sigmoidality present in the pre-flare field configuration. Comparing the orientation of the pre-eruptive structure

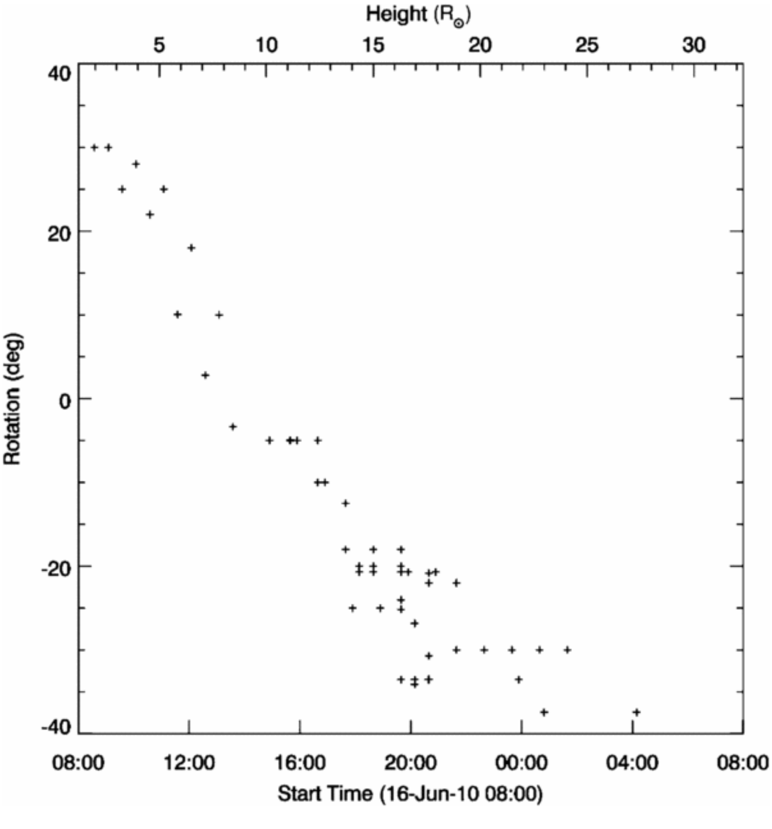

Figure 1.26: CME rotation as a function of time and heliocentric radial distance. The rotation is derived from the GCS fits to SECCHI/COR2-A, B, and LASCO/C2, C3 for heights above 3 $R_\odot$ and GCS fits to SECCHI/COR1-A and B for heights below 3 $R_\odot$. Positive angles correspond to counterclockwise rotation relative to the solar equator (adapted from Vourlidas et al., 2011).

on the Sun with the orientation of the axis of the magnetic cloud at 1 AU, the statistical studies have shown that more than 30° rotation is not uncommon for CMEs during its evolution in between Sun and Earth. However, the studies by Lynch et al. (2009) suggest that those rotation may occur very close to the Sun during the early evolutionary phase of a CME.

Yurchyshyn et al. (2009) reported that CMEs may tend to show gradual rotation towards the heliospheric current sheet. Vourlidas et al. (2011) have shown the first observational evidence of a rapidly rotating CME in the middle corona (5 to 15 $R_\odot$) as shown in Figure 1.26. They have found that the CME started to rotate above 3 $R_\odot$ and showed maximum rotation of about 35° in between 3 to 8 $R_\odot$. Above 8 $R_\odot$ the rotation slowed down and stopped at about 20 $R_\odot$. As depicted in Figure 1.26, the observed CME rotated in clockwise direction, which exactly follows the expected sense of rotation for right-handed flux ropes as suggested by Lynch et al. (2009). Therefore, both the observational (Vourlidas et al., 2013) and numerical (Lynch et al., 2009) studies show that CMEs may undergo systematic rotation in lower corona following the chirality of the associated flux ropes. The rotation stops at higher heights in the white light coronagraphic field of view, providing the opportunity to estimate the final orientation of the CME magnetic axis which can be assumed to remain unchanged up to 1 AU. However, more observational studies are required to validate this fact statistically.

1.6.3 Nature of CME expansion

Apart from the orientation of the magnetic field vectors, the geo-effectiveness of ICMEs is also governed by the strength of its internal magnetic field, which depends on the rate of expansion exhibited by the ICME during its evolution in between Sun and Earth (Gopalswamy et al., 2014). As the internal magnetic pressure of CMEs is much higher than the ambient solar wind, CMEs exhibit expansion once it is ejected into the heliosphere. The CME expansion continues during its evolution in the heliosphere, as the background solar wind pressure also decreases radially outward from the Sun. As the CME expands, its internal magnetic field strength decreases with increasing heliocentric distance. Therefore

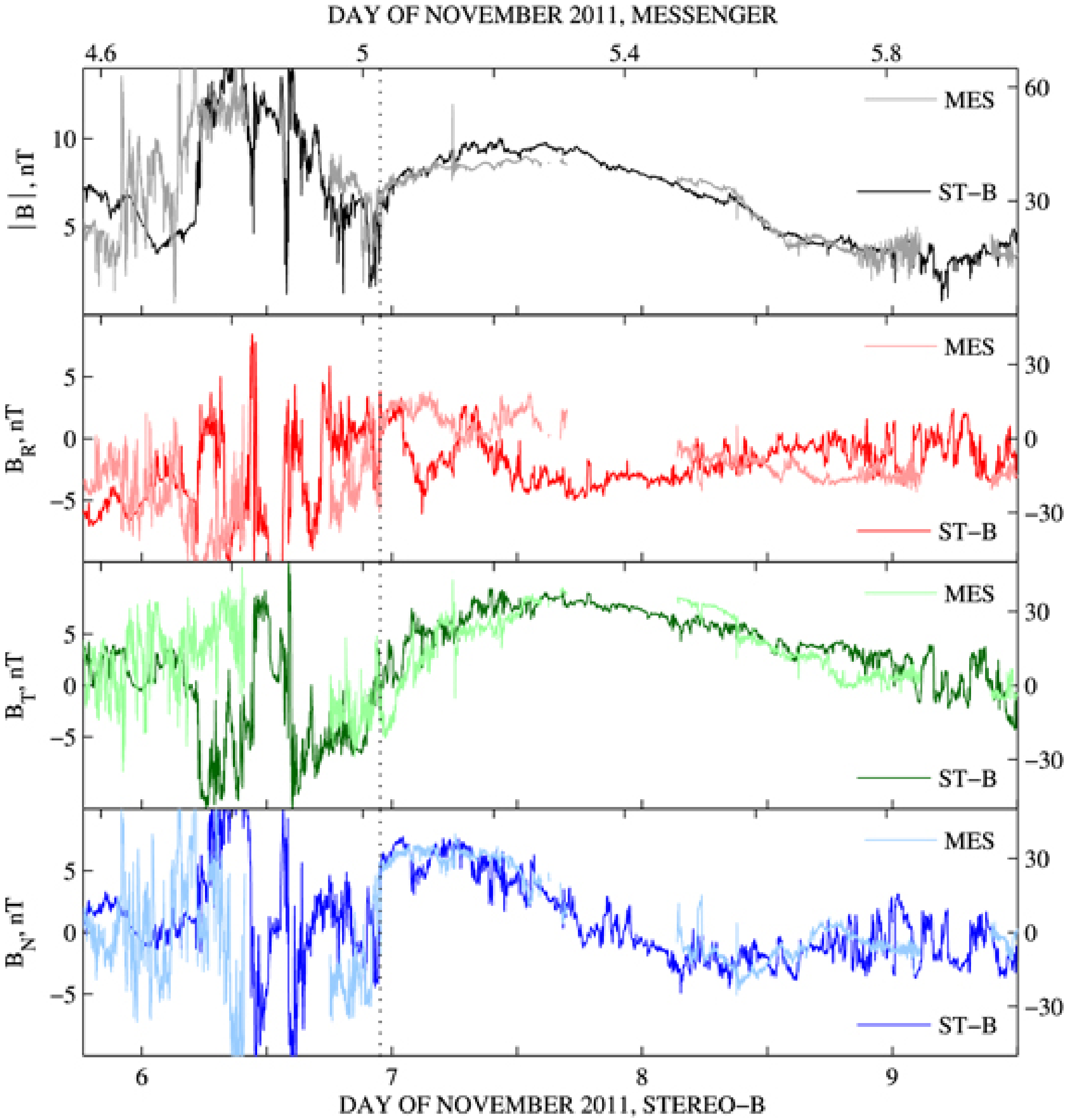

Figure 1.27: Magnetic field data at MESSENGER is overlapped with the field data at STEREO-B while normalizing both the temporal and spatial scale. The field structure at the right part of the vertical dotted line represents the same magnetic cloud sequentially observed by the radially aligned spacecraft MESSENGER and STEREO-B. The similarity of the MC field vectors at two different heliocentric distances (0.44 AU and 1.09 AU) indicates self-similar expansion exhibited by the ICME (adapted from Good et al., 2015).

the rate of CME expansion determines its final magnetic field strength at 1 AU, with which it would interact with the Earth's magnetosphere. In the context of space weather forecasting, it is important to know whether CMEs exhibit any systematic expansion which can be inferred from the remote-sensing observations.

Applying a theoretical model of erupting flux-rope dynamics on the observed kinematic evolution of a CME, (Chen et al., 2000) calculated the major radial forces acting on a CME flux rope. Krall et al. (2001) further extended the study for 11 CMEs. They have found that the forces due to gravity and magnetic tension decay quickly with distance from the Sun and become less significant compared to the drag and Lorentz-self force after the main acceleration phase of the CME which tends to occur below 2-3 $R_\odot$ (Chen & Krall, 2003; Joshi & Srivastava, 2011). Therefore, after the peak acceleration phase the Lorentz-self force alone governs the rate of CME expansion, which eventually becomes isotropic in absence of any significant magnetic tension force. This results in a systematic expansion phase, called self-similar expansion i.e., the ratio (κ) of the flux rope minor radius to its major radius remains approximately constant with time (Subramanian et al., 2014). Several studies have reported the self-similar expansion of CMEs observed in white light coronagraphic field of view (Poomvises et al., 2010; Kilpua et al., 2012). Recent studies have shown that the self-similarity is also maintained in the ICMEs during their evolution in interplanetary space as shown in Figure 1.27 (Good et al., 2019). The observations of the ICMEs sequentially detected by the radially aligned multiple spacecraft at different heliocentric distances reveal that the expansion nature of ICMEs is self-similar (Good et al., 2015; Good et al., 2019). Importantly, the ratio (κ) that constraints the self-similar expansion can be estimated from the remote-sensing data obtained from multi-vantage point coronagraphic observations. As the self-similar expansion is further maintained by the ICMEs during its rest of the propagation path, the ratio κ can be used to model the ICME expansion in between Sun and Earth. However, the self-similar expansion may not be a valid assumption if the CME interacted with another CME or with a region of high speed solar wind in the interplanetary space.

1.7 Space Weather Consequences of CMEs

CMEs are the major solar drivers for intense geomagnetic storms and hence the disturbed space weather. Indeed, the magnetic field carried by the CMEs couples the solar, interplanetary and magneto-spheric system as shown in Figure 1.28.

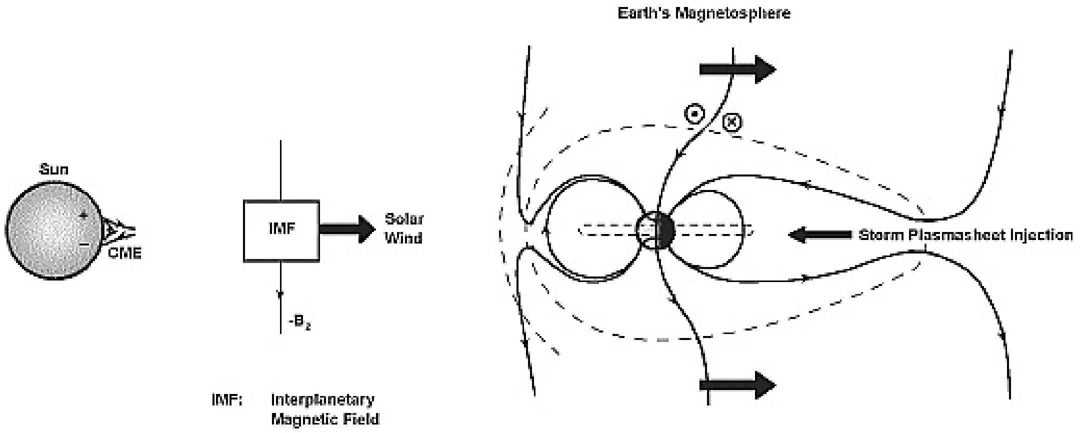
Earth's Magnetosphere
Sun
CME
IMF
Solar Wind
$-B_z$
IMF: Interplanetary Magnetic Field
Storm Plasmasheet Injection

Figure 1.28: Schematic picture of interplanetary and magnetospheric coupling, showing the reconnection process and energy injection into the night side magnetosphere, which lead to the formation of the storm-time ring current (adapted from Gonzalez & Tsurutani, 1992).

If an Earth directed ICME or the associated sheath region carries a strong southward interplanetary magnetic field (IMF) Bz, then it interacts with the Earth's magnetosphere via the process of magnetic reconnection at the day side magnetopause. This results in magnetic erosion on the day side magnetosphere and accumulation of magnetic field on the night side of the magneto-tail region. Subsequent reconnection at the magneto-tail leads to plasma injection into the night side magnetosphere. Consequently, the injected ions and electrons are trapped in the Earth's magnetic field and execute back and forth motion from one to another magnetic poles. During this motion, the highly accelerated charge particles can go deep into the Earth's ionosphere near the polar regions and excite the atoms (Oxygen) and molecules (Nitrogen) to higher energy states. The emission of photons during the transition from higher to lower energy states of those atoms and molecules results in the formation of beautiful aurorae seen in the polar regions (Figure 1.29). Due to the gradient and curvature in the Earth's magnetic field, the trapped charge particles gyrating along the Earth's magnetic field tend to execute a motion along the equatorial plane, where ions move from midnight toward dusk (i.e. westward) and electrons from midnight toward dawn (i.e. eastward), giving an overall current in westward direction around the Earth. This toroidal shaped current is known as the ring current. The magnetic field induced due to the ring current reduce the horizontal component of Earth's mag-

Figure 1.29: Aurora borealis seen in the night sky of Canada (image credit - Abigail Beall).

netic field, leading to the main phase of geomagnetic storm. The near-equatorial geomagnetic observatories record the variation of Earth's horizontal magnetic field strength as the Disturbance Storm Time (Dst) index, which is one of the important magnetic indices to represent the intensity of the associated geomagnetic storm.

Observation of geomagnetic storm was first recorded by Alexander von Humboldt in 1806 (Lakhina & Tsurutani, 2016). One of the historic geomagnetic storms was recorded during the time of famous Carrington flare. The white light solar flare on 1 September 1859 was followed by an intense magnetic storm (Dst = −1760 nT) on 1-2 September 1859, which is the biggest magnetic storm in the recorded history and popularly known as the Carrington magnetic storm. The time delay between the observed white light flare and the magnetic storm was ≈ 17 h and 40 min (Carrington, 1859). Tsurutani et al. (2003) reduced the ground magnetometer data of 1-3 September 1859 obtained from the Colaba Observatory (Mumbai, India) as shown in Figure 1.30. The Colaba Observatory magnetogram shows that the maximum H-component depression during the storm main phase

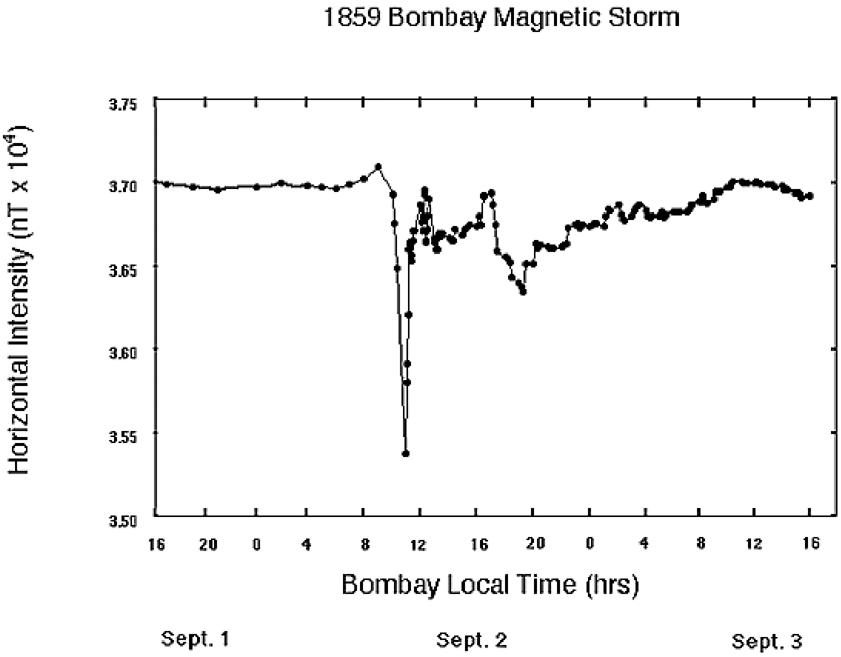

Figure 1.30: The magnetogram for the 1-2 September 1859 magnetic storm as recorded at the Colaba Observatory, Bombay (adapted from Tsurutani et al., 2003).

was $\Delta H \approx -1600$ nT and the duration of the main phase of the storm was $\approx$ 1.5 h. Tsurutani et al. (2003) concluded that the Carrington magnetic storm was possibly caused by intense Bz inside an ICME that collided with the Earth on 1-2 September 1859. The peak intensity of the Carrington magnetic storm was estimated as Dst $\approx$ -1760 nT using the empirical relation for the evolution of the ring current (Burton et al., 1975) by considering the ring current decay time as 1.5 h. The estimated value is consistent with the local measurement of $\Delta H \approx -1600$ nT at Colaba.

Importantly, the Carrington storm caused aurorae which were visible down to ± 23° magnetic latitude, at Hawaii and Santiago, Chile (Kimball, 1960). This indicates that the extreme space weather events may lead to failure of ground based electric and power grid systems even in the countries lying in the middle or lower-middle latitude belts like India. During the Carrington storm, the mid latitude areas over the United States and Europe faced electrical shocks and fires by electrical arcing from telegraph wires due to the auroral electrojet (Loomis, 1861; Tsurutani et al., 2015). The other example of an extreme space weather event

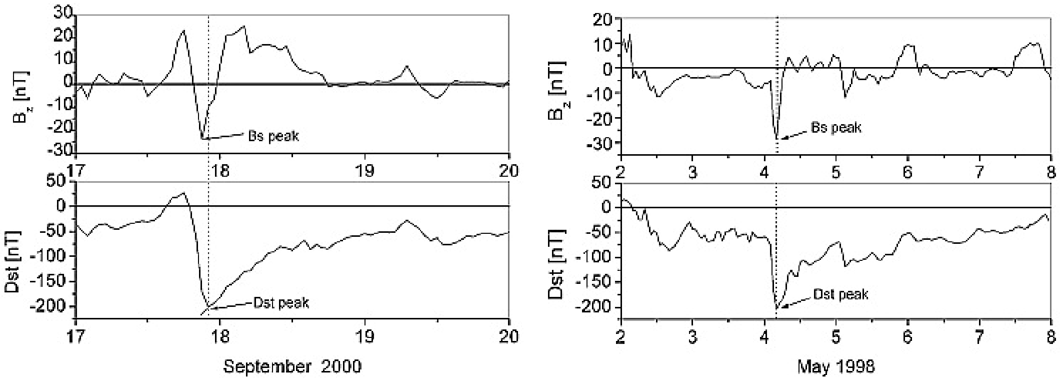

Figure 1.31: IMF Bz and Dst hourly averages are shown for two different types of geomagnetic storms. The left panel shows a normal one-step magnetic storm during 17-20 September 2000. The right panel shows a complex two-step magnetic storm during 2-8 May 1998 (adapted from Gonzalez & Echer, 2005).

caused by CME is the geomagnetic storm on 13-14 March 1989, which had an intensity of Dst (hourly average index) = -589 nT. As a consequence of this storm, the Canadian Hydro-Quebec system failed (Allen et al., 1989; Bolduc, 2002). If a geomagnetic storm with an intensity similar or greater than Carrington-type storm were to occur now, it could cause much more damage to society than in 1859 when the telegraph was the latest technology of the time. Therefore, it is required to have a prior knowledge or forecasting capacity to predict the intensity of geomagnetic storms caused by CMEs.

It is now well known that the geomagnetic storms are caused due to a strong southward IMF Bz. Following the temporal evolution of the southward IMF Bz, a geomagnetic storm may occur in one (normal and most frequently observed) or two steps (complex and less frequently observed) as shown in Figure 1.31. Several studies have shown that the intensity of a geomagnetic storm is closely related to the magnitude and duration of southward IMF Bz. Gonzalez et al. (1994) found that long duration southward Bz (>3 h) almost associated with a strong geomagnetic storm (minimum Dst < -100 nT). Wu & Lepping (2002) studied 135 magnetic clouds and reported that the Dst index correlates well with both the IMF Bz component and the solar wind electric field. They further found that the correlation coefficient for Dst index versus IMF Bz increases significantly when the solar wind speed exceeds 600 km s^{-1}. Gopalswamy et al. (2008) also reported that the Dst index is highly correlated with the solar wind speed and the IMF Bz in the magnetic clouds as well as their product. All the aforementioned studies indicate the importance of IMF Bz as the primary cause of geomagnetic storms. Therefore, the prediction of IMF Bz inside an ICME is of utmost importance in space weather research in order to forecast the intensity of the associated geomagnetic storm.

1.8 Forecasting Models to Predict Geo-effectiveness of CMEs

In order to get an advance alert regarding the space weathers hazards caused by the CMEs, the near-Sun CME properties obtained from remote-sensing observations need to be modeled from Sun to Earth. As the prediction of Bz is the prime requirement to forecast the severity of the associated geomagnetic storm, several efforts have been made towards this through analytical, semi-analytical and numerical modelings (Odstrčil & Pizzo, 1999; Shen et al., 2014; Savani et al., 2015; Jin et al., 2017; Kay & Gopalswamy, 2017; Möstl et al., 2018). The full 3-D MHD simulation codes like ENLIL, were performed to simulate the CME evolution in heliosphere and its interaction with the solar wind (Odstrcil et al., 2004). Efforts have also been carried out to include the magnetic flux rope structures in numerical simulations of CME eruption and evolution as shown in Figure 1.32 (Manchester et al., 2008; Scolini et al., 2019). However, the aforementioned 3D MHD simulations cannot be yet performed in real time to provide reliable forecast of Bz (Moreover, due to the time-varying heliospheric conditions, it is also challenging to make the realistic background solar wind model for the simulations. In order to reduce the computational time, several simplistic approaches through analytical (Savani et al., 2015) and semi-analytical (Kay & Gopalswamy, 2017) modeling have been made to forecast Bz at 1 AU. However, those modeling approaches involve many free parameters and hence, cannot be readily used for operational space weather forecasting. Moreover, none of the aforementioned numerical or analytical models can incorporate the realistic inputs that can be constrained through observations. Therefore, from space weather perspective,

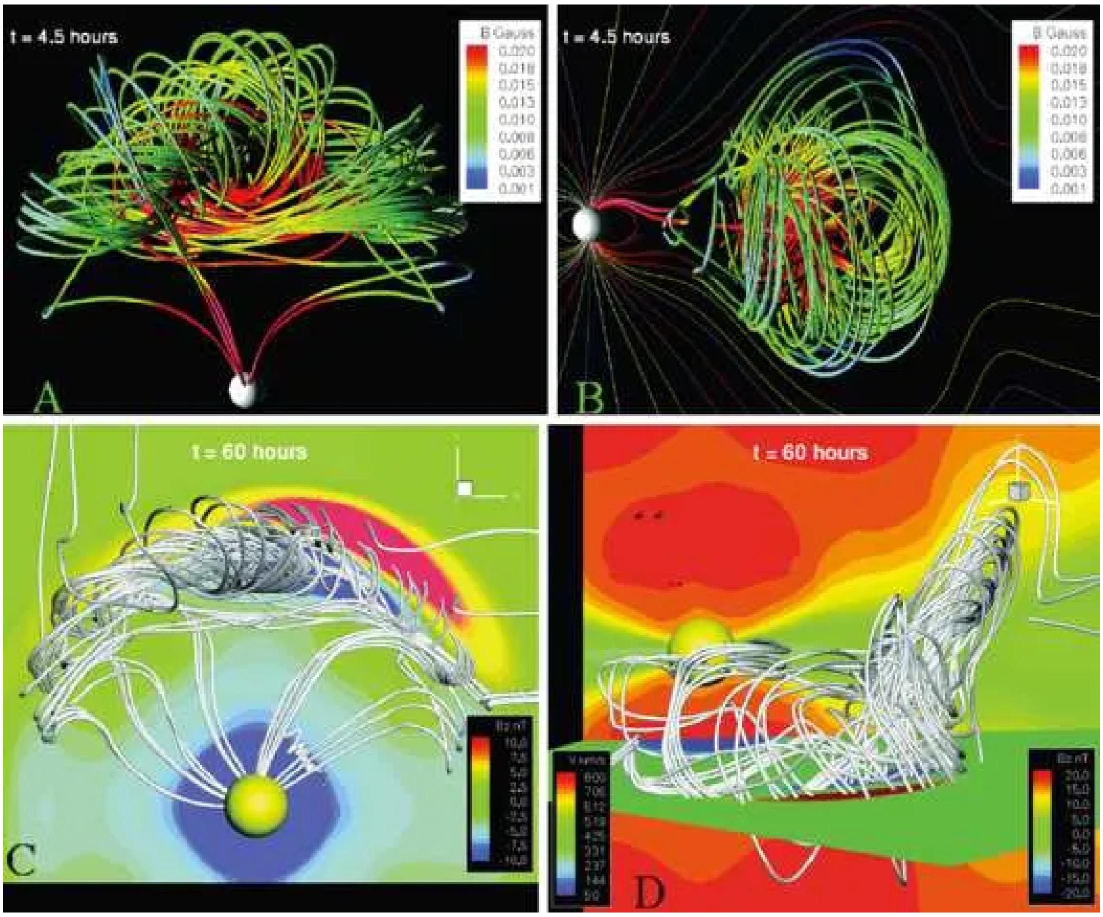
t = 4.5 hours
B Gauss
0.020
0.018
0.015
0.013
0.010
0.008
0.006
0.003
0.001
A
t = 4.5 hours
B Gauss
0.020
0.018
0.015
0.013
0.010
0.008
0.006
0.003
0.001
B
t = 60 hours
Bz nT
10.0
7.5
5.0
2.5
0.0
-2.5
-5.0
-7.5
-10.0
C
t = 60 hours
V km/s
800
706
612
519
425
331
237
144
50
Bz nT
20.0
15.0
10.0
5.0
0.0
-5.0
-10.0
-15.0
-20.0
D

Figure 1.32: Evolution of flux rope structure in a simulated CME. The spheromak flux rope is used to mimic the magnetic field structure of a CME as shown at 4.5 hours (top row) and 60 hours (bottom row) after initiation. Panels (a) and (c) show simulation results as viewed on the ecliptic plane. Panels (b) and (d) show the side and oblique views of the simulated CME respectively (adapted from Manchester et al., 2017).

new modeling efforts are required which can incorporate realistic inputs and give reliable forecast of Bz without involving any free parameters.

1.9 Motivation and Organization of the Thesis

Until recently, the understanding of origin, evolution and space weather consequences of CMEs has been limited as mentioned above because of a number of reasons. The most significant of these are the lack of high cadence and high resolution photospheric vector magnetogram data to study the CME source region characteristics, observational gap in the field-of-view of white-light imagers to capture CME initiation in lower corona below 2 $R_\odot$ and the lack of direct measurement of the near-Sun CME magnetic field strength which is a crucial input for the space weather forecasting models.

With the launch of Solar Dynamic Observatory in 2010 (Pesnell et al., 2012), it is now possible to study the evolution of the photospheric magnetic field of the CME source region with high temporal and spatial resolution. It is well known that the geo-effectiveness of any CME depends on its initial kinematics (Srivastava & Venkatakrishnan, 2002; Dumbović et al., 2015, and references therein). On the other hand, the initial kinematic properties of CMEs differ depending on its association with solar flares. Therefore, it is worthful to study the flare-CME association as the flare-rich active regions are expected to launch a high speed CME which may result in an extreme space weather event (Falconer et al., 2002; Gopalswamy et al., 2010). However, all the flare-rich active regions on the Sun are not associated with CME eruption, resulting in confined flaring events (Sun et al., 2015; Chen et al., 2015). A majority of work done so far, has been focused on the evolution of photospheric magnetic field to study the source region characteristics of flare associated CMEs (Sudol & Harvey, 2005; Wang, 2006; Petrie & Sudol, 2010; Petrie, 2012). Therefore, such studies should also be performed for the confined flaring events in order to understand the CME productivity of any flare rich active region, which in turn would help to assess the space weather impact of the associated CME if that undergoes eruption.

The space weather impact of CMEs can be even more severe when there is an interaction between two CMEs in the inner heliosphere (Wang et al., 2003; Farrugia & Berdichevsky, 2004; Farrugia et al., 2006; Lugaz & Farrugia, 2014). When they arrive at Earth, the two interacting CMEs may merge into one single CME or may maintain their two distinct structures with an interaction region in between, leading to a more intense “one step” or complex “two-step” geomagnetic storms respectively (Gonzalez & Echer, 2005). Works have been carried out to understand the nature of collision and the change in kinematics of the associated CMEs after the collision (Shen et al., 2017; Mishra et al., 2017). However, attempts have not been made to study the solar origin of those interacting CMEs. Recurrent large flares originating from same active region on the Sun, are the potential candidate to launch recurrent CMEs in the same direction, leading to a chance of CME-CME interaction. Therefore, a detail study of the source region characteristics of recurrent eruptive flares are needed to understand the physical processes behind the occurrence of those events. In depth studies towards this objective may enable us to build forecasting capacity to predict the occurrence of such recurrent solar eruptive events which have significant impact in space weather.

One of the key aspect in space weather research is to understand the conditions and triggering mechanisms leading to the genesis of CMEs. In particular, understanding the lower coronal evolution of CMEs during its initiation and post-eruptive phase is crucial to constrain the space-weather forecasting models. However, these studies are largely limited due to the observational gap between the field-of-view of EUV disk imager and white-light coronagraphs, making it challenging to continuously track a CME evolution from its initiation phase in the lower corona to the post-eruptive and propagation phase in the inner heliosphere. With the advent of recent EUV imagers like SWAP (Halain et al., 2013; Seaton et al., 2013; Santandrea et al., 2013) which can observe the Sun with larger field of view, the observational limitation to capture the CME initiation can be overcome. Combining such EUV observations with the white light data, it would be possible to track the continuous evolution of a CME to understand its nature of expansion and direction of propagation, which are the key inputs for space weather forecasting.

As CMEs are the solar origin of the major space weather disturbances, one of the important goal in space weather research aims to forecast the severity of geomagnetic storms caused by the CMEs, which relies on the prior knowledge of the strength of southward Bz inside it. However, predicting the strength of Bz is the most challenging problem in current space weather research. As already discussed in Section 1.8, to date there is no such model which is capable of giving reliable prediction of Bz at 1 AU. Therefore, combining the knowledge of CME source region characteristics and its properties of near-Sun evolution, significant efforts are required to model the CME magnetic field from Sun to Earth.

Based on the research problems as discussed above, the specific objectives of this thesis related to origin, evolution and space weather consequences of CMEs are outlined below:

1. Studying the source region characteristics of confined and eruptive events to understand the conditions leading to CME eruptions.
2. Understanding the physical conditions in solar active regions leading to large recurrent eruptive events that may result in CME-CME interactions and hence, the disturbed space weather.
3. Studying the early evolution of CMEs in lower corona to understand the CME initiation mechanism.
4. Tracking the CME evolution from lower corona to the interplanetary space to understand the nature of expansion and propagation direction of CMEs, which can be used to constrain the initial inputs for the space-weather forecasting models.
5. Using the near-Sun properties of CMEs obtained from the source region studies and remote-sensing observations, development of a space weather forecasting tool to predict the magnetic field vectors of ICMEs at any heliocentric distance to forecast the severity of the associated geomagnetic storms.

Based on the work carried out to accomplish the above mentioned objectives, the thesis is organized into seven chapters. A brief description of each chapter is given below.

Chapter 1: Introduction

In this chapter, a brief introduction to the Sun-Earth connection is presented followed by the discussions on the role of CMEs as major space weather drivers. A review of work carried out on the CME initiation, evolution and propagation in the interplanetary space is presented. The challenges and scopes of existing modeling approaches to forecast the geo-effectiveness of ICMEs based on the remote-sensing observations are also discussed briefly.

Chapter 2: Observational Data and Processing

This chapter contains the detail descriptions on the data sources and data analysis techniques. This thesis work mostly uses the data obtained from the space based observatories which include Solar Dynamic Observatory (SDO), Solar and Heliospheric Observatory (SOHO), Solar Terrestrial Relations Observatory (STEREO), PROBA-2, and WIND. For additional observations, data obtained from the ground based observatories like Multi Application Solar Telescope (MAST), Kanzelhoehe Solar Observatory (KSO), Global Oscillation Network Group (GONG) and Mauna Loa Solar Observatory (MLSO) are also used.

Chapter 3: Conditions in Source Active Regions Leading to Confined and Eruptive Events

In this chapter, we present a comparative study of the source region characteristics associated with the confined and eruptive events occurred in the largest active region (AR 12192) of solar cycle 24. This active region gave rise to several non-eruptive X-class flares as well as an eruptive M-class flare, giving a unique opportunity to study the photospheric magnetic environments of confined and eruptive events originated from a same AR. Therefore, the approach involved in this study, is free from the bias of other factors such as the scale size and complexity of the different ARs, which are believed to play major role in the eruptions. In the context of space weather studies, it is important to understand whether an active region will be CME productive or not. In this perspective, we also explore the conditions of background magnetic field over the source locations of both the confined and eruptive flares occurred in the AR, to understand the role of overlying magnetic field behind the confined nature of any eruption. The results of this work have been published in Sarkar et al. (2018) and Sarkar & Srivastava (2018)

Chapter 4: Conditions in Source Active Regions Leading to Recur-

rent Eruptive Events

In this chapter, we extend the studies of source region characteristics of solar explosive events as performed in chapter 3, to those ARs which gave rise to large recurrent eruptive events. Focusing on the space weather impact of such ARs, we have studied the recurrent eruptive flares in AR 11261 which resulted in CME-CME interaction in the inner heliosphere. Apart from exploring the possibility to forecast the occurrence of such events, we have also attempted to answer the fundamental questions related to the energy release and build-up processes behind such recurrent eruptive phenomena. With the same motivation as mentioned above, we have further extended these studies to the three large recurrent eruptive flares occurred in AR 11283. The results obtained in this work have been published in Sarkar et al. (2019a).

Chapter 5: CME Initiation and its Evolution Close to Sun

In this chapter, we have studied the CME initiation mechanism by tracking the evolution of a coronal cavity starting from its development phase in lower corona to the post-eruption phase where it was detected as the white light cavity in the associated CME. This is an unique case study where we have pieced together observations from EUV (SWAP) and white light (LASCO) images to fill the observational gap between 1.3 to 2.0 $R_\odot$. This allows us to capture the most dramatic phase of lower coronal evolution of a CME, which includes the initiation phase, initial peak acceleration phase and the dynamics related to initial deflection. In particular, we have focused on the nature of expansion and direction of propagation exhibited by the CME close to Sun, which are crucial to model a CME evolution in heliosphere. In this chapter, we have also investigated the role of MHD instabilities behind a CME eruption. The results of this work have been reported in Sarkar et al. (2019b).

Chapter 6: An Observationally Constrained Analytical Model for Predicting the Magnetic-field Vectors of ICMEs

In this chapter, incorporating the near-Sun CME properties and its nature of evolution as studied in chapter 5, we have developed an observationally constrained analytical model to predict the magnetic-field vectors of ICMEs at any heliocentric distance. The novelty of this model is that it uses the realistic inputs and does not involve any free parameters. The necessary model inputs obtained from observations and the model architecture have been discussed in detail. In order to benchmark our model, we have validated the model for a test case for the CME event on 2013 April 11. The model outputs are compared with the in situ observations obtained at 1 AU. We have also discussed the future scope of the model at the end of the chapter. The description of the model and the validation results have been published in Sarkar et al. (2020).

Chapter 7: Summary and Future Work

This chapter provides the summary of the work done highlighting the major findings in the above chapters and the scope for future work in space weather studies.

Chapter 2

Observational Data and Processing

2.1 Introduction

As described in Chapter 1, the objective of this thesis is to understand the solar origin of CMEs, its evolution in heliosphere and its space weather impact in near-Earth space. Therefore, we use both the remote sensing and in situ observations obtained from different space based and ground based observatories which can capture the initiation and evolution of CMEs close to Sun as well as its in situ properties at 1 AU. This thesis work mostly uses the data obtained from the space based observatories which include Solar Dynamic Observatory (SDO) (Pesnell et al., 2012), Solar and Heliospheric Observatory (SOHO) (Domingo et al., 1995), Solar Terrestrial Relations Observatory (STEREO) (Kaiser et al., 2008), PROBA-2 (Halain et al., 2013), and WIND (Lepping et al., 1995). For additional observations, data obtained from the ground based observatories like Multi Application Solar Telescope (MAST) of USO, Udaipur (`https://www.prl.res.in/~usodataarchive/`), Kanzelhoehe Solar Observatory (KSO) (`http://cesar.kso.ac.at/main/ftp.php`), Global Oscillation Network Group (GONG) (`https://gong2.nso.edu/archive/patch.pl?menutype=s`) and Mauna Loa Solar Observatory (MLSO) (`https://mlso.hao.ucar.edu/mlso_data_calendar.phpat`) Mauna Loa, USA are also used.

In order to understand the source region characteristics of CMEs, the different atmospheric layers of the Sun need to be imaged with high temporal and spatial resolution. For this purpose, we use the unprecedented multi-wavelength observations from the SDO. The source active regions of CMEs consist of complex magnetic structure extending from deep sub-photospheric layers, crossing through the photosphere to coronal heights. The velocity flows at the sub-photospheric layers govern the evolution of photospheric magnetic field which in turn shape up the dynamics of the solar corona. Therefore, to understand the conditions of photospheric field evolution leading to CME eruptions, we use the observations of vector magnetic field at photospheric height with high cadence and high spatial resolution as obtained from the SDO. Observations of the photospheric magnetic field also allow us to characterize the magnetic properties such as chirality and the direction of the axial magnetic field of the associated CME flux rope. To capture the CME initiation and its lower coronal evolution, we take advantage of the larger field-of-view of EUV imager onboard the PROBA2 (Santandrea et al., 2013) which fills the observational gap between 1.3 to 2 $R_\odot$. As the CME appears above 2 $R_\odot$, we use the white light coronagraphic observations obtained from the Large Angle and Spectrometric Coronagraph (LASCO) onboard the SOHO. Apart from the view obtained along the Sun-Earth line, we use the multi-vantage point observations of CMEs in white light and its lower coronal signatures in EUV passbands as obtained from the twin spacecraft STEREO A and B. Once the CME reaches to near-Earth space, we study its in situ properties from the observations of WIND spacecraft (Lepping et al., 1995; Ogilvie et al., 1995). In this chapter, we provide a brief description of the above mentioned instruments along with details of their data and techniques.

2.2 The Solar Dynamic Observatory (SDO)

The Solar Dynamics Observatory (SDO; Pesnell et al. 2012), the first space mission under the NASA's Living With a Star (LWS) program, was launched on 11 February 2010. The scientific objectives of SDO aim to understand how the magnetic field in Sun is generated, and how this stored magnetic energy is converted and released into the geo-space and heliosphere in the form of solar wind, energetic particles, and variations in the solar irradiance. SDO consists of three instruments: Atmospheric Imaging Assembly (AIA) (Lemen et al., 2012), Helioseismic and Magnetic Imager (HMI; Schou et al. 2012) and, Extreme ultraviolet Variability Explorer (EVE; Woods et al. 2012). In this thesis, we have extensively used the data obtained from both HMI and AIA instruments. We present a brief discussion on the data and capability of these two instruments in the following subsections.

2.2.1 Atmospheric Imaging Assembly (AIA)

The Atmospheric Imaging Assembly (AIA) (Lemen et al., 2012) provides the unprecedented multi-wavelength observations of different layers of the solar atmosphere. It is capable of producing multiple simultaneous high-resolution full-disk images of the Sun with $0.6''$ pixel^{-1} spatial sampling and 12-second temporal cadence. The AIA comprises of four telescopes that are optimized to observe in narrow band-passes in UV and EUV in order to observe solar emissions from the transition region and corona. Table 2.1 provides a detail of the different observing channels in AIA and the corresponding regions of solar atmosphere with different characteristic temperatures.

In this thesis, we have used the AIA images obtained in 94 Å, 193 Å, and 1600 Å passbands. AIA 94 Å images represent the hot solar corona at a temperature of six million Kelvin (emission from Fe XVIII). AIA 193 Å images capture the solar corona at a temperature of one million Kelvin (emission from Fe XII) as well as the hot material of a solar flare at a temperature of twenty million Kelvin (emission from Fe XXIV). In particular, these images are useful to study the post flare loops filled with hot plasma due to chromospheric evaporation (Doschek & Warren, 2005). AIA 1600 Å (emission from C IV) images represent the lower chromospheric region, which is known as the transition region of the solar atmosphere. These images are useful to identify the spatial locations of the flare ribbons, which are believed to be formed due to the heating of plasma as the ac-

Channel	Primary ion(s)	Region of atmosphere	Char. log(T)
4500 Å	continuum	photosphere	3.7
1700 Å	continuum	photosphere	3.7
304 Å	He II	chromosphere, transition region	4.7
1600 Å	C IV + continuum	transition region, upper photosphere	5.0
171 Å	Fe IX	quiet corona, upper transition region	5.8
193 Å	Fe XII, XXIV	corona and hot flare plasma	6.2, 7.3
211 Å	Fe XIV	active-region corona	6.3
335 Å	Fe XVI	active-region corona	6.4
94 Å	Fe XVIII	flaring corona	6.8
131 Å	Fe VIII, XXI	transition region, flaring corona	5.6,7.0

Table 2.1: Different channels of AIA centered on specific lines and corresponding regions of solar atmosphere with different characteristic temperatures (Lemen et al., 2012)

celerated particles, flowing down from the reconnection site along the reconnected magnetic field lines, hit the dense chromosphere (Priest & Forbes, 2002).

2.2.2 The Helioseismic and Magnetic Imager (HMI)

The Helioseismic and Magnetic Imager (HMI; Schou et al. 2012) onboard the SDO is designed to study the oscillations and magnetic field at solar photosphere. HMI observes the Sun in the Fe I 6173 Å absorption line with resolution of 1 $''$. It provides full-disk observations of Doppler velocity, intensity and both the line-of-sight and vector magnetogram of solar photosphere. HMI comprises of a refracting telescope of 14 cm clear aperture, a polarization selector, an image stabilization system, a narrow band tunable filter and two 4096×4096 pixel CCD cameras with mechanical shutters and control electronics.

In this thesis, we have extensively used the HMI vector magnetogram series from the version of Space weather HMI Active Region Patches (SHARP; Turmon et al. 2010) having spatial sampling of $0.5''$ pixel^{-1} and 12 minute temporal cadence. The Stokes parameters I, Q, U, and V were derived from the filtergrams of six polarization states at six wavelengths centered on the Fe I 6173 Å spectral line and were inverted using the Very Fast Inversion of the Stokes Algorithm code (Borrero et al., 2011) to obtain the vector magnetic-field components in the photosphere. The remaining 180° ambiguity in the azimuthal field component was resolved using the minimum energy method (Metcalf, 1994; Leka et al., 2009). A coordinate transformation for remapping the vector fields onto the Lambert cylindrical equal area projection was carried out, and finally the vector fields were transformed into heliocentric spherical coordinates.

2.3 PROBA-2

The PROBA2 (Santandrea et al., 2013) is a microsatellite developed as an ESA technology mission. PROBA2 carries two solar instruments: SWAP (Sun Watcher using Active Pixel System detector and Image Processing) and LYRA (Large Yield RAdiometer, formerly LYman alpha RAdiometer). In this thesis we have used the observations from SWAP which is a small EUV telescope that images the solar corona with a bandpass around 17.4 nm, corresponding to a temperature of 1 million degrees. It provides an extended (54 arc-minute) field-of-view of the lower solar atmosphere, which gives the opportunity to capture any dynamics of the solar corona upto 1.7 $R_\odot$ (upto 1.9 $R_\odot$ along the diagonal direction of the images). Apart from that, using the off-pointing ability of PROBA2, the SWAP field-of-view can be shifted in any direction in order to track coronal features of interest, upto more than 2 $R_\odot$. Therefore, it covers the field-of-view between 1 to 2 $R_\odot$ in order to study the lower coronal evolution of CMEs.

In order to increase visibility of coronal structures in the EUV images of SWAP, we have used the normalized radial graded filter (NRGF) (Morgan et al. 2006), which removes the radial gradient from coronal images. Furthermore, we have applied a high pass filter to the EUV images using the standard unsharp_mask.pro routine to enhance the image contrast.

2.4 LASCO Onboard SOHO

The Large Angle Spectrometric Coronagraph (LASCO) (Brueckner et al., 1995) is a package of three coronagraphs, which was developed for the Solar and Heliospheric Observatory (SOHO) mission (Domingo et al., 1995). The three coronagraphs in LASCO are named as C1, C2 and C3, that together can image the

	Field-of-view ($R_\odot$)	Occulter Type	Spectral Bandpass	Objective Element	Pixel Size	Brightness Range $B_\odot$
C1	1.1-3.0	Internal	Fabry-Perot	Mirror	5.6″	2×10^{-5} to 2×10^{-8}
C2	1.5-6.0	External	Broadband	Lens	11.4″	2×10^{-7} to 5×10^{-10}
C3	3.7-30	External	Broadband	Lens	56.0″	3×10^{-9} to 1×10^{-11}

Table 2.2: System parameters for C1, C2 and C3 (Brueckner et al., 1995)

solar corona from 1.1 to 30 $R_\odot$ (C1: 1.1 - 3 $R_\odot$, C2: 1.5 - 6 $R_\odot$, and C3: 3.7 - 30 $R_\odot$) (Table 2.3). The C1 coronagraph is a classical internally occulted Lyot coronagraph which observes the solar corona in emission lines of Fe XIV and Fe X, while the C2 and C3 are externally occulted instruments which image the solar corona in white light. LASCO C1 successfully observed for a period of two and a half year from January 1996 to June 1998. Unfortunately it became nonoperational after the SOHO interruption in 1998. However, C2 and C3 coronagraphs are still functional and providing regular observations of white light corona. In this thesis we have used the observations from LASCO C2 and C3.

2.5 STEREO

The NASA's twin spacecraft STEREO A & B (Kaiser et al., 2008) were launched to study the initiation of CMEs and their propagation in the inner heliosphere. Each STEREO spacecraft has identical instruments which provide the remote sensing observations in optical and radio wavelengths as well as measure the in situ properties of particles and fields. These instruments can be categorized in four different measurement packages which include SECCHI, IMPACT, PLASTIC and S/WAVES. The suite of instruments in SECCHI (Howard et al., 2008) package comprises of an Extreme Ultra Violet Imager (EUVI), two white light coronagraphs (COR1 and COR2) and two white light heliospheric imagers (HI1 and HI2) which together can image a CME from its eruption in the corona out to 1 AU. A brief description of these instruments are discussed as follows.

	Field-of-view	Wavelength	Pixel size
EUVI	Full disk image of Sun upto ± 1.7 $R_\odot$	He II 30.4 nm, Fe IX 17.1 nm Fe XII 19.5 nm & Fe XV 28.4 nm	$1.6''$
COR1	1.4 to 4 $R_\odot$	White light	$7.5''$
COR2	2.5 to 15 $R_\odot$	White light	$14.7''$
HI1	3.98 to 23.98 degree	630-730 nm	$70''$
HI2	18.68 to 88.68 degree	400-1000 nm	$4'$

Table 2.3: System parameters for SECCHI (Howard et al., 2008)

2.5.1 Extreme Ultra Violet Imager (EUVI)

The Extreme Ultra Violet Imager (EUVI) observes the chromosphere and low corona in four different EUV emission lines which include He II 30.4 nm, Fe IX 17.1 nm, Fe XII 19.5 nm, Fe XV 28.4 nm. It is a small, normal-incidence telescope with thin metal filters, multilayer coated mirrors, and a back-thinned CCD detector. The circular full sun field-of-view of EUVI extends up to 1.7 $R_\odot$ and it images with a spatial sampling of $1.6''$ pixel^{-1}.

2.5.2 COR1

COR1 is developed to image the faint solar corona visible due to the scattered light from the much brighter solar photosphere. It is a classic Lyot internally occulting refractive coronagraph (Lyot 1939) which can observe the solar corona from 1.4 to 4 $R_\odot$ in white light. COR1 provides the images with a spatial sampling of $7.5''$ pixel^{-1} and temporal cadence of 8 min.

2.5.3 COR2

Similar to LASCO-C2 and C3 coronagraphs on board SOHO spacecraft, COR2 is an externally occulted Lyot coronagraph which can image the solar corona from 2.5 to 15 $R_\odot$. In an externally occulted coronagraph, the objective lens is shielded from direct sunlight which reduces the stray light level as compared to COR1 and makes it possible to observe farther distances from the Sun. COR2 provides the images with temporal cadence of 15 min and spatial sampling of $14.7''$ pixel^{-1}.

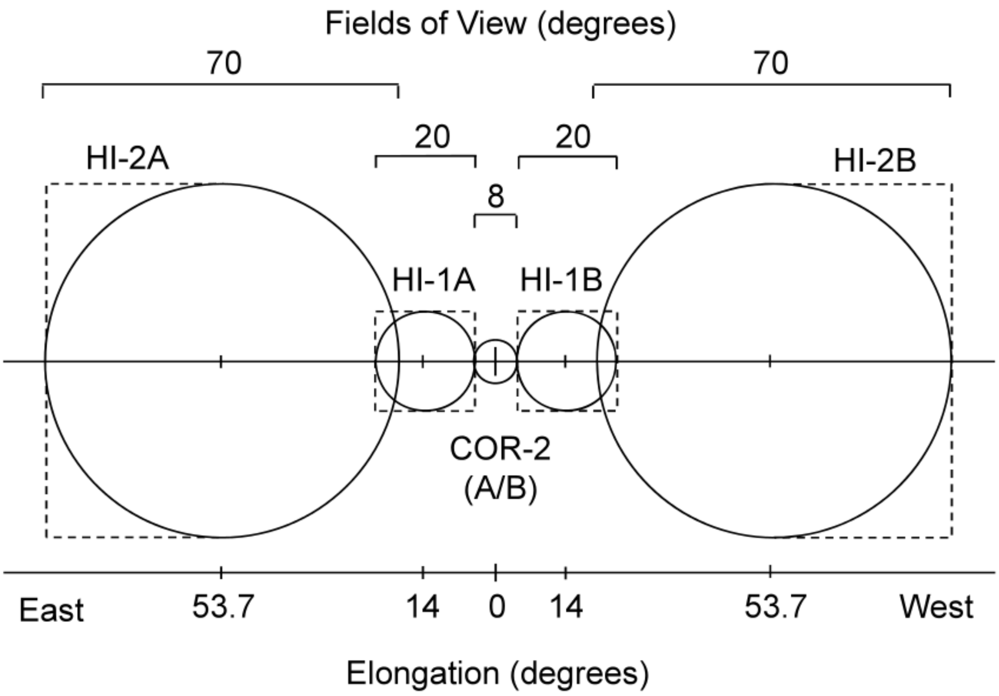

Figure 2.1: The field-of-view of the HI telescopes and the COR-2 Sun-centred coronagraphs (adopted from Eyles et al., 2009).

2.5.4 Heliospheric Imager (HI)

The Heliospheric Imager (HI) is designed to observe the region between the Sun and Earth in visible light, aiming to capture the CME propagation from the corona into the heliosphere. HI packages comprise of two wide-angle telescope systems (HI-1 and HI-2) mounted on the side of each STEREO spacecraft. The angular field-of-view of the HI-1 and HI-2 telescopes are 20° and 70° respectively. HI-1 observes the heliosphere from 4° to 24°, whereas HI-2 covers from 18.7° to 88.7° solar elongation angle (Eyles et al., 2009). Therefore, there is an overlap of about 5° in the field-of-view of HI-1 and HI-2 which allows photometric cross-calibration of the instruments.

In this thesis we have used the observations from EUVI, COR1 and COR2 to understand the near-Sun evolution of CMEs. We have used secchi_prep.pro routine available in the STEREO software package in SSW to process the images. We have also done suitable background subtractions so that the CME morphology can be clearly identified in the white light images.

2.6 In Situ Observations from WIND

The in situ observations of the CME properties at 1 AU are obtained from the WIND spacecraft. WIND was launched in 1994 and is located near the L1 point. This spacecraft consists of total nine instruments and continuously monitors the solar wind plasma, magnetic fields, radio and plasma waves, energetic particles, as well as cosmic gamma ray bursts. In this thesis, we have used the observations from two instruments namely Magnetic Field Instrument (MFI) (Lepping et al., 1995) and Solar Wind Experiment (SWE) (Ogilvie et al., 1995). MFI comprises of boom-mounted double tri-axial sensors, which is designed to measure the interplanetary magnetic field. SWE instrument is a suite of two Faraday cup (FC) sensors, Vector Electron and Ion Spectrometer (VEIS), and a strahl sensor. FC sensors measure the temperature, density and velocity of the solar wind. VEIS measures the foreshock (region upstream of the bow shock) ions and electrons that are reflected from the bow shock. Strahl sensor can measure the velocity distribution function of electrons near the direction of the magnetic field. In this thesis we have used the WIND data averaged over 1 minute temporal window.

2.7 Summary

In this chapter, we have presented a brief discussion on the data sources that we have used in this thesis. In order to study the evolution of photospheric magnetic field governing the conditions leading to solar explosive events like flares and CMEs, we have used the HMI/SDO vector magnetogram data (Chapters 3 and 4). We have also used the multi-wavelength observations from AIA/SDO in 94 Å, 193 Å and 1600 Å bandpass channels to image the post flare loops and flare ribbons. We have utilized the large field-of-view of SWAP imager onboard the PROBA-2 to capture the CME initiation in lower corona (Chapter 5). In order to understand the pre-eruptive stability conditions of solar prominences, we have used the multi vantage point observations from EUVI onboard STEREO A & B to track a prominence associated coronal cavity during its different phases of evolution. To capture the complete evolution of the erupting cavity, we have combined the EUV observations of SWAP with the white light observations from LASCO as described in Chapter 5. Using the multi vantage point white light observations from LASCO, STEREO A & B, we have performed the three dimensional reconstruction of CME morphology which helped us to estimate observationally constrained realistic input parameters required to run the model that we have developed to predict the magnetic field vectors of ICMEs (Chapter 6). In order to validate the model results as described in Chapter 6, we have used the in situ data obtained from WIND spacecraft. As a complementary data set, we have used the observations from MAST, KSO, GONG and MLSO. For the analysis of the observational data obtained from different ground based and space-borne observatories, we have developed several routines in IDL. We have also used the available SSW packages for analyzing those data.

Chapter 3

Conditions in Source Active Regions Leading to Confined and Eruptive Events

3.1 Introduction

Solar flares and coronal mass ejections (CMEs) are the most energetic phenomena that occur in the solar atmosphere. Together they can release large amounts of radiation, accelerated high-energy particles and gigantic clouds of magnetized plasma that may have severe space-weather impacts (Gosling, 1993; Siscoe, 2000; Daglis et al., 2004; Green et al., 2018). Depending on the association with CMEs, solar flares are broadly classified into two distinct categories: confined and eruptive events. Several studies have been made to understand the physical processes behind the origin of CMEs and flares (Kahler, 1992; Gosling, 1993; Nitta, 2002; Gopalswamy, 2016). Nevertheless, the initiation mechanism of CMEs and their association with flares still remain as one of the most elusive topics in solar physics (Schrijver, 2009; Kawabata et al., 2018, and references therein).

Complex large active regions (ARs) on the Sun are the main sources of large flares and most energetic CMEs (Zirin & Liggett, 1987; Sammis et al., 2000; Falconer et al., 2002; Wang & Zhang, 2008; Tschernitz et al., 2018; Toriumi & Wang, 2019). Therefore, understanding the characteristics of AR parameters associated with confined and eruptive flares can shed light on the conditions leading to flare-CME association. Furthermore, the continuous monitoring of spatio-temporal evolution of AR parameters may play an important role to forecast the CME productivity of any AR and the associated space-weather impacts.

Earlier studies reveal that flares and CMEs can be regarded as two different manifestations of the same energy release process (Harrison, 1995; Zhang et al., 2001; Harrison, 2003). Zhang et al. (2001) illustrated that the fast acceleration phase of CMEs in the inner corona is temporally correlated with the rise time of the associated soft X-ray flares, suggesting both the phenomena to be connected through the same physical process, possibly via magnetic reconnection (Lin & Forbes, 2000; Priest & Forbes, 2002). Despite the intrinsic physical relationship between flares and CMEs, observations reveal that not all flares are associated with CMEs (Andrews, 2003; Yashiro et al., 2005; Sun et al., 2015; Chen et al., 2015).

Several attempts have been made to explore the possible circumstances under which solar flares may lead to failed eruptions. Based on a study of four eruptive and four non-eruptive X-class flares produced from different active regions (AR), Wang & Zhang (2007) concluded that the confined flares tend to occur close to the magnetic center of the AR whereas the eruptive ones generally occur away from the magnetic center. Török & Kliem (2005), Kliem & Török (2006), Fan & Gibson (2007), and Olmedo & Zhang (2010) investigated the conditions leading to instability of the flux rope structures in the context of the torus instability, which is one of the ideal MHD instabilities (Priest, 2014). They found that the decay index (defined in Section 1.5.4.4) i.e. the gradient of the overlying magnetic field strength exhibits a critical limit (≈ 1.5) that may determine whether the flux rope will result in eruption or not. Furthermore, Liu (2008) carried out a comparative study among the ten events including four failed eruptions, four eruptions due to torus instability (TI) and two eruptions due to kink instability (KI) from different ARs. The results suggested that the gradient of overlying magnetic field strength decays faster in TI and KI driven events in comparison to the FE events. A detailed description on the torus and kink instabilities has been discussed in Section 1.5.4.

The above studies highlight the role of background magnetic-field strength in determining the confinement behavior of solar eruptions. To understand the distinct properties of confined and eruptive events in details, we studied the eruptive and non-eruptive flares produced by AR 12192, which was the largest active region of Solar Cycle 24. This AR was unique as it produced six X-class flares during its disc passage but none of them were associated with CMEs. An earlier study by Yashiro et al. (2006) on flare-CME association rate shows that 75 % of GOES flare $\geq$ X1.0 class are CME productive, and for the flare class $\geq$ X2.5 the CME association rate is more than 90 %. Thus the flare-rich but CME-poor AR 12192 drew considerable attention from the solar physics community (Sun et al., 2015; Chen et al., 2015; Thalmann et al., 2015; Liu et al., 2016; Jiang et al., 2016). AR 12192 produced only one CME associated with an M4.0 class flare.

The AR 12192 was a unique representative case to carry out a comparative study of the evolution of photospheric magnetic field during the eruptive and non-eruptive flares originating from the same AR. In order to understand the changes in photospheric magnetic field related to flares, several studies have been made in the past (Sudol & Harvey, 2005; Wang, 2006; Petrie & Sudol, 2010; Kumar et al., 2016a). Wang & Liu (2010) found an increase of transverse field at the polarity inversion line (PIL) for 11 X-class flares. Petrie (2012) analyzed six major flares of four active regions, NOAA 11158, 11166, 11283, and 11429, and found an increase in field strength in each case at the time of the flare, particularly in its transverse component close to the polarity inversion line (PIL). Notably, the timescale of evolution of the plasma dominated solar photosphere is different than the magnetically dominated solar corona as the photosphere evolves on a timescale of hours or day, whereas the flare-related coronal changes occur in a matter of minutes (Petrie, 2019). Therefore, the photospheric magnetic field changes observed to occur over a timescale of minutes during the flares as reported in the above studies (Wang & Liu, 2010; Petrie & Sudol, 2010; Petrie, 2012), depict the scenario where coronal forces significantly impact the photosphere.

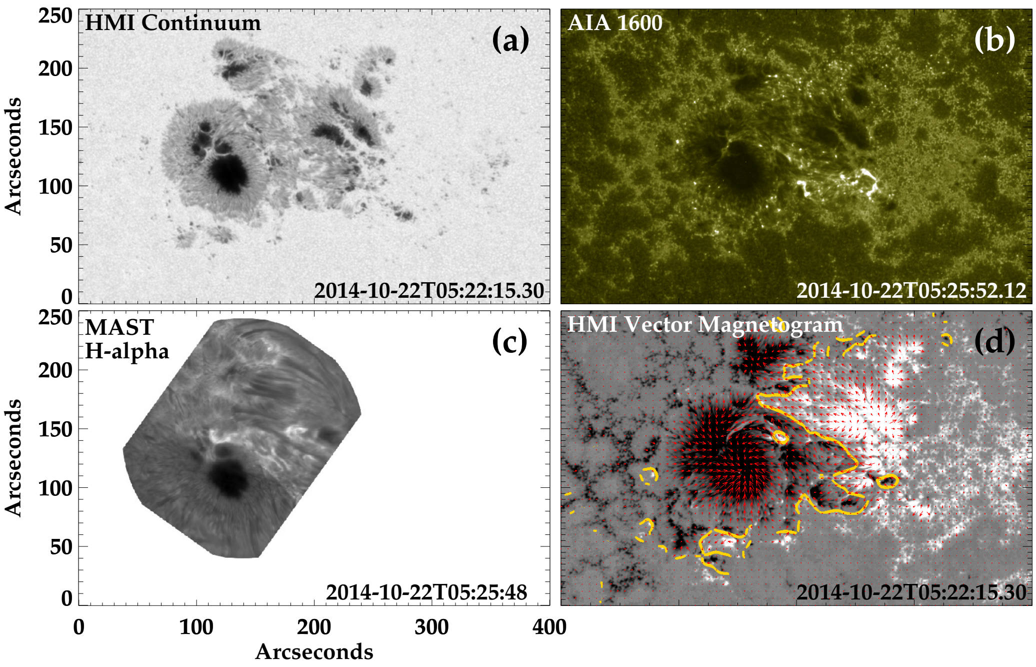
HMI Continuum
(a)
2014-10-22T05:22:15.30
AIA 1600
(b)
2014-10-22T05:25:52.12
MAST
H-alpha
(c)
2014-10-22T05:25:48
HMI Vector Magnetogram
(d)
2014-10-22T05:22:15.30
Arcseconds
0
50
100
150
200
250
0
100
200
300
400

Figure 3.1: *Panel a*: HMI continuum intensity-map of AR 12192. *Panel b*: AR 12192 in AIA 1600 Å image. *Panel c*: high resolution Hα image of AR 12192 taken from Multi Application Solar Telescope (MAST) at the Udaipur Solar Observatory. Due to the large size of AR 12192, the whole AR could not be captured within the field of view (3 arc-minutes) of MAST. *Panel d*: HMI vector magnetogram of the AR. The radial component [B_r] of magnetic field is shown in gray scale and the horizontal component [B_h] of that by red arrows, with saturation values ±1000 G. The yellow lines in the panel illustrate the polarity inversion line.

It is noteworthy that the Lorentz force is the only dominant force in the solar corona as compared to the gas-pressure gradients and gravity (Fisher et al., 2012). The change in Lorentz force can reconfigure the global magnetic field structure of solar corona, resulting in flares and CMEs. The significant magnetic stress, presented in the complex solar active regions (ARs) due to the underlying sub-photospheric or photospheric flows, is responsible for the development of Lorentz force and magnetic free energy in the AR magnetic field. During the flares, the magnetic stress of the AR magnetic field is released, resulting in a Lorentz force impulse impacting on the solar photosphere that can change the configuration of photospheric magnetic field (Hudson, 2000).

Hudson (2000) conjectured that the abrupt release of free magnetic energy during a solar flare would lead to magnetic implosion which would cause magnetic loops to contract and collapse toward the photosphere, resulting in shorter, lower-lying loops after the flare as compared to before (Hudson et al., 2008). They have also proposed that as a result of magnetic implosion an abrupt vertical Lorentz force impulse would act on the solar photosphere. The observational evidences of increased transverse component of photospheric magnetic field accompanied by a large, abrupt, downward vertical Lorentz-force change during the solar flares (Wang & Liu, 2010; Petrie & Sudol, 2010; Petrie, 2012) indeed support the idea of magnetic implosion as proposed by Fletcher & Hudson (2008). The computation of the Lorentz-force change in the above mentioned study was based on the formulation given by (Fisher et al., 2012). The change in the horizontal and radial component of the Lorentz force within a temporal window of δt is given as

$$\delta F_{\mathrm{r}} = \frac{1}{8\pi} \int_{A_{\mathrm{ph}}} (\delta {B_{\mathrm{r}}}^2 - \delta {B_{\mathrm{h}}}^2) \, \mathrm{dA} \tag{3.1}$$

$$\delta F_{\mathrm{h}} = \frac{1}{4\pi} \int_{A_{\mathrm{ph}}} \delta(B_{\mathrm{h}} B_{\mathrm{r}}) \, \mathrm{dA} \tag{3.2}$$

where B_{h} and B_{r} are the horizontal and radial components of the magnetic field, F_{h} and F_{r} are the horizontal and radial components of the Lorentz force calculated over the volume of the active region, A_{ph} is the area of the photospheric domain containing the active region, and dA is the elementary surface area on the photosphere. Following the formulation used by Petrie (2012), the signs in Equations 3.1 and 3.2 have been reversed as compared to the Equations 9 and 10 of Fisher et al. (2012), in order to consider the forces acting on the photosphere from the above atmospheric volume instead of the equal and opposite forces acting on the above atmosphere from below.

Although the flare related photospheric magnetic field and Lorentz force changes are studied extensively for the large eruptive flares as mentioned above, they are poorly studied in the case of confined flares. Importantly, the magnitude of Lorentz force impulse acting on the solar photosphere during the eruptive flares is believed to be proportional to the associated CME momentum (Fisher et al., 2012). Therefore, it is important to understand if the flare associated Lorentz force impulse significantly differs in magnitude for the cases of confined flares as compared to the eruptive ones. In this regard, AR 12192 gave a unique opportunity to compare the flare associated Lorentz force changes associated with the confined and eruptive flares occurred in the same AR.

In this chapter, we perform a detailed comparative study of the morphological and magnetic characteristics associated with the confined and eruptive flares produced by AR 12192. In addition, we examine the pre-flare overlying coronal magnetic environment for both the eruptive and non-eruptive zone of the AR to understand the favorable conditions leading to CME eruption. We present an overview of AR 12192 and the associated flaring events in Section 3.2. In Section 3.3, we discuss the data analysis techniques and methodology. The distinct properties of the confined and eruptive flares are given in Section 3.4. Finally, we summarize our results in Section 3.5.

3.2 Overview of the Active Region Under Study

During the maximum phase of solar cycle 24, the largest solar active region of the cycle appeared on the solar disc as NOAA 12192 in October 2014 (Figure 3.1). Interestingly, this sunspot group was the return of AR 12172 from its previous rotation. It returned back in the next two rotations as NOAA 12209 and NOAA 12237, respectively, as shown in Figure 3.2. In the previous rotation also, it was non-eruptive in nature and produced 12 C-class and 1 M-class flares during its disc passage from September 21 to October 3. After disappearing behind the limb on October 3, it could be tracked in GONG farside images (Figure 3.3). From October 4 to October 16 it crossed the far side of the Sun and evolved to grow as a giant sunspot group and on October 17, it appeared as AR 12192 on the eastern limb of visible solar disc. However, it started showing pre-signatures of its appearance from October 14 when it was behind the eastern limb. Hinode flare catalog revealed two M-class flares on October 14 and 3 C-class and 1 M-class flare on October 16 at the location S14 E88. These strong flares behind the eastern limb and the appearance of a big spot in GONG far side image (Figure 3.3) on

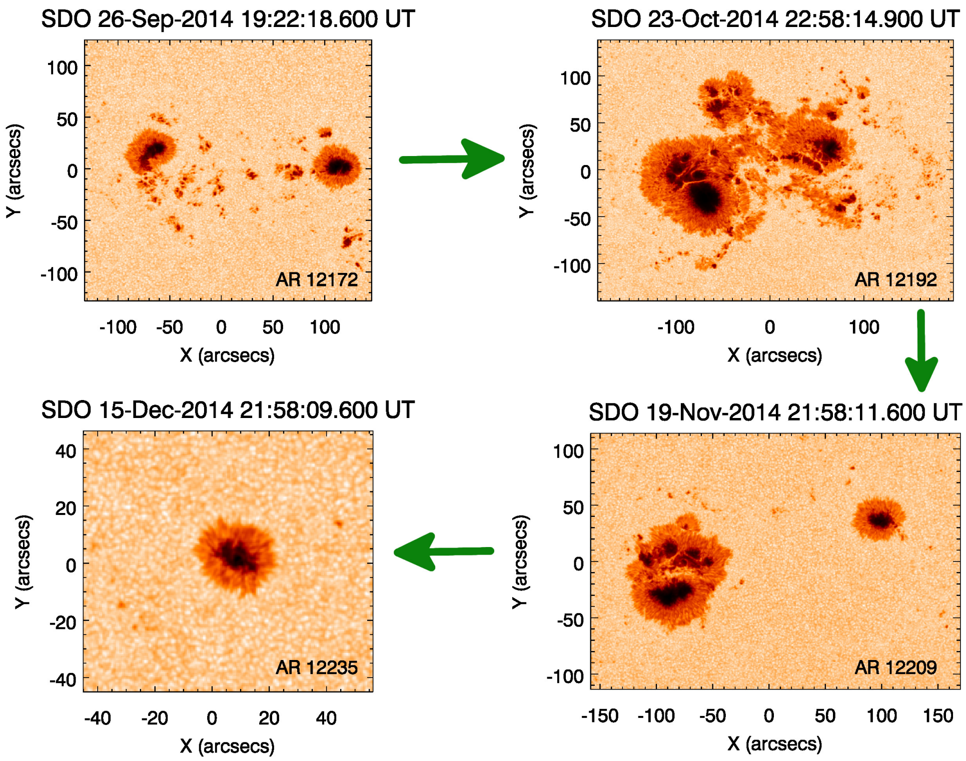
SDO 26-Sep-2014 19:22:18.600 UT
AR 12172
SDO 23-Oct-2014 22:58:14.900 UT
AR 12192
SDO 15-Dec-2014 21:58:09.600 UT
AR 12235
SDO 19-Nov-2014 21:58:11.600 UT
AR 12209
Y (arcsecs)
X (arcsecs)

Figure 3.2: Images show the SDO continuum intensity map of AR 12192 (b) in its previous rotation (a), and subsequent rotations (c) and (d), respectively. The heliographic coordinates of the ARs illustrated in the above panels are S11W05, S12W08, S13W06 and S14E15 respectively from left to right.

October 14, were the distinct signatures of an active region group approaching over the eastern limb.

AR 12192 crossed the visible solar disc from 2014 October 17 to 30 and produced 6 X-class flares, 22 M-class flares, and 53 C-class flares. Notably, all of the energetic confined flares produced by AR 12192 occurred in the core region of that AR i.e. the region near the center of the AR area. On October 24, this AR produced one X3.1-class flare, which became a record-setting event in flare energy associated with a confined eruption (RHESSI, science nugget no.239). As the location (S16W21) of this high energetic X3.1-class flare was very close to the solar disc center, an Earthward halo CME event was expected in association with this event. However, no CME was observed. Throughout the whole disc passage only one CME was produced by this AR associated with an M4.0-class flare that occurred away from the core region on October 24. Li et al. (2015) reported that this eruptive flare occurred close to the open-field-line region in

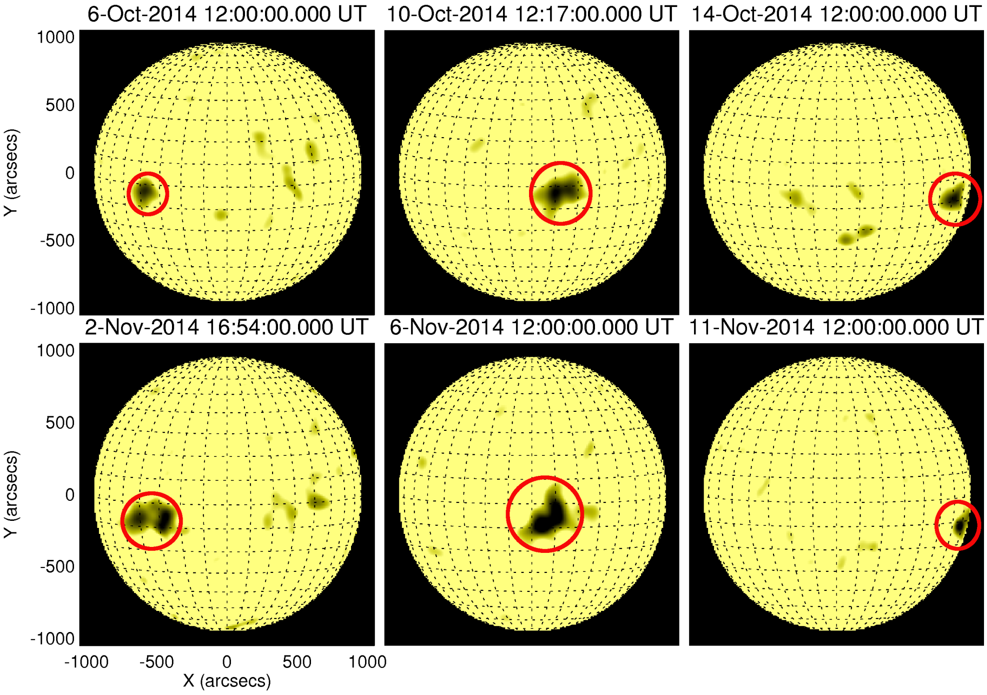
6-Oct-2014 12:00:00.000 UT
10-Oct-2014 12:17:00.000 UT
14-Oct-2014 12:00:00.000 UT
2-Nov-2014 16:54:00.000 UT
6-Nov-2014 12:00:00.000 UT
11-Nov-2014 12:00:00.000 UT
Y (arcsecs)
X (arcsecs)
1000
500
0
-500
-1000
-1000
-500
0
500
1000

Figure 3.3: The upper panels show the appearance of AR 12192 (indicated by the red circles) in GONG far-side images in between the first and second rotation. The bottom panels show the same in between the second and third rotation.

which large coronal loops, appearing as extreme ultraviolet (EUV) structures, fan out rapidly. They suggested that the interaction between the flare material and the neighboring open field lines may have caused the M4.0-class flare to become eruptive.

On October 31, AR 12192 disappeared behind the western limb and returned back in the next rotation on November 13 as NOAA 12209 with a reduced size. From November 13 to November 26 NOAA 12209 was visible on the solar disc and produced 16 C class flares. After that, it went behind the visible solar disc and further reduced to even smaller size and again became visible on the solar disc for the last time in the next rotation from December 10 to 22 as NOAA 12237.

3.3 Data Analysis

The evolution of AR 12192 in the course of its disc passage was well recorded by the observations from the AIA and the HMI onboard SDO. To study the

No.	Flares (GOES)					Location	Nature of eruption
	Date	Start	Peak	End	Class		
		Time (UT)					
1	22 Oct. 2014	01:16	01:59	02:28	M8.7	S13E21	Non eruptive
2	22 Oct. 2014	14:02	14:06	22:30	X1.6	S14E13	Non eruptive
3	24 Oct. 2014	07:37	07:48	07:53	M4.0	S19W05	Eruptive
4	24 Oct. 2014	20:50	21:15	00:14	X3.1	S16W21	Non eruptive
5	25 Oct. 2014	16:55	17:08	18:11	X1.0	S10W22	Non eruptive

Table 3.1: Major M and X-class flares observed in NOAA 12192 during 2014 October 22 - 25

photospheric magnetic-field evolution of AR 12192, we have used the HMI vector magnetogram series from the version of Space weather HMI Active Region Patches (SHARP). The more details on the SHARP data and the processing techniques have been discussed in Section 2.2.2.

As the errors in the horizontal-field components of the vector magnetic field increase towards the limb, we have restricted our analysis to only those major flares which were produced by AR 12192 when its center position was well within ± 45° from the central meridian. Thus the data set considered for analysis includes three X-class flares and two M-class flares observed during 2014 October 22 - 25 close to disc center (Table 3.1). The typical error in the transverse magnetic field of the SHARP data product is 100 Gauss, whereas the error in the line-of-sight component is 5 - 10 Gauss (Liu et al., 2012; Hoeksema et al., 2014).

AR 12192 can be classified as a complex $\beta\gamma\delta$ class of Sunspot group, with Sunspots of opposite sign in the same penumbrae. AR 12192 showed morphological changes (Figure 3.4) as well as changes in magnetic topology during its evolution throughout its disc passage. Therefore, the analysis for each flare under study have been carried out within different bounded regions enclosing the locations of sheared horizontal field close to the polarity inversion line (PIL) where the major changes in horizontal field and Lorentz force are expected to occur (Petrie, 2012). In order to define the size, orientation, and location of the selected boxes we examined the post-flare loops in AIA 94 Å images. As the post-flare arcades are believed to be the regions above which magnetic reconnection occurs (Liu et al., 2013; Chen et al., 2014; Joshi et al., 2014; Kumar et al.,

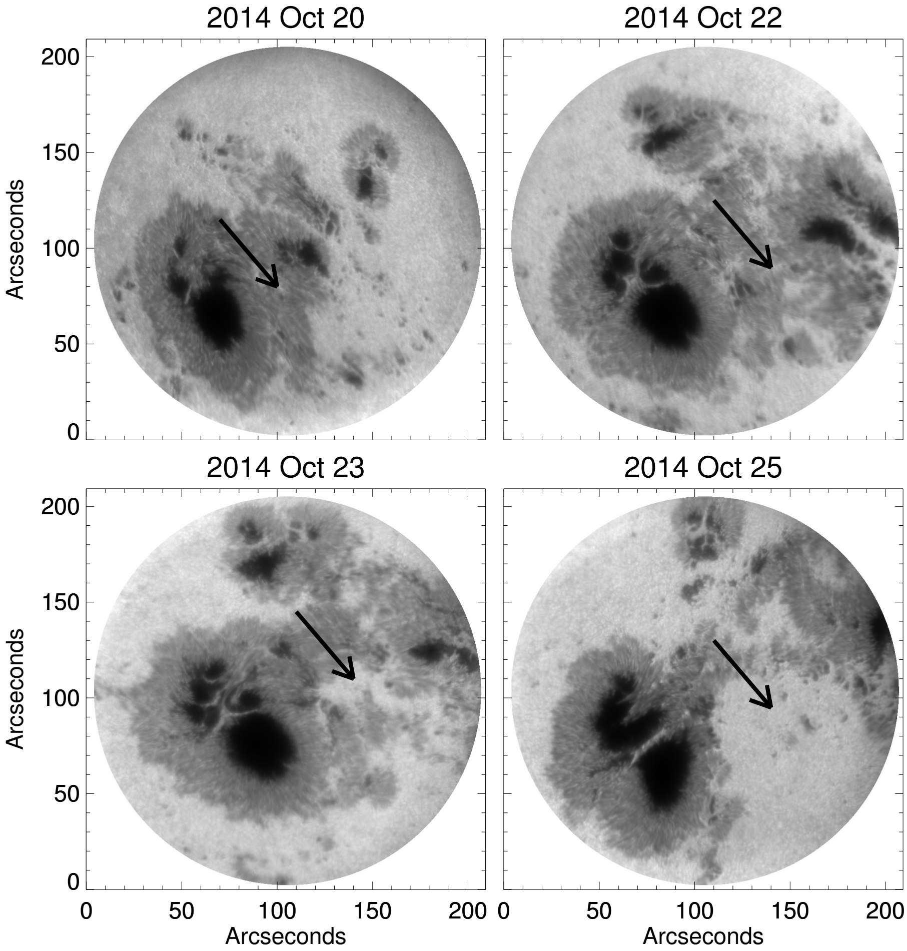

Figure 3.4: G-band images of AR 12192 taken from Multi Application Solar Telescope (MAST) at the Udaipur Solar Observatory. The black arrows mark the core region of AR 12192 where significant morphological changes took place. Due to the large size of AR 12192, the whole AR could not be captured within the field of view (3 arcminutes).

2016b), we have selected our region of interest by enclosing the major post flare arcade structures seen in AIA 94 Å images (Figure 3.5). A time-series analysis of photospheric magnetic-field evolution and Lorentz-force changes for the five major flares (listed in Table 3.1) produced by AR 12192 was carried out on those bounded regions. In order to confirm that the selected boxes cover the region of sheared PIL where the major flares observed, we have overplotted the flaring pixels observed in the AIA 1600 Å image at the flare peak time and drawn the PIL on the magnetogram (Figure 3.5) for each flare of our data set.

For identification of the PIL we have carried out the following steps: First we have convolved all of the pixels with a Gaussian kernel. Then, centering each pixel

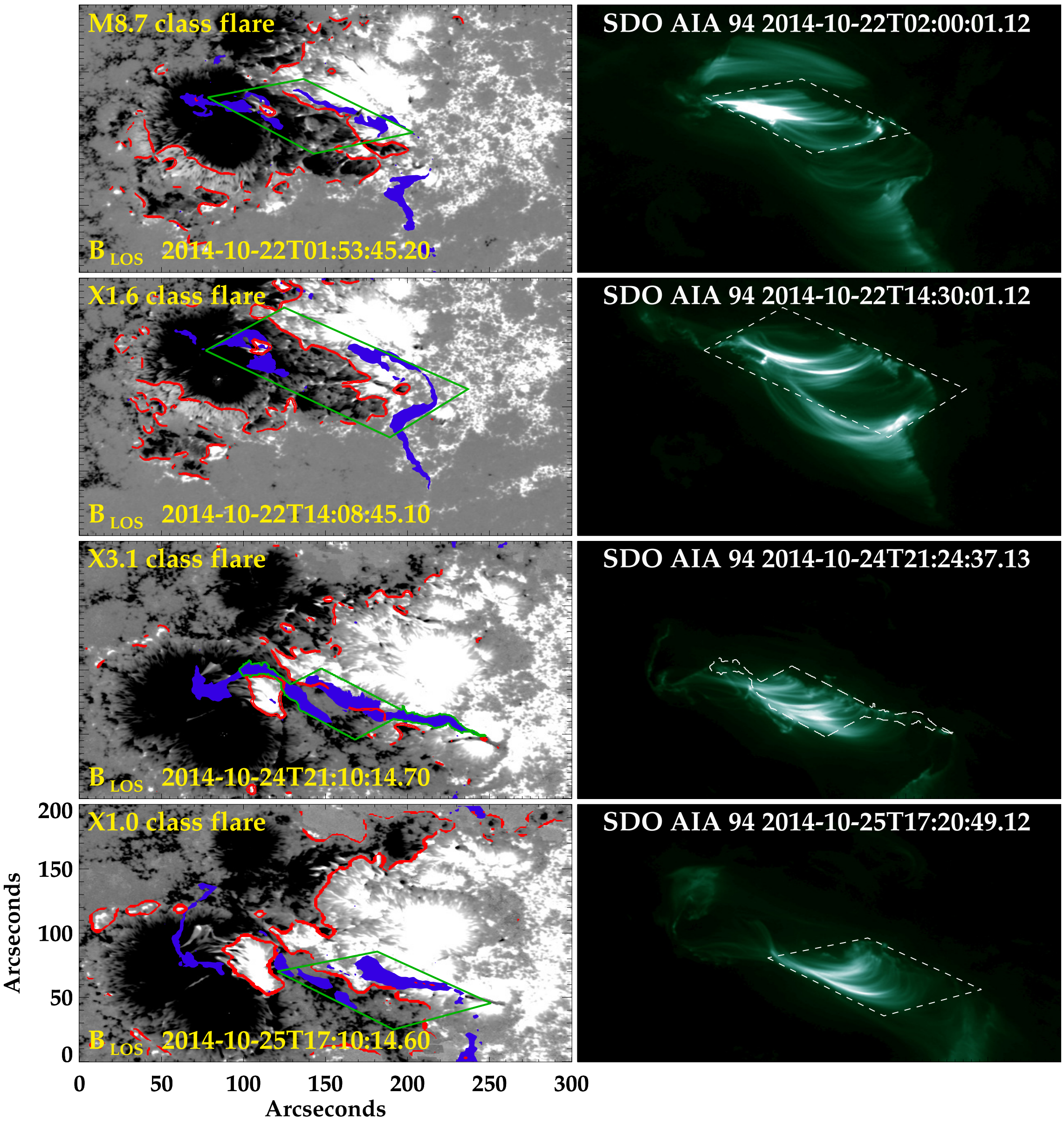
M8.7 class flare
B LOS 2014-10-22T01:53:45.20
SDO AIA 94 2014-10-22T02:00:01.12
X1.6 class flare
B LOS 2014-10-22T14:08:45.10
SDO AIA 94 2014-10-22T14:30:01.12
X3.1 class flare
B LOS 2014-10-24T21:10:14.70
SDO AIA 94 2014-10-24T21:24:37.13
X1.0 class flare
B LOS 2014-10-25T17:10:14.60
SDO AIA 94 2014-10-25T17:20:49.12
Arcseconds
0
50
100
150
200
Arcseconds
0
50
100
150
200
250
300

Figure 3.5: *Left column*: HMI line-of-sight magnetic field during the non-eruptive flares. The red lines denote the polarity inversion line and the blue regions are the over-plotted flaring pixels from AIA 1600 Å images. The green boundary denotes the selected region within which all the calculations have been done. *Right column*: the post-flare arcade in AIA 94 Å images. The white dashed boundary in each image of right column shows the selected region bounded by the green-solid line in the left column.

of the magnetogram of vertical component of magnetic field, we have scanned five consecutive pixels in both the horizontal and vertical directions. After that we compared the maximum and minimum values of each vertical and horizontal array of five pixels. If these two values are opposite in sign and the magnitude of these two values are greater than the noise level of 10 Gauss on either of the two arrays, then the pixel that is in between these two minimum and maximum valued pixels is identified as the pixel tracing the PIL. These pixels were then connected to delineate the PIL.

To calculate the Lorentz-force changes we have used the formulation introduced by Fisher et al. (2012) as discussed in Section 3.1. To study the flare-related morphological changes in AR 12192 we have used the HMI full-disc continuum images observed in the Fe I absorption line at 6173 Å with a spatial scale of $0.5''$ per pixel and temporal scale of 12 minutes. We have taken a cutout of the whole active region from the full-disc continuum intensity map and then all of the images were differentially rotated to the solar disc center in order to co-align them. To identify the umbra–penumbra and penumbra–quiet-Sun boundaries, we first have normalized the brightness values of all the pixels within the cutout region by the median of brightness values of a 10×10 pixel^2 quiet-Sun region surrounding the sunspot. Then a cumulative histogram (Pettauer & Brandt, 1997; Mathew et al., 2007) of the intensity of each pixel's brightness is computed within the cutout, which encloses the umbral and penumbral region as well as the immediately surrounding quiet-Sun region. This cumulative histogram (Figure 3.6) is used to calculate the intensity threshold for defining the umbra–penumbra and penumbra–quiet-Sun boundary.

The steep rise in the histogram plot (upper panel of Figure 3.6) near the normalized intensity unity corresponds to the quiet-Sun region, whereas the flattest part of the plot corresponds to the umbral region. In between the above two parts of the plot, the less steep and moderately flat part denotes the penumbral region. In order to obtain the threshold values, the nearly flat portions of the plots were fitted with a linear curve. The maximum intensity at which the linearly fitted straight lines start deviating from the plot is considered to be the intensity threshold. Applying the above procedure to the cumulative histogram computed from the cutout region enclosing the source location of eruptive M4.0-class flare on 2014 October 24, we found the normalized intensity threshold for the umbra–penumbra boundary as 0.56 and that of penumbra–quiet-Sun boundary as 0.92. These values were then used to calculate the penumbral area variation during the

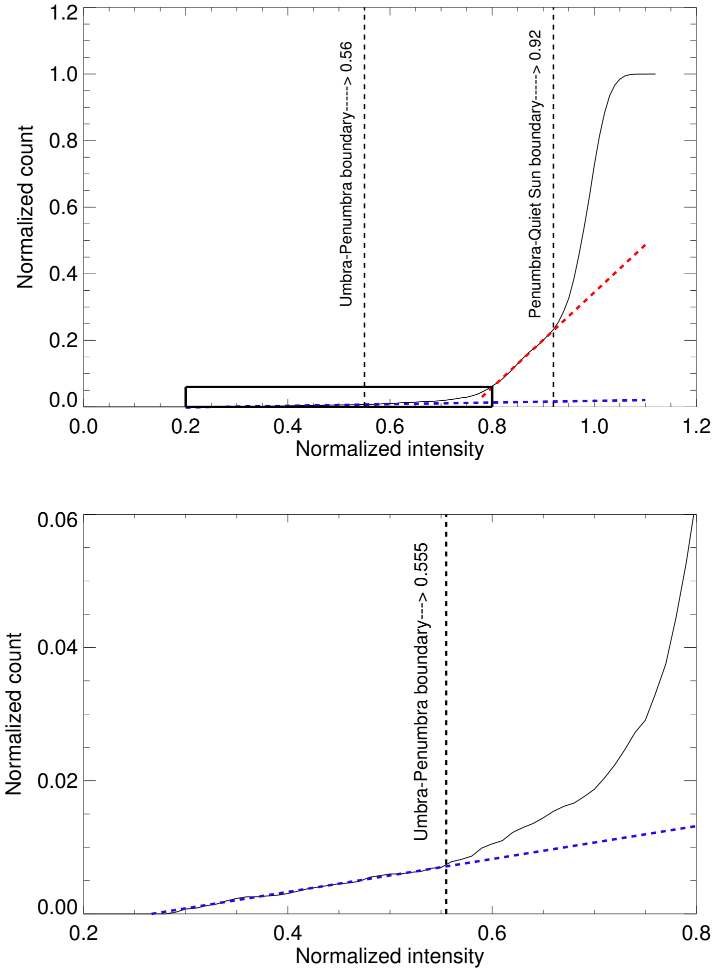

Figure 3.6: *Top panel*: the cumulative intensity histogram for identifying the umbra–penumbra and penumbra–quiet-Sun boundary. The blue and red dashed lines in the top panel are the linearly fitted lines to the two nearly flat part of the plot corresponding to umbral and penumbral region respectively. The vertical dashed lines mark the values obtained for umbra–penumbra and penumbra–quiet-Sun boundaries. *Bottom panel*: the linearly fitted flattest part of the plot enlarged from the rectangular box shown in the top panel (within normalized intensity range 0.2 to 0.8 and normalized count values 0.00 to 0.06).

eruptive M4.0-class flare. To study the overall umbral and penumbral area variation of the whole AR, the cumulative histograms were computed for all the days during the disc passage of AR 12192 from 2014 October 21 to 26 when its longitude was within ±75° from the central meridian. From this, we have found the normalized intensity threshold for umbral-penumbral boundary as 0.53 and that of penumbral-quiet Sun boundary as 0.90 for the whole AR. In order to remove the projection effect of the spot area, we have used the algorithm introduced by

Çakmak (2014). This method calculates the true area of sunspot group in units of square degrees by computing the heliospheric coordinates of each pixels on the image.

Furthermore, to investigate the overlying magnetic-field strength for both the eruptive and non-eruptive region of AR 12192, we have extrapolated the photospheric magnetic field using the non linear force free field (NLFFF) model (Aschwanden, 2016). From the extrapolated magnetic field we have estimated the decay index as defined in Section 1.5.4.4 in the context of torus instability. The estimation of decay index has been done over both the non-eruptive and flaring regions of AR 12192 in order to compare the gradient of overlying magnetic-field strength over those regions.

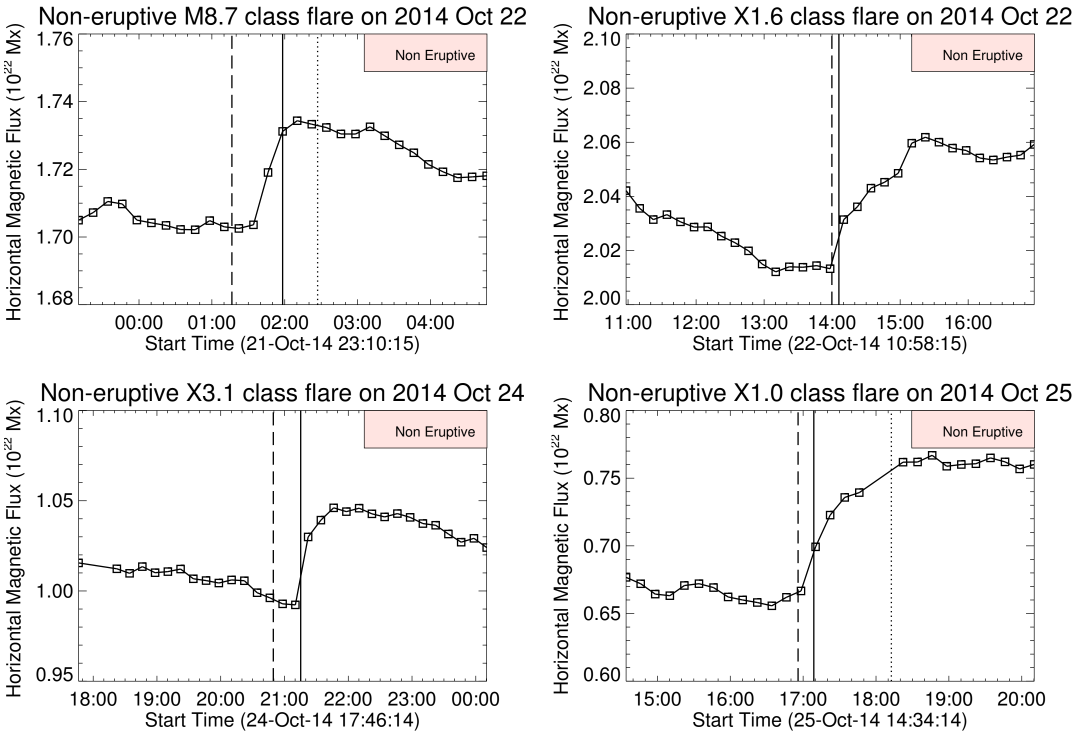

Figure 3.7: Horizontal magnetic-field evolution during the non-eruptive flares. The dashed, solid, and dotted vertical lines denote the flare onset, peak, and decay times respectively.

3.4 Comparative Study of Confined and Eruptive Events: Results

3.4.1 Magnetic-field evolution for the non-eruptive flares

Analyzing the six-hour series of vector magnetogram data centered at the peak of the non-eruptive flares of our dataset, we have found that the integrated transverse magnetic flux over the selected regions near the PIL, increased permanently for all of the cases (Figure 3.7). This result is consistent with the earlier flare-related transverse-magnetic-field changes reported by Wang (2006) and Petrie (2012). Here the changes in the horizontal magnetic flux have been found to be persistent up to more than two hours after the peak time of each flare. These permanent changes ensure that the temporal evolution of the horizontal magnetic flux was real and did not include any flare-related artifact, as the flare-related artifacts are transient in nature and do not cause any permanent changes in

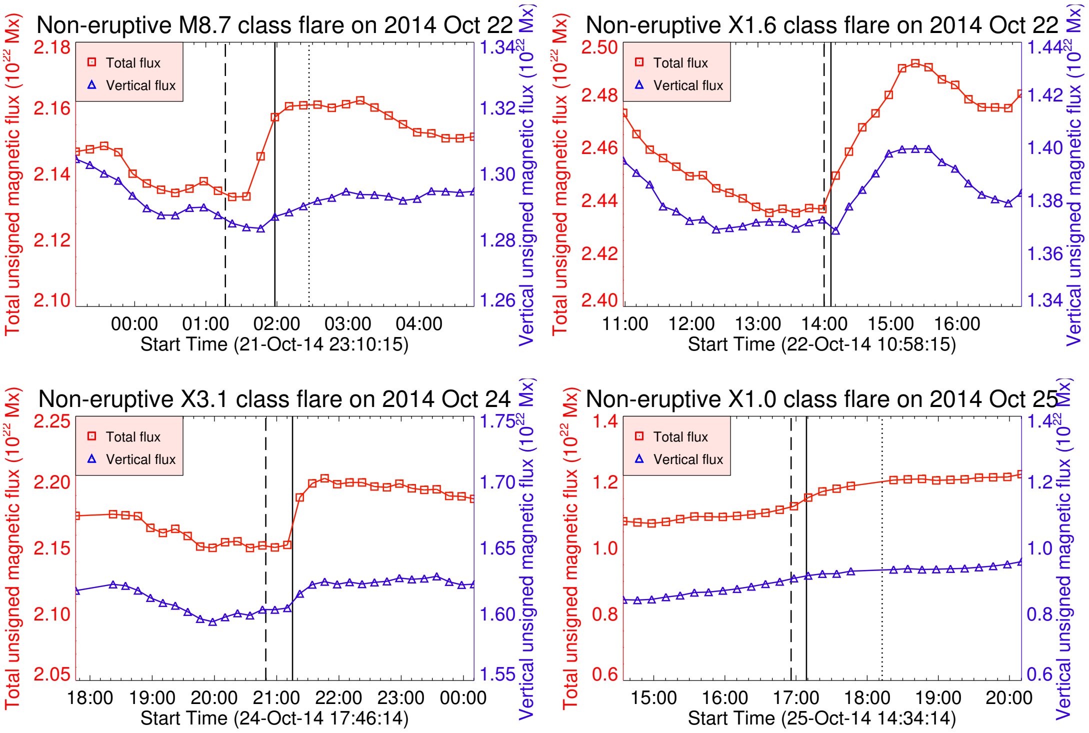

Figure 3.8: Temporal evolution of the total and vertical magnetic flux for the non-eruptive flares. The dashed, solid, and dotted vertical lines denote the flare onset, peak, and decay times respectively.

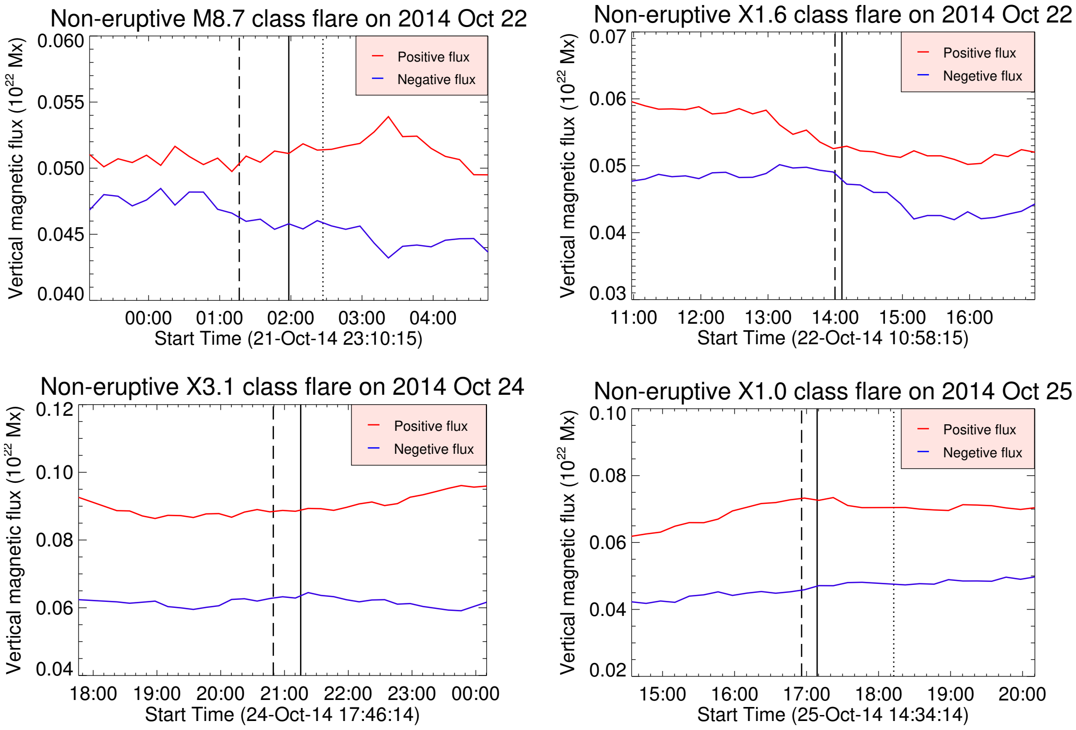

Figure 3.9: The temporal evolution of positive and negative magnetic flux for the four non-eruptive flares in AR 12192. The dashed, solid, and dotted vertical lines denote the flare onset, peak, and decay times respectively.

the temporal profile of the measured magnetic field (Sun et al., 2017). Figure 3.7 shows the temporal evolution of the horizontal magnetic flux for the non-eruptive flares. Error bars in the horizontal magnetic flux were too small ($\approx 10^{-3}$ times the calculated values) to be plotted. The change in horizontal magnetic flux has been found to range between 3×10^{20} and 7×10^{20} Mx within less than half an hour for the four non-eruptive flares which imply approx 2 % to 10 % change from its initial value in the pre-flare stage.

In Figure 3.8, we show the temporal evolution of the total and vertical magnetic flux in the non-eruptive flares. The red-solid lines in the figure depict the changes in total magnetic flux. Notably, the temporal profile of the vertical magnetic flux does not show any significant changes during the flares, which is in agreement with earlier results (Petrie 2012). The temporal profiles of the positive and negative flux (Figure 3.9) show that there was no significant flux cancellation along the PIL associated with the confined flares.

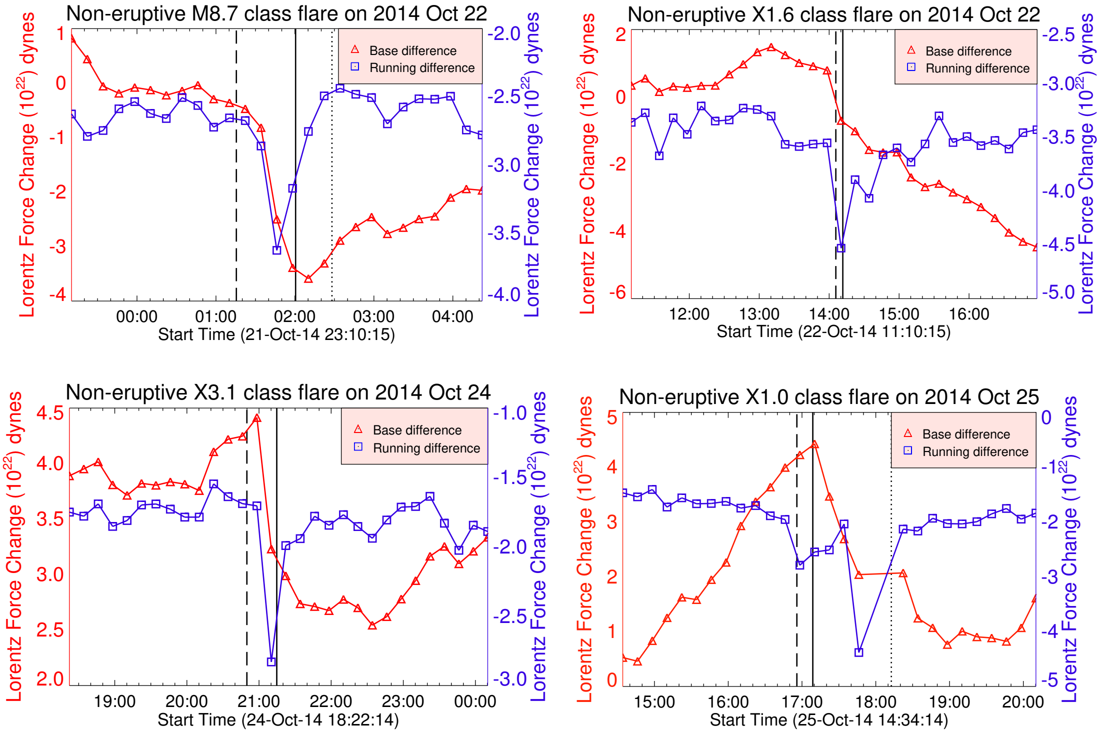

Figure 3.10: The changes in radial component of Lorentz force for the non-eruptive flares. The dashed, solid, and dotted vertical lines denote the flare onset, peak, and decay times respectively.

The Lorentz-force changes for the non-eruptive flares have been illustrated in Figure 3.10. During each of the flares, the radial component of the Lorentz force underwent a large and abrupt downward change. The magnitude of these force changes, ranging from about 2.0×10^{22} dyne to 2.6×10^{22} dyne, are comparable to those found in the previous estimates of flare-related Lorentz-force changes (Petrie, 2012; Wang et al., 2012). For the four non-eruptive flares, the change in Lorentz force per unit area ranges between 390 dyne cm^{-2} to 1390 dyne cm^{-2}. Earlier study by Petrie (2013) reported that the change in Lorentz force per unit area is of the order of 10^3 to 10^4 dyne cm^{-2} for eruptive flare.

3.4.2 Magnetic-field evolution for the eruptive flare

The eruptive M4.0-class flare occurred away from the core region of AR 12192. The source region of this flare is depicted in Figure 3.11, where the blue box in the left panel denotes the flaring location identified from the AIA 1600 Å images. In this case, the increment in the horizontal magnetic flux (Figure 3.12) was about

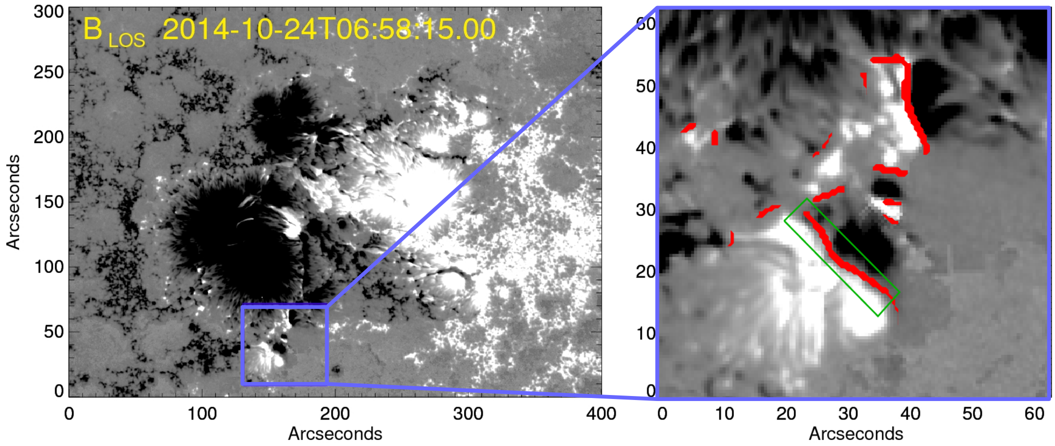
B LOS 2014-10-24T06:58:15.00
Arcseconds
300
250
200
150
100
50
0
0
100
200
300
400
Arcseconds
60
50
40
30
20
10
0
0
10
20
30
40
50
60
Arcseconds

Figure 3.11: *Left panel*: HMI line-of-sight magnetic field during the eruptive M4.0-class flare. *Right panel*: the line-of-sight magnetic field enlarged from the selected region shown in the left panel. The thick red lines denotes the polarity inversion line. The green boundary in the right panel denotes the selected region within which all the calculations have been done.

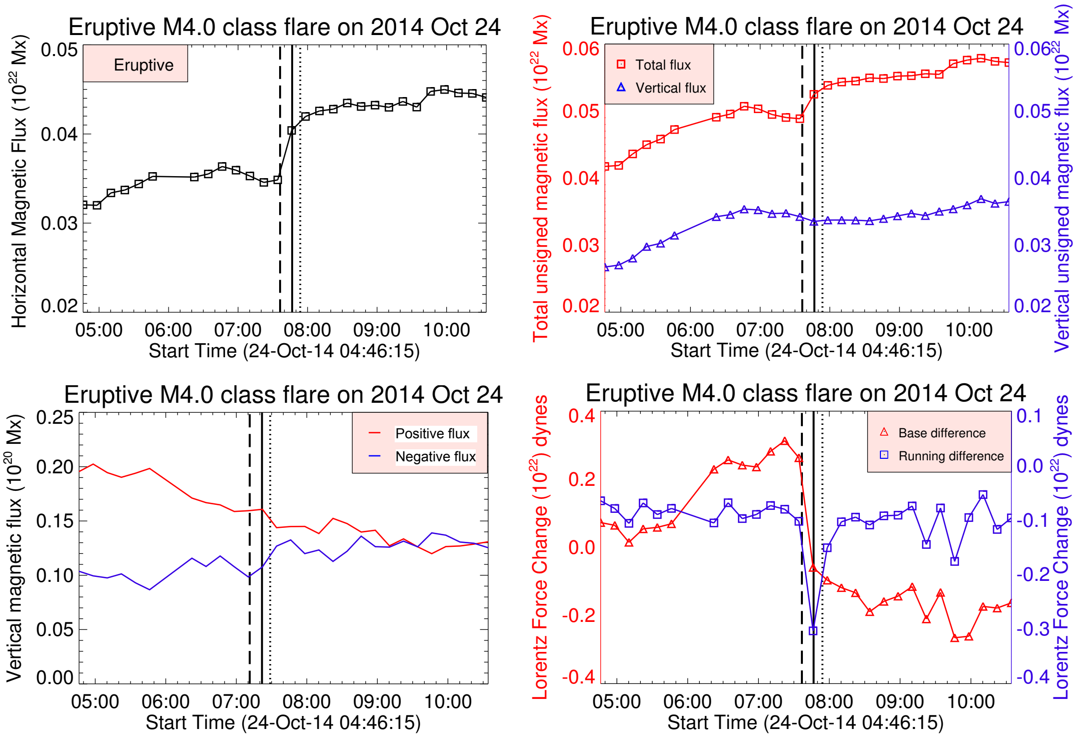

Figure 3.12: Magnetic-field evolution and Lorentz-force changes for the eruptive M4.0-class flare. *Upper-left panel*: the evolution of horizontal magnetic field. *Upper-right panel*: the temporal evolution of the total and vertical magnetic flux. *Lower-left panel*: the temporal evolution of positive and negative magnetic flux. *Lower-right panel*: the changes in radial component of Lorentz force. The dashed, solid and dotted vertical lines denote the flare onset, peak, and decay times respectively.

$1{\times}10^{20}$ Mx. The change in horizontal magnetic flux for this eruptive flare was about 30 % from its initial value in the pre-flare stage, in contrast to changes (2 % to 10 %) measured for the confined flares. Similar to the non-eruptive flares, no significant changes in the vertical component of the magnetic field (upper-right panel of Figure 3.12) have been found for this flare within the selected region shown by the green boundary in the right panel of Figure 3.11.

The change in Lorentz force during this eruptive flare was about $0.3{\times}10^{22}$ dyne (Figure 3.12). Noticeably, the change in Lorentz force per unit area for this case was about 4040 dyne cm^{-2}, which is almost three times larger than the maximum change found in the four non-eruptive cases. Also, the change in mean horizontal magnetic field during the eruptive flare has been found to be about 135 Gauss, which is much larger than that of the confined flares (15 to 35 Gauss).

3.4.3 Morphological evolution of AR 12192

AR 12192 underwent a gradual growth starting from the previous disc passage during which the umbral and penumbral area increased from ∼40 to ∼85 MSH (Millionths of Solar Hemisphere) and ∼300 to ∼500 MSH respectively (Figure 3.13). The further growth of the AR occurred on the backside of the visible solar disc. Finally, when it appeared as AR 12192 in the second rotation, both the penumbral and umbral area grew almost 6 times larger than in the previous rotation. During October 23 and 24 it attained the massive size of about 4700 MSH (Figure 3.14) and became the largest active region of Solar Cycle 24. From October 24, both the umbral and penumbral area (Figure 3.13) of AR 12192 decayed gradually from its maximum value. The morphological changes of AR 12192 due to this gradual decay of penumbral area are shown in Figure 3.4, as observed in the high-resolution (0.2 arcsecond) images obtained by MAST. MAST G-band images for four different days reveal the significant penumbral decay near the core region (marked by black arrows in Figure 3.4) of AR 12192 where all of the four major X-class flares took place. In the third rotation, the active region area decreased by almost ten times of that from the previous rotation. Notably, in all the three rotations the penumbral to umbral area ratio

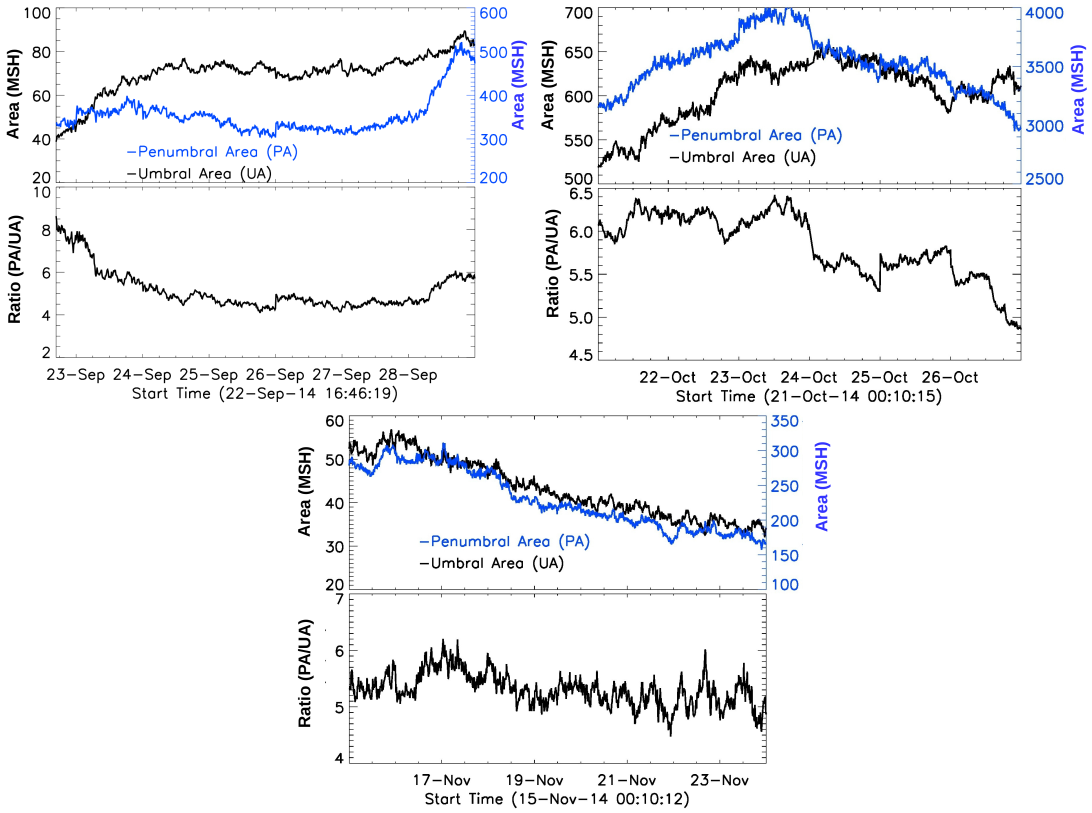

Figure 3.13: Variation of umbral and penumbral area of AR 12192 during its disk passage (upper right panel), previous (upper left panel) and next rotation (lower). Temporal evolution of the area ratio of penumbra to umbra is shown in the second row of each panels.

remained almost constant (approximately 5.5), implying that both the umbra and penumbra evolved almost in a similar fashion during the entire period of observation.

Besides the gradual change, we have also found flare-related abrupt penumbral area decay away from the PIL of the source region of eruptive M4.0-class flare on 2014 October 24. The region of rapid penumbral area decay is illustrated in Figure 3.15. The blue box in the upper panels shows the bounded region within which the maximum change in penumbral area is observed. The temporal profile of integrated normalized intensity (panel [e] of Figure 3.15) calculated within the bounded box exhibits a permanent increment after the flare, suggesting the permanent disappearance of the penumbral area after the flare. Importantly, this rapid decay in penumbral area was associated with the permanent decay in horizontal magnetic field within the same region. The mean horizontal magnetic

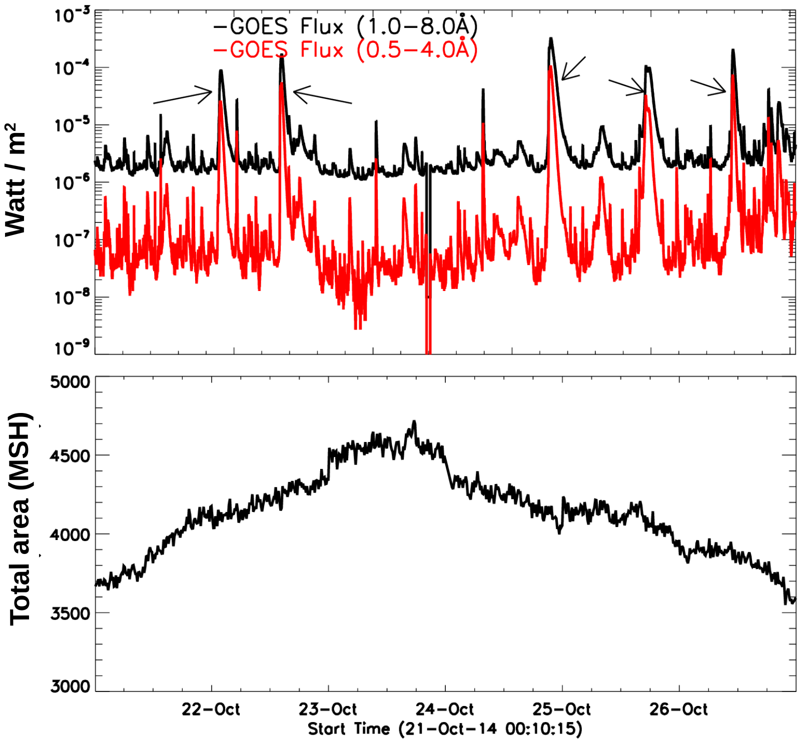

Figure 3.14: *Top panel*: the temporal profile of GOES X-ray flux during 2014 October 21 - 26. The black arrows in the panel mark the X-class flares. *Bottom panel*: the total area variation of AR 12192 during the same period.

field, calculated within the bounded box shown in Figure 3.15, decreased permanently by almost half of its initial value from about 600 Gauss to 300 Gauss (panel [e]) within less than half an hour during this eruptive flare. This scenario is consistent with the earlier finding of flare-related rapid penumbral decay away from the PIL and the associated permanent decrease in horizontal magnetic field (Xu et al., 2016). To further quantify this flare-related penumbral area decay, the time evolution of the penumbral area variation is illustrated in Figure 3.16. The penumbral area is calculated for the contoured sunspot (upper-panel of Figure 3.16), which was the source region of the eruptive flare. The white and blue contours in the figure mark the umbra–penumbra and penumbra–quiet-Sun boundaries, which are determined by using the normalized intensity thresholds calculated from the cumulative intensity histogram (Figure 3.6). Noticeably, the temporal profile of penumbral area (lower panel of Figure 3.16) exhibits a permanent decrement from about 140 to 80 Mm^2 within less than half an hour during the flare.

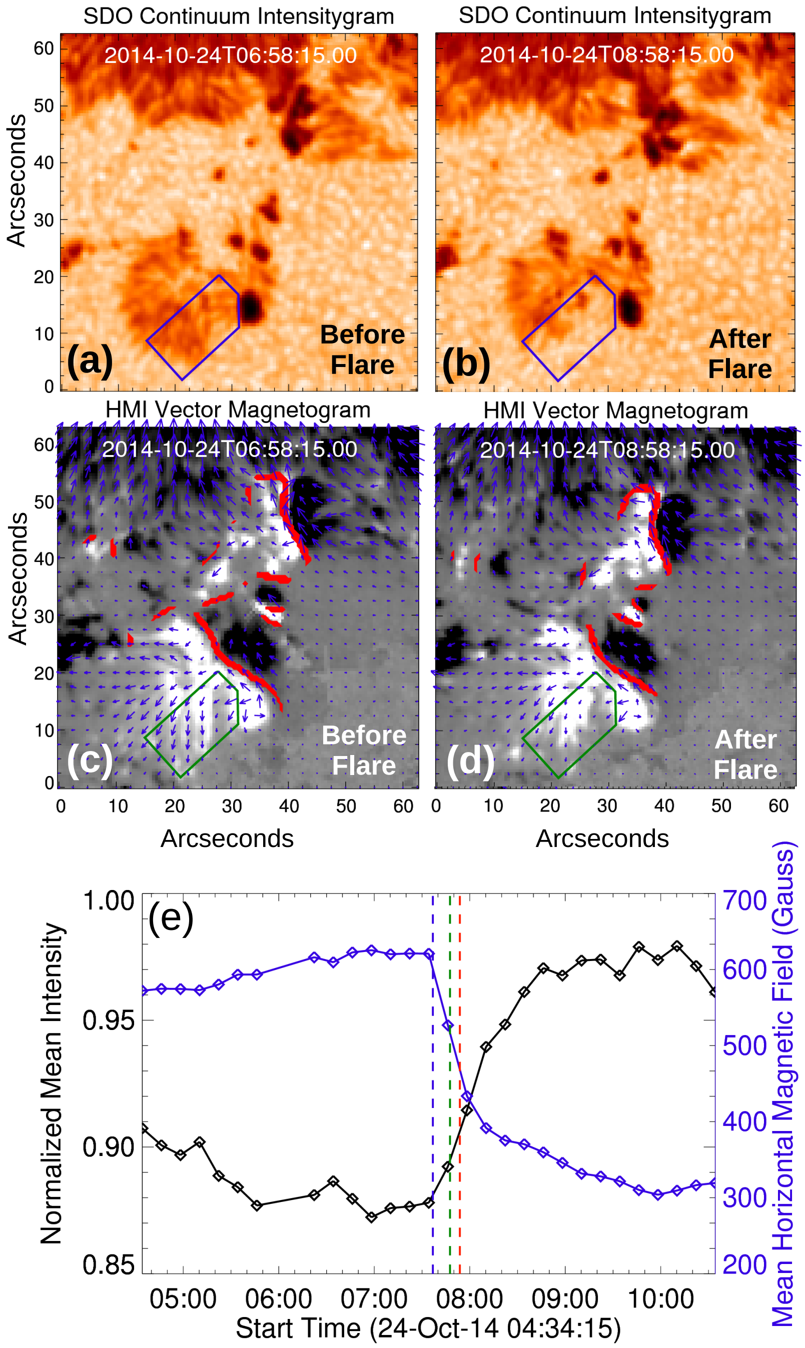

Figure 3.15: The morphological structure of the penumbral region away from the core region of AR 12192 before (a) and after (b) the eruptive M4.0-class flare respectively. The blue boxes in panels (a) and (b) denote the bounded region where the maximum changes in the penumbral area occurred. Panels (c) and (d) depict the vector magnetograms of the same region shown in panels (a) and (b). The green boxes in panels (c) and (d) denote the same bounded region marked by the blue boxes in panels (a) and (b). In the panel (e) the black-solid line represents the temporal variation of normalized intensity and the blue-solid line represents the variation of transverse magnetic field calculated within the box shown in the above panels.

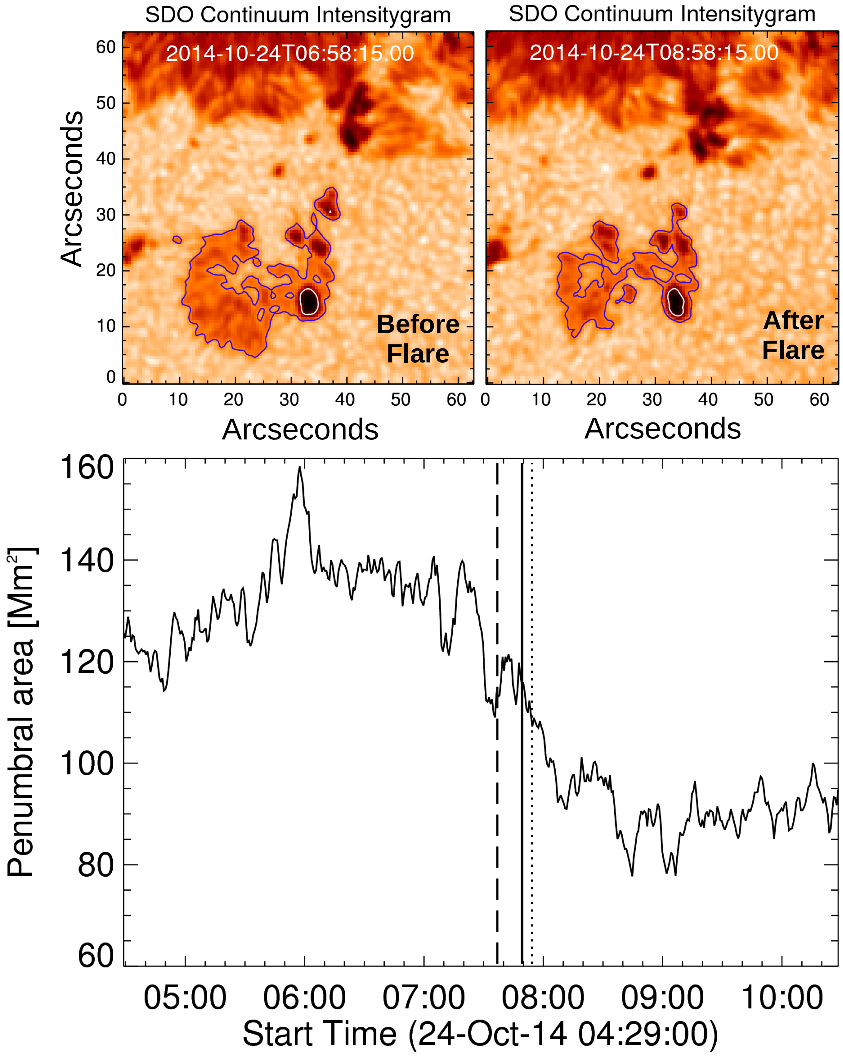

Figure 3.16: *Lower-panel*: the areal variation of the contoured penumbral region shown in *upper-left* and *upper-right* panels. The dashed, solid, and dotted vertical lines in the *lower-panel* denote the flare onset, peak, and decay times respectively.

3.4.4 Comparison of overlying magnetic-field strength for both the eruptive and non-eruptive region

All of the non-eruptive high energetic flares occurred in the core region of AR 12192 (Figure 3.5). However, the eruptive flare occurred away from the core region (Figure 3.17 a,b). From the study of extrapolated magnetic field, we have found that the overlying magnetic-field strengths were different for the eruptive and non-eruptive flaring regions. In order to quantify the overlying magnetic-field strength, we have calculated the decay index over the whole AR. To compare the decay-index profile for both the eruptive and non-eruptive region of AR 12192,

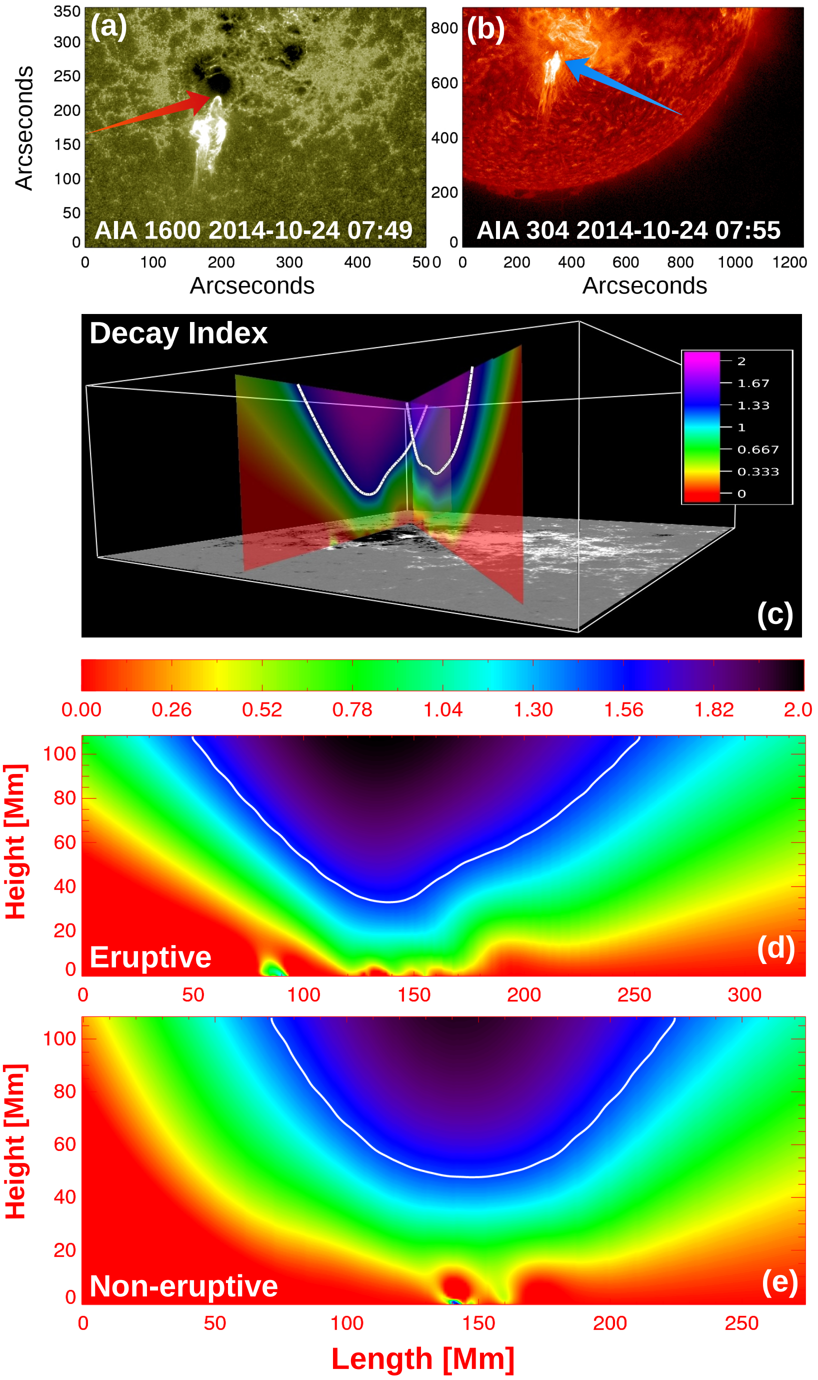

Figure 3.17: The red and blue arrows in panels (a) and (b) mark the source location of the eruption on 2014 October 24 in AIA 1600 Å and 304 Å images respectively. Panel (c) depicts the two decay-index profiles drawn over the HMI line-of-sight magnetogram. The right-hand decay index profile in panel (c) is along the main PIL of the non-eruptive core region and the left-hand decay index profile is drawn over the eruptive flaring region. The two decay index profiles shown in panel (c) are illustrated separately in panels (d) and (e) respectively.

two 2D profiles of decay index are plotted in Figure 3.17, where one of them is along the main PIL of the core region, which was the non-eruptive zone, and the other one is over the source region of the eruptive flare, which occurred away from the core region. Interestingly, the two decay index profiles show different depths in the contour drawn for 1.5 value, which is believed to be the critical decay index for the onset of the torus instability (Török & Kliem, 2005; Wang & Zhang, 2007; Liu, 2008). The critical decay index was achieved at a height about 52 Mm over the non-eruptive core region of AR 12192, whereas the decay index decreased to the critical value (1.5) at height 35 Mm over the eruptive region. This implies that the external magnetic field decays faster over the erupting region than the non-eruptive one. This result further suggests that the strength of the overlying magnetic field plays a decisive role in determining whether the AR will be CME-productive or not.

3.5 Summary and Conclusion

Our results based on a comparative study of the morphological and magnetic field evolution of the eruptive and non-eruptive flares produced by the largest AR of Solar Cycle 24 i.e. AR 12192 are summarized in Table 3.2.

By comparing the magnetic characteristics for both the eruptive and non-eruptive flares, we conclude that the eruptive flare left a significant magnetic imprint on the solar photosphere, whereas the photospheric magnetic field changes were comparatively small in the case of the confined flares. In contrast to the eruptive flare, the confined flares exhibited very weak changes in horizontal magnetic-field and Lorentz force per unit area (Table 3.2). This scenario is consistent with the flare-related momentum balance condition where the Lorentz-force impulse is believed to be proportional to the associated CME momentum (Fisher et al., 2012; Wang et al., 2012). Thus, if a flare is not associated with a CME then the Lorentz-force impulse during that confined flare is expected to be smaller. Our results from the analysis of selected four non-eruptive flares support this

Date	October 22	October 22	October 24	October 24	October 25
GOES peak time [UT]	01:59	14:06	07:48	21:15	17:08
GOES flare class	M8.7	X1.6	M4.0	X3.1	X1.0
Nature of eruption	Non eruptive	Non eruptive	Eruptive	Non eruptive	Non eruptive
Change in horizontal magnetic flux [Mx]	$\approx 3{\times}10^{20}$	$\approx 5{\times}10^{20}$	$\approx 1{\times}10^{20}$	$\approx 5{\times}10^{20}$	$\approx 7{\times}10^{20}$
Percentage of change in horizontal magnetic flux	$\approx 2\%$	$\approx 2.5\%$	$\approx 30\%$	$\approx 5\%$	$\approx 10\%$
Change in mean B_{h} [Gauss]	≈ 15	≈ 15	≈ 135	≈ 25	≈ 30
Change in Lorentz force [dyne]	$\approx 2.6{\times}10^{22}$	$\approx 1.5{\times}10^{22}$	$\approx 0.3{\times}10^{22}$	$\approx 1.7{\times}10^{22}$	$\approx 2{\times}10^{22}$
Change in Lorentz force per unit area [dyne cm^{-2}]	≈ 1390	≈ 390	≈ 4040	≈ 890	≈ 960
Morphological change	Not significant	Not significant	Significant	Not significant	Not significant
Overlying magnetic-field strength	Strong	Strong	Weak	Strong	Strong

Table 3.2: Comparison between the eruptive and non-eruptive flares produced by AR 12192

idea. All of the five flares that occurred in AR 12192 showed abrupt and permanent changes in photospheric magnetic field, which is a common feature in major flares (Wang et al., 2012; Sun et al., 2012). However, our results suggest that the changes are larger in magnitude for the eruptive flares as compared to that in confined ones. Therefore, the flare-related temporal changes in magnitude of the transverse magnetic field and Lorentz-force impulse appeared to be well correlated with the nature of eruptions. The weak changes in the magnetic characteristics during the four non-eruptive flares support the earlier results of Sun et al. (2015) where they compared the photospheric changes during one non-eruptive X3.1-class flare produced by AR 12192 with those during two eruptive X5.4 and X2.2-class flares produced by different ARs, i.e. AR 11429 and AR 11158 respectively. However, our approach is different as we compared the photospheric magnetic environments of the four highly energetic non-eruptive flares with those for the eruptive flare which originated from the same AR (AR 12192). Therefore, our analysis is free from the bias of other factors, such as the scale size and complexity of the different ARs, which are believed to play a key role in the solar eruptive events.

The significant growth in the AR area is reflected in the build up of the magnetic energy content of AR 12192, as it produced six highly energetic X-class flares within an interval of one to two days during its disc passage. This implies that the huge size of AR 12192 may be responsible for its energy storage being sufficient to trigger the recurrent highly energetic flares. The rapid penumbral-area decay observed during the eruptive M4.0-class flare reveals how the strong Lorentz force impulse can shape the dynamics of the solar eruptions and cause morphological changes in the photospheric features. The physical explanation behind these flare-related photospheric morphological changes is given in Xu et al. (2016). They showed that during the flare, due to the magnetic-pressure imbalance between the reconnection site and the outer atmosphere, the Lorentz force away from the PIL acts in the upward direction to lift up the magnetic field lines from the outer higher magnetic-pressure region towards the reconnection site. Therefore, away from the PIL the more horizontal field lines in the preflare stage become more vertical after the flare and release the magnetic pressure due to the upward impulse of the Lorentz force, resulting in a decrement in horizontal magnetic-field strength and disappearance of penumbral area. However, in the case of the non-eruptive flares we did not find any noticeable flare-related permanent and abrupt changes in the umbral or penumbral area. The presence of weak Lorentz-force impulse during the confined flares may be attributed to the insignificant morphological changes found in those cases. Repeated reconnection in the same magnetic field structure (Thalmann et al., 2015) could also be the reason behind the approximately similar morphology observed during the confined flares.

Comparison of the overlying coronal magnetic field environment in the pre-flare stages reveals that the gradient of overlying magnetic-field strength decayed faster over the eruptive region of AR 12192 as compared to that over the non-eruptive zone, suggesting the overlying field strength was stronger over the non-eruptive core area of the AR than the eruptive zone. This result is similar to the earlier finding by Cheng et al. (2011) where they did a comparative study of the critical decay index (1.5) height for the onset of the torus instability over both the eruptive and non-eruptive regions belonging to same AR (NOAA AR 10720) and reported that the decay index of the transverse magnetic field in the low corona ($\approx$10 Mm) is larger for eruptive flares than for confined ones.

In short, our comparative study of both the eruptive and non-eruptive flares produced from AR 12192 suggests that, although the flare-related permanent and abrupt changes in photospheric magnetic field and Lorentz forces are a common feature in large flares, the magnitude of those changes is smaller in the case of the confined flares compared to the eruptive ones. We conclude that the highly energetic flares leave a magnetic imprint on the solar photosphere that carries information on the nature of eruption. In addition, the comparative study of overlying coronal magnetic field environments for both the confined and eruptive flares reveal that the decay rate of the overlying magnetic-field strength can be used as a key parameter to determine whether a flare productive complex active region would lead to a CME eruption or not. More statistical studies of confined and eruptive events may confirm this result which will be useful in the context of space weather predictions by getting an early warning of CME eruptions.

Chapter 4

Conditions in Source Active Regions Leading to Recurrent Eruptive Events

4.1 Introduction

Complex large active regions (ARs) on the Sun may lead to episodic energy release processes in the solar corona, which give rise to large recurrent flares from a same AR (Zirin & Liggett, 1987; Sammis et al., 2000; Falconer et al., 2002; Wang & Zhang, 2008; Tschernitz et al., 2018; Toriumi & Wang, 2019). This has significant implications from space-weather perspective, as it may lead to recurrent CMEs and hence to their interaction, if the following CME has a larger speed than the preceding one. The interaction between the two CMEs can significantly enhance their geo-effectiveness leading to severe space weather impacts (Wang et al., 2003; Farrugia & Berdichevsky, 2004; Farrugia et al., 2006; Lugaz & Farrugia, 2014).

Understanding the energy build-up and release processes in solar corona are important to address the challenging questions regarding the conditions that lead to large recurrent flares (Nitta & Hudson, 2001; DeVore & Antiochos, 2008; Archontis et al., 2014; Romano et al., 2015). In particular, it is not well understood whether these events occur due to the continuous supply of free magnetic energy to the solar corona or because not all of the available free magnetic energy is released during a single flaring event. Emergence of new magnetic flux (Nitta & Hudson, 2001) or photospheric shearing motions (Romano et al., 2015) have been observed during recurrent flares. However, quantitatively it is difficult to track the temporal evolution of the free magnetic energy of any AR because of lack of a direct method to measure the vector magnetic field in the coronal volume (Wiegelmann et al., 2014). Therefore, the spatial and temporal evolution of source region parameters which can be solely estimated from the photospheric magnetic fields becomes important to probe the energy generation processes responsible for solar flares.

Hudson et al. (2008) were the first to quantitatively estimate the back reaction forces on the solar surface resulting from the implosion of the coronal magnetic field, which is required to release the energy during flares. They proposed that the photospheric magnetic fields should become more horizontal after the flare due to the vertical Lorentz forces acting on the solar surface.

A practical method to calculate the total Lorentz force acting on the solar photosphere was introduced by Fisher et al. (2012) (Section 3.3). Since then, the volume averaged net Lorentz force change has been considered as an important non-potential parameter to study the flare-associated changes in the source region characteristics. Earlier studies revealed that large eruptive flares are associated with an abrupt downward change of the Lorentz force (Petrie & Sudol, 2010; Petrie, 2012). Our results on comparison of the magnitude of those changes associated with eruptive and confined flares, as reported in Chapter 3, suggest that the change in Lorentz force is larger for eruptive flares. In this chapter, we focus on the evolution of the photospheric magnetic field and the associated Lorentz force changes for the case of recurrent eruptive large flares which have not been addressed in earlier works (Petrie & Sudol, 2010; Petrie, 2012). For this, we study the source region characteristics of recurrent large flares which occurred in AR 11261 and AR 11283. Tracking the evolution of the Lorentz force over the period of all the recurrent flares under study, we seek an answer to the following key questions in this chapter.

(i) Are the observed changes in Lorentz force during the flare related to the

Active region no.	Flares (GOES) Date yyyy/mm/dd	Start time (UT) hh:mm	Peak time (UT) hh:mm	End time (UT) hh:mm	Class	Location
11261	2011/08/03	13:17	13:45	14:30	M6.0	N17W30
11261	2011/08/04	03:41	03:45	03:57	M9.3	N16W38
11283	2011/09/06	01:35	01:50	02:05	M5.3	N13W07
11283	2011/09/06	22:12	22:20	22:24	X2.1	N14W18
11283	2011/09/07	22:32	22:38	22:44	X1.8	N14W31

Table 4.1: Recurrent flares observed in AR 11261 and AR 11283

linear momentum of the associated CME?

(ii) If there are any distinct signatures related to the Lorentz force evolution which might reveal the restructuring of the magnetic field after the first flare and its associated CME? If so, whether these signatures are suggestive of re build-up of non-potentiality of the coronal magnetic field and hence the imminent more powerful flare/CME.

(iii) Which factors are responsible for the build-up of free magnetic energy between the successive flares?

4.2 Overview of the Recurrent Events and Analysis Methods

All the large recurrent M and X-class flares that occurred in ARs 11261 and 11283 were well observed by the AIA and HMI onboard the SDO. To study the evolution of the photospheric magnetic field associated with the recurrent flares, we have used the HMI vector magnetogram series from the version of Space weather HMI Active Region Patches (SHARP).

As the errors in the vector magnetic field increase towards the limb, we have restricted our analysis to only those flares for which the flaring location of the AR was well within ± 40° from the central meridian. Out of those flares which satisfy the above criteria, we select the recurrent flares that originated from the same part of the polarity inversion line (PIL) of the AR and occurred within a

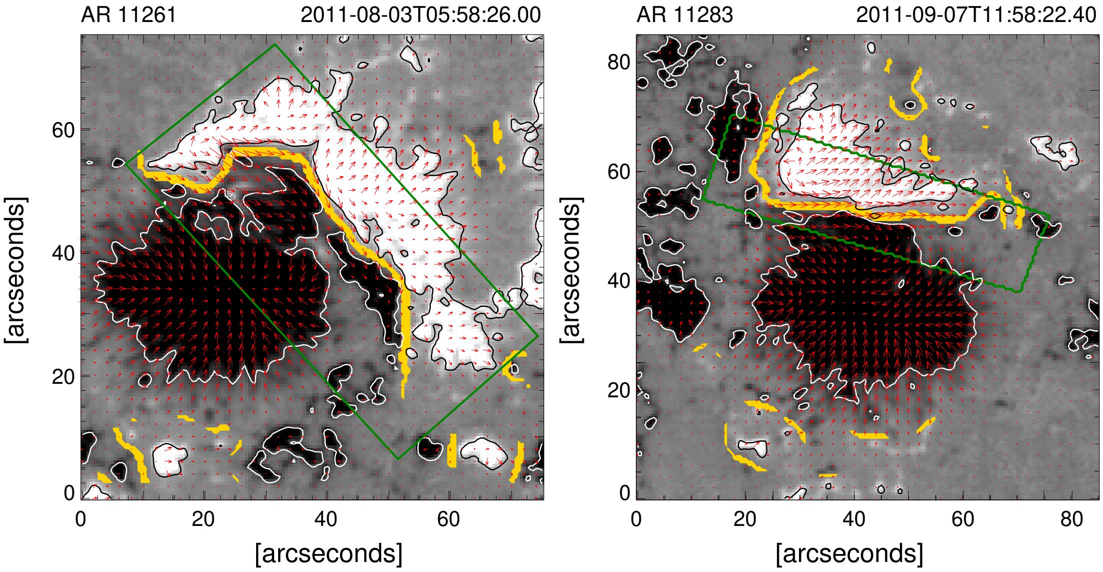

Figure 4.1: HMI vector magnetogram of AR 11261 (Left panel) and AR 11283 (Right panel). The radial component (B_r) of the magnetic field is shown in gray scale and the horizontal component (B_h) by red arrows, with saturation values ±500 G. The white/black solid line contours the region of negative/positive polarity of B_r having a magnitude greater than 500 G. The green rectangular boundary encloses the selected region within which all the calculations have been done. The yellow lines illustrate the polarity inversion line.

period of 24 hrs or less. This approach is helpful in understanding the energy release and re-build up processes related to the successive flares by tracking the magnetic properties of same flare-productive part of an AR over a period of several days. Following the aforementioned criteria, we analyze the two recurrent M-class (M6.0 & M9.3) flares which occurred in AR 11261 during 2011 August 3 to 4 and three recurrent flares (M5.3, X2.1 & X1.8) which occurred in AR 11283 during the period 2011 September 5 to 8 as listed in Table 4.1. To calculate the Lorentz-force changes in the source AR we have used the formulation by Fisher et al. (2012) which has been described in detail in Section 3.1.

We have selected sub-domains (shown by the region enclosed by the green rectangular boxes in Figure 4.1) near the PIL on the flare productive part of each AR to carry out our analysis. This is done as the flare related major changes in horizontal magnetic field and Lorentz forces are expected to occur close to the polarity inversion line (PIL) (Petrie & Sudol, 2010; Wang, 2006; Petrie, 2012; Sarkar & Srivastava, 2018). Moreover, as the successive flares reported in this study originated from the same part of the PIL, we are able to track the evolution of the

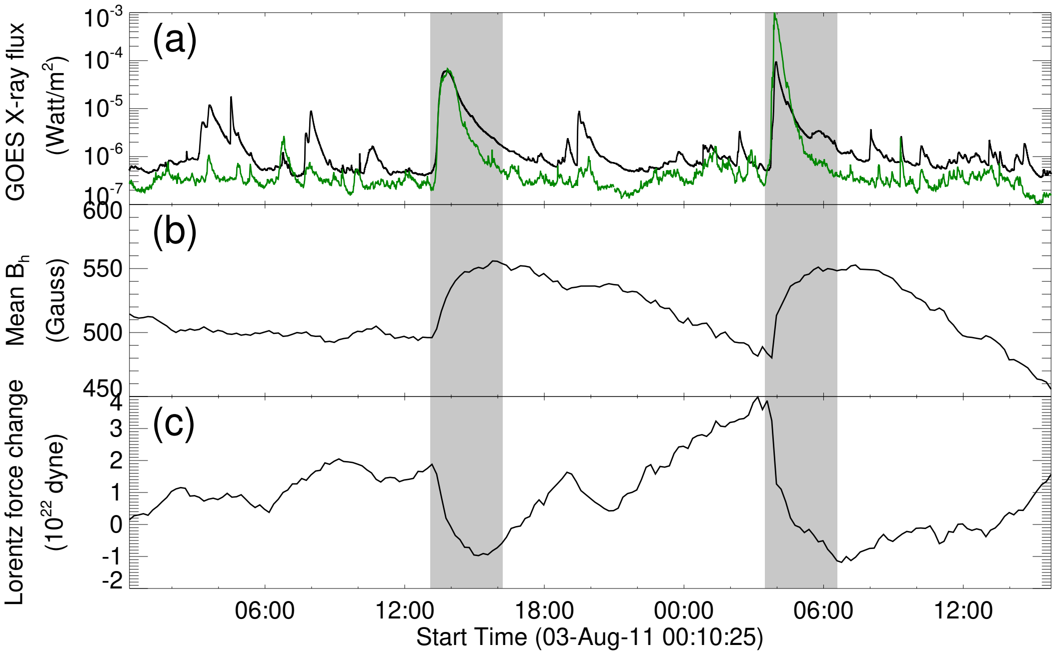

Figure 4.2: Temporal profile of the GOES 1-8 Å X-ray flux during the recurrent flares that occurred in AR 11261 (a). The solid green curves denote the temporal evolution of the brightening calculated within the field-of-view of the AR in the AIA 1600 Å channel. Evolution of the horizontal magnetic field (b) and changes in the radial component of the Lorentz force (c) within the selected regions (shown by rectangular boxes in Figure 4.1) of AR 11261.

magnetic field over several days including the time of each flare within the same selected domain on the AR. In order to define the size, orientation, and location of the selected domains the images taken in the AIA 171 Å and 193 Å channels have been examined. Several studies have shown that the flare-reconnection process results in the simultaneous formation of a post-eruption arcade (PEA) and a flux rope above the PEA during solar eruptive events (Leamon et al., 2004; Longcope et al., 2007; Qiu et al., 2007; Hu et al., 2014). Therefore in order to capture the magnetic imprints of the recurrent large eruptive flares on the solar photosphere, we selected our region of interest so as to enclose the major post flare arcade structures (as observed in AIA images) formed during each flare within that domain. The choice of such sub-domains enables us to assume that the magnetic field on the side-boundaries enclosing the volume over those selected regions is largely invariant with time and the field strength on the top boundary is negligible as compared to that at the lower boundary on the photosphere. Therefore,

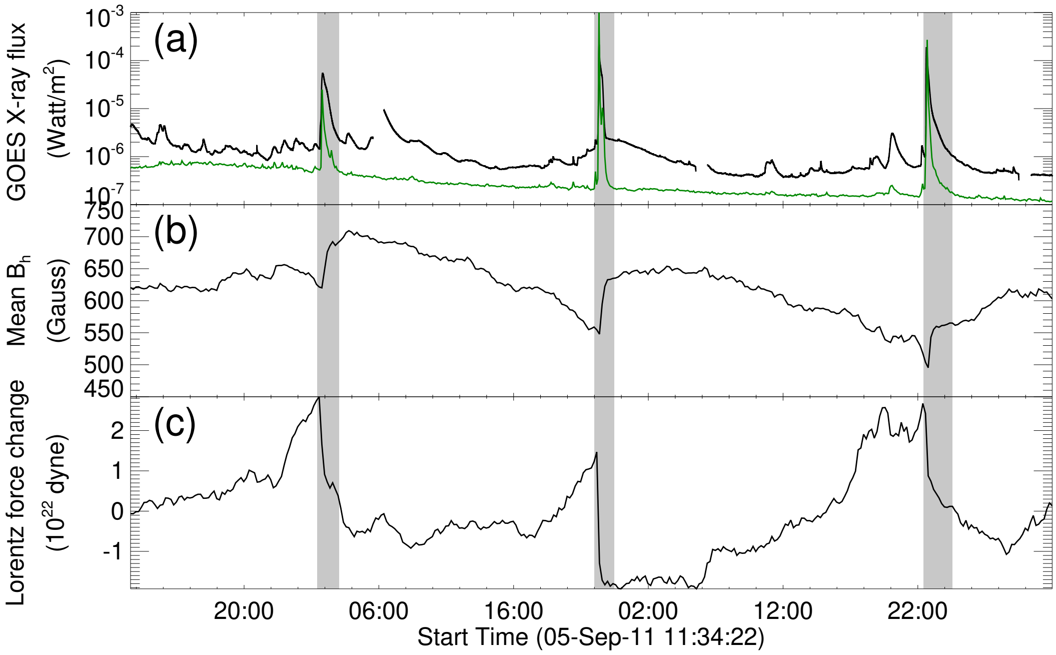

Figure 4.3: Temporal profile of the GOES 1-8 Å X-ray flux during the recurrent flares that occurred in AR 11283 (a). The solid green curves denote the temporal evolution of the brightening calculated within the field-of-view of the AR in the AIA 1600 Å channel. Evolution of the horizontal magnetic field (b) and changes in the radial component of the Lorentz force (c) within the selected regions (shown by rectangular boxes in Figure 4.1) of AR 11283.

only the photospheric magnetic field change contributes to the surface integrals as shown in Equations 3.1 and 3.2 to estimate the change in net Lorentz force acting on the photosphere from the above atmospheric volume.

4.3 Magnetic Field Evolution in Recurrent Eruptive Events

4.3.1 Abrupt changes in magnetic field and Lorentz force

Figures 4.2 and 4.3 depict the abrupt changes in horizontal magnetic field and the radial component of Lorentz forces calculated within the selected region of interest as shown in Figure 4.1. The distinct changes in the magnetic properties of AR 11261 and AR 11283 associated with the recurrent large M- and X-class flares are discussed in the following sections.

4.3.1.1 Magnetic field evolution in AR 11261

During the first M6.0 class flare that occurred in AR 11261, the mean horizontal magnetic field increased approximately from 500 to 550 G and the associated net Lorentz force showed an abrupt downward change by approximately 2.8×10^{22} dyne. After the M6.0 class flare the mean horizontal magnetic field started to decrease and reached about 490 G prior to the M9.3 class flare. During the successive M9.3 class flare, the mean horizontal magnetic field again increased to $\approx$550 G. The associated change in net Lorentz force during this flare is about 5.1×10^{22} dyne which is almost two times larger than that associated with the previous M6.0 class flare.

Considering an error of ± 50 Gauss (Δx) per pixel in estimating the horizontal magnetic field and the area of interest is of the order of 500×500 pixel^2, the error in estimating the mean horizontal magnetic field comes in the order of 10^{-1} Gauss ($\Delta x/\sqrt{n}$, where, $\Delta x = 50$ and n=500×500). Therefore, the changes in mean horizontal magnetic field as reported in this study are significant.

To investigate if the kinematic properties of the associated CMEs are related to the flare induced Lorentz force changes or not, we consider the value of true mass and the deprojected speed of each flare-associated CME estimated in Mishra et al. (2017). The two recurrent CMEs associated with the preceding M6.0 class and the following M9.3 class flares are hereinafter referred to as CME1 and CME2, respectively. CME2 was launched with a speed $\approx$1700 km s^{-1}, which is about 1.5 times higher than that of CME1 (v $\approx$ 1100 km s^{-1}). The true masses of CME1 and CME2, estimated from the two viewpoints i.e. STEREO-A and -B coronagraph data, were reported as 7.4×10^{12} kg and 10.2×10^{12} kg, respectively in their work. Considering an error of ± 100 km s^{-1} in the estimation of CME speed (Mishra et al., 2017) and ± 15 % in CME mass respectively (Bein et al., 2013; Mishra & Srivastava, 2014), we estimated the momentum of CME2 as $(17 \pm 4) \times 10^{15}$ kg km s^{-1}, which is about two times the momentum of CME1 ($8 \times 10^{15} \pm 2 \times 10^{15}$ kg km s^{-1}). This suggests that the magnitude of change in the net Lorentz force impulse during the two recurrent flares is correlated with the associated CME momentum. This scenario is also consistent with the flare-related

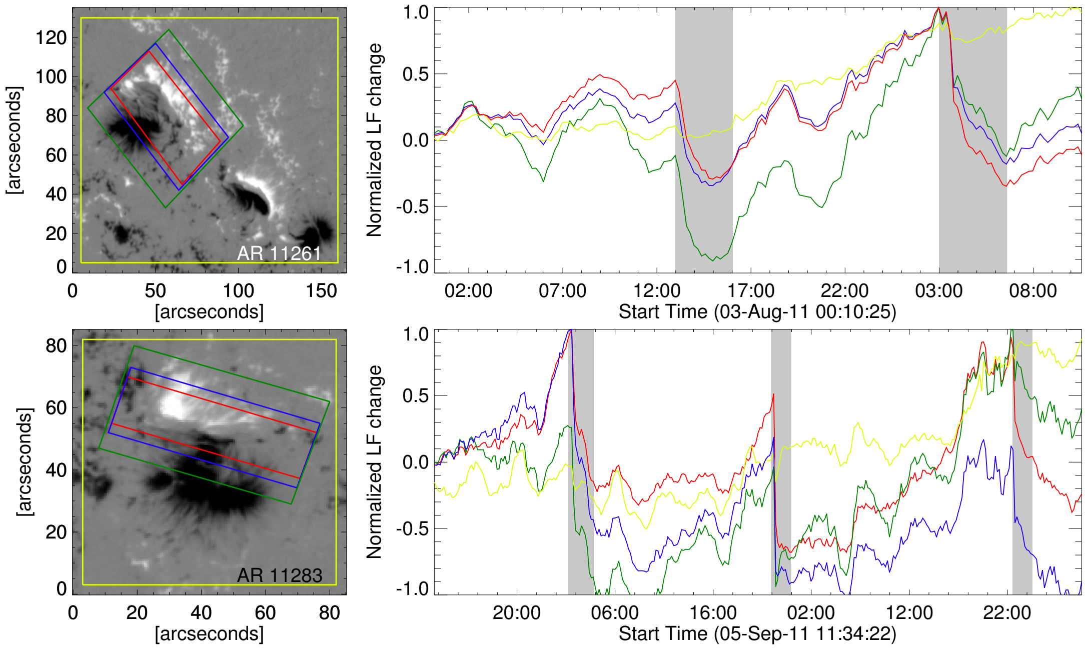

Figure 4.4: Radial component of HMI vector magnetic field of AR 11261 (upper-left panel) and AR 11283 (lower-left panel). The red, blue, green and yellow solid curves in upper-right/lower-right panel show the evolution of the normalized net Lorentz force estimated within the bounding box as marked by the red, blue, green and yellow rectangles in upper-left/lower-left panel respectively. The gray shaded regions mark the temporal window that covers the start to end time of the recurrent large flares.

momentum balance condition where the Lorentz-force impulse is considered to be proportional to the associated CME momentum (Fisher et al., 2012; Wang et al., 2012).

As the masses of the two CMEs were comparable, the successive Lorentz force impulse within a time window of approximately 14 hours from the same PIL of the AR with a larger change in magnitude during the following flare appears to be an important characteristic of the source AR in order to launch a CME at a higher speed compared to that of the preceding one. This is an ideal condition for interaction of the two CMEs. Eventually, as reported in Mishra et al. (2017), the two CMEs interacted at a distance of 145 $R_\odot$ from the Sun. Notably, the reduction of magnetic tension, due to the opening of overlying magnetic field lines during the previous CME event could also be the reason behind the higher energetics of the following CME.

4.3.1.2 Magnetic field evolution in AR 11283

For all the three recurrent flares which occurred in AR 11283, the horizontal magnetic field and the net Lorentz force showed abrupt changes during each flare (Figure 4.3). The plot shows that the net Lorentz force increased substantially 2-4 hours prior to the occurrence of each flare, followed by a steep decrease of the same. The changes in net Lorentz force during the successive M5.3, X2.1, X1.8-class flares were approximately 4×10^{22}, 3.5×10^{22} and 3.5×10^{22} dyne respectively. All the three flares were eruptive and the associated deprojected CME speeds were 640, 773 and 751 km s^{-1} respectively as reported in Soojeong Jang's Catalog (http://ccmc.gsfc.nasa.gov/requests/fileGeneration.php). This implies that the magnitude of change in net Lorentz force were almost comparable and the associated CME speeds also do not differ much in case of these 3 flares. As the associated CMEs were launched within an interval of a day and with approximately similar speed, it is not expected that the CMEs would interact among them in the interplanetary space within 1 AU. Further, the linear momentum of the CME and the associated change in net Lorentz force could not be compared because of poor mass estimation as reported in the CDAW catalog (https://cdaw.gsfc.nasa.gov/CME_list/).

In strong events, flare induced artifacts in the magnetic field vectors may result in magnetic transients during the step-wise changes of the photospheric magnetic field (Sun et al., 2017). Therefore, it is important to understand whether the flare related changes in magnetic field evolution and the associated net Lorentz force as reported in this study are real or include flare induced artifacts. Notably, the magnetic transients as reported by Sun et al. (2017) are spatially localized in nature and temporally can be resolved within a timescale of ≈ 10 minutes. Moreover, the transient features do not show any permanent changes in the magnetic field evolution during the flares. The evolution of the horizontal magnetic field and the net Lorentz force as shown in Figures 4.2 and 4.3 are estimated within a large area on the photosphere using the 12 minute cadence vector magnetogram data. Therefore, within the time-window of the stepwise changes in the horizontal magnetic field, there is no discontinuity found in the field evolution during

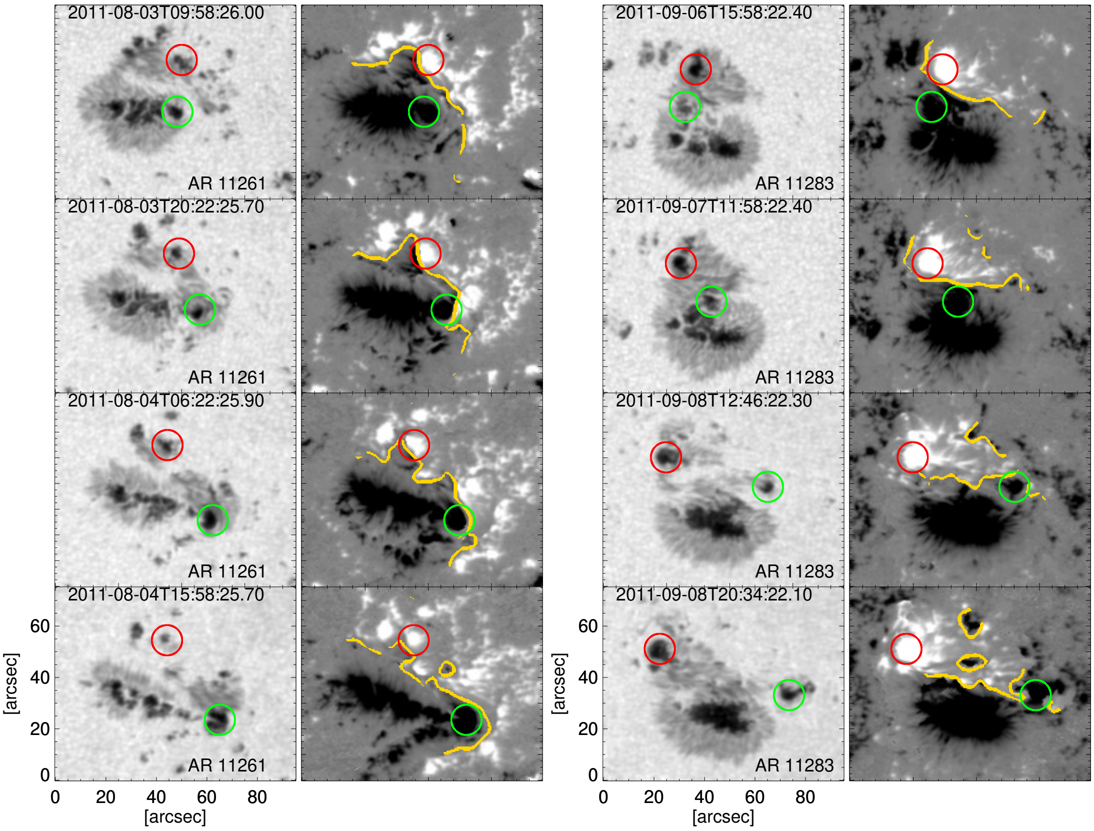
2011-08-03T09:58:26.00
AR 11261
2011-08-03T20:22:25.70
AR 11261
2011-08-04T06:22:25.90
AR 11261
2011-08-04T15:58:25.70
AR 11261
2011-09-06T15:58:22.40
AR 11283
2011-09-07T11:58:22.40
AR 11283
2011-09-08T12:46:22.30
AR 11283
2011-09-08T20:34:22.10
AR 11283
0
20
40
60
80
[arcsec]
0
20
40
60
[arcsec]

Figure 4.5: HMI continuum images of the flare-productive part of AR 11261 (First column) and the radial component of the HMI vector magnetic field (Second column) within the same field-of-view as shown in the first column. HMI continuum images of the flare-productive part of AR 11283 (Third column) and the radial component of the HMI vector magnetic field (Fourth column) within the same field-of-view as shown in the third column. Continuum images in each row of the first/third column are co temporal with the magnetic field maps shown in the same row of second/fourth column. The red and green circles depict the two prominent moving magnetic features of opposite polarities which show continuous anti-parallel motion along the polarity inversion line denoted by the yellow solid lines.

the flares under this study as potentially occurring magnetic transients would be spatially and temporally averaged out. Hence, there are no flare related artifacts involved in the derivation of the net Lorentz force in this study.

4.3.2 Lorentz force re-build up in between the successive flares in the ARs

After the abrupt downward change in net Lorentz force during each large flare that occurred in AR 11261 and AR 11283, the net Lorentz force started to rebuild-

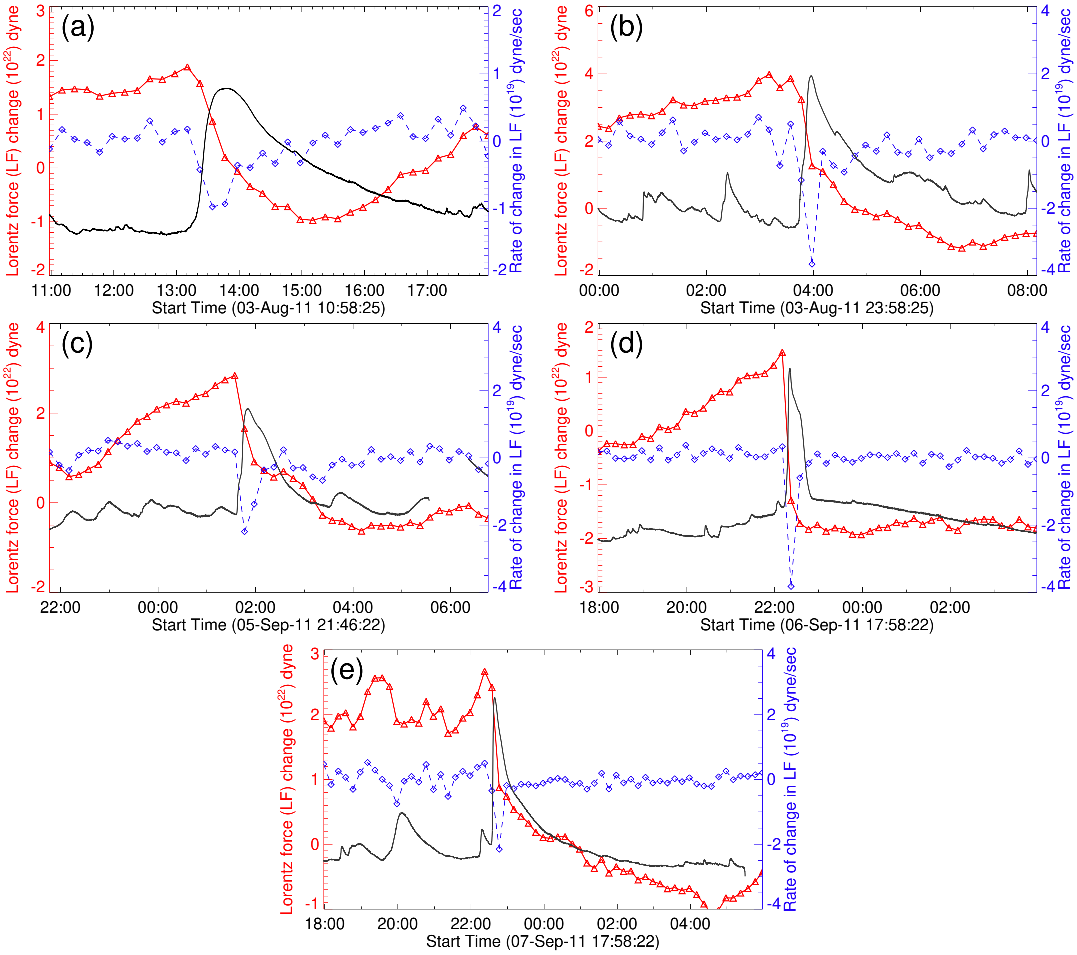

Figure 4.6: Relative evolution of GOES 1-8 Å X-ray flux (black solid lines) with that of the associated Lorentz force (red solid lines) during the recurrent flares under study. The blue dotted line denotes the rate of change in Lorentz force during the flares.

up in between the successive flares (see Figures 4.2 and 4.3). Starting from the magnitude of -1×10^{22} dyne after the M6.0 class, the change in net Lorentz force reached a value of 4×10^{22} dyne until the next M9.3 class flare occurred in AR 11261. Similarly in AR 11283, the net Lorentz force was rebuilt-up by approximately 2×10^{22} dyne in between the M5.3 and X2.1 class flares, and again rebuilt-up by approximately 4×10^{22} dyne before the X1.8 class flare. This rebuild-up of the Lorentz force reveals the restructuring of the magnetic field configuration in the vicinity of the PIL in order to increase the non-potentiality of the coronal magnetic field which in turn relaxes after the occurrence of the next recurrent flare.

We have tested the sensitivity of the obtained results on the size of the bounding boxes selected around the PIL. Figure 4.4 shows that the evolutionary pattern of the net Lorentz force remains unchanged if the width of the bounding boxes is increased from ≈ 20 Mm to ≈ 40 Mm (from red to green rectangular regions). The red rectangular regions are the same as shown by the green rectangular regions in the Figure 4.1. As the size of these bounding regions are comparable to that of the main flaring area and the associated post eruption arcade, the dynamics related to the recurrent flares under study are well captured within the volume over those selected areas. Therefore, we observe the flare related abrupt and downward changes in net Lorentz force (the red, blue and green curves in upper-right and lower-right panels of Figure 4.4) estimated over those bounding regions. However, integrating the Lorentz force density over the whole AR area dilutes the flare associated changes in the estimated net Lorentz force profile (the yellow curves in upper-right and lower-right panels of Figure 4.4). Therefore, we suggest that the net Lorentz force should be estimated near the PIL instead of the whole AR, in order to capture the flare associated dynamics.

The rebuild-up of net Lorentz force in between the recurrent flares could be the consequence of the continuous shearing motion along the PIL. Figure 4.5 shows the shearing motion observed for the two prominent moving magnetic features (MMF) of opposite magnetic polarities (indicated by the red and green circles). The anti-parallel motions of these MMFs along the two sides of the PIL of each AR during the recurrent flares provide evidence for rebuild-up of non-potential energy in between the successive flares. Therefore, the evolution of Lorentz force appears to be suggestive of energy rebuild-up processes in order to produce successive flares from the same part of any AR.

The results obtained in this study are significant as it shows the evolution of a non-potential parameter (net vertical Lorentz force change) that reveals the rebuild-up of non-potentiality of the AR in between the successive large flares. Indeed, these results are important in the context of space weather predictions, as the evolutionary pattern of the net vertical Lorentz force change can be used for forecasting the recurrent large eruptive flares from the same AR. Further, the associated successive CMEs from the same AR, will in turn enhance their chance of being launched in the same direction. In this scenario, the following faster CME may interact with the preceding slower one in the corona or interplanetary space, which is expected to enhance their geo-effectiveness (Wang et al., 2003; Farrugia & Berdichevsky, 2004; Farrugia et al., 2006; Lugaz & Farrugia, 2014).

4.3.3 Evolution of GOES X-ray flux and the associated Lorentz force during the recurrent flares

The temporal evolution of the GOES 1-8 Å X-ray flux and the associated change in Lorentz force shows that the Lorentz force starts to decrease at the start of rising phase of the GOES flare (Figure 4.6) and follows a similar evolutionary pattern as the decay phase of the GOES X-ray flux during all the flares. Among all the five flares as listed in Table 4.1, the decay phase of the X2.1 class flare (panel (d) of Figure 4.6) was significantly steeper than the other four flares. This is also reflected in the associated changes in Lorentz force profile. The Lorentz force also decreases sharply during that X2.1 class flare in comparison to the other flares. The derived rate of change in net Lorentz force associated with the X2.1 class flare is 3×10^{19} dyne/sec (Figure 4.6), which is the highest among all the five flares studied in this work.

Our results provide evidence that the change in Lorentz force is not only related to the phase of impulsive flare energy release, but also takes place over a longer interval and follows a similar evolutionary pattern like the decay phase of the GOES soft x-ray flux. This could be associated with a slower restructuring of the coronal magnetic field during the decay phase of the flaring events.

4.4 Conclusion

The evolution of the photospheric magnetic field and the associated Lorentz force change reveals the energy build up processes during the recurrent large flares that occurred in AR 11261 and AR 11283. We find that the vertical component of Lorentz force undergoes abrupt downward changes during all the flares, which is consistent with the previous results as obtained by Petrie & Sudol (2010);

Wang (2006); Petrie (2012); Sarkar & Srivastava (2018). The observed increase in horizontal magnetic field during each flare supports the conjecture given by Hudson et al. (2008), which suggests that the magnetic loops should undergo a sudden shrinkage or implosion due to the energy release processes during flares. This is also consistent with the results obtained by Romano et al. (2015), who showed a decrease in the dip angle after each large flare that occurred in AR 11283. Interestingly, the decrease in horizontal magnetic field in between the successive flares reported in our study, could be due to the storage of newly supplied energy that increases the coronal magnetic pressure, thereby stretches the magnetic loops upwards as proposed by Hudson (2000).

Our study also reveals that the decrease in Lorentz force is not only related to the phase of impulsive flare energy release, but takes place over a longer interval that covers also the decay phase of the flaring events. The magnitude of change in net Lorentz forces reported in this work, appears to be correlated with the linear momentum of the associated CME. This scenario is consistent with the flare-related momentum balance condition where the Lorentz-force impulse is believed to be proportional to the associated CME momentum (Fisher et al., 2012; Wang et al., 2012).

It is noteworthy that the flare associated momentum conservation is not only related to the bodily transfer of mass in the form of CMEs, but also includes the effects related to explosive chromospheric evaporation (Hudson et al., 2012). However, quantification of the momentum related to the chromospheric evaporation during the flares is not feasible, as it requires spectroscopic observations of both the hot upflowing and cool downflowing plasma which are rarely available. If we compare the values of CME momentum, which is of the order of 10^{15} kg km s^{-1}, with the momentum related to chromospheric evaporation flows in large flares as reported by Zarro et al. (1988); Canfield et al. (1990); Hudson et al. (2012), which is of the order of $10^{13} - 10^{14}$ kg km s^{-1}, we may conclude that the momentum changes due to the CME are the dominant. Therefore, the correlation between the Lorentz force impulse and the CME momentum in the large recurrent eruptive flares reported in our study is valid as the effects of impulsive chromospheric evaporation are at least an order of magnitude smaller.

Our study reveals that after the abrupt downward changes during each flare, the net Lorentz force increases by (2-5)$\times 10^{22}$ dyne in between the successive flares. This distinct rebuild-up of net Lorentz forces is the first observational evidence found in the evolution of any non-potential parameter of solar ARs, which suggests that new energy was supplied to the ARs in order to produce the recurrent large flares. The rebuild-up of magnetic free energy of the ARs is further confirmed by the observations of continuous shearing motion of moving magnetic features of opposite polarities near the polarity inversion line. The evolutionary pattern of the net Lorentz force changes reported in this study has significant implications, in particular, for the forecasting of recurrent large eruptive flares from the same AR and hence the chances of interaction between the associated CMEs.

Currently available machine learning algorithms for flare prediction use, among many other parameters, the evolution of Lorentz force integrated over the whole AR, which does not show high skill score in the forecast verification metrics (Bobra & Couvidat, 2015). However, the distinct changes in the vertical component of the Lorentz forces integrated near the PIL demonstrated in our study, could prove to be an important parameter to train and test the machine-learning algorithms in order to improve the current capability of flare-forecasting.

Chapter 5

CME Initiation and its Evolution Close to Sun

5.1 Introduction

The physical processes behind the CME initiation are one of the key topics in space-weather research. In Chapters 3 and 4, we investigated the conditions leading to CME eruption from the flare productive complex active regions on the Sun. However, apart from the solar active regions, the source region of CMEs may also reside in the quiet regions on the Sun which are associated with prominence/filament eruptions. Therefore, for a better and complete understanding, it is worthful to study the physical conditions leading to prominence/filament associated CME eruption. In this chapter, we focus on such prominence associated CME eruption aiming to understand the triggering mechanism behind the genesis of CMEs. In particular, we study the solar prominence which is approximately elongated along the line-of-sight of the observer and therefore, associated with a coronal cavity when viewed in limb observations. The motivation behind the choice of such cavity associated prominence system comes from the fact that the coronal cavities provide a unique opportunity to probe the cross-sectional morphology of the associated magnetic flux rope which hold the prominence material in their lower lying region (Gibson & Fan, 2006). Cavities are believed to be density depleted cross section of the magnetic flux ropes, where the magnetic field strength attains a much higher value compared to the background corona (Low & Hundhausen, 1995; Rachmeler et al., 2013). They are ubiquitously observed as dark ellipses or partial ellipses at the limb in white light (Waldmeier, 1970), soft X-ray (SXR) (Vaiana et al., 1973) and extreme ultraviolet (EUV) (Schmahl, 1979) observations.

Coronal cavities may remain quiescent in solar atmosphere for days or even weeks (Gibson & Fan, 2006), and evolve as dark structures seen in white light inside the associated CMEs when they erupt (Fisher et al., 1981; Illing & Hundhausen, 1985; Hundhausen, 1999; Yurchyshyn, 2002; Maričić et al., 2004; Sterling & Moore, 2004; Vršnak et al., 2004; Gibson & Fan, 2006; Vourlidas et al., 2013; Howard et al., 2017). Therefore, observing the evolution of cavities in lower coronal regions during its quiescent and pre-eruptive phases may provide intriguing clues to the state of the pre-eruptive equilibria and the triggering mechanism behind the CME initiation. More importantly, the erupting cavities depict the cross-sectional morphology of the associated CME flux ropes. Therefore, tracking the kinematics and morphological evolution of such cavities during the eruptive phase may shed light on the nature of CME evolution close to Sun, which is crucial to constrain the space-weather forecasting models. In short, combining the observations of coronal cavities during its different phases of evolution, this chapter aims to investigate the CME initiation mechanism and the nature of evolution of its near-Sun properties, which are one of the prime objective of the thesis.

Earlier studies have shown that the initiation and main acceleration phase of CMEs mostly occur below 2 - 3 $R_\odot$ (MacQueen & Fisher, 1983; Chen & Krall, 2003; Joshi & Srivastava, 2011). Therefore, by the time CMEs appear into the field-of-view (FOV) of LASCO C2 which observes from 2 $R_\odot$, the initiation and impulsive acceleration phase of most of the CMEs cannot be captured.

The SWAP EUV imager onboard the PROBA2 provides an extended (54 arc-minute) FOV of the lower solar atmosphere, which gives the opportunity to capture the evolution of erupting cavities upto 1.7 $R_\odot$ (upto 1.9 $R_\odot$ along the diagonal direction of the images) around the 17.4 nm wavelength bandpass. Apart from that, using the off-pointing capability of PROBA2, the SWAP FOV can be shifted in any direction in order to track coronal features of interest, upto more than 2 $R_\odot$. Therefore, it fills the observational gap between 1 to 2 $R_\odot$. When combined with LASCO C2/C3 white-light observations (Brueckner et al., 1995) this enables us to study the evolution of erupting cavities in the outer corona. The large FOV of SWAP observations were useful in several studies of large coronal structures. These include, capturing the different phases of prominence eruptions (e.g. Mierla et al. 2013) and the evolution of a large-scale coronal pseudo-streamer in association with cavity system (Guennou et al., 2016). SWAP observations also have been used in conjunction with the ground-based Mauna Loa Solar Observatory (MLSO) Mark-IV K-coronameter (Mk4: Elmore et al. 2003) to study the initiation phase of a two stage eruptive event (Byrne et al., 2014).

Statistical studies have been made in order to distinguish the morphological characteristics of eruptive and non-eruptive cavities (Gibson & Fan, 2006; Forland et al., 2013). Using the AIA 193 Å passband observations, Forland et al. (2013) studied the morphological structure of 129 EUV cavities and found that cavities with a teardrop-shape are more likely to erupt. On the other hand, partial or complete eruption of white-light cavities which formed CMEs have been studied combining the observations of MK4 and LASCO coronagraphs (Gibson & Fan, 2006; Liu et al., 2012). Comparing the MK4 observations of pre-eruptive white-light cavities with those observed a few days before the eruption, Gibson & Fan (2006) found that the cavities show an increase in their height in the days leading up to an eruption. However, due to the absence of multiple line-of-sight observations, they concluded that it is hard to determine whether these changes in cavity height are due to the true evolution of a rising cavity or the appearance of a higher portion of the three-dimensional cavity along the line-of-sight. Nonetheless, they found that there is an absolute upper limit to cavity height (0.6 $R_\odot$ above the solar surface), above which no non-erupting cavities were observed in white light images. Gibson et al. (2010) proposed an observationally constrained three-dimensional (3D) cavity model which reproduced the observed cavity morphology reasonably well, as seen from the different view-points of the two STEREO spacecraft. However, the temporal evolution of roughly the same portion of the 3D cavity morphology, starting from its long lived quiescent phase to the eruptive phase in association with CMEs, has not been previously reported. Tracking the cavity centroid height for such cases is crucial to examine the stability conditions of the cavity system in the context of torus instability.

In this chapter, we present a comprehensive study of a coronal cavity which exhibited almost a two-week long quiescent phase starting from 2010 May 30 to 2010 June 13 on the visible solar disk and finally erupted from the north-west solar limb on 2010 June 13. Using the SDO/AIA observations, Régnier et al. (2011) studied the spatial relationship of this coronal cavity together with its associated prominence structure during the pre-eruptive phase. They reported the presence of magnetic curvature forces that balance the gravitational force in order to hold the cold and dense plasma of the prominence material underlying the cavity. However, using the multi-vantage point observations from SDO/AIA, STEREO A/B and PROBA2/SWAP EUV imager during the long lived quiescent phase and combining the FOV of SWAP, LASCO C2/C3 during the eruptive phase, we study the complete evolution of the cavity with an objective to address the following key questions regarding the genesis of CMEs:

(i) Does the morphological evolution of the quiescent cavity hold clues to the underlying magnetostatic equilibria of the cavity system?

(ii) What determines the initiation height of CMEs?

(iii) What are the conditions that can lead to a cavity eruption?

(iv) How do EUV cavities seen in the lower corona evolve into the white light cavities seen during CME eruptions?

(v) How do the magnetic forces drive the “impulsive” and “residual” acceleration phases of the CME?

(vi) Do the CMEs undergo significant deflection in the lower corona?

(vii) Do the CMEs exhibit self-similar expansion in the lower corona? If not, then what is the critical height above which its nature of expansion is self-similar?

To answer these questions, we have organized this chapter as follows. In Section 5.2 we present the observations of a quiescent cavity that erupted later

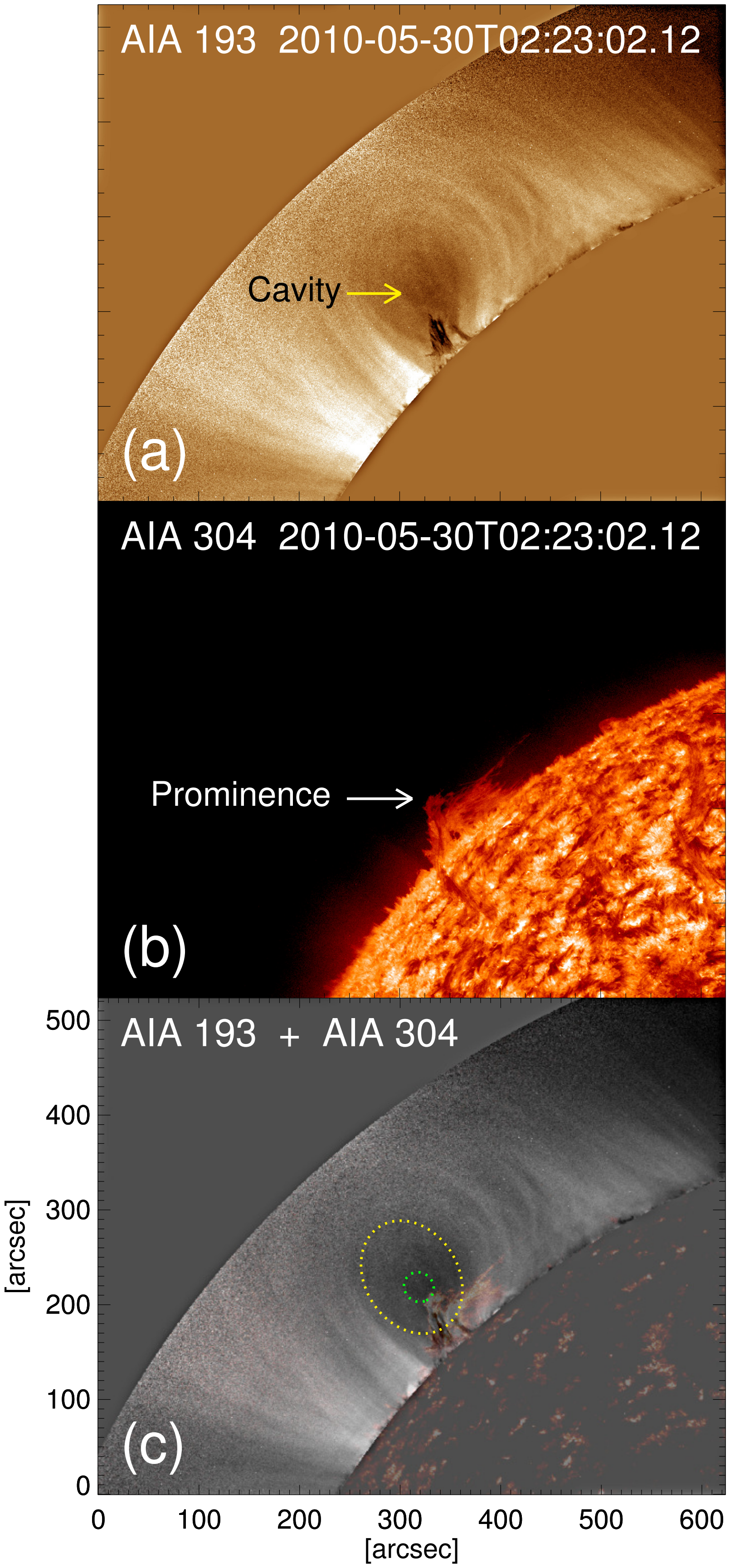
AIA 193 2010-05-30T02:23:02.12
Cavity
(a)
AIA 304 2010-05-30T02:23:02.12
Prominence
(b)
AIA 193 + AIA 304
(c)
500
400
300
200
100
0
[arcsec]
0
100
200
300
400
500
600
[arcsec]

Figure 5.1: Observation of the coronal cavity in the AIA 193 Å channel (a). The associated prominence structure as seen in the AIA 304 Å channel (b). The superimposed images of panels (a) and (b) are shown in panel (c). The green dotted line denotes the outer boundary of the true cavity. The yellow dotted line depicts the approximate outer boundary of the flux-rope.

into a CME. We discuss the dynamics of that cavity during the eruptive phase in Section 5.3. In Section 5.4 we present the results based on our analysis. Finally, we summarize and discuss the implications of these results in Section 5.5.

5.2 Observations of the Coronal Cavity During Quiescent Phase

The evolution of the coronal cavity in the lower corona during the different stages in its quiescent phase was well captured by the SDO/AIA, STEREO SECCHI/EUVI, and PROBA2/SWAP EUV imagers. The cavity was first observed on the north-east solar limb on 2010 May 30 in association with a northern polar crown filament/prominence (Figure 5.1). Over the period from 2010 May 30 to 2010 June 13, the cavity rotated across the solar disk and remained in a quiescent phase before its eruption on 2010 June 13 at around 6:30 UT close to the north-west solar limb.

In order to investigate the spatial association between the prominence material and the dark cavity, we have superimposed the image of prominence structure observed in the 304 Å channel on top of the dark cavity as observed in the 193 Å, 195 Å and 174 Å channels of AIA, EUVI and SWAP respectively (see Figures 5.1, 5.3 and 5.4).

Figure 5.1 shows the appearance of the dark cavity over the east solar limb as seen in the AIA 193 Å channel on 2010 May 30 within the FOV between 1.0 to 1.3 R_s. The polar crown prominence structure associated with this cavity system can be seen in AIA 304 Å channel observations (see panel (b) in Figure 5.1). In order to distinguish the true cavity from the outside region of dipped field-lines which carry the prominence material, we have marked the cavity morphology, as observed in the AIA 193 Å image, with the green dotted boundary drawn on the superimposed co-temporal images taken in AIA 193 and 304 Å channels (see panel (c) in Figure 5.1). Here we refer to the "true" cavity as the central non-dipped part of the magnetic flux-rope following the classification described in Gibson (2015). The combined images of the prominence structure and the cavity

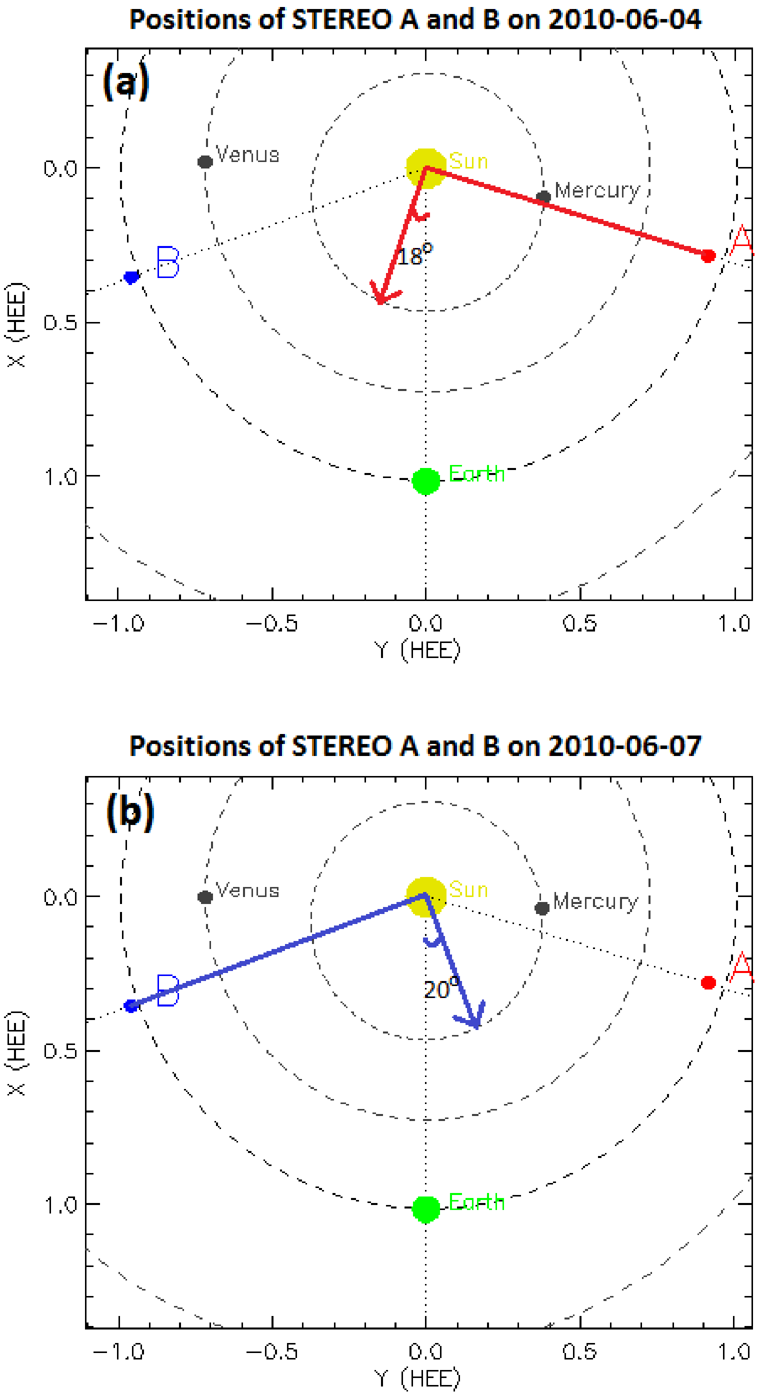

Figure 5.2: Positions of STEREO A and B. The red and blue arrows drawn on (a) and (b) denote the direction of the plane-of-sky as viewed by EUVI on 2010 June 4 by STEREO A and on 2010 June 7 by STEREO B.

morphology, seen in Figure 5.1, indicates that the cavity is located exactly on the top of the prominence boundary. The yellow dotted elliptical boundary outside the dark cavity approximately encloses the outer boundary of the flux-rope.

Outside the yellow dotted boundary the bright arched like structures resemble the overlying magnetic field lines.

During its passage across the solar disk, the polar crown filament was well observed from multiple view points of SDO, PROBA2 and the twin spacecraft STEREO A and B. As it crossed close to the central meridian, as seen from the perspective of Earth, the associated cavity morphology became visible in the plane-of-sky (POS) EUVI observations from the STEREO satellites. At that time STEREO A and B were positioned approximately 70° from the Sun-Earth line (see Figure 5.2). On 2010 June 4 the cavity appeared in the POS, from the perspective of STEREO-A (Figure 5.3), which was approximately 18° east of the Sun-Earth line (see Figure 5.2). Between 2010 June 4 to 2010 June 7, the cavity crossed the solar disk center as viewed by Earth and rotated about 20° further from the Sun-Earth line towards the west. At around 14:00 UT on 2010 June 7 it became visible in POS EUVI observations from STEREO-B. Figure 5.3 shows the appearance of the dark cavity and the associated prominence structure as observed from the two perspectives of STEREO A and B in the 195 Å (top panels) and 304 Å (middle panels) bandpasses respectively. The green and yellow dotted boundaries, highlighting the true cavity and flux-rope outer boundary respectively, drawn on the superimposed images (bottom panels of Figure 5.3) are the same as those described for Figure 5.1.

As the filament rotated towards the west solar limb, the associated cavity started to appear on the north-west solar limb as viewed from the perspective of Earth. The cavity can be observed from 2010 June 11, and is clearest at the end of 2010 June 12. Figure 5.4 shows the cavity morphology as observed in the SWAP 174 Å (left panel), the associated prominence structure in AIA 304 Å (middle panel) and a combination of both bandpasses (right panel). As one of the major goals of this study is to track the complete evolution of the eruptive cavity, we take the advantage of SWAP's large FOV, the ability to track the cavity out to ≈ 1.7 $R_\odot$ (compared to the AIA FOV which is limited to 1.3 $R_\odot$), and focus on SWAP observations throughout the cavity evolution from the quiescent to eruptive phase on the north-west solar limb. In order to increase the signal-to-

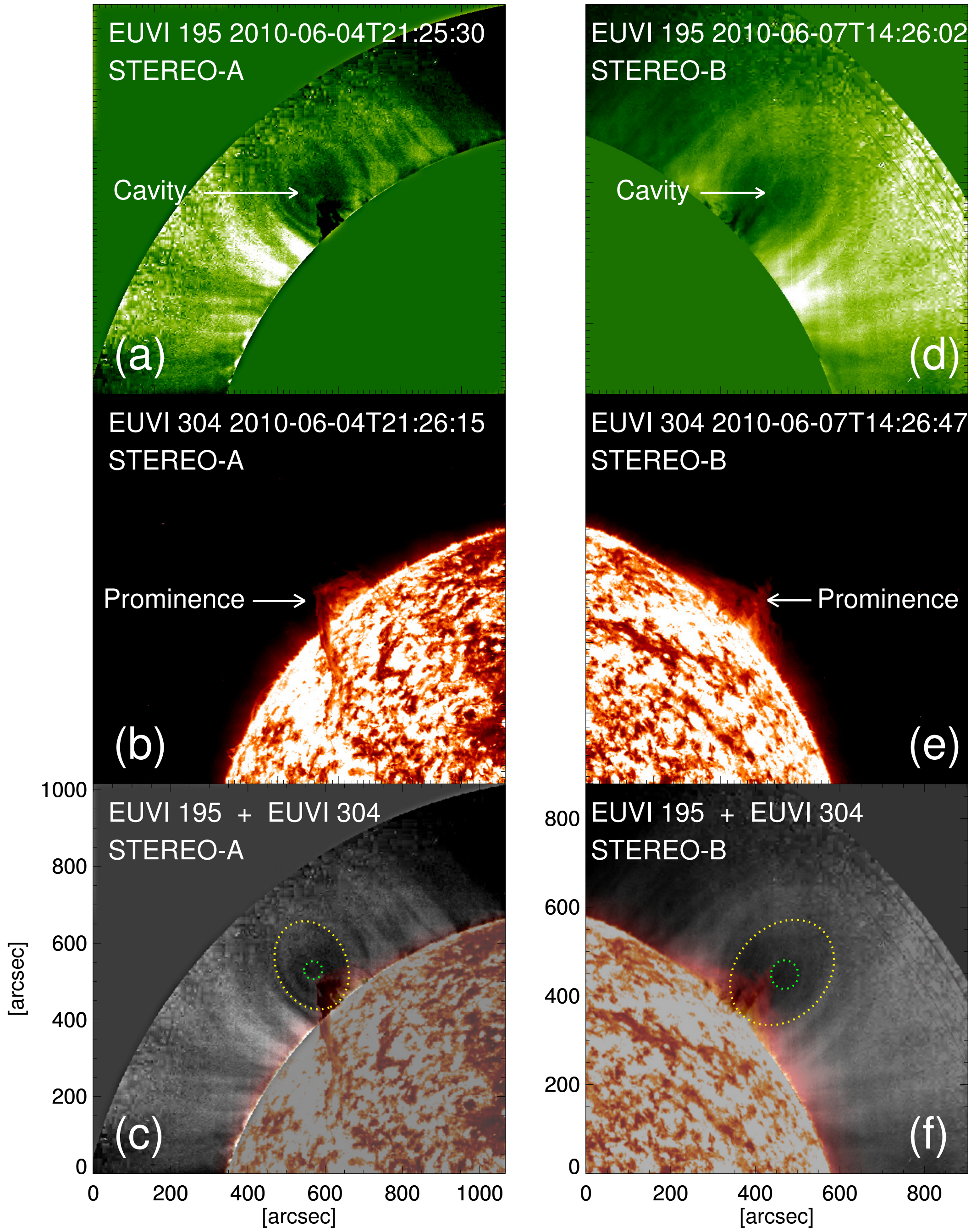
EUVI 195 2010-06-04T21:25:30
STEREO-A
Cavity
(a)
EUVI 195 2010-06-07T14:26:02
STEREO-B
Cavity
(d)
EUVI 304 2010-06-04T21:26:15
STEREO-A
Prominence
(b)
EUVI 304 2010-06-07T14:26:47
STEREO-B
Prominence
(e)
EUVI 195 + EUVI 304
STEREO-A
(c)
EUVI 195 + EUVI 304
STEREO-B
(f)
[arcsec]
0
200
400
600
800
1000
[arcsec]

Figure 5.3: Observations of the coronal cavity as seen in the 195 Å bandpass of EUVI on STEREO A and B (panels (a) and (d) respectively), the associated prominence structure in 304 Å bandpass (panels (b) and (e)) and a superposition of the 195 Å and 304 Å bandpasses (panels (c) and (f)). The green and yellow dotted lines are the same as those described for Figure 5.1.

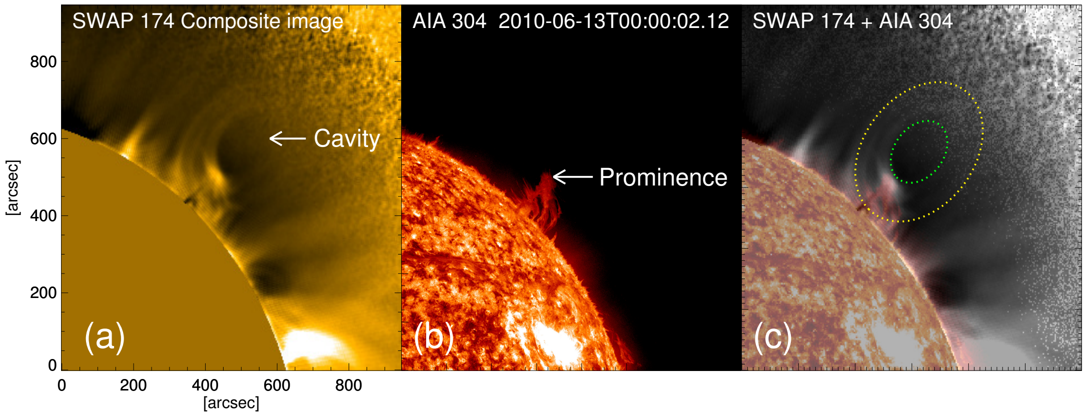

Figure 5.4: Observations of the coronal cavity as viewed in SWAP composite images (a) and the associated prominence structure as seen in the AIA 304 Å channel (b). The superimposed images of cavity morphology and the prominence structure as depicted in panels (a) and (b) are shown (c). In panel (c), the background image in gray scale represents the cavity morphology as depicted in panel (a) and the foreground image in AIA 304 Å color scale represents the prominence structure as shown in panel (b). The green and yellow dotted lines are the same as those described for Figure 5.1.

noise in the far field of the SWAP images, the 1.6 minute cadence images between 00:00 UT and 01:35 UT on 2010 June 13 have been processed using a median stacking technique to capture the cavity morphology before eruption. Finally, the cavity erupted at around 06:30 UT from the north-west solar limb as viewed by Earth and evolved into a CME as observed in LASCO C2/C3 images.

In order to associate the morphological evolution of the EUV cavity with that of the three part structure of the associated CME seen in white light observations, it is important to understand whether the cross-sectional profiles of the cavity, as observed in EUV and white-light images, resemble the same morphological structure or not. Comparing the EUV and white-light observations of an erupting loop system that formed a CME, Byrne et al. (2014) found an inconsistency between the evolutionary profiles of the erupting structure as seen in EUV and white-light images. It is important to note that the white-light observations, which capture the Thomson scattered light from the free electrons of the solar corona, are dependent on the electron density and are most sensitive to features near the POS (Vourlidas & Howard, 2006; Howard & DeForest, 2012; Inhester, 2015). Whereas, the EUV observations are primarily sensitive to both the temperature and den-

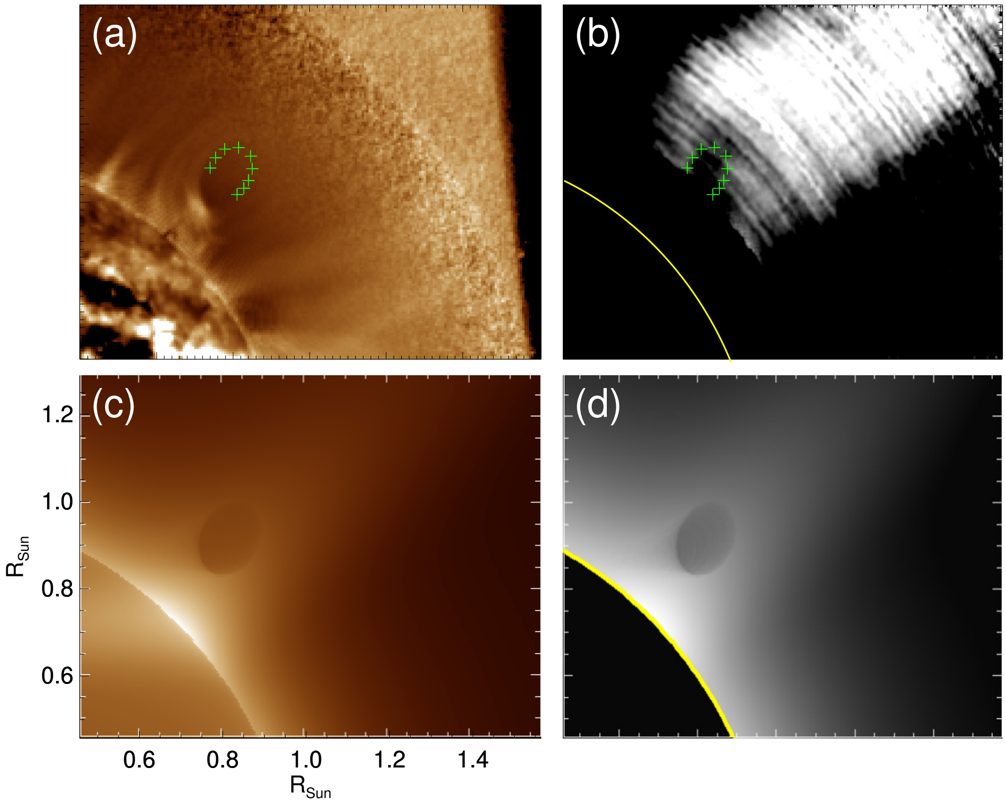

Figure 5.5: Cavity morphology as seen in SWAP composite images stacked over the period between 00:00 UT to 01:35 UT on 2010 June 13 (a). The daily averaged polarized brightness as imaged by the groundbased coronagraph MK4 on 2010 June 13 (b). The green cross-marks drawn on panel (b) approximately indicate the outer-boundary of the white-light cavity embedded in a coronal streamer. The same green cross-marks shown in panel (b) have been drawn on panel (a). FORWARD-modeled (line-of-sight integrated) EUV emission in 174 Å passband (c) and the white-light polarized brightness (d) using the model density and temperature of the cavity embedded in a coronal streamer.

sity of the plasma (Martínez-Sykora et al., 2011; Del Zanna & Mason, 2018), and are less preferentially sensitive to features based on their location with respect to the POS, as it is the case for white-light coronagraph images. Therefore, any coronal feature, such as the erupting loop system studied in Byrne et al. (2014), which lies away from the POS will appear as different morphological structures in EUV and white-light observations.

Coronal cavities are extended tunnel like structures which are mostly associated with the polar crown filaments (Gibson, 2015). When these large structures line up along the line-of-sight, they appear like a dark croissant-like features in the POS observations due to the density depletion in comparison to the surrounding corona. In particular, any portion of the cavity is best seen when it lies on the POS (Gibson et al., 2010). Therefore, the line-of-sight integrated Thomson scattered brightness, as obtained by the white-light coronagraphs, and the line-of-sight integrated EUV emission as obtained by SWAP or AIA in 174 Å and 193 Å passbands which are also sensitive to the electron density due to the presence of Fe IX and Fe XII emission lines (Martínez-Sykora et al., 2011), should reveal an identical morphology for any observed coronal cavity. In order to validate this we have compared the SWAP EUV observations of the cavity morphology with the white-light observations as obtained from the Mk4 coronagraph, which observes between 1.1 to 2.8 $R_\odot$.

Panel (b) in Figure 5.5 shows the cavity morphology as seen in the daily averaged polarized brightness observations obtained from the ground-based Mk4 coronagraph on 2010 June 13. The green cross-marks drawn on panel (b) approximately indicate the outer-boundary of the white-light cavity embedded in a coronal streamer. The same green cross-marks have been over-plotted on the SWAP EUV image in panel (a), which clearly shows that the EUV and white-light cavity morphology are the same. Furthermore, using an observationally constrained 3D cavity model (Gibson et al., 2010) we have FORWARD (Gibson et al., 2016) modeled the cavity morphology in both the EUV emission lines and the Thomson scattered polarized brightness. The line-of-sight integrated EUV emission in 174 Å passband (panel (c)) and the Thomson scattered polarized brightness (panel (d)) has been obtained using the model density and temperature of the coronal cavity, embedded in a coronal streamer (Gibson et al., 1999). The similarity between the cavity morphology seen in the synthesized EUV and white-light images reveals that both the EUV and white-light cavities possess a fundamentally identical morphology, colocated in a large 3D structure.

Observation time yyyy/mm/dd hh:mm:ss UT	Observing instrument	longitude of the cavity in Stonyhurst / Carrington heliographic coordinates	Cavity centroid height [$R_\odot$]	Cavity morphology	Cavity diameter [$R_\odot$]
2010/05/30 02:32:02	SDO/AIA	90° E / 136°	1.10	≈ Circular	0.016± 0.002
2010/06/04 21:25:30	STEREO-A/SECCHI EUVI	18° E / 132°	1.13	≈ Circular	0.039± 0.008
2010/06/07 14:26:02	STEREO-B/SECCHI EUVI	20° W / 134°	1.17	≈ Circular	0.054± 0.008
2010/06/13 04:00:00	PROBA2/SWAP	90° W / 132°	1.23 ± 0.02	Elliptical	0.09± 0.02

Table 5.1: Cavity morphology throughout the quiescent phase

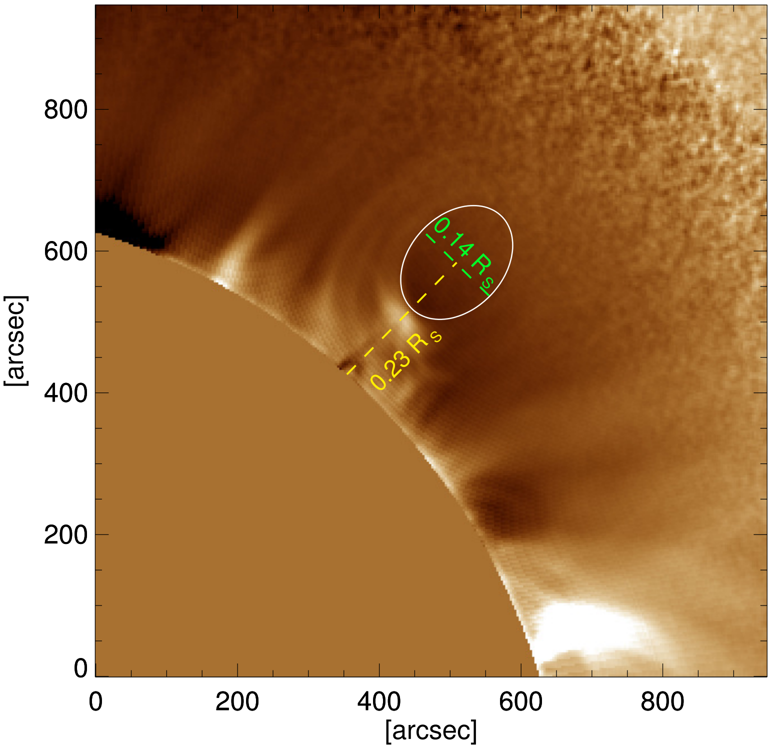

Figure 5.6: Cavity morphology as seen in SWAP composite images stacked over the period between 00:00 UT to 01:35 UT on 2010 June 13. The cross sectional dimension of the cavity and the distance to the cavity centroid from the solar surface are indicated.

5.3 Evolution of the Coronal Cavity During Eruptive Phase

5.3.1 Morphological evolution of the cavity

The cavity morphology as observed in the SWAP EUV image is best fitted with the elliptical boundary where the cavity centroid reached a height of ≈ 0.23 $R_\odot$ above the solar surface at approximately 00:00 UT on 2010 June 13, prior to the eruption (see Figure 5.6).

Although the cavity boundary is clearly detectable in the SWAP composite images, it is difficult to detect the full outer boundary of the cavity in each individual SWAP image. Only the lower boundary of the cavity can be identified due to the emission from the lower lying prominence material which acts as the outer boundary of the cavity. Therefore, we have traced the coordinates along the lower-half boundary of the cavity structure at different times throughout its

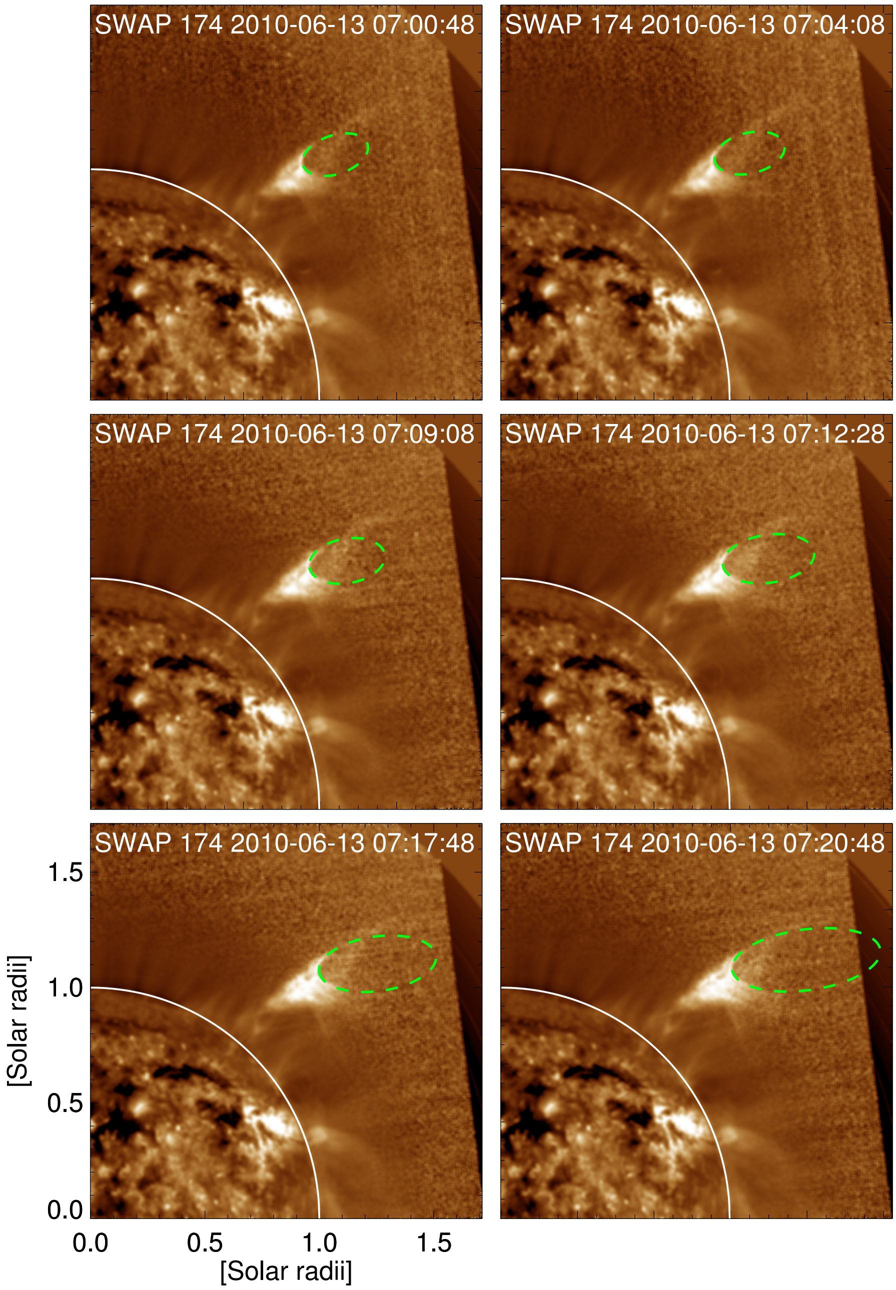
SWAP 174 2010-06-13 07:00:48
SWAP 174 2010-06-13 07:04:08
SWAP 174 2010-06-13 07:09:08
SWAP 174 2010-06-13 07:12:28
SWAP 174 2010-06-13 07:17:48
SWAP 174 2010-06-13 07:20:48
1.5
1.0
0.5
0.0
[Solar radii]
0.0
0.5
1.0
1.5
[Solar radii]

Figure 5.7: Cavity morphology as observed in the SWAP EUV images during the eruptive phase. The solid white line in each panel highlights the position of the solar limb. The green dashed ellipses depict the geometrical fit to the cavity morphology.

eruption. These traced coordinates are then fitted with an elliptical geometry, assuming that the upper part of the cavity morphology is symmetrical as the lower-half (see Figure 5.7). Figure 5.8 depicts the morphological evolution of the cavity within SWAP FOV where each of the ellipses represents the geometrically fitted structure of the cavity morphology at different instants during its eruptive phase as shown in Figure 5.7.

In order to understand how the EUV cavity in the lower corona evolved into the white light cavity associated with the CME, we have combined the SWAP observations with the white light coronagraphic images as captured by the LASCO C2/C3. Figure 5.9 depicts the transformation of the cavity from EUV to white light observations, and its evolution as a three part structure of the associated CME. In order to capture the complete evolution of the cavity, we also apply the geometrical fitting to the white-light cavity morphology. The outer boundary of

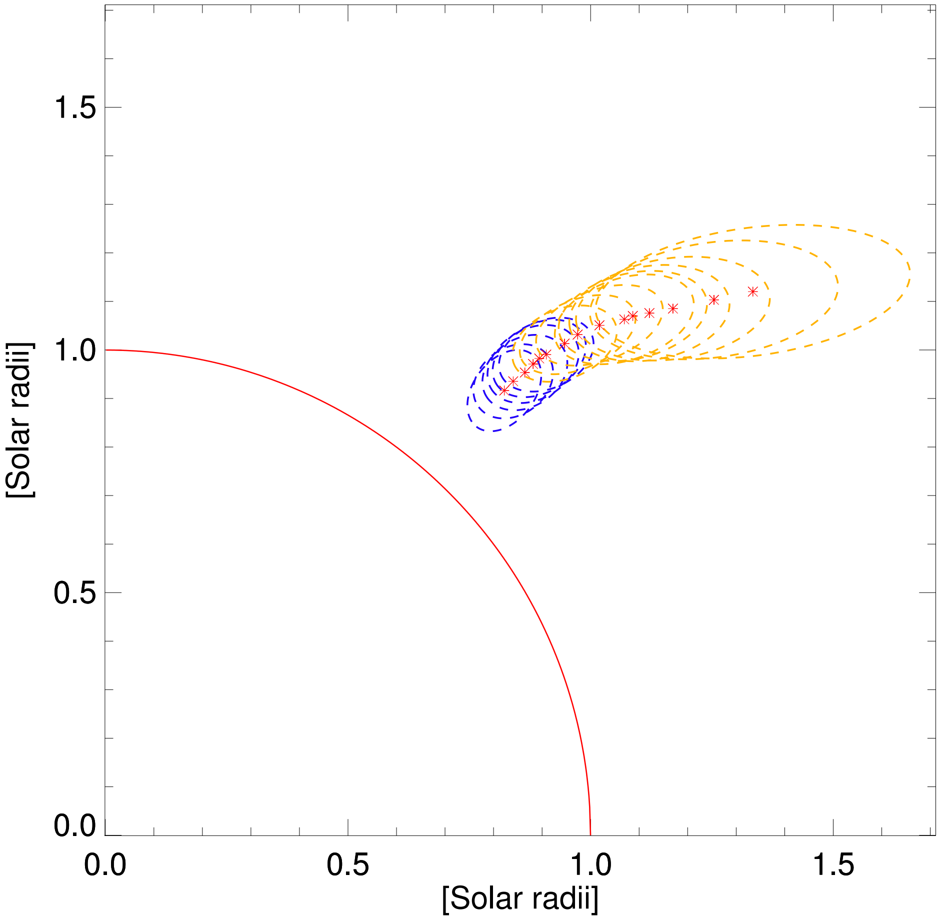

Figure 5.8: Morphological evolution of the cavity system within SWAP FOV during the eruptive phase. The red boundary highlights the solar limb. The blue dotted ellipses denote the geometrical fit to the cavity morphology during the radial motion within 1.3 $R_\odot$, whereas the yellow dotted ellipses denote the same during the non-radial motion after the deflection at $\approx$ 1.3 $R_\odot$. The red asterisks depict the trajectory of the cavity centroid.

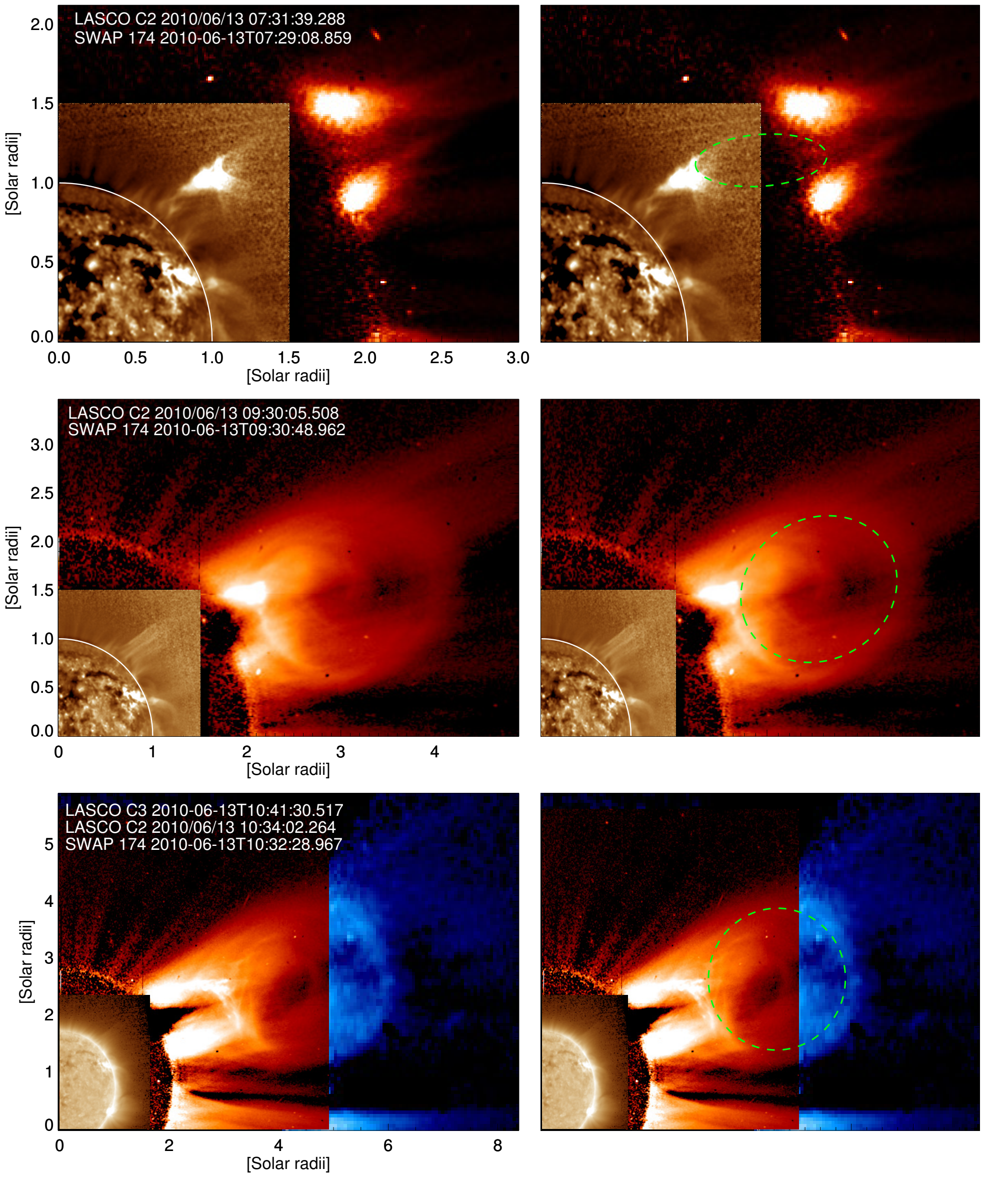
LASCO C2 2010/06/13 07:31:39.288
SWAP 174 2010-06-13T07:29:08.859
[Solar radii]
0.0
0.5
1.0
1.5
2.0
2.5
3.0
LASCO C2 2010/06/13 09:30:05.508
SWAP 174 2010-06-13T09:30:48.962
0
1
2
3
4
LASCO C3 2010-06-13T10:41:30.517
LASCO C2 2010/06/13 10:34:02.264
SWAP 174 2010-06-13T10:32:28.967
5
6
8

Figure 5.9: Cavity morphology as observed in white-light coronagraphic images of LASCO C2 and C3 observations (red and blue respectively), with SWAP observations superimposed in the center. The white solid lines highlight the solar limb. The green dashed lines show the geometrical fit to the cavity morphology.

the dark cavity on the top of the bright filament as observed in LASCO C2/C3 has been fitted up to a height of 8 R$_\odot$. Beyond 8 R$_\odot$ the cavity morphology became too diffused to be fitted with certainty. It was possible to track the centroid of the EUV cavity out to 1.8 R$_\odot$ using the morphological fit to its lower boundary, even when the cavity centroid height exceeded the outer extent of SWAP FOV. Similarly, we have fitted the upper-half of the white-light cavity in LASCO FOV for several frames where the lower part of the cavity was obscured by the occulter

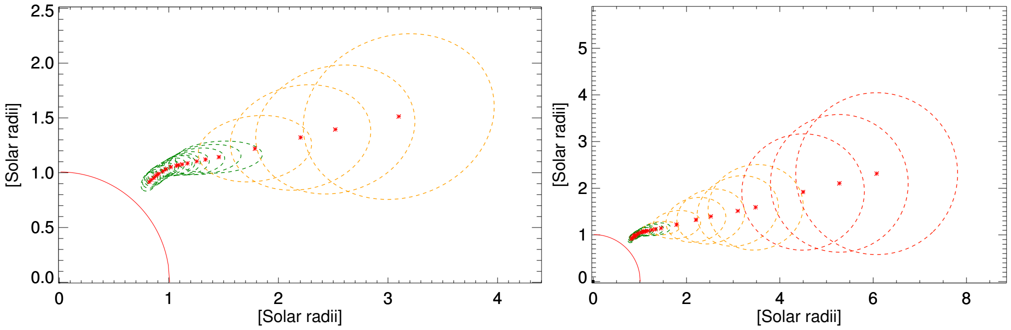

Figure 5.10: The left panel shows the geometrical fit to the cavity morphology observed in the combined FOV of SWAP (green ellipses) and LASCO C2 (yellow ellipses). The right panel shows the geometrical fit to the cavity morphology observed in the combined FOV of SWAP (green dotted ellipses), LASCO C2 (yellow dotted ellipses) and LASCO C3 (red dotted ellipses). The red solid boundary highlights the solar limb. The red asterisks depict the trajectory of the cavity centroid.

and the cavity centroid height resided below 2 $R_\odot$. Therefore, the small observational gap (1.8 to 2 $R_\odot$) between the SWAP and LASCO FOV did not affect the continuous tracking of the erupting cavity. The morphological evolution of the coronal cavity starting from its initial centroid height at 1.23 $R_\odot$ up to 8 $R_\odot$ can be seen in Figure 5.10.

5.3.2 Kinematic evolution of the cavity-prominence system

As discussed in Section 5.2, during the quiescent phase, the spatial association between the prominence structure and the cavity morphology shows that the prominence material lies exactly at the bottom of the cavity (see Figures 5.1, 5.3 and 5.4). In order to investigate whether this spatial relationship is maintained during the eruptive phase also, we have separately tracked the top boundary of the prominence material as observed in AIA 304 Å channel and the bottom boundary of the coronal cavity as observed in SWAP EUV images. This was done by placing a slit at a position angle of 317° on both the SWAP and AIA images, and stacking the evolution of the cavity and filament boundary with time within the respective slits. Figure 5.11 shows the position of the slits (top panels) in the SWAP EUV and AIA 304 Å images respectively. The bottom

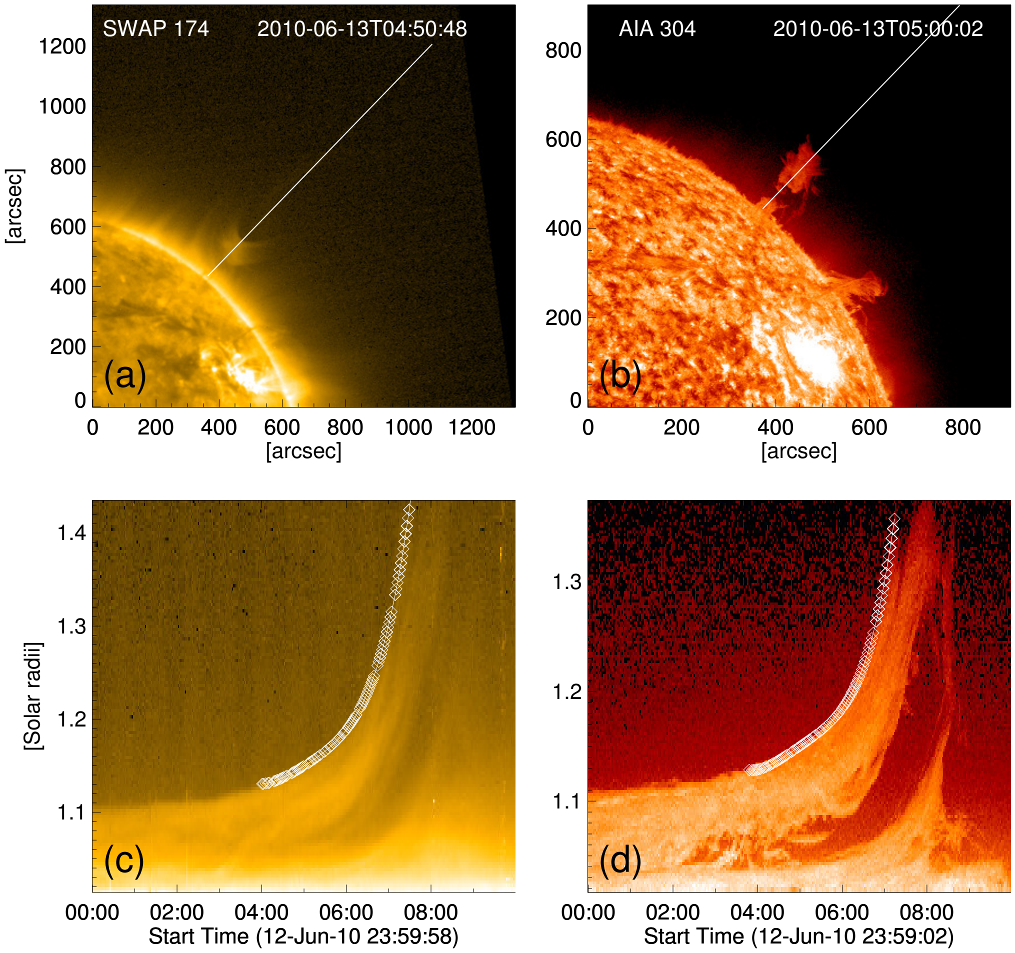

Figure 5.11: The position of the slits superimposed on the SWAP and AIA images (panels (a) and (b) respectively) along with the height-time profiles for the lowermost boundary of the cavity (c) and the top-most part of the prominence (d).

panels of Figure 5.11 illustrate the evolution of the bottom boundary of the cavity (panel (c)) and the top boundary of the filament (panel (d)). In order to compare these two height-time profiles, we have selected the points with proper coordinate informations along the two height-time curves as marked by the square diamond shaped symbols drawn on the two time-slice diagrams (Figure 5.11). These selected points along the two height-time curves are then over-plotted in Figure 5.12. The error bars (± 0.006 $R_\odot$) are a measure of the uncertainty in selecting the points along the curve boundary. In order to estimate the above mentioned error, the curve boundary was fitted several times which gave the standard deviation as ± 2 pixels which is ± 0.006 $R_\odot$ in physical units.

5.4 Results

5.4.1 Spatial relation between the EUV cavity and the associated prominence

Combining the observations of the erupting cavity and the associated prominence structure we have examined the spatial relationship between them in lower corona during both the quiescent and eruptive phases. Figure 5.12 clearly shows that the height-time profiles of the filament top and the cavity bottom boundary coincide with each other. This indicates that throughout the eruptive phase the cavity is located exactly on the top of the prominence which is in agreement with the understanding of the classical three part structure of CMEs.

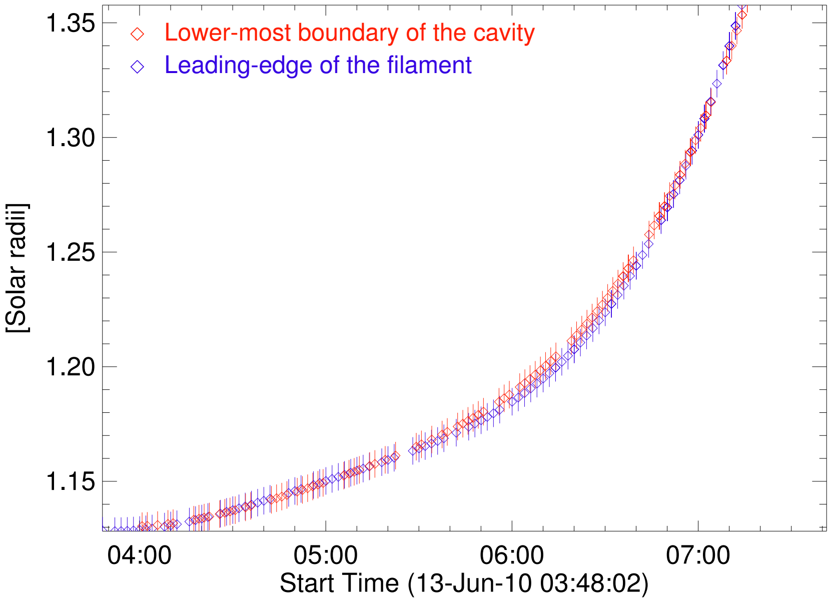

Figure 5.12: The height-time profiles of the lowermost boundary of the cavity (red) and the leading edge of the filament (blue), as recorded in Figure 5.11.

5.4.2 Cavity morphology during the quiescent phase

By using the multi-spacecraft observations from SDO, STEREO and PROBA2 we have tracked the gradual evolution of the stable EUV cavity at different times during its passage across the solar disk.

However, in order to relate the different evolutionary phases of the quiescent cavity it is important to track the same portion of the large 3D structure associ-

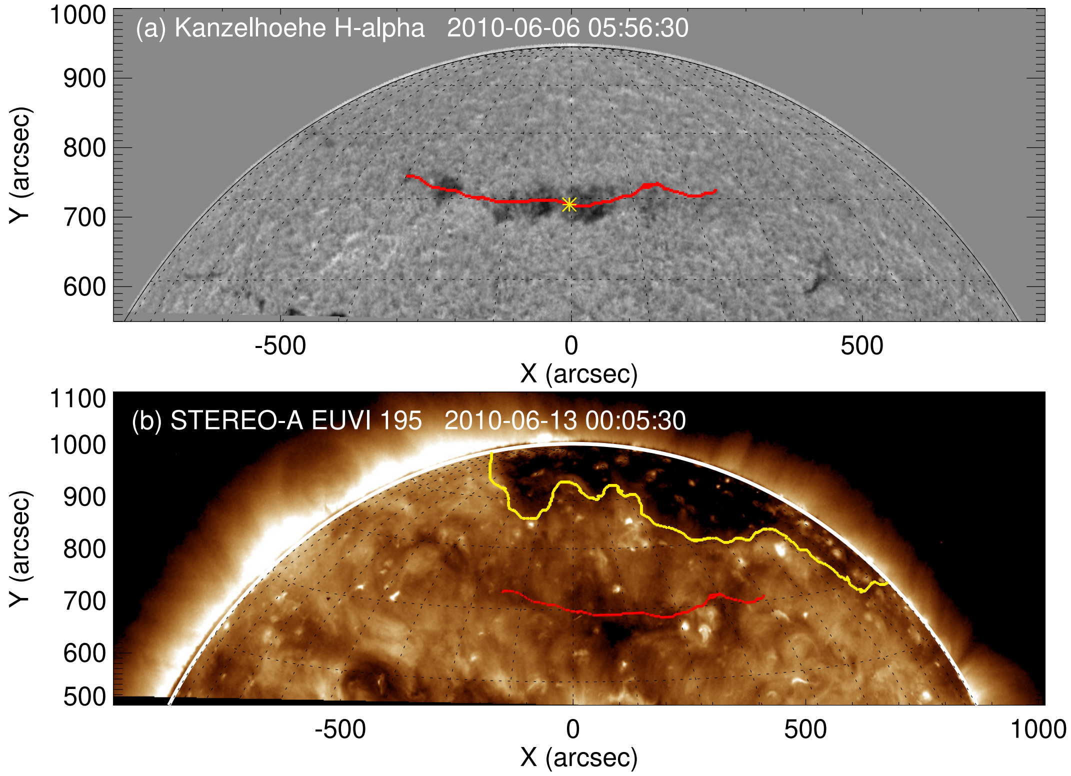

Figure 5.13: Hα image of the polar crown filament on 2010 June 6 (a). The red solid line, drawn over the image, depicts the approximate position of the filament channel on the solar disk. The yellow star mark approximately locates the central part of the long filament channel. STEREO-A EUVI 195 Å image on 2010 June 13 (b). The yellow solid line denotes the boundary of the northern polar coronal hole. The red solid line in panel (b) indicates the location of the same filament channel as shown in panel (a).

ated with it. Figure 5.13 shows the location of the associated H-alpha filament channel on 2010 June 6, when it was close to the solar disc center. The longitudinal extent of the filament channel was approximately 60° and the Carrington heliographic longitude of the central part (indicated by the yellow star mark in panel (a) of Figure 5.13) of this long filament channel was 132 ± 4°. Noticeably, the Carrington longitude of the quiescent cavity system on 2010 May 30, June 4, June 7 and June 13 as observed sequentially by the SDO, STEREO-A, STEREO-B and PROBA2 was 136°, 132°, 134° and 132° respectively (see Table 5.1) which was nearly the same as the Carrington longitude of the central part of the filament channel. Moreover, as the orientation of the filament channel was nearly horizontal with respect to the solar equator, the associated flux-rope possessed a close to azimuthally symmetric structure with respect to the solar rotational axis. Therefore, all the observations depicting different phases of the quiescent cavity, capture the same part of the large 3D structure and hence reveal the true evolution of the cavity during its long-lived quiescent phase.

The geometrical fit to the cavity structure reveals that the cavity boundary had a near circular morphology when it appeared on the east solar limb, and maintained this shape when it was positioned near disk centre, as seen from the POS EUVI observations of STEREO A and B (see Figures 5.1 and 5.3). However, the cavity morphology evolved into a more elliptical shape as it approached the west solar limb, prior to eruption (see Figure 5.4). Apart from the morphological change, the quiescent cavity also undergoes a slow rise and expansion phase. As the cavity rotated across the solar disk from east to west solar limb, its diameter increased from 0.016 ± 0.002 to 0.09 ± 0.02 $R_\odot$ and the cavity centroid height raised from 1.10 to 1.23 ± 0.002 $R_\odot$ (see Table 5.1) before it finally erupted from the west solar limb.

5.4.3 Cavity dynamics during the eruptive phase

Using the large FOV of SWAP we have sequentially captured the evolution of the erupting cavity morphology in the lower corona up to 1.7 $R_\odot$. Figure 5.8 presents a clear depiction of a significant non-radial motion exhibited by the cavity at about 1.3 $R_\odot$ where its position angle changed from approximately 310° to 270°. In general, the equator-ward deflection of CMEs is believed to be due to the influence of polar coronal holes (Cremades et al., 2006; Panasenco et al., 2011). However, the EUV images obtained from the AIA and SWAP on 2010 June 13 do not show any signature of a polar coronal hole in the northern hemisphere which may be due to the line-of-sight tilt of the solar magnetic axis. Therefore, in order to identify the presence of a polar coronal hole we have used the EUV observations of Sun on the same day from the perspective of STEREO-A (see the position of STEREO-A in Figure 5.2).

Panel (b) in Figure 5.13 clearly shows the presence of a northern polar coronal hole on 2010 June 13 as observed by STEREO-A EUVI in 195 Å passband. In order to identify the location of the filament channel on the EUVI 195 Å image, we first computed the Carrington longitude and latitude of the points along the Hα filament channel (indicated by the red solid line in panel (a) of Figure 5.13) as observed on 2010 June 6. Using the information of the Carrington heliographic coordinates of these points, the same filament channel has been overlaid on the STEREO-A EUVI 195 Å image. The location of the filament channel in the vicinity of the northern polar coronal hole reveals that the open magnetic field-lines originating from the polar coronal hole might have channeled the trajectory of the erupting cavity towards the heliospheric current-sheet. Therefore, the cavity deflected from a higher latitude to a lower one. More precisely, the change in magnetic pressure around the region of strong magnetic field associated with the coronal hole might have exerted magnetic pressure gradient force on the CME, resulting the deflected trajectory of the CME.

By combining the observations from SWAP and LASCO C2/C3 we have studied the association between the EUV and white light observations of the cavity. Figure 5.10 shows that during the eruptive phase the cavity morphology gradually evolved from an initial elliptical shape to a semi-circular one (see left panel of Figure 5.10) within the FOV of LASCO C2. As the cavity evolved further, it became almost circular after about 4 $R_\odot$. Noticeably, after the initial deflection at about 1.3 $R_\odot$ the cavity maintained the same position angle (270°) throughout the rest of its propagation trajectory.

We noticed that the elliptical geometry of the cavity, as obtained during its lower coronal evolution, is elongated along the direction of propagation. The gradual transformation of the cavity morphology from elliptical to near about circular shape also occurs along the propagation direction. Therefore, it cannot be associated with projection effect due to any significant line-of-sight velocity component because that would cause the geometrical transformation either in vertical or horizontal direction on the plane-of-sky.

It is also important to note that the orientation of the filament channel was nearly horizontal with respect to the solar equator. Therefore, the magnetic axis of the flux rope was almost along the line-of-sight before eruption. This suggests that the pre-eruptive elliptical morphology was not associated with any projection effect that could arise due to any misalignment of the flux rope axis with respect to the line-of-sight. Therefore, the elliptical morphology depicted the true geometry of the flux-rope cross-section. During the eruptive phase, any rotation (on the plane perpendicular to the plane-of-sky) of the flux-rope axis from its initial line-of-sight orientation would increase the eccentricity of the elliptical morphology which is not the case in this study. Therefore, we can conclude that the transformation of the flux rope morphology from elliptical to nearly circular shape was not associated with any rotation of the flux rope axis.

5.4.4 Nature of expansion of the erupting cavity

In order to investigate whether the cavity evolution was self-similar or not, we have plotted the evolution of the cavity aspect-ratio with respect to the cavity centroid height. The numerator of the aspect-ratio is the length of the semi-major axis of the cavity ellipse and the denominator is the distance from Sun center to the cavity centroid along the non-radial trajectory of the cavity propagation.

The upper panel of Figure 5.14 shows the evolution of the cavity width to centroid height aspect-ratio, which can be seen to gradually increase to 0.25 ± 0.03 at 2.2 ± 0.2 $R_\odot$, after which it became approximately constant for the remainder of its propagation. This clearly shows that within 2.2 ± 0.2 $R_\odot$ the cavity exhibited non-self similar expansion whereas beyond 2.2 ± 0.2 $R_\odot$ it enters into a regime of self similar expansion. The non-self similarity in the cavity evolution is also reflected in its expansion profile in the lower corona. The bottom panel of Figure 5.14 shows that the cavity diameter (length along the major axis of the ellipses fitted to the cavity morphology) expands linearly after 2.2 ± 0.2 $R_\odot$, whereas it evolves in a different fashion within the non-self similar regime in lower corona. Noticeably, this critical height (2.2 ± 0.2 $R_\odot$) resembles the radius of source surface (2.5 ± 0.25 $R_\odot$) where the coronal magnetic field-lines are believed to become radial (Hoeksema et al., 2014).

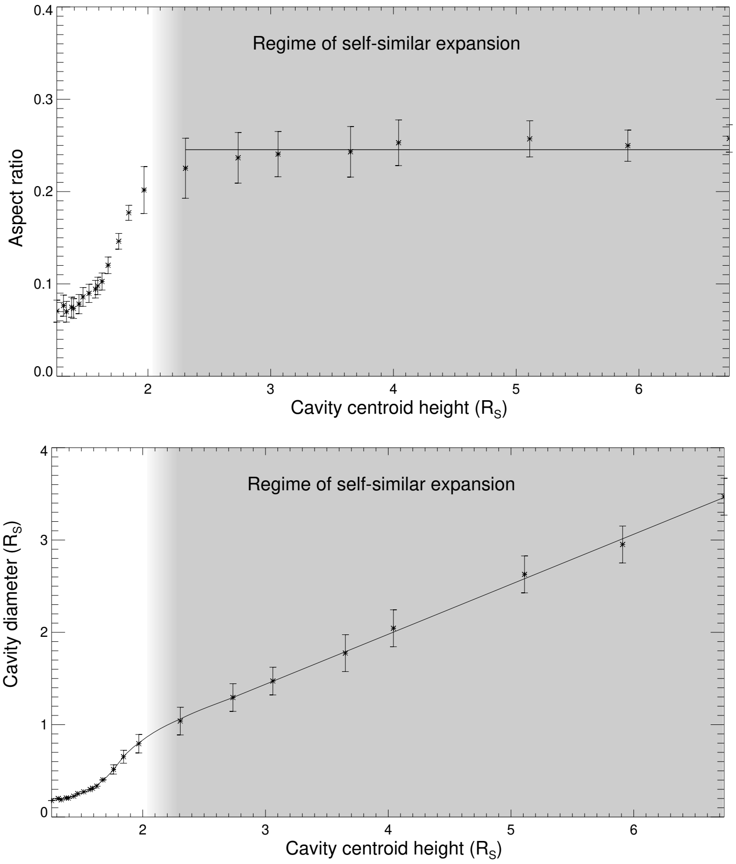

Figure 5.14: The evolution of the cavity width to centroid height aspect-ratio (top panel). Evoloution of the length along the semi-major axis of the cavity with respect to the cavity centroid height (bottom panel).

5.4.5 Kinematic evolution of the cavity

Investigating the kinematics of the erupting cavity we find that the individual height-time profiles of cavity top, centroid and bottom part evolve in a different manner due to the internal expansion of the cavity structure (panel (a) of Figure 5.15). Interestingly, the velocity profiles shown in Figure 5.15 depict that the erupting cavity undergoes two distinct phases of kinematic evolution.

During the first phase, the speed of the top, centroid and bottom part of the cavity quickly reached approximately 350, 250, 150 km s^{-1} respectively within $\approx$ 1.8 R$_\odot$. However, the second phase of the kinematic evolution starts after 2 R$_\odot$ where the speeds of the three different parts of the cavity increase more gradually in comparison to the first kinematic phase. Comparatively lower energetics observed during the second phase of the kinematic evolution, could be associated with the energy loss involved in opening the overlying magnetic field.

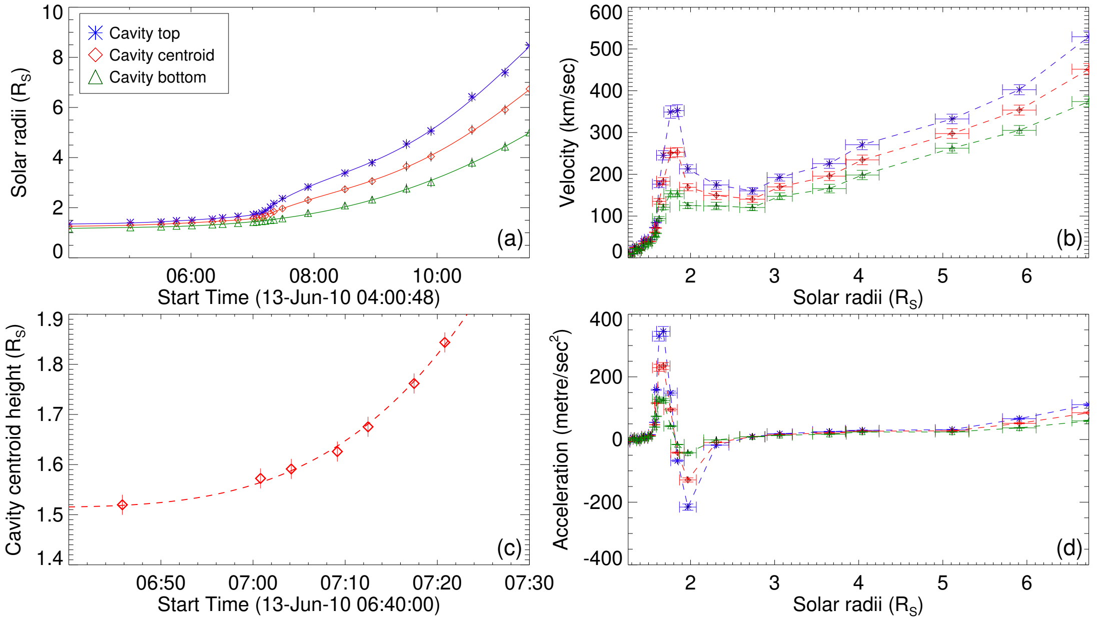

Figure 5.15: Height-time profiles for the cavity top, cavity centroid and cavity bottom (a). Velocity profiles for the cavity top, cavity centroid and cavity bottom (b). Polynomial fit to the cavity centroid height during the time interval 06:40 to 07:30 UT on 2010 June 13 (c). Acceleration profiles for the cavity top, cavity centroid and cavity bottom (d).

Noticeably, the cavity centroid exhibited the peak acceleration at 1.67 ± 0.08 $R_{\odot}$ where the top, center and bottom part of the cavity attained the accelerations of 345 ± 15, 234 ± 11 and 124 ± 6 m s^{-1} respectively. This impulsive phase of acceleration is believed to be governed by the Lorentz self-force where the outward magnetic pressure dominates over the external and/or internal magnetic tension force (Byrne et al., 2010). Importantly, the peak acceleration height (1.67 ± 0.08 $R_{\odot}$) of the cavity obtained in this study is in agreement with the mean value (1.72 $R_{\odot}$) of that found for the filament associated CMEs studied by Bein et al. (2012). However, after 2 $R_{\odot}$ the average acceleration reduces to below 50 m s^{-1} which is believed to be the "residual acceleration phase" of the CME where the Lorentz self-force undergoes the declining phase and the flux-rope dynamics become strongly dependent on the drag force (Chen & Krall, 2003).

In order to initiate the first phase of the kinematic evoluton, several triggering mechanisms have been proposed (see the review by Chen, 2011). Catastrophic loss of equilibrium, ideal MHD instabilities, tether-cutting, magnetic breakout, triggering by flux-emergence or cancellation and mass drainage are believed to be one of the possible driving mechanisms for triggering the initial acceleration phase. Interestingly, by fitting the height-time profiles of the kinematic evolution with a power-law polynomial and by comparing it with the results obtained from different numerical simulations, one may get clues to the underlying eruption mechanism (Török & Kliem, 2005; Williams et al., 2005; Mierla et al., 2013).

Schrijver et al. (2008) have shown that the rapid-acceleration phases of erupting prominences are best characterized by a height dependent function, $h(t) \propto t^m$, where h(t) is the instantaneous height at any time t and m is the power law exponent. Using this power law function, we have fitted the height-time profile of the cavity centroid during its impulsive acceleration phase in between 06:40 to 07:30 UT on 2010 June 13. The red dashed line in panel (c) of Figure 15 shows the curve of best fit obtained by using $m = 3.6$. Noticeably, an exponent value (m) close to 3 corresponds to the torus-instability scenario (Schrijver et al., 2008). Therefore, our results suggest that the impulsive acceleration phase was most likely driven by the torus instability.

5.4.6 Eruption mechanism of the coronal cavity in the context of torus instability

Observation time yyyy/mm/dd hh:mm:ss (UT)	Decay index at the top of the prominence	Decay index at the cavity centroid
2010/05/30 02:32:02	0.75 ± .07	0.80 ± .06
2010/06/04 21:25:30	0.7 ± .2	0.7 ± .2
2010/06/07 14:26:02	0.7 ± .1	0.8 ± .1
2010/06/13 04:00:00	1.2 ± .1	1.3 ± .1

Table 5.2: Temporal evolution of decay index

In order to understand the pre eruptive stability conditions for quiescent cavities and the triggering mechanisms for those structures to erupt, we have examined the role of the background magnetic field in the context of torus instability.

In order to obtain the information of the overlying magnetic field we have used the Potential Field Source Surface (PFSS) extrapolation code (Schrijver & De Rosa, 2003) available in SolarSoft packages. As the minimum time-cadence of the available extrapolated fields from PFSS model is 6 hours, we have used the extrapolations carried out within the minimum temporal window from the observing time of the cavity. For each of the four different days when the cavity was observed sequentially on the east-limb, POS of STEREO A, STEREO B and west-limb, the decay index of the overlying magnetic field has been evaluated along the radial direction through the cavity centroid lying on the respective POS. In order to calculate the decay-index we have used the formulation as introduced in Equation 1.5.4.4 (Chapter 1), where the external magnetic field is obtained from the PFSS extrapolations (Török & Kliem, 2005).

The critical value ($n_{critical}$) of decay index for the onset of the torus instability is believed to be close to 1.5 (Kliem & Török, 2006). However, depending on the typical range of current-channel thickness expected in the corona, $n_{critical}$ can vary within a range between 1.2 to 1.5 (Démoulin & Aulanier, 2010). From the observational studies on prominence eruptions, the value of $n_{critical}$ (0.9 to 1.1) at the top of the prominence has been found to be less than that found in the MHD simulations (Filippov, 2013; Zuccarello et al., 2014; McCauley et al., 2015). Addressing this discrepancy between the models and observations, Zuccarello et al. (2016) performed a set of MHD simulations and have shown that the value of $n_{critical}$ computed at the flux rope axis is 1.4 ± 0.1, while at the height of the top of the prominence this value is 1.1 ± 0.1 . These results suggest that the choice of location (prominence top or the cavity centroid) to evaluate the decay index is important for comparing the observational and theoretical values of $n_{critical}$. The temporal evolution of the altitude of prominence top and the cavity centroid, as presented in the current study, allows us to address the above mentioned issue observationally.

Figure 5.16 shows four decay index profiles as calculated for the four different POS observations of the cavity along 90°E, 18°E, 20°W and 90°W in Stonyhurst heliographic coordinates (Thompson, 2006) on 2010 May 30, June 4, 7 and 13 respectively. The overplotted black dashed and solid lines mark the decay index values at the top of the filament and the cavity centroid respectively, which are listed in Table 5.4.6.

The decay index values for the first three positions of the cavity during the observational period from 2010 May 4 to 2010 June 7 indicate that both the filament top and the cavity centroid reside well below the critical decay index limit, while the cavity was in a stable condition (see Table 5.4.6). However, the decay index value (1.3 ± 0.1) at the cavity centroid height reached the critical limit 1.4 ± 0.1 for the onset of torus instability prior to the eruption on 2010 June 13. Noticeably, the altitude of the filament top also reached the decay index value (1.2 ± 0.1) which resembles the "apparent" critical value (1.1 ± 0.1) of decay index at the filament top as obtained from the simulational results of Zuccarello et al. (2016). Importantly, the good agreement between the observational (1.3 ± 0.1) and simulational (1.2 to 1.5) results for the critical decay index value at the cavity centroid height suggests that the cavity centroid should be used as the preferable location to evaluate the decay index value in order to reduce the discrepancy between the observational and theoretical critical limit for $n_{critical}$.

Furthermore, our results also suggest that the decay index value at the cavity centroid height can be used as a good indicator for determining whether the cavity will result in an eruption or not.

5.5 Discussion and Conclusions

For a two week long quiescent phase of the coronal cavity, we have studied its morphological evolution by tracking the same portion of a large 3D structure associated with it. Combining the observations from the SWAP, LASCO C2 and C3, we have also captured its evolution during the eruptive phase which enables us to associate the erupting EUV cavity with its white-light counterpart as observed in the outer corona. The evolution of the cavity morphology at different stages of its quiescent and eruptive phases reveals the underlying eruption mechanism and the role of magnetic forces governing the cavity dynamics.

Observations from different vantage points during the quiescent phase reveal that the cavity morphology maintained a close to circular shape as it rotated across the solar disk. Eventually, the circular shape evolved into an elliptical one by the time the cavity reached the west solar limb, just prior to the eruption. It is important to note that the cavity centroid height slowly increased from 1.10 to 1.23 $R_\odot$ in association with a slow expansion in the cavity size as it rotated from the east to west solar limb (see Table 5.1). Gibson & Fan (2006) demonstrated that an expanding flux rope may achieve an equilibrium configuration when the forces causing the expansion are counterbalanced by the confining magnetic tension forces exerted by the overlying magnetic field. As the magnetic field strength drops off radially with height, it is expected that the flux rope equilibrium will be governed by a lateral confinement rather than a vertical one, resulting in an elliptical morphology of the flux-rope cross-section (Gibson, 2015). Observations of the slowly rising and expanding cavity morphology presented in this work reveal that the cavity undergoes a series of stable equilibria during its quiescent phase. As the quiescent cavity expands and reaches higher heights in the corona it becomes more elliptical due to the excess magnetic pressure in the lateral direction exerted by the overlying magnetic field.

Interestingly, during the eruptive phase the elliptical cavity morphology again transformed back into a close to circular shape when the cavity centroid height crossed $\approx 4\ R_\odot$ in the FOV of LASCO C3. This implies that the confining magnetic tension forces fall off more rapidly with increasing radial height in comparison to the internal forces, causing the cavity expansion. Therefore, the domination of the internal expansion forces over the external magnetic tension force results in an isotropic expansion of the cavity which makes the cavity morphology close to circular in shape. This scenario is in agreement with the earlier findings of Chen et al. (2000) where it has been shown that the role of magnetic tension forces becomes less significant compared to the drag and hoop force after the main acceleration phase of the CME which tends to occur below 2-3 $R_\odot$ (Chen & Krall, 2003; Joshi & Srivastava, 2011).

The slowly rising and expanding phase of the quiescent cavity (see Table 5.1)

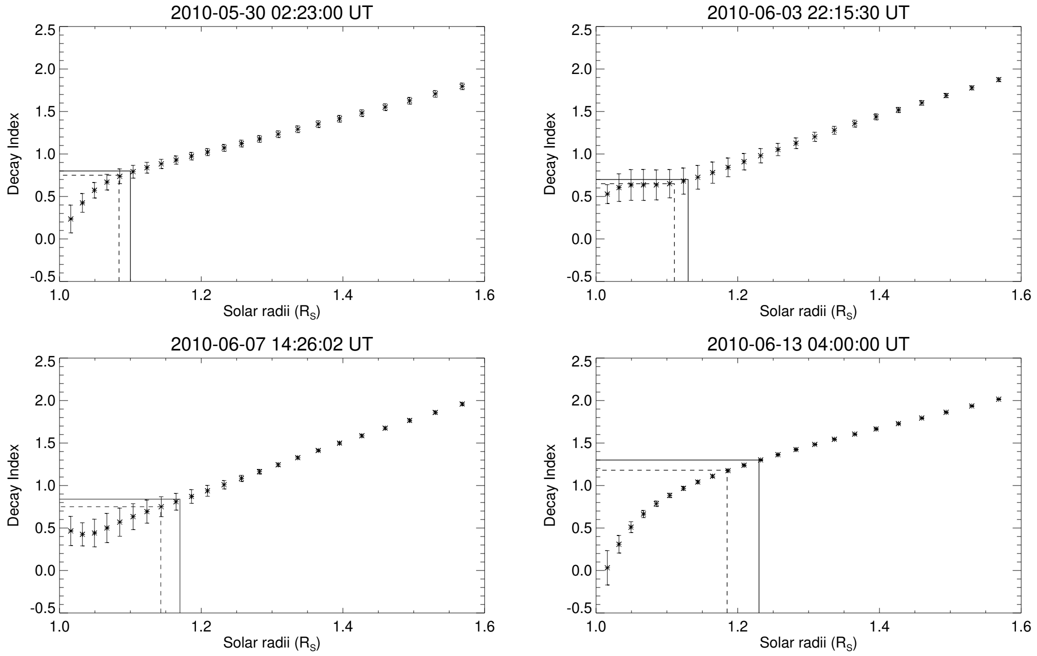

Figure 5.16: Decay index profiles for the different phases of the quiescent cavity. The black solid and dashed lines mark the decay index values at the cavity centroid and the top of the filament respectively.

during its passage from the east to west solar limb holds the intriguing clues to the underlying magnetostatic equilibria of the cavity system. During this stage, the injection of helical poloidal flux through flows or flux emergence from the lower boundary may gradually increase the toroidal current of the associated flux-rope which results in a gradual build-up in Lorentz self-force of the cavity system (Chen et al., 2006). Therefore, the cavity centroid height showed a slow rise (Table 5.1) due to the gradual increase in the upward Lorentz self force against the downward magnetic tension force exerted by the overlying magnetic field. Examining the decay index-profiles during the quiescent phase of the cavity, we have found that the decay-index value (<1.0) at the cavity centroid height resided well below the critical value (1.2 to 1.5) for the onset of torus instability. This implies that although there was a slow build-up in the Lorentz self-force of the cavity system, it was not strong enough to overcome the downward magnetic tension forces due to the strong overlying magnetic-field strength. However, when the cavity appeared on the west solar limb, its centroid height attained a decay index value (1.3 ± .01) which belongs to the critical range (1.2 to 1.5) for the onset of a torus instability and eventually it erupted from the west solar limb.

Therefore, we conclude that the decay-index value at the cavity centroid height can be used as a good indicator to examine whether a cavity will lead to an eruption or not.

In what follows, we summarize the answers to the key questions (outlined in Section 5.1) which have been addressed in this study:

(i) The slowly rising and expanding phase of the quiescent cavity hold important clues to its morphological evolution which reveals that the cavity undergoes a sequence of quasi-static equilibria during its long-lived quiescent phase. As the slowly rising cavity reaches higher heights in the corona, its morphology transforms from a nearly circular to an elliptical shape due to the excess magnetic pressure in the lateral direction exerted by the overlying magnetic field.

(ii) Throughout the quiescent phase, the cavity centroid height resided well below the critical limit for the onset of torus instability. However, the cavity centroid reached the critical height for the onset of torus instability just prior to the eruption. This critical height (1.23 $R_{\odot}$) in the lower corona determines the initiation height of the associated CME.

(iii) Evaluating the decay-index profiles at both the top-most part of the filament and the cavity centroid height, we conclude that the cavity centroid should be used as the preferable location to evaluate the decay index value in order to reduce the discrepancy between the observational and theoretical critical limit for $n_{critical}$. Moreover, the decay index value of the cavity-centroid height can be used as a good indicator to determine whether the cavity will result in an eruption or not.

(iv) Using the combined FOV of SWAP, LASCO C2 and C3, we have shown how an EUV cavity evolved into a white-light cavity, as one of the three part structures of a CME, while maintaining the same spatial relationship with the underlying prominence material.

(v) The kinematic study of the cavity evolution successfully captures two distinct phases of acceleration, where the impulsive acceleration phase was observed at 1.67 ± 0.08 $R_{\odot}$. The exponent value for the polynomial fit to the height-time profile of the erupting cavity reveals that the impulsive acceleration phase was most likely to be driven by the torus instability. However during the residual acceleration phase, the Lorentz self-force was less dominant and the kinematic evolution became strongly dependent on the drag force.

(vi) The significant non-radial motion observed in the SWAP FOV shows a strong deflection of the CME at lower coronal height (≈ 1.3 $R_\odot$). A deflection ($\approx 40°$ towards the equator) of the CME trajectory from higher to lower latitudes indicates that the polar coronal hole has significant influence on the CME kinematics, deflecting the CME towards the heliospheric current-sheet. However, the influence of coronal holes behind the CME deflection seems to be significant only close to Sun, as the CME under this study does not suffer any further deflection and propagates in an approximately constant direction during the rest of its observed trajectory.

(vii) Finding the critical height above which the CME undergoes a self-similar expansion is one of the important results of this study. Interestingly, the critical height (2.2 ± 0.2 $R_\odot$) below which the cavity exhibited non-self similar expansion, points to the spatial scale of magnetic field lines fundamentally changing from a closed to an open regime, as they open into the solar wind. Notably, above that critical height, the CME maintains its nature of expansion as self-similar during its rest of the observed propagation path.

These findings can be statistically validated with a larger dataset of events, which is beyond the scope of this chapter. In the future, we plan to carry out a statistical study on the erupting cavities in order to get deeper insight into the CME initiation mechanism. Nonetheless, the results obtained in this study on the nature of CME expansion and its direction of propagation, provides the observational constrains on the CME evolution. These understandings build up the stepping stone to model the CME evolution from Sun to Earth in order to forecast the strength and orientation of its magnetic field at 1 AU, as discussed in the next chapter.

Chapter 6

An Observationally Constrained Analytical Model for Predicting the Magnetic-field Vectors of ICMEs

6.1 Introduction

Once a CME is launched from the Sun in a direction towards the Earth, it may arrive at near-Earth space within several hours to days. If the CME speed is high and its north-south magnetic field component (Bz) is directed towards the south, an intense magnetic storm occurs upon the impact of the CME on Earth's magnetosphere (Wilson, 1987; Tsurutani et al., 1988; Gonzalez et al., 1999; Huttunen et al., 2005; Yurchyshyn et al., 2005; Gopalswamy et al., 2008). The storm can occur when the interplanetary flux rope (FR) and/or the sheath between the FR and the associated shock has southward Bz (see Figure 1.28). Therefore, the ultimate goal of this thesis is to predict the strength and orientation of the ICME magnetic field at 1 AU in order to forecast the severity of the associated geomagnetic storms. The advance prediction of the CME magnetic field at 1 AU requires the knowledge of near-Sun CME parameters which can be modeled from Sun to Earth based on the nature of evolution of the CME properties in heliosphere. Therefore, the understanding of CME source region characteristics as developed in Chapters 3 and 4, and the nature of CME evolution close to the Sun as explored in Chapter 5, sets the basis to initiate the development of a model in order to forecast the strength and orientation of CME magnetic field at 1 AU. Using the near-Sun CME properties as initial inputs, in this chapter we develop an observationally constrained analytical model for predicting the magnetic-field vectors of ICMEs.

Several modeling efforts have been made earlier in order to predict Bz at 1 AU (Odstrčil & Pizzo, 1999; Shen et al., 2014; Savani et al., 2015; Jin et al., 2017; Kay & Gopalswamy, 2017; Möstl et al., 2018). However, due to the complexity of the Sun-Earth system in a time-dependent heliospheric context, the semi-analytical and global MHD models are usually unable to reproduce the strength and orientation of the magnetic field vectors observed by the in-situ spacecraft (review by Manchester et al. 2017). The FR from Eruption Data (FRED) technique developed by Gopalswamy et al. (2018a) is useful to obtain the magnetic properties of the near-Sun coronal FRs from the photospheric magnetic flux under post eruption arcades and the geometric properties of the FR obtained from the fitting of white-light coronagraphic structures (Gopalswamy et al., 2018b). In this chapter, we report on the development of an analytical model, the INterplanetary Flux ROpe Simulator (INFROS), that utilizes FRED parameters as realistic inputs and evolves those parameters in real time to predict the magnetic field vectors of ICMEs reaching at Earth.

Apart from using the realistic inputs, we have formulated a new approach in our model to incorporate the expanding nature and the time-varying axial magnetic field-strength of the FR during its passage over the spacecraft. In contrast to the existing models (Savani et al., 2015; Kay & Gopalswamy, 2017; Möstl et al., 2018) our approach is unique in that it does not involve any free parameters e.g. the dimension, axial field strength, time of passage and the speed of ICME at 1 AU. Therefore, INFROS is the first such model which uses the realistic inputs to predict the magnetic field vectors of ICMEs without involving any free parameters.

In principle, INFROS can be used to estimate the magnetic field vectors of ICMEs at any heliocentric distance. Importantly, the prediction of magnetic field vectors of Earth-reaching ICMEs at 1 AU is crucial for space-weather forecasting. Therefore, in the following discussions we have considered this heliocentric distance as 1 AU for explaining the formulation of the model.

We have organized this chapter as follows. The observational reconstruction techniques to obtain the near-Sun FR parameters are discussed in Section 6.2. In Section 6.3, we have described the model architecture developed to predict the ICME vector profiles at 1 AU. We validate INFROS model for an observational event discussed in Section 6.4. Finally, we summarize our results and discuss their implications for space-weather forecasting in Section 6.5.

6.2 Near-Sun Observations of Flux Rope Properties

We determine the geometric and magnetic properties of the near-Sun FRs using the FRED technique as described in this section.

6.2.1 Geometrical properties

We determine the three-dimensional morphology and the propagation direction of CMEs by using the graduated cylindrical shell (GCS) (Thernisien, 2011) model. This is an empirical model to represent the three dimensional (3D) large-scale structure of flux-rope-like CMEs. This model considers conical legs and pseudo-circular front with circular cross section which result in a “hollow croissant” like shape to represent the CME morphology. Figures 6.1 (a) and (b) show a face-on and an edge-on representation of the model respectively. One of the important assumptions of this model is that the GCS structure expands in a self-similar way.

The GCS model fitting requires at least two different vantage point observations to reconstruct the 3D morphology of CMEs. Therefore, we have used simultaneous multiple vantage point observations of CMEs as obtained from the

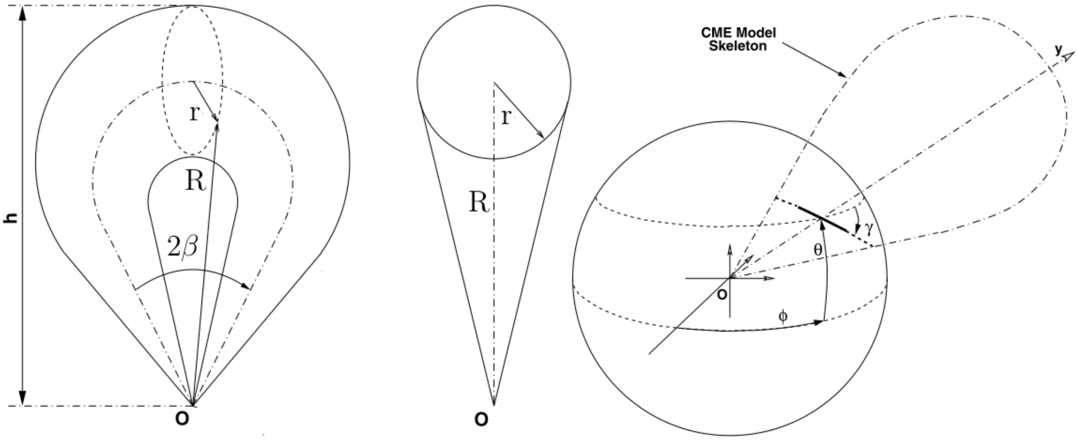

(a) (b) (c)

Figure 6.1: The face-on (a) and edge-on (b) views of Graduated Cylindrical Shell (GCS) model are shown with several positioning parameters (c). The face-on angular width is represented by 2β, the leading edge height is shown as h and the aspect ratio (κ) is defined as $\kappa = r/R$. The dash-dotted loop in panel (c) represents the axis through the center of the cylindrical shell and the solid line represents a planar cut through the shell. The ϕ and θ are the longitude and latitude of the axis of symmetry of the model respectively, and γ is the tilt angle around that axis (adapted from Thernisien et al. 2009 with few changes made in the notations to represent the different parameters of the model)

white-light coronagraphs such as C2 and C3 in the LASCO, and COR1 and COR2 in STEREO A & B to apply the GCS model. The GCS fitting tool involves adjusting six free parameters i.e. the propagation longitude (ϕ) and latitude (θ), half-angular width (β), aspect ratio (κ), tilt angle (γ) with respect to the solar equator and the leading-edge height (h) of the CME so that the resulting GCS structure matches well with the observed morphology of the CME FR. The best fit aforementioned six parameters obtained from the model fitting, are then used to study the 3D morphology, position, and kinematics of CMEs,

The parameter κ constrains the rate of expansion of the CME FR under the assumption of self-similar expansion. Therefore, the cross-sectional radius (r) of the self-similarly expanding FR at any heliocentric distance R ($= h - r$), can be obtained using the relation, r= κh/(1+κ). On the other hand, the length (L) of the flux-rope can be estimated from the relation, $L = 2\beta R$, where 2β is the separation angle between the two legs of the CME in radian.

6.2.2 Magnetic properties

Based on the formulation provided by previous works, the observational approaches to determine the three magnetic parameters which completely define any force-free FR are discussed as follows.

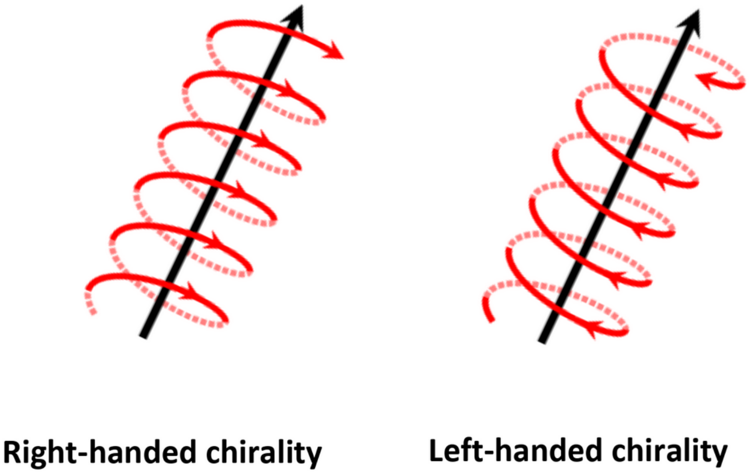

Figure 6.2: A schematic picture that shows two flux ropes (FRs) with different chirality. The FR shown in left panel follows the right handed chirality and the FR shown in left panel follows the left handed chirality. The black arrow along the FR axis shows the direction of axial magnetic field of the FRs (regenerated from Palmerio et al. (2018)).

6.2.2.1 Chirality and the direction of axial magnetic field of the flux rope

Chirality:

In order to determine the helicity sign (chirality) associated with the FR, we first apply the hemispheric helicity rule to the source active region of the CME as first order approximation (Pevtsov et al., 1995; Bothmer & Schwenn, 1998). However, the statistical studies by Liu et al. (2014) show that the hemispheric rule is followed only in 60% of cases. Therefore, in order to confirm the chirality of the FRs we use other signatures such as pre-flare sigmoidal structures (Rust & Kumar, 1996), J-shaped flare ribbons (Janvier et al., 2014), coronal dimmings (Webb et al., 2000; Thompson et al., 2000; Gopalswamy et al., 2018c), coronal cells (Sheeley et al., 1980) or filament orientations (Hanaoka & Sakurai, 2017). Analyzing the locations of the two core dimming regions or the two ends of the pre-flare sigmoidal structure, one can identify the locations of the two foot points of the FR. Thereafter, the locations of the FR foot points can be overlaid on the line-of-sight magnetogram to determine in which magnetic polarities the FR is rooted (Palmerio et al., 2017). Once the direction of the axial field is determined, one can confirm the helicity sign (chirality) from the positive and negative polarities that are divided by the neutral line (Bothmer & Schwenn, 1998; Marubashi et al., 2015; Gopalswamy et al., 2018a).

Direction of axial magnetic field:

The orientation of the flux rope as obtained from the analysis of coronal dimming regions gives the on-disk estimation of the direction of the axial field. However, CMEs may undergo rotation in the lower corona depending on the amount of sigmoidality or the skew present in the associated pre-eruptive FR structure (Lynch et al., 2009). Therefore, one can get mismatch between the FR orientation determined from the on-disk observations and the tilt angle of the CME obtained from the GCS fitting. Moreover, considering an uncertainty of ± 20° in determining the on-disk axis orientation (Palmerio et al., 2018) and ± 10° in determining the GCS tilt angle (Thernisien et al., 2009), one may obtain difference in angle upto ± 30° between the GCS tilt and the on-disk axis orientation, in absence of any significant rotation of the associated CME. Therefore, in order to resolve the 180° ambiguity in determining the FR axis orientation from the GCS tilt, we consider the smallest angle ($< 180°$) between the on-disk and the GCS axis orientation. In this way we can determine the direction of axial magnetic field of the CME observed in coronagraphic field-of-view.

6.2.2.2 Axial field strength (B_0)

Several studies have shown that the azimuthal (poloidal) flux of magnetic FRs formed due to the reconnection is approximately equal to the low-coronal reconnection flux (Figure 6.3), which can be obtained either from the photospheric magnetic flux underlying the area swept out by the flare ribbons (Longcope et al., 2007; Qiu et al., 2007) or the magnetic flux underlying the post eruption arcades

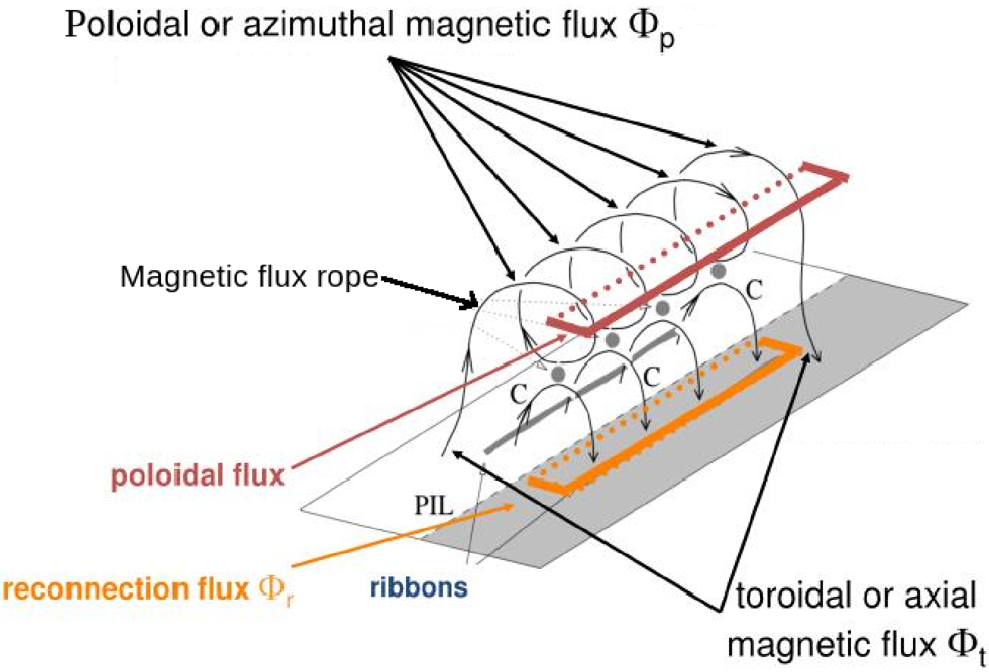
Poloidal or azimuthal magnetic flux Φ_p
Magnetic flux rope
C
C
C
poloidal flux
PIL
reconnection flux Φ_r
ribbons
toroidal or axial magnetic flux Φ_t

Figure 6.3: A schematic picture that shows the formation of a magnetic flux rope (the helical field line as indicated by a black arrow) and underlying post arcade loops (denoted by C) as a result of magnetic reconnection. The amount of magnetic flux passing through the red rectangular area contributes to the poloidal flux (ϕ_p) of the flux rope, which can be equated to the magnetic flux enclosed in the yellow rectangular region, known as the reconnection flux (ϕ_r) (adapted from Longcope et al., 2007).

(Gopalswamy et al., 2017). Combining the geometrical parameters of the FR obtained from the GCS fitting as discussed in Section 6.2.1 with the estimation of reconnected magnetic flux, Gopalswamy et al. (2018b) introduced the FRED model which shows that the axial magnetic-field strength of the FR can be determined using a constant alpha force-free FR model (Lundquist, 1950). Thereby, we obtain the magnetic field strength (B_0) along the FR axis using the relation (Gopalswamy et al., 2018a,b),

$$B_0 = \frac{\phi_p x_{01}}{Lr} \tag{6.1}$$

where ϕ_p is the azimuthal magnetic flux taken as the reconnection flux, x_{01} (= 2.4048) is the first zero of the Bessel function J_0, L is the length and r is the cross-sectional radius of the FR.

6.3 Development of INFROS Model to Estimate the Magnetic Field Vectors of ICMEs

We track the evolution of the near-Sun FR properties using the analytical model (INFROS) and estimate the magnetic field vectors of the associated interplanetary FRs known as the magnetic clouds (MCs). Notably, the MCs are a subset of ICMEs which show enhanced magnetic fields with a smooth rotation in the direction of field vectors, and low proton temperature during its passage over the in-situ spacecraft (see Section 1.4.2.2). On the other hand, the ICMEs which

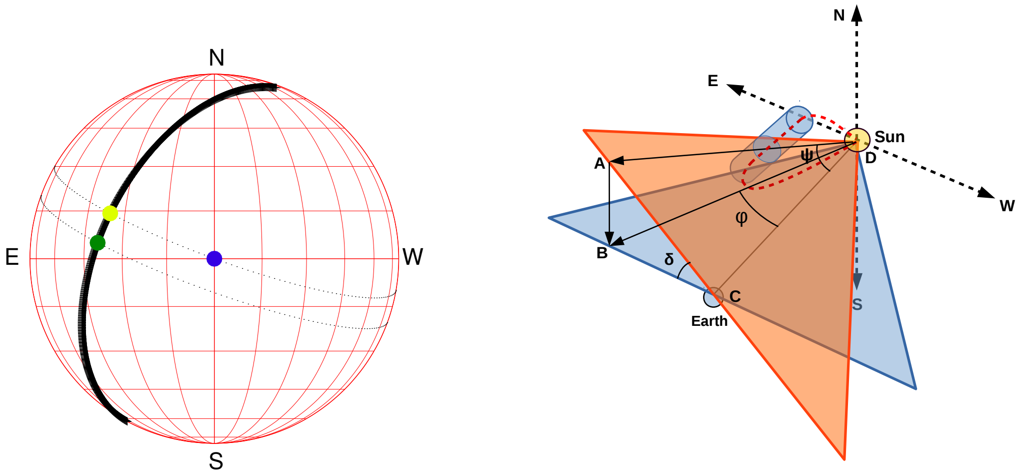

Figure 6.4: *Left panel*: The black solid line denotes the projected CME axis on the solar disc. Solar grids are shown in red with 15° intervals in both longitude and latitude. The projected location of Earth is indicated by the blue dot; the green dot marks the center of the CME axis. The yellow dot marks the location on the CME axis which is intersected by the black dotted line connecting the blue dot and perpendicular to the CME axis. *Right panel*: Schematic picture of an MC propagating through the interplanetary space in between the Sun and Earth. The red dashed line indicates the axis of the MC. Locations of the Sun and Earth are indicated by the points D and C respectively. The blue plane depicts the ecliptic plane, whereas the orange one is perpendicular to the MC axis and passes through the Sun-Earth line (CD). The MC axis is tilted by an angle γ with respect to the ecliptic plane. Therefore, the plane (orange) perpendicular to the MC axis makes an angle $\delta(= 90^o - \gamma)$ with respect to the ecliptic plane (blue). The line connecting A and D lies on the orange plane and intersects the MC axis along the longitudinal direction ϕ (longitude of the yellow dot marked in the right panel) with respect to the Sun-Earth line. BD is the projection of line AD on the ecliptic plane (blue). The angle (ψ) between AD and CD, denotes the separation angle between the MC axis and the Sun-Earth line.

lack the MC signatures in their in-situ profile are known as non-cloud ejecta (Rouillard, 2011). The internal magnetic field structure of those ICMEs does not resemble that of a magnetic FR. However, it is important to note that all ICMEs may have the FR structures, but their in-situ observations may lack that coherent magnetic structure depending on the path of the observing spacecraft (Kim et al., 2013; Gopalswamy, 2006). Therefore, similar to the existing semi-analytical and analytical models (Savani et al., 2015; Kay & Gopalswamy, 2017; Möstl et al., 2018), INFROS is applicable for all ICMEs in general, but can be validated only for those ICME events which show MC signatures in their in-situ profile.

As significant deflection and rotation of CMEs generally occur very close (less than 10 $R_\odot$) to the Sun (Kay & Opher, 2015; Lynch et al., 2009), we assume that the propagation direction and the axis-orientation of the CME obtained from the GCS fitting at approximately 10 $R_\odot$ are maintained throughout its evolution from the Sun to Earth. We also do not consider any CME-CME interaction in the interplanetary space which may change the propagation trajectory of the CME. Assuming that the CMEs expand in a self-similar manner (Subramanian et al., 2014; Good et al., 2019; Vršnak et al., 2019) during its interplanetary propagation, we estimate the geometrical parameters of the CME upon its arrival at 1 AU. Using the conservation principle of the magnetic flux and helicity, we determine the magnetic properties of the FR when it is intersected by the spacecraft at 1 AU. Finally, incorporating those estimated geometrical and magnetic parameters of the FR in a constant alpha force-free FR solution (Lundquist, 1950) we estimate the expected magnetic vector profiles of Earth-impacting ICMEs. The detailed description of the INFROS model is as follows.

6.3.1 Estimating the impact distance

In order to estimate which part of the ICME will be intersected by the observing spacecraft at 1 AU, it is important to first determine the impact distance that is the closest distance between the MC axis and the location of the spacecraft.

According to the geometry illustrated in Figure 6.4, we can write

$$BC = R_{SE} \times tan\phi \tag{6.2}$$

where, R_{SE} is the distance between Sun and Earth and ϕ is the longitudinal direction of the line DA. As the plane perpendicular to the MC axis is tilted by an angle δ, we can further write

$$AC = \frac{BC}{cos\delta} = R_{SE} \times \frac{tan\phi}{cos\delta} \tag{6.3}$$

Using the value of AC from Equation 6.3, we can obtain the minimum separation angle ψ between the axis of the MC and the Sun-Earth line using the following relation

$$tan\psi = \frac{AC}{R_{SE}} = \frac{tan\phi}{cos\delta} \tag{6.4}$$

After determining the value of ψ, the impact distance (d) of the MC at any heliocentric distance (R) along the Sun-Earth line can be obtained using the following equation

$$d = R \times sin\psi = R \times sin(tan^{-1}\frac{tan\phi}{cos\delta}) \tag{6.5}$$

6.3.2 Cross-sectional radius of the flux rope when the spacecraft just encounters the arrival of MC

In order to infer the axial field-strength of the MC from the conservation of magnetic flux, we need to estimate its cross-sectional area during its passage over the spacecraft. Figure 6.5 depicts a schematic picture of an MC cross-section when the spacecraft just encounters its arrival. According to the geometry as illustrated in Figure 6.5, we can write

$$R_c \times cos\psi + \sqrt{R_i^2 - {R_c}^2 \times sin^2\psi} = R_{SE} \tag{6.6}$$

where, R$_C$ is the radial distance of the MC axis from the Sun-center, ψ is the separation angle between the MC axis and the Sun-Earth line and R$_i$ is the

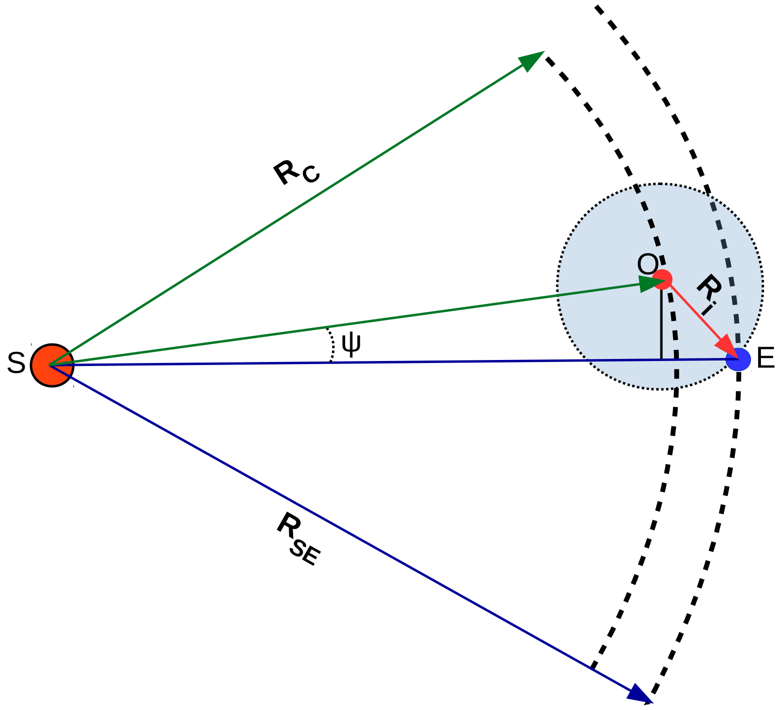

Figure 6.5: Schematic picture of the MC cross-section on the plane (the orange plane as depicted in Figure 6.4) perpendicular to the MC axis. The MC axis is pointing out of the plane at point O. The angle ψ denotes the separation angle between the MC axis and the Sun-Earth line. R_C is the radial distance of the MC axis from the Sun-center and R_i is the radius of cross-section when the spacecraft just encounters the arrival of MC

radius of cross-section of the MC. Assuming that the CME has evolved self-similarly between Sun and Earth, we can replace R_c in Equation 6.6 using the relation $R_i = \kappa R_c$, where κ is the aspect ratio of the CME FR obtained from the observations as discussed in 6.2.1. Thereby, we can estimate the initial radius of the FR cross-section upon its arrival at Earth using the following equation

$$R_i = \frac{\kappa \times R_{SE}}{cos\psi + \sqrt{\kappa^2 - sin^2\psi}} \tag{6.7}$$

For, ψ=0, Equation 6.7 reduces to Equation 6.8, which is the scenario when the spacecraft passes through the center of the FR cross-section.

$$R_i = \frac{\kappa \times R_{SE}}{1 + \kappa} \tag{6.8}$$

6.3.3 Self-similar approach to incorporate the flux rope expansion during its passage through the spacecraft

Figure 6.6 depicts the spacecraft trajectory inside the MC which is assumed to expand isotropically with expansion speed V_{exp}. The MC axis propagates with a speed V_{pro} along the direction depicted by the black arrows in Figure 6.6. Therefore, in the FR frame of reference, the spacecraft traverses from the point A (lies on the front-boundary of the MC) to the point B (lies on the rear boundary of the MC) with a speed V_{pro}. If t_p is the travel time for the spacecraft to complete the path AB, we can write

$$\sqrt{R_i^2 - d^2} + \sqrt{R_f^2 - d^2} = v_{pro} \times t_p \tag{6.9}$$

where, R_i and R_f are the cross-sectional radius of the front and rear boundary

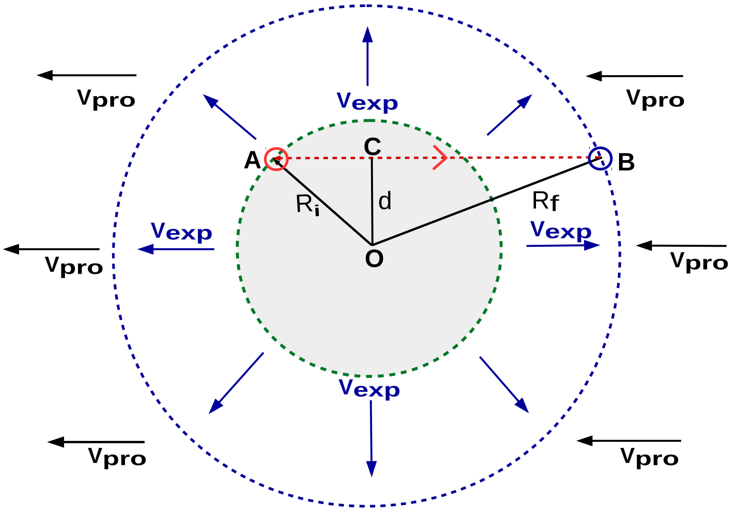

Figure 6.6: Schematic picture of the cross-section of an expanding FR as it passes over the spacecraft with a propagation speed V_{pro} and expansion speed V_{exp}. The black arrows denote the direction of the MC propagation, whereas the blue arrows represent the isotropic expansion of the MC. The spacecraft intersects the MC at an impact distance “d” denoted by OC. The gray shaded region encircled by the green dashed line denotes the initial boundary of the FR with cross-sectional radius R_i when the spacecraft just encounters the arrival of MC at point A marked by the red circle. The red dotted line illustrates the trajectory of the spacecraft from A to B inside the expanding MC. R_f is the final radius of the MC cross-section encircled by the blue dashed line when the spacecraft encounters the end-boundary of the MC.

of the MC respectively and 'd' is the impact distance of the spacecraft from the MC axis. By the time (t_p) the spacecraft traversed the path AB, the cross-sectional radius of the MC increased from R_i to R_f with the expansion speed V_{pro}. Therefore, we can write

$$R_f - R_i = v_{exp} \times t_p \tag{6.10}$$

Considering a general case, where the MC axis takes t_{travel} time to traverse a distance R_{tip} with a speed v_{pro}, we can write

$$R_{tip} = v_{pro} \times t_{travel} \tag{6.11}$$

During the time t_{travel}, as the cross-sectional area of the MC also expands with a speed v_{exp}, the final radius of the MC cross-section after t_{travel} can be written as

$$R_{cross} = v_{exp} \times t_{travel} \tag{6.12}$$

Using the properties of self-similar expansion, R_{cross} and R_{tip} can be related as $R_{cross} = \kappa R_{tip}$. Therefore, using the Equations 6.11 and 6.12, we can relate v_{pro} and v_{exp} through the following relation

$$\frac{R_{cross}}{R_{tip}} = \frac{v_{exp}}{v_{pro}} = \kappa \tag{6.13}$$

Using the Equations 6.9, 6.10 and 6.13, we can write

$$\frac{R_f - R_i}{\sqrt{R_i^2 - d^2} + \sqrt{R_f^2 - d^2}} = \frac{v_{exp}}{v_{pro}} = \kappa \tag{6.14}$$

In Equation 6.14, R_i, d and κ are the known parameters. R_i is obtained from Equation 6.7, impact distance 'd' is obtained from the Equation 6.5 and the value of κ is obtained from the observations as discussed in the Section 6.2.1. Rewriting the Equation 6.14, we get the following quadratic equation of R_f

$$R_f^2 + b \times R_f + c = 0. \tag{6.15}$$

where,

$$b = \frac{2 \times (R_i + \kappa \times \sqrt{R_i^2 - d^2})}{\kappa^2 - 1}$$

$$c = \frac{(R_i + \kappa \times \sqrt{R_i^2 - d^2}\ )^2 - d^2 \times \kappa^2}{1 - \kappa^2}$$

Therefore, solving the Equation 6.15 we can estimate the final radius (R_f) of the expanding FR when the spacecraft encounters the rear-boundary of the MC. After estimating R_i (initial radius of the MC front-boundary), R_f (final radius of the MC rear-boundary) and 'd' (impact distance), we can estimate the path AB as depicted in Figure 6.6. In order to capture the full expansion profile of the MC, next we need to determine the cross-sectional radius of the expanding FR at any distance x traversed by the spacecraft throughout the path AB (Figure 6.6). Let us consider, at any time t ($0 \leq t \leq t_p$) the SC traverses a distance x with a speed v_{pro} along AB in the frame of reference attached to the MC axis. Therefore we can write,

$$x = v_{pro} \times t \tag{6.16}$$

During the time t, the cross-sectional radius of the FR increases from R_i to R_t with a speed v_{exp}. Therefore we can write

$$R_t - R_i = v_{exp} \times t \tag{6.17}$$

Using the Equations 6.14, 6.16 and 6.17, we can further write

$$\frac{R_t - R_i}{x} = \frac{v_{exp}}{v_{pro}} = \kappa \tag{6.18}$$

Rewriting the Equation 6.18 we get

$$R_t = R_i + \kappa \times x \tag{6.19}$$

Therefore at any distance x along the path AB (Figure 6.6), we can estimate the cross-sectional radius ($R_i \leq R_t \leq R_f$) of the expanding FR using the Equation 6.19. It is noteworthy that we have started our formulation with the unknown parameters V_{exp}, V_{pro} and t_p (see Equations 6.9 and 6.10) and finally arrived to the Equations 6.15 and 6.18, which are independent of the aforementioned variables. This is the major advantage of this formulation as we have incorporated the FR expansion in such a way so as to get rid of the free or unknown parameters like the expansion speed (V_{exp}), propagation speed (V_{pro}) and the time of passage (t_p) of the ICMEs at 1 AU.

6.3.4 Estimating the final magnetic field profiles of the MC at 1 AU using a cylindrical flux rope solution

It is expected that the FR axial field strength (B_0) will decrease as the length ($L = \frac{2\beta}{\kappa} r$) and cross-sectional radius (r) of the FR will increase during its expansion and propagation throughout the interplanetary space (see the expression of B_0 in Equation 6.1). Assuming that the angular width (2β) of the CME remains constant throughout its propagation and the nature of expansion is self-similar, we can consider that $L \propto r$. Further, neglecting the effect of magnetic erosion or any addition of magnetic flux due to the interaction with the interplanetary magnetic field (IMF), we can assume that the magnetic flux inside the flux rope will be conserved. Therefore, considering $\phi_p = constant$, the axial magnetic field-strength (B_0) of any FR having a cross-sectional radius r will follow the relation

$$B_0 \propto \frac{1}{r^2} \tag{6.20}$$

Thereby, knowing the cross-sectional radius R_t ($R_i \leq R_t \leq R_f$) of the FR during its passage through the spacecraft using the Equation 6.19, we can estimate its axial field-strength (B_t) at any time t ($0 \leq t \leq t_p$) using the following relation

$$B_t = B_{0_{CME}} \times \frac{{r_{CME}}^2}{{R_t}^2} \tag{6.21}$$

where, r_{CME} is the cross-sectional radius and $B_{0_{CME}}$ is the axial magnetic-field strength of the near-Sun FR obtained from the observations as discussed in Section 3.1.

As the spacecraft intersects the MC along the path AB (see Figure 6.6), at any location (x) along AB the magnetic field vectors of the FR can be obtained using a cylindrical flux rope solution (Lundquist 1950) in a local cylindrical coordinate (r, ϕ, z) attached to the MC axis. The magnetic vectors in the aforementioned (r, ϕ, z) coordinate system will be

$$B_r = 0 \tag{6.22}$$

$$B_\phi = H \times B_t \times J_1(\alpha r) \tag{6.23}$$

$$B_z = B_t \times J_0(\alpha r) \tag{6.24}$$

where, H=±1 is the handedness or sign of the helicity which is same as that of the near-Sun FRs according to the conservation of helicity rule, α is the constant force-free factor, and J_0 and J_1 are the Bessel functions of order 0 and 1, respectively. The boundary of the FR is located at the first zero of J_0, which leads to $\alpha = \frac{2.41}{R_t}$ and R_t is therefore the radius of the flux rope. B_t and R_t evolve according to the relation described in Equations 6.21 and 6.19 respectively.

As we have assumed that after 10 $R_\odot$ the CME does not suffer any significant rotation and deflection, therefore the final elevation angle (θ) of the MC axis at 1 AU should follow the tilt angle (δ) of the CME and the azimuthal angle of the MC should follow the propagation longitude (ϕ) of the CME obtained from the GCS fitting as discussed in Section 6.2.1. In order to get the final magnetic field vectors in Geocentric Solar Ecliptic (GSE) coordinate system (Hapgood, 1992), we first transform the B_r, B_θ and B_ϕ from the local cylindrical coordinate (r, θ, z) to the local cartesian coordinate $(x^{'}, y^{'}, z^{'})$ attached to the MC axis. Thereafter, knowing the azimuthal (ϕ) and elevation (θ) angle of the MC axis we transform the magnetic vectors $B_{x^{'}}, B_{y^{'}}$ and $B_{z^{'}}$ from the local cartesian coordinate $(x^{'}, y^{'}, z^{'})$ to the GSE coordinate system (x, y, z). Thus, we get the predicted magnetic vectors B_x, B_y and B_z of the ICME to be detected by the spacecraft at 1 AU.

6.4 Validation of INFROS Model for the CME Event on 2013 April 11

As a proof of concept we validate our model (INFROS) for an Earth-directed CME which erupted from the Sun on 2013 April 11 at around 06:50 UT. The CME was associated with an M6.6 class solar flare (Cohen et al., 2014; Lario et al., 2014; Vemareddy & Zhang, 2014; Vemareddy & Mishra, 2015; Joshi et al., 2016; Fulara et al., 2019) that occurred in the active region AR 11719. Its arrival at the L1 point was detected with the signature of a shock arrival on 2013 April 13 at 22:54 UT, FR leading edge on 2013 April 14 at 17:00 UT and a trailing edge on 2013 April 15 at 19:30 UT. The smooth variation and rotation in its in-situ magnetic field profile along with the low proton temperature hold the characteristic signatures of an MC (Burlaga, 1988). Moreover, the CME did not exhibit any interaction with other CMEs and evolved as an isolated magnetic structure from the Sun to Earth. Therefore, the basic assumptions made in our model hold good for this case study. Notably, we do not consider any addition or reduction of magnetic flux inside the CME due to its interaction with the IMF, which may effect the model results if such effects were present in this event.

The evolution of the flare ribbons and the formation of post eruption arcades (PEAs) associated with the M6.6 class flare (see Figure 6.7) were well observed by the AIA and HMI onboard SDO (Pesnell et al., 2012). Furthermore, the multi-vantage point observations from STEREO-A, STEREO-B and LASCO were suitable to reconstruct the 3D morphology of the associated CME. Therefore, we are able to determine all the near-Sun FR properties of the CME in order to use those as realistic inputs for INFROS model.

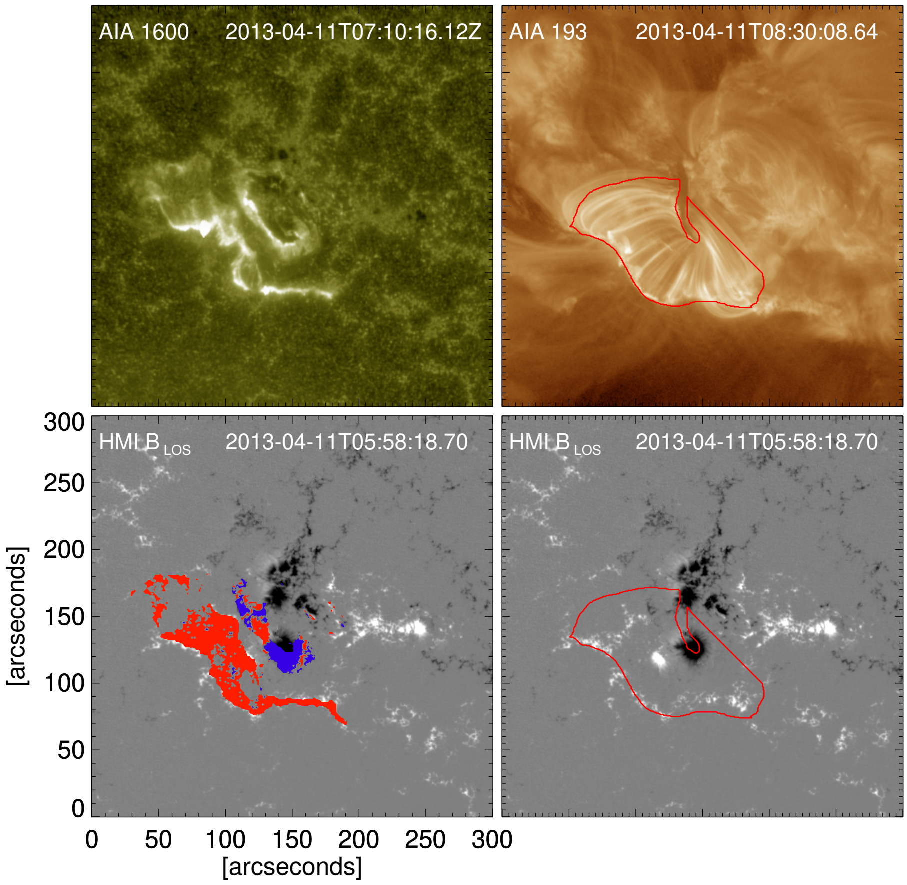

Figure 6.7: Upper-left panel depicts the flare ribbon in AIA 1600 Å image. The red boundary line in upper-right panel marks the post eruption arcades (PEAs) in AIA 193 Å image. Lower-left and lower-right panel illustrate the HMI line-of-sight magnetic field. The red and blue regions in lower-right panel depict the cumulative flare ribbon area overlying the positive and negative magnetic field respectively. The red boundary in lower-right panel is the over-plotted PEA region.

6.4.1 Inputs to INFROS model for the CME event on 2013 April 11

6.4.1.1 Poloidal flux content of the flux-rope

We calculate the flare associated reconnection flux by applying both the methods (Longcope et al., 2007; Qiu et al., 2007; Gopalswamy et al., 2017) as described in Section 6.2.2.2. The red and blue regions in the lower left panel of Figure 6.7 show the cumulative flare ribbon area overlying the positive and negative polarities of photospheric magnetic field respectively. The average of the absolute values of positive and negative magnetic fluxes underlying the cumulative flare ribbon area yield the value of reconnection flux as 1.9×10^{21} Mx. Taking into account the formation-height of the flare ribbons, we have incorporated a 20% correction (Qiu et al., 2007) in the estimation of reconnection flux in order to avoid over-estimation. The half of the total unsigned magnetic flux underlying the PEA (the region enclosed by the red boundary as shown in upper-left and lower-left panels of Figure 6.7) yield the value of reconnection flux as 2.3×10^{21} Mx. In order to determine the magnetic properties of the associated CME we equate the poloidal flux content of the FR to the average value (2.1×10^{21} Mx) of the reconnection fluxes obtained from the aforementioned two methods.

6.4.1.2 Chirality and the direction of the axial-magnetic field of the flux-rope

The source location of the M6.6 flare that occurred in AR 11719, was associated with a pre-eruptive sigmoidal structure (Vemareddy & Mishra, 2015; Joshi et al., 2016). Panel (a) of Figure 6.8 shows the highly skewed pre-flare sigmoid observed in EUV images of AIA passbands (94 Å, 335 Å and 193 Å). The observed inverse S-shaped morphology of the sigmoidal structure (indicated by the red dashed line) has been overlaid on the HMI line-of-sight magnetogram (panel (b) of Figure 6.8), which reveals the left handed chirality of the associated flux-rope. This follows the hemispheric helicity rule (Bothmer & Schwenn, 1998) as the source region of the CME was located in the northern solar hemisphere.

We identify the two boundaries as shown by the blue and green dashed lines in panel (a) of Figure 6.8, where the two ends of the bundle of sigmoidal field lines are rooted during the pre-eruptive phase. The two aforementioned boundaries are overlaid on the HMI line-of-sight magnetic field and the regions are marked by the yellow ellipses (see panel (b)). The simple connectivity (without considering any twist) between the two opposite magnetic polarities underlying the regions marked by the yellow ellipses suggests the north-west direction (as shown by the yellow arrow) as the axial orientation of the FR at higher heights in the corona (above $\approx 5\ R_{\odot}$). This is expected as the apex-orientation of the left-handed FR should rotate in counter-clockwise direction to release the axial twist or writhe

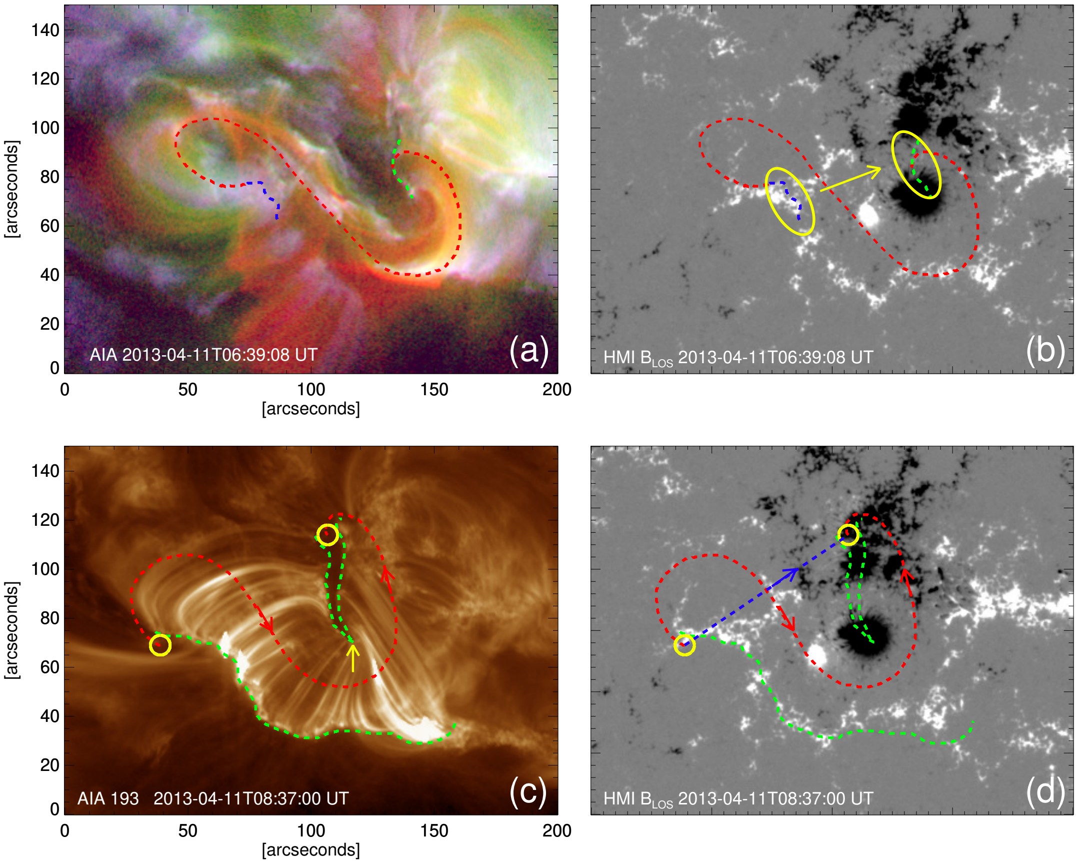
140
120
100
80
60
40
20
0
[arcseconds]
AIA 2013-04-11T06:39:08 UT
(a)
0
50
100
150
200
[arcseconds]
HMI B_{LOS} 2013-04-11T06:39:08 UT
(b)
AIA 193 2013-04-11T08:37:00 UT
(c)
HMI B_{LOS} 2013-04-11T08:37:00 UT
(d)

Figure 6.8: The pre-flare sigmoidal structure observed in the composite images constructed from the AIA 94 Å (red), 335 Å (green) and 193 Å (blue) passband observations (a). The associated HMI line-of-sight magnetic field plotted in gray scale within saturation values ± 500 G (b). The red dashed line (plotted in panel (a)) that approximately resembles the sigmoidal structure has been overlaid on the HMI line-of-sight magnetic field in panel (b). The blue and green dashed lines in panel (a) approximately denote the boundaries where the two ends of the bundle of sigmoidal field lines are rooted. The same blue and green dashed lines are overlaid in panel (b). The post-eruption arcades (PEAs) observed in AIA 193 Å passbands (c) and the associated HMI line-of-sight magnetic field (d). The green-dashed lines in panel (c) mark the two side boundaries of the PEA and the same is overlaid in panel (d). The red dashed line is drawn along the approximate center of the two side boundaries of the PEA, connecting the two expected foot-point locations (shown by the yellow circles) of the erupting flux rope. The blue-dashed line connecting the flux rope foot-points and the blue-arrow in panel (d) indicate the north-west direction.

during its evolution in the lower corona below 5 $R_\odot$ (Lynch et al., 2009).

In order to confirm the axial orientation of the FR, we further investigate the morphology of the associated PEA formed during the flare. Panel (c) of Figure 6.8 shows that the eastern part of the PEA channel is tilted towards the

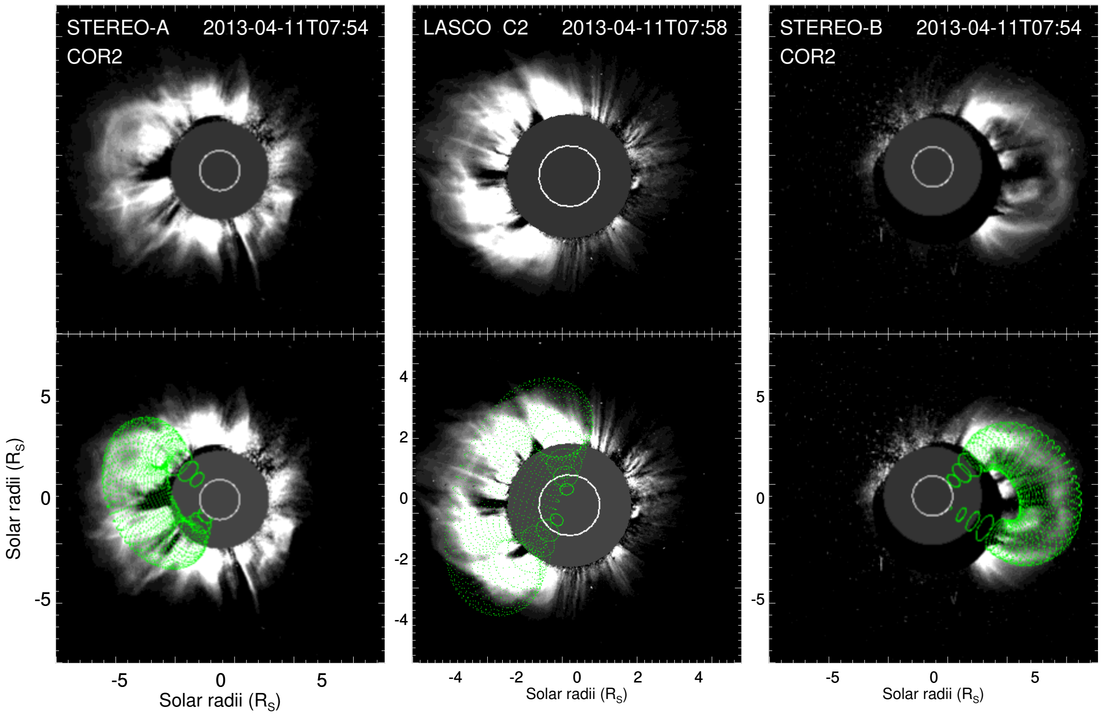

Figure 6.9: Top panels depict the CME morphology observed in COR2-A (top-left), LASCO C2 (top-middle), and COR2-B (top-right), respectively, at 07:54 UT on 2013 April 11. Bottom panels illustrate the overplot of the best-fitted wire frame (green dotted marks) of the FR using the GCS model.

south-west direction and further bends towards the north-west direction at the location indicated by the yellow arrow, forming a nearly U-shaped morphology. This is certainly a complex morphology which makes the event more complicated. Considering the apex orientation of the FR inferred only from the eastern part of the PEA channel, Palmerio et al. (2018) found contradiction between the estimated direction of the FR at Sun and at 1-AU. However, we have focused on the full U-shaped morphology of the PEA channel in this study. Considering the full extent of the PEAs allows us to analyze the FR structure beyond the sigmoidal pre-eruptive configuration and, therefore, to capture the complete evolution of the FR in the lower corona during the phase of sigmoid to arcade formation. According to the standard flare model in three dimension (Shibata et al., 1995; Moore et al., 2001; Priest & Forbes, 2002), the foot-points of the eruptive FRs are believed to be located on either side of the two ends of the PEA channel. Therefore, considering the left-handed chirality, we mark the expected locations of the two foot-points of the FR as shown by the yellow circles at the two ends of the U-shaped PEA channel. The red dashed curve connecting the two yellow circles indicates the possible writhe presented in the FR during the formation phase. This is in agreement with the observed writhing motion of that FR during the eruptive phase as reported by Joshi et al. (2016). Therefore, due to the writhing motion the FR would have relaxed the axial-twist during its evolution in the lower corona, resulting in an orientation following the straight connectivity (shown by the blue dashed line in panel (d) of Figure 6.8) between the two foot-point locations. In such a scenario, the magnetic polarities underlying the two yellow circles clearly indicates that the axial orientation of the FR is directed towards north-west.

From the GCS fitting (Figure 6.9) of the observed white-light morphology of the CME at $\approx$ 10 $R_\odot$, we estimate the tilt angle of the CME axis as $73 \pm 10^\circ$ with respect to the ecliptic plane. Minimizing the difference in angle between the GCS tilt and the axial direction (north-west) of the FR inferred from the on-disk observations, we obtain the axial magnetic-field direction of the CME FR at $\approx$ 10 $R_\odot$ along $73 \pm 10^\circ$, measured in counter-clockwise direction with respect to the solar equator. Assuming that no major rotation occurs after 10 $R_\odot$, we consider this axis orientation, as the final orientation of the associated MC axis at 1 AU.

6.4.1.3 Axial field-strength of the flux-rope

In order to estimate the axial field-strength of the near-Sun FR we first determine the geometrical parameters associated with it. The top panels of Figure 6.9 show the white-light morphology of the CME as observed in base difference images obtained from STEREO-A/B and LASCO. The GCS fitting (bottom panels of Figure 6.9) to the multi-vantage point observations of the CME yields the aspect ratio (κ) and the half-angular width (β) of the CME as 0.22 and 26° respectively. Therefore, the length ($L = 2\beta R$) of the associated FR at a radial distance (R) of 10 $R_\odot$ is estimated as approximately 9 $R_\odot$. Using Equation 6.1, we obtain the axial field-strength of the FR at 10 $R_\odot$ as 52 mG.

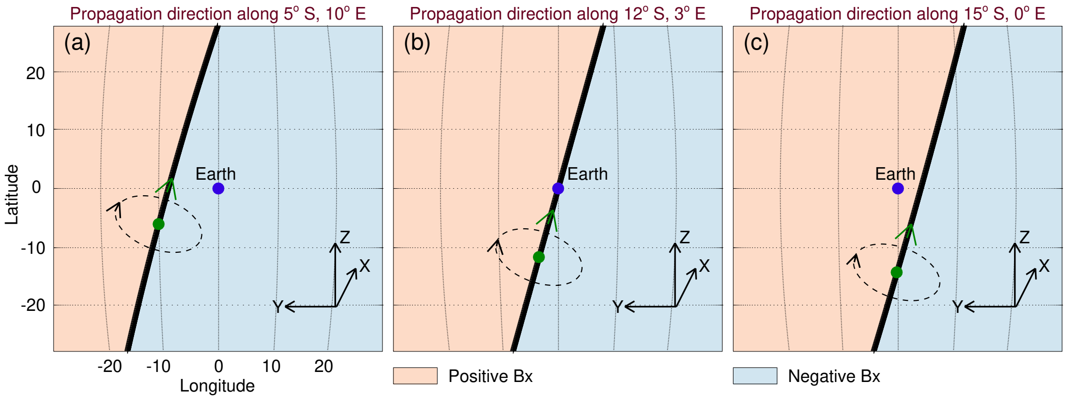

Figure 6.10: Location of Earth (blue dots) with respect to the magnetic axis (black solid lines) of the CME projected on the solar disk. The green dots in each panels show the three different propagation direction of the CME. The black and green arrows denote the direction of poloidal and axial magnetic field of the flux-rope respectively. Any virtual space-craft that resides at the left/right side of the magnetic axis (denoted by the pink and blue shaded region respectively) will encounter the B_x component of the flux-rope as positive/negative in GSE coordinate system.

6.4.1.4 Propagation direction of the CME

The GCS fitting (Figure 6.9) of CME morphology at $\approx$ 10 $R_\odot$ yields the propagation direction of the CME along S05E10. Taking into account an uncertainty of 10° in determining both the longitude and latitude of propagation direction, we have performed the GCS fitting several times and found the propagation direction of the CME to lie within the range $0 - 10°$ E and $5 - 15°$ S. Using the range of values of the propagation direction and the tilt angle ($73 \pm 10°$) of the CME as inputs, we estimate the impact distance of the CME magnetic axis at 1 AU within the range 0 to 21 $R_\odot$.

6.4.2 Sensitivity of the estimated magnetic vectors to the propagation direction and tilt angle of the CME

We notice that the sign of B_x component for the estimated magnetic vectors of the ICME as detected by any spacecraft aligned along Sun-Earth line is very sensitive to the propagation direction of the CME. The three panels in Figure 6.10 depict the location of Earth (denoted by blue dots) with respect to the magnetic axis (denoted by black solid lines) of the CME propagating along three different directions which are within the error limits as estimated in Section 6.4.1.4. In each of the three panels, the Sun-grids are shown within ± 30° longitude and latitude where the projected location of Earth on the solar disk resides at 0° longitude and 0° latitude. Keeping the tilt angle as 73° we project the magnetic axis of the CME on the solar disk as shown by the black solid lines in each panel. The green dots and arrows on the magnetic axis denote the propagation direction of the CME and the direction of axial magnetic field of the associated FR respectively. The arrows along the black dashed lines surrounding the CME magnetic-axis depict the direction of poloidal magnetic field according to the left-handed chirality of the associated FR.

Notably, at any projected location on the solar disk which lies on the left/right side of the CME axis, the direction of poloidal magnetic field will be towards/outwards the Sun. Accordingly, the sign of B_x will change at any location on the either side of the magnetic axis which we have shown by the pink and blue regions where B_x possesses positive and negative values respectively. Panel (a) in Figure 6.10 shows that the projected location of the Earth lies on the region of negative B_x for the estimated direction (10°E, 5°S) and tilt (73° with respect to the ecliptic plane) of the MC axis as obtained from GCS fitting. However, a small shift in the propagation direction from 10°E, 5°S to 3°E, 12°S results in a zero impact distance between the MC axis and the Sun-Earth line (see panel (b) in Figure 6.10) for which the estimated B_x component turns out to be zero. If we further shift the propagation direction of the MC axis from 3°E, 12°S to 0°E, 15°S within the error limits, the sign of B_x becomes positive as the location of Earth or any spacecraft aligned along Sun-Earth line lies on the left side of the MC axis where the direction of poloidal magnetic field is towards the Sun (see panel (b) in Figure 6.10). Therefore, our analysis shows that within the error limits of the propagation direction of the CME, B_x can have both positive and negative components in the estimated magnetic vectors of the ICME at 1 AU.

It is noteworthy that the above mentioned scenario is true for any tilt angle of the FR orientation where the propagation direction is very close to the Sun-

Earth line. Interestingly, the sign or the direction of variation (positive to negative or vice-versa) of the estimated B_y and B_z components are not sensitive to the small variations ($\pm 10°$) in the propagation direction and tilt angle of the CME. Therefore, we expect less uncertainty in the prediction of B_y and B_z components of the MC.

6.4.3 INFROS model outputs

Using the near-Sun FR properties of the associated CME as described in Section 6.4.1, we estimate the magnetic vectors of the ICME as intersected by the spacecraft at 1 AU. The curves shown by the black solid lines in Figure 6.11 depict the observed magnetic vectors of the ICME as detected by the WIND spacecraft (Ogilvie & Desch, 1997). We have used observations of the in situ magnetic field

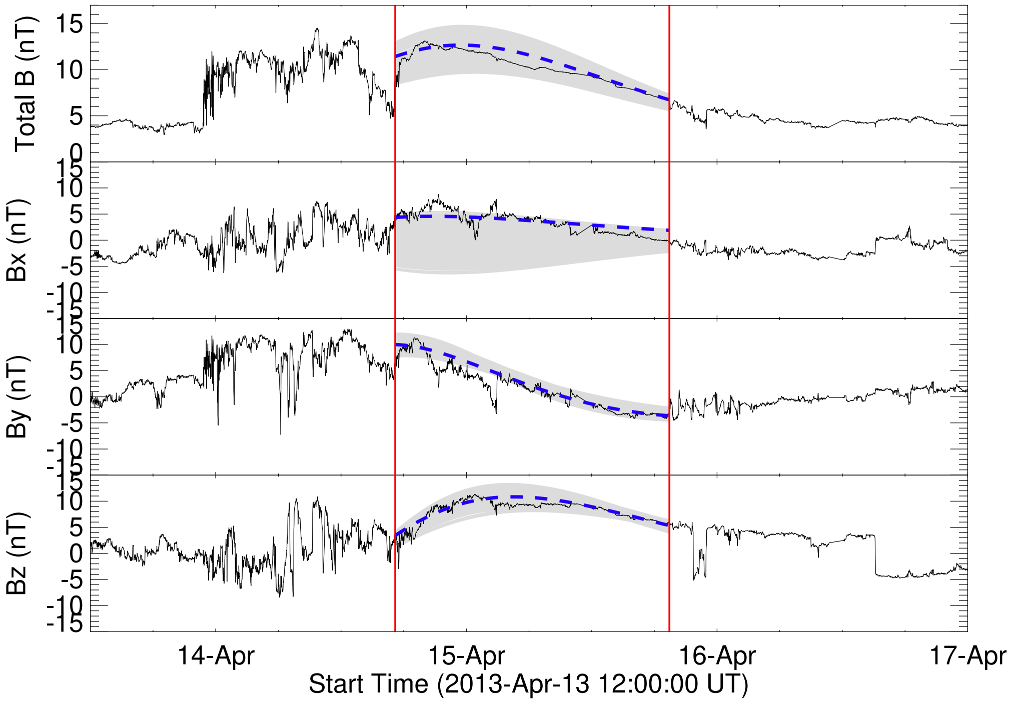

Figure 6.11: Magnetic vectors as detected by the WIND spacecraft for 2013 April 14 ICME event. The two red vertical lines denote the magnetic cloud boundary. The blue dashed lines denote the predicted magnetic vectors obtained from the model which best match the observed magnetic profiles of the MC. The gray shaded regions denote the uncertainty in predicting the respective magnetic vectors.

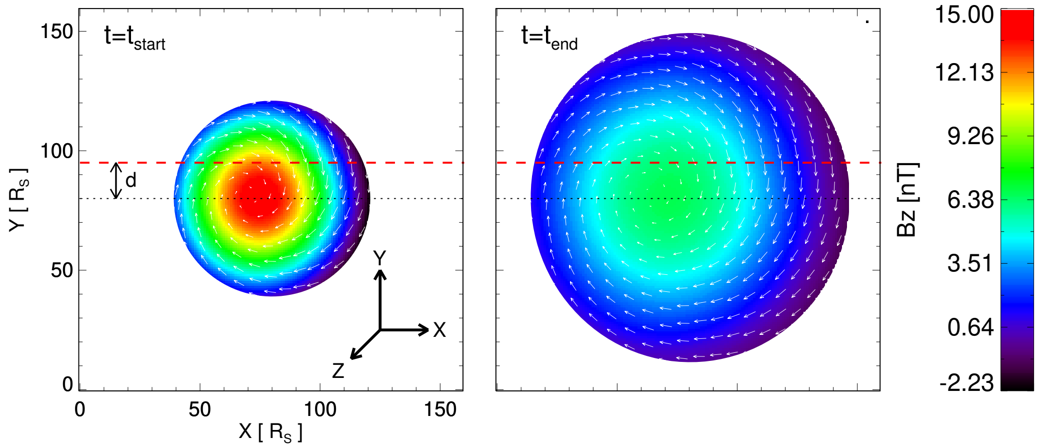

Figure 6.12: Left panel: Cross-section of the flux rope as viewed on the ecliptic plane when the spacecraft at 1 AU just encounters the arrival of the magnetic cloud (MC). Right panel: Cross-section of the expanded flux-rope when the spacecraft completes its passage through the magnetic cloud and reaches to the rear boundary of the MC at 1 AU. The color bar shows the strength of the southward component of magnetic magnetic field in GSE coordinate which is positive outwards the plane of the paper. The black dotted line passes through the axis of the flux-rope. The white arrows mark the direction of magnetic field component lies on the ecliptic plane inside the MC boundary. The red dashed line at a distance d (impact distance) from the black dotted line shows the spacecraft trajectory along which the MC is intersected by it at 1 AU.

vectors as well as the relevant plasma parameters and followed the criteria given by Burlaga (1988) to select the front and rear boundary of the MC as denoted by the red vertical lines in Figure 6.11.

Incorporating the uncertainties in the GCS parameters involved in the modeling, we generate all the possible input data-sets from the range of values of the input parameters, i.e. the propagation direction (0 – 10°E, 5 – 15°S), tilt-angle (63 – 83°) and aspect-ratio (0.20 – 0.24) of the CME. Further, considering an error of 2×10^{20} Mx (standard deviation of the two values of reconnection flux obtained from the two different methods as discussed in Section 6.4.1.1) in determining the poloidal flux and ± 0.02 in determining the CME aspect-ratio, we get 20% error in estimating the axial field strength ($B_{0_{CME}}$) of the CME. This yields the estimated range of $B_{0_{CME}}$ at 10 R$_\odot$ as 42 – 62 mG, with a mean value of 52 mG. This is consistent with the average value (52 mG) of the distribution of axial fields at 10 R$_\odot$ (Gopalswamy et al., 2018b). Using these sets of input data we run our model and generate synthetic magnetic profiles of the MC. Among these sets

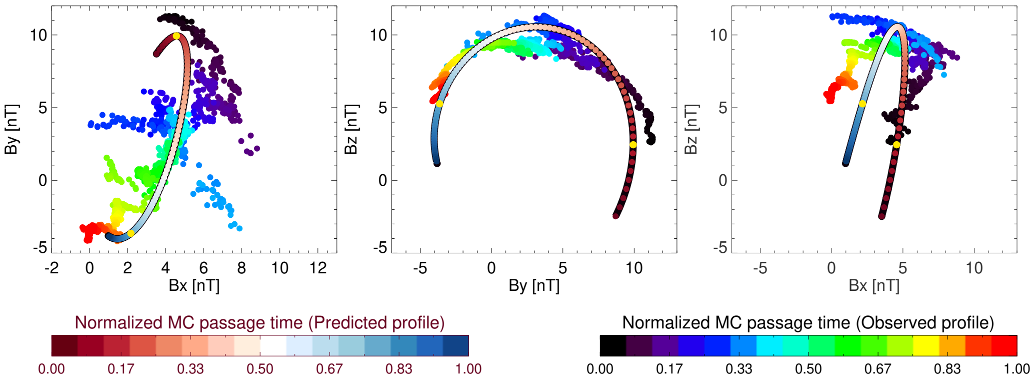

Figure 6.13: Hodogram plot of the magnetic field vectors within the MC for both observed and modeled data values. The yellow dots drawn over the plots for modeled data values denote the data points which approximately match the front and rear boundary of the observed MC.

of predicted magnetic vectors, we find that the magnetic profiles (shown by the blue dashed lines in each panels of Figure 6.11), which best match the observed magnetic vectors of the MC, can be obtained by using the propagation direction along 0°E, 15°S, the tilt angle as 73°, the aspect-ratio as 0.22 and the axial field strength at 10 $R_\odot$ as 52 mG. For this set of input parameters, we show the spacecraft trajectory through the MC and the magnetic field profiles of the FR cross-section when the spacecraft intersects the front and rear boundary of the MC (Figure 6.12). The uncertainty in predicting the magnetic vectors as shown by the gray shaded region in each panel of Figure 6.11 is obtained by overplotting all the sets of output magnetic profiles.

In order to overplot the modeled magnetic vectors within the temporal window of the observed MC, we identify the front and rear boundary of the modeled MC from the hodogram analysis. Figure 6.13 shows the scattered plots among the magnetic field vectors within the MC for both observed and modeled data values. The yellow dots drawn over the plots for modeled data values denote the data points which approximately match the front and rear boundary of the observed MC. Therefore, we take the observed MC boundary as a reference boundary and overplot the data-points of the modeled magnetic vectors which lie in between the two yellow dots.

Figure 6.11 shows that the predicted magnetic field profiles of the MC obtained from our model are in good agreement with those of the observed profiles as detected by the WIND spacecraft. In comparison to the B_y and B_z components, the larger uncertainty arisen in predicting the B_x component is due to its sensitivity towards the propagation direction of the CME which we have discussed in Section 6.4.2. Nevertheless, the predicted profiles for B_y and B_z components show good agreement with the observed profiles. The predicted strength of the B_z component has been found to be 10.5 ± 2.5 nT when the MC axis makes its closest approach to the spacecraft. This is in agreement with the maximum observed strength (11 nT) of the B_z component obtained from the in-situ data. Therefore, our model successfully predicts both the strength and the general profile of the B_z component of the MC with a good accuracy.

6.5 Conclusion

We have developed an analytical model (INFROS) to predict the magnetic field vectors of ICMEs based on realistic inputs obtained from near-Sun observations. As a proof of concept, we validate INFROS model for the 2013 April 11 CME event. The predicted magnetic field-vectors of the ICME obtained from INFROS show good agreement with those observed by the WIND spacecraft at 1 AU. This shows promising results in forecasting of Bz in real time.

There are several key aspects in which INFROS appears to be superior than the existing semi-analytical (Kay et al., 2017) and analytical (Savani et al., 2015) models. The analytical model proposed by Savani et al. (2015) does not incorporate the expanding nature of the ICME during its passage through the spacecraft which yields an unrealistic symmetric profile of the total magnetic field strength of the ICME with time. Kay et al. (2017) included the expanding nature of ICMEs in their semi-analytical model using the speed and duration of passage of the ICME measured at 1 AU as free parameters. However, the formulation developed in INFROS incorporates the FR expansion in such a way so as to get rid of the unknown parameters like the expansion speed (V_{exp}), propagation speed

(V_{pro}) and the time of passage (t_p) of the ICMEs at 1 AU (see Section 6.3.3). Importantly, the existing models (Savani et al., 2015; Kay & Gopalswamy, 2017; Möstl et al., 2018) can only predict the trend in the variation of magnetic field vectors of a ICME, but cannot estimate the strength of its field vectors as they use the axial field strength of the flux rope as a free parameter. Therefore, they are not capable of forecasting the strength of the southward component of magnetic field (Bz) embedded in the ICMEs in order to predict the severity of the associated geomagnetic storms. It may be highlighted that INFROS is capable of predicting the time-varying axial field strength and the expanding nature of the interplanetary FR without involving any free parameters, as all the input parameters are constrained either by the near-Sun observations or the inherent assumptions (self-similar expansion) made in the model. Although many of the assumptions made in the model may not hold good for all events, but as a first order approximation, INFROS could prove to be a promising space-weather forecasting tool for advance prediction of magnetic field vectors of ICMEs.

Chapter 7

Summary and Future Work

7.1 Summary

Exploiting both observational and modeling approaches, in this thesis we have addressed key scientific problems related to CMEs which are one of the major solar origins of space weather disturbances. As the modern high-tech society is vulnerable to the space weather events, this thesis makes an effort towards building the pathway to forecast such space weather hazards caused by CMEs.

The primary objective of the thesis was broadly divided into three major research topics. In the first part, we focused on the source region characteristics of CMEs, aiming to understand the conditions leading to CME eruption from flare productive complex active region. Our efforts also focused on the investigation of source region characteristics of recurrent large eruptive flares originating from same complex active regions in order to predict the occurrence of such successive events and the chances of interaction between the associated CMEs. In the second part, we focused on understanding the CME initiation and the evolution of their properties close to the Sun. In the third part, building upon the knowledge of source region characteristics of CMEs and the nature of evolution of their properties close to the Sun, our ultimate goal was to model the evolution of the CME magnetic field from Sun to Earth, with the scope of providing a useful tool for space weather predictions.

To address the first objective, we performed a comparative study of the source region characteristics associated with the confined and eruptive events occurred in the largest active region (AR) of solar cycle 24 i.e. AR 12192 which gave rise to several non-eruptive X-class flares as well as an eruptive M-class flare (Chapter 3). Based on our study of the four confined and one eruptive flare occurred in AR 12192, we found that the integrated transverse magnetic flux near the polarity inversion line (PIL), increased permanently for all the cases. Importantly, the change in mean horizontal magnetic field during the eruptive flare has been found to be nearly six times larger than the average of that obtained for all the confined cases. During each of the flares, the radial component of the Lorentz force underwent a large and abrupt downward change. Noticeably, the change in Lorentz force per unit area for the eruptive flare was about 4040 dyne cm^{-2}, which is almost three times larger than the maximum change (1390 dyne cm^{-2}) found in the four confined cases. Our results strongly suggested that, although the flare-related permanent and abrupt changes in photospheric magnetic field and Lorentz forces are a common feature in large flares, the magnitude of those changes is smaller in the case of confined flares compared to the eruptive ones. We concluded that the highly energetic flares leave distinct magnetic imprint on the solar photosphere which is stronger for the eruptive events than the confined ones. Furthermore, our results suggest a strong confinement of the overlying magnetic field that could play a key role to suppress the eruptions over the source location of confined flares. We found that the critical decay index for the onset of torus instability was achieved at a higher height over the source region of confined flares as compared to that over the source location of the eruptive flare. The implication of this result is very important as it suggests that the decay rate of the overlying magnetic-field strength can be used as a key parameter to determine whether an eruption would be confined or eruptive.

Extending the studies of solar origin of space weather events, we attempted to address a long standing problem in flare physics, viz, whether the recurrent eruptive flares from a same AR occur due to the continuous supply of free magnetic energy to the solar corona or because not all of the available free magnetic energy is released during a single major flaring event (Chapter 4). Based on our analysis of two ARs (NOAA 11261 and 11283) that produced recurrent large eruptive events, we have found distinct rebuild-up of net Lorentz force in between the successive flares. This was the first observational evidence found in the evolution of any non-potential parameter of solar ARs, that confirmed the energy build-up scenario in the solar corona during the recurrent events. The rebuild-up of magnetic free energy of the ARs was further confirmed by the observations of continuous shearing motion of moving magnetic features of opposite polarities near the polarity inversion line. These results led us to conclude that the recurrent large flares occur due to the newly supplied energy to the AR, instead of consuming the available residual energy. Another highlight of our results is that the evolutionary pattern of the volume averaged net Lorentz force changes over such source ARs can be used for the forecasting of recurrent large eruptive flares from a same AR and hence the chances of interaction between the associated CMEs. Thus, in the first part, the solar sources of CMEs were explored by investigating their magnetic imprint on the photosphere.

As a next step, in the second part of the thesis, we further focused on the initiation of CMEs in the lower corona and their subsequent evolution in the interplanetary space. For the purpose, using the multiple vantage point observations from SDO, STEREO (A & B), PROBA2 and LASCO, we tracked the evolution of a coronal cavity from a quasi-static equilibrium in the lower corona to its eruption into the interplanetary space (Chapter 5). Based on our observations of the two-week long quiescent phase of the cavity, we examined the conditions that led to its instability, particularly in the context of torus instability. Our results reveal that the height of the cavity centroid plays a decisive role in the triggering of the eruption of associated CME. We concluded that monitoring the critical cavity-centroid-height at which the onset of torus instability takes place can serve as a useful space weather forecasting tool to predict when a cavity system would get de-stabilized and give rise to an eruption. Further, utilizing the large field-of-view of SWAP EUV imager and combining the EUV observations with the white-light images obtained from LASCO coronagraph, we could track the lower coronal evolution of the erupting cavity starting from its initiation to post-eruptive phase. Our results showed that the nature of expansion of the coronal cavity was non-self similar below a critical height (2.2 ± 0.2 $R_\odot$). However, the CME expansion became self-similar above that critical height and maintained the same nature throughout the rest of the propagation path. We have also found that the CME exhibited a strong deflection at $\approx$ 1.3 $R_\odot$ which suggested a strong coronal channeling of the CME trajectory. However, the propagation trajectory of the CME remained unchanged in the interplanetary space after the initial deflection close to Sun. The knowledge of the initial kinematics of CMEs as gained by exploiting the PROBA2 and Coronagraphic observations has important implications for estimating the impact of the CMEs at the Earth, which was applied next.

In Chapter 6, we accomplished the final objective of the thesis i.e. to model the CME magnetic field from Sun to Earth in order to forecast the strength of Bz at 1 AU. The results obtained in Chapter 5 provided the important observational constraints on both the nature of expansion and direction of propagation of CMEs, which we have used to develop an observationally constrained analytical model, the INterplanetary Flux ROpe Simulator (INFROS), to predict the magnetic field vectors of ICMEs at any heliocentric distance. In order to benchmark the model, we validated it for an observed Earth-reaching CME which occurred on 2013 April 11. The predicted magnetic field-vectors of the ICME obtained from INFROS showed remarkably good agreement with those observed by the WIND spacecraft at 1 AU. This showed promising results in forecasting of Bz in near real time. The INFROS model is advantageous in many aspects compared to the existing Bz forecasting models, as it uses the realistic inputs obtained from observations and is capable of predicting the time-varying axial field strength and the expanding nature of the ICME without involving any free parameters. Although many of the assumptions made in the model may not hold good for all events, but as a first order approximation, INFROS can be used as a promising space-weather forecasting tool where the magnetic field vectors of the ICMEs can be predicted well in advance using the near-Sun observations of CMEs.

In essence, this thesis explores the origin and evolution of CMEs aiming to forecast its space weather impact at Earth. Based on the observational and modeling efforts, this thesis provides novel techniques to predict the magnetic field vectors of ICMEs which build the stepping stones towards the forecasting of intensity of the associated geomagnetic storms at near-Earth space.

7.2 Future Work

The work presented in this thesis is based on addressing the questions related to solar origins of space weather, primarily using the remote sensing and in situ observations of the Sun and interplanetary medium. On the lines of the investigations that have been carried out in this thesis, the scope for future studies should include the continuation of such exploration on the origin and evolution of CMEs by studying a large set of events which will lead to better theoretical understanding of the underlying physics. Moreover, further advancements can be made in the modeling techniques to forecast the space weather impact of CMEs at Earth. In this regard, some of the future studies which may be carried out are briefly listed below.

(1) The results obtained in this thesis on the initiation and evolution of CMEs can be statistically validated by studying a large set of confined and eruptive flares as well as more number of events associated with erupting cavities leading to CMEs. The PROBA2/SWAP observations used in this thesis were vital as the large field-of-view of the SWAP instrument allowed us to track the cavity up to almost 1.7 $R_\odot$ which was not possible earlier because of the observational constraints. This study sets the stage for future studies that are being planned with the Enhanced Visible Emission Line Coronagrah (E-VELC) (Raghavendra et al., 2017) aboard the Aditya-L1 mission (Seetha & Megala, 2017) of ISRO which will observe the lower corona from 1.05 - 3.0 $R_\odot$, a crucial regime where the initiation of coronal mass ejections takes place. In particular, it will help in predicting the triggering of CMEs to get advance warnings by monitoring the height at which the critical value of decay index is achieved for the cavity centroid.

(2) The energy release and build-up scenario during the solar flares as ex-

plored in this thesis in Chapter 4 is based on the evolution of volume averaged Lorentz force which acts as proxy for the free energy storage in the solar corona. However, the direct estimation of free magnetic energy can be done by applying the magnetic virial theorem (Klimchuk et al., 1992) on the atmospheric layers such as solar chromosphere where the magnetic field satisfies the force free condition. The Multi Application Solar Telescope (MAST) installed in Udaipur Solar Observatory has the capability to record observations of the vector magnetic field in the solar chromosphere as well as photosphere. Once such observations become available from MAST, we plan to study the evolution of magnetic energy of active regions during the solar flares in order to get in depth knowledge about energy build-up and release processes in solar corona.

(3) The present analytical model INFROS uses the cylindrical geometry for the flux-rope model in order to predict the magnetic field vectors of ICMEs. We plan to modify the model assuming a different magnetic field configuration of the FR i.e., the toroidal geometry instead of cylindrical and study the impact on the vector field predictions of ICMEs.

(4) Incorporating the above mentioned modifications, we plan to validate INFROS for more set of events for which cradle-to-grave evolution tracking is possible.

(5) As a future step, we also propose to implement the INFROS model to CMEs sequentially detected at different heliocentric distances from the Sun using multi-spacecraft observations from MESSENGER (Anderson et al., 2007), VEX (Titov et al., 2006), MAVEN (Jakosky et al., 2015) and Parker Solar Probe (PSP) (Fox et al., 2016) which will help to validate the model results and improve our understanding of the CME evolution in heliosphere.

(6) Combining the strength of Bz obtained from our model outputs with the predicted speed of the CME at 1 AU from drag based model (Vršnak et al., 2013) results, we plan to predict the magnitude of the resulting geomagnetic storm given by the Dst index and then compare the predicted values of Dst with the actual observations. The successful prediction of Dst index would lead us to develop an operational space weather forecasting tool to predict the severity of resulting

geomagnetic storms.

Bibliography

Allen, J., Frank, L., Sauer, H., & Reiff, P. 1989, EOS Transactions, 70, 1479

Anderson, B. J., Acuña, M. H., Lohr, D. A., et al. 2007, *Space Sci. Rev.*, 131, 417

Andrews, M. D. 2003, *Solar Phys.*, 218, 261

Antiochos, S. K., DeVore, C. R., & Klimchuk, J. A. 1999, *Astrophys. J.*, 510, 485

Archontis, V., Hood, A. W., & Tsinganos, K. 2014, *Astrophys. J. Lett.*, 786, L21

Aschwanden, M. J. 2016, *Astrophys. J. Suppl.*, 224, 25

Bahcall, J. N., Huebner, W. F., Lubow, S. H., Parker, P. D., & Ulrich, R. K. 1982, Reviews of Modern Physics, 54, 767

Bateman, G. 1978, MHD instabilities

Bein, B. M., Berkebile-Stoiser, S., Veronig, A. M., et al. 2011, *Astrophys. J.*, 738, 191

Bein, B. M., Berkebile-Stoiser, S., Veronig, A. M., Temmer, M., & Vršnak, B. 2012, *Astrophys. J.*, 755, 44

Bein, B. M., Temmer, M., Vourlidas, A., Veronig, A. M., & Utz, D. 2013, The Astrophysical Journal, 768, 31

Belcher, J. W., & Davis, Leverett, J. 1971, *J. Geophys. Res.*, 76, 3534

Bemporad, A., Poletto, G., Suess, S. T., et al. 2006, *Astrophys. J.*, 638, 1110

Benz, A. O. 2008, Living Reviews in Solar Physics, 5, 1

Bobra, M. G., & Couvidat, S. 2015, The Astrophysical Journal, 798, 135

Bolduc, L. 2002, Journal of Atmospheric and Solar-Terrestrial Physics, 64, 1793

Borrero, J. M., Tomczyk, S., Kubo, M., et al. 2011, *Solar Phys.*, 273, 267

Bothmer, V., & Schwenn, R. 1998, Annales Geophysicae, 16, 1

Brueckner, G. E., Howard, R. A., Koomen, M. J., et al. 1995, *Solar Phys.*, 162, 357

Burlaga, L., Sittler, E., Mariani, F., & Schwenn, R. 1981, *J. Geophys. Res.*, 86, 6673

Burlaga, L., Fitzenreiter, R., Lepping, R., et al. 1998, *J. Geophys. Res.*, 103, 277

Burlaga, L. F. 1988, *J. Geophys. Res.*, 93, 7217

Burlaga, L. F., Ness, N. F., Acuña, M. H., et al. 2008, *Nature*, 454, 75

Burton, R. K., McPherron, R. L., & Russell, C. T. 1975, *J. Geophys. Res.*, 80, 4204

Byrne, J. P., Maloney, S. A., McAteer, R. T. J., Refojo, J. M., & Gallagher, P. T. 2010, Nature Communications, 1, 74

Byrne, J. P., Morgan, H., Seaton, D. B., Bain, H. M., & Habbal, S. R. 2014, *Solar Phys.*, 289, 4545

Çakmak, H. 2014, Exp. Astron., 37, 539

Canfield, R. C., Zarro, D. M., Metcalf, T. R., & Lemen, J. R. 1990, *Astrophys. J.*, 348, 333

Carrington, R. C. 1859, *Mon. Not. Roy. Astron. Soc.*, 20, 13

Chen, H., Zhang, J., Cheng, X., et al. 2014, *Astrophys. J. Lett.*, 797, L15

Chen, H., Zhang, J., Ma, S., et al. 2015, *Astrophys. J. Lett.*, 808, L24

Chen, J., & Krall, J. 2003, Journal of Geophysical Research (Space Physics), 108, 1410

Chen, J., Marqué, C., Vourlidas, A., Krall, J., & Schuck, P. W. 2006, *Astrophys. J.*, 649, 452

Chen, J., Santoro, R. A., Krall, J., et al. 2000, *Astrophys. J.*, 533, 481

Chen, J., Santoro, R. A., Krall, J., et al. 2000, The Astrophysical Journal, 533, 481

Chen, P. F. 2011, Living Reviews in Solar Physics, 8, 1

Cheng, X., Zhang, J., Ding, M. D., Guo, Y., & Su, J. T. 2011, *Astrophys. J.*, 732, 87

Cohen, C. M. S., Mason, G. M., Mewaldt, R. A., & Wiedenbeck, M. E. 2014, The Astrophysical Journal, 793, 35

Cowen, R. 2012, *Nature*, 489, 20

Cremades, H., Bothmer, V., & Tripathi, D. 2006, Advances in Space Research, 38, 461

Daglis, I., Baker, D., Kappenman, J., Panasyuk, M., & Daly, E. 2004, Space Weather, 2, S02004

Del Zanna, G., & Mason, H. E. 2018, Living Reviews in Solar Physics, 15, 5

Demastus, H. L., Wagner, W. J., & Robinson, R. D. 1973, *Solar Phys.*, 31, 449

Démoulin, P., & Aulanier, G. 2010, *Astrophys. J.*, 718, 1388

DeVore, C. R., & Antiochos, S. K. 2008, The Astrophysical Journal, 680, 740

Domingo, V., Fleck, B., & Poland, A. I. 1995, *Solar Phys.*, 162, 1

Doschek, G. A., & Warren, H. P. 2005, AGU Spring Meeting Abstracts

Dryer, M. 1994, *Space Sci. Rev.*, 67, 363

Dumbović, M., Devos, A., Vršnak, B., et al. 2015, *Solar Phys.*, 290, 579

Elmore, D. F., Burkepile, J. T., Darnell, J. A., Lecinski, A. R., & Stanger, A. L. 2003, in Proceedings of SPIE, Vol. 4843, Polarimetry in Astronomy, ed. S. Fineschi, 66–75

Eyles, C. J., Harrison, R. A., Davis, C. J., et al. 2009, *Solar Phys.*, 254, 387

Falconer, D. A., Moore, R. L., & Gary, G. A. 2002, *Astrophys. J.*, 569, 1016

Fan, Y., & Gibson, S. E. 2007, *Astrophys. J.*, 668, 1232

Farrugia, C., & Berdichevsky, D. 2004, Annales Geophysicae, 22, 3679

Farrugia, C. J., Jordanova, V. K., Thomsen, M. F., et al. 2006, Journal of Geophysical Research (Space Physics), 111, A11104

Feynman, J., & Hundhausen, A. J. 1994, *J. Geophys. Res.*, 99, 8451

Filippov, B. 2013, *Astrophys. J.*, 773, 10

Fisher, G. H., Bercik, D. J., Welsch, B. T., & Hudson, H. S. 2012, *Solar Phys.*, 277, 59

Fisher, R. R., Lee, R. H., MacQueen, R. M., & Poland , A. I. 1981, *Applied Optics*, 20, 1094

Fletcher, L., & Hudson, H. S. 2008, *Astrophys. J.*, 675, 1645

Forbes, T. G. 2000, *J. Geophys. Res.*, 105, 23153

Forland, B. C., Gibson, S. E., Dove, J. B., Rachmeler, L. A., & Fan, Y. 2013, Solar Physics, 288, 603

Fox, N. J., Velli, M. C., Bale, S. D., et al. 2016, *Space Sci. Rev.*, 204, 7

Fulara, A., Chandra, R., Chen, P. F., et al. 2019, Solar Physics, 294, 56

Gaizauskas, V. 2008, *Astrophys. J.*, 686, 1432

Gibson, S. 2015, Coronal Cavities: Observations and Implications for the Magnetic Environment of Prominences, ed. J.-C. Vial & O. Engvold (Cham: Springer International Publishing), 323–353

Gibson, S. E., & Fan, Y. 2006, Journal of Geophysical Research (Space Physics), 111, A12103

Gibson, S. E., Fludra, A., Bagenal, F., et al. 1999, *J. Geophys. Res.*, 104, 9691

Gibson, S. E., Kucera, T. A., Rastawicki, D., et al. 2010, *Astrophys. J.*, 724, 1133

Gibson, S. E., Kucera, T. A., White, S. M., et al. 2016, Frontiers in Astronomy and Space Sciences, 3, 8

Gold, T., & Hoyle, F. 1960, *Mon. Not. Roy. Astron. Soc.*, 120, 89

Gonzalez, W. D., & Echer, E. 2005, *Geophys. Res. Lett.*, 32, L18103

Gonzalez, W. D., Joselyn, J. A., Kamide, Y., et al. 1994, *J. Geophys. Res.*, 99, 5771

Gonzalez, W. D., & Tsurutani, B. T. 1992, Terrestrial Response to Eruptive Solar Flares - Geomagnetic Storms, ed. Z. Svestka, B. V. Jackson, & M. E. Machado, Vol. 399, 277

Gonzalez, W. D., Tsurutani, B. T., & Clúa de Gonzalez, A. L. 1999, *Space Sci. Rev.*, 88, 529

Good, S. W., Forsyth, R. J., Raines, J. M., et al. 2015, *Astrophys. J.*, 807, 177

Good, S. W., Kilpua, E. K. J., LaMoury, A. T., et al. 2019, Journal of Geophysical Research: Space Physics, 124, 4960

Gopalswamy, N. 2006, *Space Sci. Rev.*, 124, 145

Gopalswamy, N. 2006, Space Science Reviews, 124, 145

Gopalswamy, N. 2016, Geoscience Letters, 3, 8

Gopalswamy, N., Akiyama, S., Yashiro, S., & Mäkelä, P. 2010, Astrophysics and Space Science Proceedings, 19, 289

Gopalswamy, N., Akiyama, S., Yashiro, S., Michalek, G., & Lepping, R. P. 2008, Journal of Atmospheric and Solar-Terrestrial Physics, 70, 245

Gopalswamy, N., Akiyama, S., Yashiro, S., & Xie, H. 2018a, in IAU Symposium, Vol. 335, Space Weather of the Heliosphere: Processes and Forecasts, ed. C. Foullon & O. E. Malandraki, 258–262

Gopalswamy, N., Akiyama, S., Yashiro, S., & Xie, H. 2018b, Journal of Atmospheric and Solar-Terrestrial Physics, 180, 35

Gopalswamy, N., Akiyama, S., Yashiro, S., et al. 2014, Geophysical Research Letters, 41, 2673

Gopalswamy, N., Mäkelä, P., Akiyama, S., et al. 2018c, Journal of Atmospheric and Solar-Terrestrial Physics, 179, 225

Gopalswamy, N., Mäkelä, P., Xie, H., Akiyama, S., & Yashiro, S. 2009, Journal of Geophysical Research (Space Physics), 114, A00A22

Gopalswamy, N., Yashiro, S., Akiyama, S., & Xie, H. 2017, *Solar Phys.*, 292, 65

Gopalswamy, N., Kaiser, M. L., Lepping, R. P., et al. 1998, *J. Geophys. Res.*, 103, 307

Gosling, J. T. 1993, Phys. Fl. B, 5, 2638

Gosling, J. T., Hildner, E., MacQueen, R. M., et al. 1974, *J. Geophys. Res.*, 79, 4581

Gosling, J. T., Thomsen, M. F., Bame, S. J., & Zwickl, R. D. 1987, *J. Geophys. Res.*, 92, 12399

Green, L. M., & Kliem, B. 2014, in IAU Symposium, Vol. 300, Nature of Prominences and their Role in Space Weather, ed. B. Schmieder, J.-M. Malherbe, & S. T. Wu, 209–214

Green, L. M., Török, T., Vršnak, B., Manchester, W., & Veronig, A. 2018, *Space Sci. Rev.*, 214, 46

Guennou, C., Rachmeler, L., Seaton, D., & Auchère, F. 2016, Frontiers in Astronomy and Space Sciences, 3, 14

Gui, B., Shen, C., Wang, Y., et al. 2011, *Solar Phys.*, 271, 111

Halain, J.-P., Berghmans, D., Seaton, D. B., et al. 2013, *Solar Phys.*, 286, 67

Hanaoka, Y., & Sakurai, T. 2017, *Astrophys. J.*, 851, 130

Hanaoka, Y., Kurokawa, H., Enome, S., et al. 1994, *Pub. Astron. Soc. Japan*, 46, 205

Hapgood, M. A. 1992, Planet. Space Sci., 40, 711

Harrison, R. A. 1995, *Astron. Astrophys.*, 304, 585

—. 2003, Space Res., 32, 2425

Henke, T., Woch, J., Mall, U., et al. 1998, *Geophys. Res. Lett.*, 25, 3465

Hewish, A., Scott, P. F., & Wills, D. 1964, *Nature*, 203, 1214

Hiei, E., Hundhausen, A. J., & Sime, D. G. 1993, *Geophys. Res. Lett.*, 20, 2785

Hirayama, T., & Nakagomi, Y. 1974, *Pub. Astron. Soc. Japan*, 26, 53

Hirshberg, J., Asbridge, J. R., & Robbins, D. E. 1971, *Solar Phys.*, 18, 313

Hoeksema, J. T., Liu, Y., Hayashi, K., et al. 2014, *Solar Phys.*, 289, 3483

Hood, A. W., & Priest, E. R. 1979, *Solar Phys.*, 64, 303

Houminer, Z., & Hewish, A. 1974, *Planetary Space Science*, 22, 1041

House, L. L., Wagner, W. J., Hildner, E., Sawyer, C., & Schmidt, H. U. 1981, *Astrophys. J. Lett.*, 244, L117

Howard, R. A., Moses, J. D., Vourlidas, A., et al. 2008, *Space Sci. Rev.*, 136, 67

Howard, T. 2011, Springer-Verlag New York, 376, doi:10.1007/978-1-4419-8789-1

Howard, T. A., & DeForest, C. E. 2012, *Astrophys. J.*, 752, 130

Howard, T. A., DeForest, C. E., Schneck, U. G., & Alden, C. R. 2017, *Astrophys. J.*, 834, 86

Hoyng, P., Duijveman, A., Machado, M. E., et al. 1981, *Astrophys. J. Lett.*, 246, L155

Hu, Q., Qiu, J., Dasgupta, B., Khare, A., & Webb, G. M. 2014, *Astrophys. J.*, 793, 53

Hudson, H. S. 2000, *Astrophys. J. Lett.*, 531, L75

Hudson, H. S., Fisher, G. H., & Welsch, B. T. 2008, in Astronomical Society of the Pacific Conference Series, Vol. 383, Subsurface and Atmospheric Influences on Solar Activity, ed. R. Howe, R. W. Komm, K. S. Balasubramaniam, & G. J. D. Petrie, 221

Hudson, H. S., Fletcher, L., Fisher, G. H., Abbett, W. P., & Russell, A. 2012, *Solar Phys.*, 277, 77

Hundhausen, A. 1999, in The many faces of the sun: a summary of the results from NASA's Solar Maximum Mission., ed. K. T. Strong, J. L. R. Saba, B. M. Haisch, & J. T. Schmelz, 143

Hundhausen, A. J. 1993, *J. Geophys. Res.*, 98, 13177

Hundhausen, A. J., Gilbert, H. E., & Bame, S. J. 1968, *Astrophys. J. Lett.*, 152, L3

Huttunen, K. E. J., Schwenn, R., Bothmer, V., & Koskinen, H. E. J. 2005, Annales Geophysicae, 23, 625

Illing, R. M. E., & Hundhausen, A. J. 1985, *J. Geophys. Res.*, 90, 275

Inhester, B. 2015, arXiv e-prints, arXiv:1512.00651

Jakosky, B. M., Lin, R. P., Grebowsky, J. M., et al. 2015, *Space Sci. Rev.*, 195, 3

Janvier, M., Aulanier, G., Bommier, V., et al. 2014, *Astrophys. J.*, 788, 60

Jiang, C., Wu, S. T., Yurchyshyn, V., et al. 2016, *Astrophys. J.*, 828, 62

Jin, M., Manchester, W. B., van der Holst, B., et al. 2017, *Astrophys. J.*, 834, 173

Joshi, A. D., & Srivastava, N. 2011, *Astrophys. J.*, 739, 8

Joshi, B., Kushwaha, U., Veronig, A. M., et al. 2016, The Astrophysical Journal, 834, 42

Joshi, N. C., Magara, T., & Inoue, S. 2014, *Astrophys. J.*, 795, 4

Kahler, S. W. 1992, Annu. Rev. Astron. Astrophys., 30, 113

Kaiser, M. L., Kucera, T. A., Davila, J. M., et al. 2008, *Space Sci. Rev.*, 136, 5

Kawabata, Y., Iida, Y., Doi, T., et al. 2018, *Astrophys. J.*, 869, 99

Kay, C., & Gopalswamy, N. 2017, Journal of Geophysical Research (Space Physics), 122, 11

Kay, C., Gopalswamy, N., Reinard, A., & Opher, M. 2017, *Astrophys. J.*, 835, 117

Kay, C., & Opher, M. 2015, *Astrophys. J. Lett.*, 811, L36

Kay, C., Opher, M., & Evans, R. M. 2013, *Astrophys. J.*, 775, 5

—. 2015, *Astrophys. J.*, 805, 168

Kilpua, E., Koskinen, H. E. J., & Pulkkinen, T. I. 2017a, Living Reviews in Solar Physics, 14, 5

Kilpua, E. K. J., Balogh, A., von Steiger, R., & Liu, Y. D. 2017b, *Space Sci. Rev.*, 212, 1271

Kilpua, E. K. J., Mierla, M., Rodriguez, L., et al. 2012, *Solar Phys.*, 279, 477

Kilpua, E. K. J., Pomoell, J., Vourlidas, A., et al. 2009, Annales Geophysicae, 27, 4491

Kim, R. S., Gopalswamy, N., Cho, K. S., Moon, Y. J., & Yashiro, S. 2013, *Solar Phys.*, 284, 77

Kim, R.-S., Gopalswamy, N., Cho, K.-S., Moon, Y.-J., & Yashiro, S. 2013, Solar Physics, 284, 77

Kimball, D. 1960, Sci Rpt., 6, UAG R109

Klein, L. W., & Burlaga, L. F. 1982, *J. Geophys. Res.*, 87, 613

Kliem, B., & Török, T. 2006, Physical Review Letters, 96, 255002

Klimchuk, J. A., Canfield, R. C., & Rhoads, J. E. 1992, *Astrophys. J.*, 385, 327

Ko, Y.-K., Raymond, J. C., Rakowski, C., & Rouillard, A. 2013, in American Institute of Physics Conference Series, Vol. 1539, Solar Wind 13, ed. G. P. Zank, J. Borovsky, R. Bruno, J. Cirtain, S. Cranmer, H. Elliott, J. Giacalone, W. Gonzalez, G. Li, E. Marsch, E. Moebius, N. Pogorelov, J. Spann, & O. Verkhoglyadova, 207–210

Koomen, M., Howard, R., Hansen, R., & Hansen, S. 1974, *Solar Phys.*, 34, 447

Krall, J., Chen, J., Duffin, R. T., Howard, R. A., & Thompson, B. J. 2001, *Astrophys. J.*, 562, 1045

Krieger, A. S., Timothy, A. F., & Roelof, E. C. 1973, *Solar Phys.*, 29, 505

Kumar, B., Bayanna, A. R., Venkatakrishnan, P., & Mathew, S. K. 2016a, Res. Astron. Astrophys., 16, 129

Kumar, S., Bhattacharyya, R., Joshi, B., & Smolarkiewicz, P. K. 2016b, *Astrophys. J.*, 830, 80

Lakhina, G. S., & Tsurutani, B. T. 2016, Geoscience Letters, 3, 5

Lang, K. R. 2006, Sun, Earth and Sky

Lario, D., Raouafi, N. E., Kwon, R.-Y., et al. 2014, The Astrophysical Journal, 797, 8

Leamon, R. J., Canfield, R. C., Jones, S. L., et al. 2004, Journal of Geophysical Research (Space Physics), 109, A05106

Leibacher, J. W., Noyes, R. W., Toomre, J., & Ulrich, R. K. 1985, Scientific American, 253, 48

Leighton, R. B., Noyes, R. W., & Simon, G. W. 1962, *Astrophys. J.*, 135, 474

Leka, K. D., Barnes, G., & Crouch, A. 2009, in CS-Astron. Soc. Pacific, San Francisco, Vol. 415, The Second Hinode Science Meeting: Beyond Discovery-Toward Understanding, ed. B. Lites, M. Cheung, T. Magara, J. Mariska, & K. Reeves, 365

Lemen, J. R., Title, A. M., Akin, D. J., et al. 2012, *Solar Phys.*, 275, 17

Lepping, R. P., Acũna, M. H., Burlaga, L. F., et al. 1995, *Space Sci. Rev.*, 71, 207

Lepri, S. T., & Zurbuchen, T. H. 2004, Journal of Geophysical Research (Space Physics), 109, A01112

—. 2010, *Astrophys. J. Lett.*, 723, L22

Lepri, S. T., Zurbuchen, T. H., Fisk, L. A., et al. 2001, *J. Geophys. Res.*, 106, 29231

Li, X., Yang, S., Chen, H., Li, T., & Zhang, J. 2015, *Astrophys. J. Lett.*, 814, L13

Lin, J., & Forbes, T. G. 2000, *J. Geophys. Res.*: Space Phys., 105, 2375

Liu, C., Deng, N., Lee, J., et al. 2013, *Astrophys. J. Lett.*, 778, L36

Liu, L., Wang, Y., Wang, J., et al. 2016, *Astrophys. J.*, 826, 119

Liu, R., Liu, C., Wang, S., Deng, N., & Wang, H. 2010, *Astrophys. J. Lett.*, 725, L84

Liu, Y. 2008, *Astrophys. J. Lett.*, 679, L151

Liu, Y., Hoeksema, J. T., Bobra, M., et al. 2014, *Astrophys. J.*, 785, 13

Liu, Y., Hoeksema, J. T., Scherrer, P. H., et al. 2012, Solar Physics, 279, 295

Longcope, D., Beveridge, C., Qiu, J., et al. 2007, *Solar Phys.*, 244, 45

Loomis, E. 1861, American Journal of Science, 32, 318

Low, B. C., & Hundhausen, J. R. 1995, *Astrophys. J.*, 443, 818

Lugaz, N., Downs, C., Shibata, K., et al. 2011, *Astrophys. J.*, 738, 127

Lugaz, N., & Farrugia, C. J. 2014, *Geophys. Res. Lett.*, 41, 769

Lundquist, S. 1950, Ark Fys, 2, 361

Lynch, B. J., Antiochos, S. K., Li, Y., Luhmann, J. G., & DeVore, C. R. 2009, *Astrophys. J.*, 697, 1918

Ma, S., Attrill, G. D. R., Golub, L., & Lin, J. 2010, *Astrophys. J.*, 722, 289

MacQueen, R. M., & Fisher, R. R. 1983, *Solar Phys.*, 89, 89

Manchester, Ward B., I., Vourlidas, A., Tóth, G., et al. 2008, *Astrophys. J.*, 684, 1448

Manchester, W., Kilpua, E. K. J., Liu, Y. D., et al. 2017, *Space Sci. Rev.*, 212, 1159

Maričić, D., Vršnak, B., Stanger, A. L., & Veronig, A. 2004, *Solar Phys.*, 225, 337

Martin, S. F. 1998, *Solar Phys.*, 182, 107

Martínez-Sykora, J., De Pontieu, B., Testa, P., & Hansteen, V. 2011, *Astrophys. J.*, 743, 23

Marubashi, K., Akiyama, S., Yashiro, S., et al. 2015, Solar Physics, 290, 1371

Mathew, S. K., Martínez Pillet, V., Solanki, S. K., & Krivova, N. A. 2007, *Astron. Astrophys.*, 465, 291

McCauley, P. I., Su, Y. N., Schanche, N., et al. 2015, *Solar Phys.*, 290, 1703

Metcalf, T. R. 1994, *Solar Phys.*, 155, 235

Mierla, M., Seaton, D. B., Berghmans, D., et al. 2013, *Solar Phys.*, 286, 241

Mishra, W., & Srivastava, N. 2013, *Astrophys. J.*, 772, 70

—. 2014, *Astrophys. J.*, 794, 64

Mishra, W., Srivastava, N., & Davies, J. A. 2014, *Astrophys. J.*, 784, 135

Mishra, W., Wang, Y., Srivastava, N., & Shen, C. 2017, *Astrophys. J. Suppl.*, 232, 5

Mohamed, A. A., Gopalswamy, N., Yashiro, S., et al. 2012, Journal of Geophysical Research (Space Physics), 117, A01103

Moore, R. L., & Labonte, B. J. 1980, in IAU Symposium, Vol. 91, Solar and Interplanetary Dynamics, ed. M. Dryer & E. Tandberg-Hanssen, 207–210

Moore, R. L., Sterling, A. C., Gary, G. A., Cirtain, J. W., & Falconer, D. A. 2011, *Space Sci. Rev.*, 160, 73

Moore, R. L., Sterling, A. C., Hudson, H. S., & Lemen, J. R. 2001, *Astrophys. J.*, 552, 833

Morgan, H., Habbal, S. R., & Woo, R. 2006, *Solar Phys.*, 236, 263

Möstl, C., Rollett, T., Frahm, R. A., et al. 2015, Nature Communications, 6, 7135

Möstl, C., Amerstorfer, T., Palmerio, E., et al. 2018, Space Weather, 16, 216

Möstl, C., Rollett, T., Lugaz, N., et al. 2011, The Astrophysical Journal, 741, 34

Nitta, N. V. 2002, in ESA Special Publication, Vol. 1, Solar Variability: From Core to Outer Frontiers, ed. A. Wilson, 189–192

Nitta, N. V., & Hudson, H. S. 2001, Geophysical Research Letters, 28, 3801

Odstrcil, D., Riley, P., & Zhao, X. P. 2004, Journal of Geophysical Research (Space Physics), 109, A02116

Odstrčil, D., & Pizzo, V. J. 1999, *J. Geophys. Res.*, 104, 483

Ogilvie, K., & Desch, M. 1997, Advances in Space Research, 20, 559 , results of the IASTP Program

Ogilvie, K. W., Chornay, D. J., Fritzenreiter, R. J., et al. 1995, *Space Sci. Rev.*, 71, 55

Olmedo, O., & Zhang, J. 2010, *Astrophys. J.*, 718, 433

Palmerio, E., Kilpua, E. K. J., James, A. W., et al. 2017, Solar Physics, 292, 39

Palmerio, E., Kilpua, E. K. J., Möstl, C., et al. 2018, Space Weather, 16, 442

Panasenco, O., Martin, S., Joshi, A. D., & Srivastava, N. 2011, Journal of Atmospheric and Solar-Terrestrial Physics, 73, 1129

Parker, E. N. 1958, *Astrophys. J.*, 128, 664

Patsourakos, S., Vourlidas, A., & Stenborg, G. 2013, *Astrophys. J.*, 764, 125

Pesnell, W. D., Thompson, B. J., & Chamberlin, P. C. 2012, *Solar Phys.*, 275, 3

Petrie, G. J. D. 2012, *Astrophys. J.*, 759, 50

Petrie, G. J. D. 2013, *Solar Phys.*, 287, 415

Petrie, G. J. D. 2019, The Astrophysical Journal Supplement Series, 240, 11

Petrie, G. J. D., & Sudol, J. J. 2010, *Astrophys. J.*, 724, 1218

Pettauer, T., & Brandt, P. N. 1997, Solar Physics, 175, 197

Pevtsov, A. A., Canfield, R. C., & Metcalf, T. R. 1995, *Astrophys. J. Lett.*, 440, L109

Poomvises, W., Zhang, J., & Olmedo, O. 2010, *Astrophys. J. Lett.*, 717, L159

Priest, E. 2014, Magnetohydrodynamics of the Sun (Cambridge University Press), doi:10.1017/CBO9781139020732

Priest, E. 2014, Cambridge University Press, Cambridge, UK

Priest, E. R., & Forbes, T. G. 2002, *Astron. Astrophys. Rev.*, 10, 313

Qiu, J., Hu, Q., Howard, T. A., & Yurchyshyn, V. B. 2007, *Astrophys. J.*, 659, 758

Rachmeler, L. A., Gibson, S. E., Dove, J. B., DeVore, C. R., & Fan, Y. 2013, Solar Physics, 288, 617

Raghavendra, P. B., Banerjee, D., Singh, J., et al. 2017, Current Science, 113, 613

Régnier, S., Walsh, R. W., & Alexander, C. E. 2011, *Astron. Astrophys.*, 533, L1

RHESSI. science nugget no.239

Richardson, I. G. 2018, Living Reviews in Solar Physics, 15, 1

Richardson, I. G., & Cane, H. V. 1993, *J. Geophys. Res.*, 98, 15295

—. 2004, Journal of Geophysical Research (Space Physics), 109, A09104

Richardson, I. G., Farrugia, C. J., & Cane, H. V. 1997, *J. Geophys. Res.*, 102, 4691

Richardson, J. D., Kasper, J. C., Wang, C., Belcher, J. W., & Lazarus, A. J. 2008, *Nature*, 454, 63

Riley, P., Lionello, R., Mikić, Z., & Linker, J. 2008, *Astrophys. J.*, 672, 1221

Robbrecht, E., Patsourakos, S., & Vourlidas, A. 2009, *Astrophys. J.*, 701, 283

Romano, P., Zuccarello, F., Guglielmino, S. L., et al. 2015, *Astron. Astrophys.*, 582, A55

Rouillard, A. P. 2011, Journal of Atmospheric and Solar-Terrestrial Physics, 73, 1201

Rust, D. M., & Hildner, E. 1976, *Solar Phys.*, 48, 381

Rust, D. M., & Kumar, A. 1996, *Astrophys. J. Lett.*, 464, L199

Sakurai, T. 1976, *Pub. Astron. Soc. Japan*, 28, 177

Sammis, I., Tang, F., & Zirin, H. 2000, *Astrophys. J.*, 540, 583

Santandrea, S., Gantois, K., Strauch, K., et al. 2013, *Solar Phys.*, 286, 5

Sarkar, R., Gopalswamy, N., & Srivastava, N. 2020, *Astrophys. J.*, 888, 121

Sarkar, R., & Srivastava, N. 2018, *Solar Phys.*, 293, 16

Sarkar, R., Srivastava, N., & Dhara, S. K. 2018, in IAU Symposium, Vol. 335, Space Weather of the Heliosphere: Processes and Forecasts, ed. C. Foullon & O. E. Malandraki, 32–35

Sarkar, R., Srivastava, N., Mierla, M., West, M. J., & D'Huys, E. 2019a, *Astrophys. J.*, 875, 101

Sarkar, R., Srivastava, N., & Veronig, A. M. 2019b, *Astrophys. J. Lett.*, 885, L17

Savani, N. P., Vourlidas, A., Szabo, A., et al. 2015, Space Weather, 13, 374

Schmahl, E. J. 1979, in IAU Colloq. 44: Physics of Solar Prominences, ed. E. Jensen, P. Maltby, & F. Q. Orrall, 102–120

Schou, J., Scherrer, P. H., Bush, R. I., et al. 2012, *Solar Phys.*, 275, 229

Schrijver, C. J. 2009, Space Res., 43, 739

Schrijver, C. J., & De Rosa, M. L. 2003, *Solar Phys.*, 212, 165

Schrijver, C. J., Elmore, C., Kliem, B., Török, T., & Title, A. M. 2008, *Astrophys. J.*, 674, 586

Schwenn, R. 2006, Living Reviews in Solar Physics, 3, 2

Schwenn, R., Rosenbauer, H., & Muehlhaeuser, K. H. 1980, *Geophys. Res. Lett.*, 7, 201

Scolini, C., Rodriguez, L., Mierla, M., Pomoell, J., & Poedts, S. 2019, *Astron. Astrophys.*, 626, A122

Seaton, D. B., Berghmans, D., Nicula, B., et al. 2013, *Solar Phys.*, 286, 43

Seetha, S., & Megala, S. 2017, Current Science, 113, 25

Sharma, R., & Srivastava, N. 2012, Journal of Space Weather and Space Climate, 2, A10

Sheeley, N. R., J., Michels, D. J., Howard, R. A., & Koomen, M. J. 1980, *Astrophys. J. Lett.*, 237, L99

Shen, C., Wang, Y., Gui, B., Ye, P., & Wang, S. 2011, *Solar Phys.*, 269, 389

Shen, F., Shen, C., Zhang, J., et al. 2014, Journal of Geophysical Research (Space Physics), 119, 7128

Shen, F., Wang, Y., Shen, C., & Feng, X. 2017, *Solar Phys.*, 292, 104

Shibata, K., Masuda, S., Shimojo, M., et al. 1995, *Astrophys. J. Lett.*, 451, L83

Siscoe, G. 2000, *J. Atmos. Solar-Terr. Phys.*, 62, 1223

Skoug, R. M., Bame, S. J., Feldman, W. C., et al. 1999, *Geophys. Res. Lett.*, 26, 161

SONG, H. Q., CHEN, Y., ZHANG, J., et al. 2015, *Astrophys. J. Lett.*, 808, L15

Srivastava, N., & Schwenn, R. 2000, in The Outer Heliosphere: Beyond the Planets, ed. K. Scherer, H. Fichtner, & E. Marsch, 12–40

Srivastava, N., & Venkatakrishnan, P. 2002, *Geophys. Res. Lett.*, 29, 1287

Sterling, A. C., & Hudson, H. S. 1997, *Astrophys. J. Lett.*, 491, L55

Sterling, A. C., & Moore, R. L. 2004, *Astrophys. J.*, 602, 1024

Stone, E. C., Cummings, A. C., McDonald, F. B., et al. 2005, Science, 309, 2017

Subramanian, P., Arunbabu, K. P., Vourlidas, A., & Mauriya, A. 2014, The Astrophysical Journal, 790, 125

Sudol, J. J., & Harvey, J. W. 2005, *Astrophys. J.*, 635, 647

Sun, X., Hoeksema, J. T., Liu, Y., Kazachenko, M., & Chen, R. 2017, The Astrophysical Journal, 839, 67

Sun, X., Hoeksema, J. T., Liu, Y., Kazachenko, M. D., & Chen, R. 2017, in AAS/Solar Phys. Div. Meet., Vol. 48, 300.01

Sun, X., Hoeksema, J. T., Liu, Y., et al. 2012, *Astrophys. J.*, 748, 77

Sun, X., Bobra, M. G., Hoeksema, J. T., et al. 2015, *Astrophys. J. Lett.*, 804, L28

Temmer, M., Veronig, A. M., Vršnak, B., et al. 2008, The Astrophysical Journal, 673, L95

Thalmann, J. K., Su, Y., Temmer, M., & Veronig, A. M. 2015, *Astrophys. J. Lett.*, 801, L23

Thernisien, A. 2011, *Astrophys. J. Suppl.*, 194, 33

Thernisien, A., Vourlidas, A., & Howard, R. A. 2009, *Solar Phys.*, 256, 111

Thompson, B. J., Cliver, E. W., Nitta, N., Delannée, C., & Delaboudinière, J. P. 2000, Geophysical Research Letters, 27, 1431

Thompson, B. J., Plunkett, S. P., Gurman, J. B., et al. 1998, *Geophys. Res. Lett.*, 25, 2465

Thompson, W. T. 2006, *Astron. Astrophys.*, 449, 791

Titov, D. V., Svedhem, H., McCoy, D., et al. 2006, Cosmic Research, 44, 334

Toriumi, S., & Wang, H. 2019, Living Reviews in Solar Physics, 16, 3

Török, T., & Kliem, B. 2005, *Astrophys. J. Lett.*, 630, L97

Tousey, R. 1973, in Space Research Conference, Vol. 2, 713–730

Tschernitz, J., Veronig, A. M., Thalmann, J. K., Hinterreiter, J., & Pötzi, W. 2018, The Astrophysical Journal, 853, 41

Tsurutani, B. T., Gonzalez, W. D., Lakhina, G. S., & Alex, S. 2003, Journal of Geophysical Research (Space Physics), 108, 1268

Tsurutani, B. T., Gonzalez, W. D., Tang, F., Akasofu, S. I., & Smith, E. J. 1988, *J. Geophys. Res.*, 93, 8519

Tsurutani, B. T., Hajra, R., Echer, E., & Gjerloev, J. W. 2015, Annales Geophysicae, 33, 519

Turmon, M., Jones, H. P., Malanushenko, O. V., & Pap, J. M. 2010, *Solar Phys.*, 262, 277

Ulrich, R. K. 1970, *Astrophys. J.*, 162, 993

Vaiana, G. S., Krieger, A. S., & Timothy, A. F. 1973, Solar Physics, 32, 81

van Ballegooijen, A. A., & Martens, P. C. H. 1989, *Astrophys. J.*, 343, 971

Vandas, M., Fischer, S., Dryer, M., Smith, Z., & Detman, T. 1996, *J. Geophys. Res.*, 101, 2505

Vemareddy, P., & Mishra, W. 2015, *Astrophys. J.*, 814, 59

Vemareddy, P., & Zhang, J. 2014, *Astrophys. J.*, 797, 80

Vlasov, V. I. 1981, Geomagnetism and Aeronomy, 21, 441

Vourlidas, A., Colaninno, R., Nieves-Chinchilla, T., & Stenborg, G. 2011, *Astrophys. J. Lett.*, 733, L23

Vourlidas, A., & Howard, R. A. 2006, *Astrophys. J.*, 642, 1216

Vourlidas, A., Lynch, B. J., Howard, R. A., & Li, Y. 2013, *Solar Phys.*, 284, 179

Vršnak, B., Amerstorfer, T., Dumbović, M., et al. 2019, The Astrophysical Journal, 877, 77

Vršnak, B., Ruždjak, D., Sudar, D., & Gopalswamy, N. 2004, *Astron. Astrophys.*, 423, 717

Vršnak, B., Žic, T., Vrbanec, D., et al. 2013, *Solar Phys.*, 285, 295

Waldmeier, M. 1970, *Solar Phys.*, 15, 167

Wang, H. 2006, *Astrophys. J.*, 649, 490

Wang, H., & Liu, C. 2010, *Astrophys. J. Lett.*, 716, L195

Wang, R., Liu, Y. D., Dai, X., et al. 2015, *Astrophys. J.*, 814, 80

Wang, R., Liu, Y. D., Dai, X., et al. 2015, The Astrophysical Journal, 814, 80

Wang, S., Liu, C., Liu, R., et al. 2012, *Astrophys. J. Lett.*, 745, L17

Wang, S., Liu, C., & Wang, H. 2012, *Astrophys. J. Lett.*, 757, L5

Wang, Y., Shen, C., Wang, S., & Ye, P. 2004, *Solar Phys.*, 222, 329

Wang, Y., Wang, B., Shen, C., Shen, F., & Lugaz, N. 2014, Journal of Geophysical Research (Space Physics), 119, 5117

Wang, Y., & Zhang, J. 2007, *Astrophys. J.*, 665, 1428

Wang, Y., & Zhang, J. 2008, The Astrophysical Journal, 680, 1516

Wang, Y. M., & Muglach, K. 2007, *Astrophys. J.*, 666, 1284

Wang, Y. M., Ye, P. Z., & Wang, S. 2003, Journal of Geophysical Research (Space Physics), 108, 1370

Webb, D. F., Cliver, E. W., Crooker, N. U., Cry, O. C. S., & Thompson, B. J. 2000, *J. Geophys. Res.*, 105, 7491

Webb, D. F., & Howard, T. A. 2012, Living Reviews in Solar Physics, 9, 3

Wiegelmann, T., Thalmann, J. K., & Solanki, S. K. 2014, Astronomy and Astrophysics Review, 22, 78

Williams, D. R., Török, T., Démoulin, P., van Driel-Gesztelyi, L., & Kliem, B. 2005, *Astrophys. J. Lett.*, 628, L163

Wilson, R. M. 1987, Planet. Space Sci., 35, 329

Woods, T. N., Eparvier, F. G., Hock, R., et al. 2012, *Solar Phys.*, 275, 115

Wu, C.-C., & Lepping, R. P. 2002, Journal of Geophysical Research (Space Physics), 107, 1346

Wu, Y. Q., Tang, Y. H., Dai, Y., & Wu, G. P. 2002, *Solar Phys.*, 207, 159

Xu, Z., Jiang, Y., Yang, J., Yang, B., & Bi, Y. 2016, *Astrophys. J. Lett.*, 820, L21

Yashiro, S., Akiyama, S., Gopalswamy, N., & Howard, R. A. 2006, *Astrophys. J. Lett.*, 650, L143

Yashiro, S., Gopalswamy, N., Akiyama, S., Michalek, G., & Howard, R. A. 2005, *J. Geophys. Res.*(Space Phys.), 110, A12S05

Yurchyshyn, V., Abramenko, V., & Tripathi, D. 2009, *Astrophys. J.*, 705, 426

Yurchyshyn, V., Yashiro, S., Abramenko, V., Wang, H., & Gopalswamy, N. 2005, *Astrophys. J.*, 619, 599

Yurchyshyn, V. B. 2002, *Astrophys. J.*, 576, 493

Zarro, D. M., Canfield, R. C., Strong, K. T., & Metcalf, T. R. 1988, *Astrophys. J.*, 324, 582

Zarro, D. M., Sterling, A. C., Thompson, B. J., Hudson, H. S., & Nitta, N. 1999, *Astrophys. J. Lett.*, 520, L139

Zhang, J., & Dere, K. P. 2006, *Astrophys. J.*, 649, 1100

Zhang, J., Dere, K. P., Howard, R. A., Kundu, M. R., & White, S. M. 2001, *Astrophys. J.*, 559, 452

Zhao, X. P., & Webb, D. F. 2003, Journal of Geophysical Research (Space Physics), 108, 1234

Zharkov, S., Green, L. M., Matthews, S. A., & Zharkova, V. V. 2011, *Astrophys. J. Lett.*, 741, L35

Zhou, G., Wang, J., & Cao, Z. 2003, *Astron. Astrophys.*, 397, 1057

Zirin, H., & Liggett, M. A. 1987, *Solar Phys.*, 113, 267

Zuccarello, F. P., Aulanier, G., & Gilchrist, S. A. 2016, The Astrophysical Journal, 821, L23

Zuccarello, F. P., Seaton, D. B., Mierla, M., et al. 2014, The Astrophysical Journal, 785, 88

Zurbuchen, T. H., Fisk, L. A., Lepri, S. T., & von Steiger, R. 2003, in American Institute of Physics Conference Series, Vol. 679, Solar Wind Ten, ed. M. Velli, R. Bruno, F. Malara, & B. Bucci, 604–607

Zurbuchen, T. H., & Richardson, I. G. 2006, *Space Sci. Rev.*, 123, 31

Publications attached with the thesis

1. **Sarkar, R.**, Srivastava, N., & Veronig, A. M. 2019, *"Lorentz Force Evolution Reveals the Energy Build-up Processes during Recurrent Eruptive Solar Flares"*, **Astrophysical Journal Letters**, 885, L17.

2. **Sarkar, R.**, Gopalswamy, N. & Srivastava, N. 2020, *"An Observationally Constrained Analytical Model for Predicting Magnetic Field Vectors of ICMEs at 1 AU"*, **Astrophysical Journal**, 888, 121.

The Astrophysical Journal Letters, 885:L17 (8pp), 2019 November 1 https://doi.org/10.3847/2041-8213/ab4da2

© 2019. The American Astronomical Society. All rights reserved.

Lorentz Force Evolution Reveals the Energy Build-up Processes during Recurrent Eruptive Solar Flares

Ranadeep Sarkar[1], Nandita Srivastava[1], and Astrid M. Veronig[2,3]

[1] Udaipur Solar Observatory, Physical Research Laboratory, Badi Road, Udaipur 313001, India; ranadeep@prl.res.in

[2] Institute of Physics, University of Graz, A-8010 Graz, Austria

[3] Kanzelhöhe Observatory for Solar and Environmental Research, University of Graz, A-9521 Treffen, Austria

Received 2019 September 6; revised 2019 October 11; accepted 2019 October 12; published 2019 October 30

Abstract

The energy release and build-up processes in the solar corona have significant implications in particular for the case of large recurrent flares, which pose challenging questions about the conditions that lead to the episodic energy release processes. It is not yet clear whether these events occur due to the continuous supply of free magnetic energy to the solar corona or because not all of the available free magnetic energy is released during a single major flaring event. In order to address this question, we report on the evolution of photospheric magnetic field and the associated net Lorentz force changes in ARs 11261 and 11283, each of which gave rise to recurrent eruptive M- and X-class flares. Our study reveals that after the abrupt downward changes during each flare, the net Lorentz force increases by (2–5) × 10^{22} dyne in between the successive flares. This distinct rebuild-up of net Lorentz forces is the first observational evidence found in the evolution of any nonpotential parameter of solar active regions (ARs), which suggests that new energy was supplied to the ARs in order to produce the recurrent large flares. The rebuild-up of magnetic free energy of the ARs is further confirmed by the observations of continuous shearing motion of moving magnetic features of opposite polarities near the polarity inversion line. The evolutionary pattern of the net Lorentz force changes reported in this study has significant implications, in particular, for the forecasting of recurrent large eruptive flares from the same AR and hence the chances of interaction between the associated CMEs.

Unified Astronomy Thesaurus concepts: Solar flares (1496); Solar active region magnetic fields (1975); Solar coronal mass ejections (310)

1. Introduction

Solar flares and coronal mass ejections (CMEs) are the most energetic phenomena that occur in the solar atmosphere. Together they can release large amounts of radiation, accelerated high-energy particles and gigantic clouds of magnetized plasma that may have severe space-weather impacts (Gosling 1993; Siscoe 2000; Daglis et al. 2004; Green et al. 2018). Therefore, understanding the source region characteristics of these solar energetic events has become a top priority in space-science research.

Complex large active regions (ARs) on the Sun are the main sources of large flares and most energetic CMEs (Zirin & Liggett 1987; Sammis et al. 2000; Falconer et al. 2002; Wang & Zhang 2008; Tschernitz et al. 2018; Toriumi & Wang 2019). Understanding the energy build-up processes in the source ARs has significant implications, in particular, for the case of recurrent flares, which may lead to recurrent CMEs and hence to their interaction, if the following CME has a larger speed than the preceding one.

Recurrent large flares pose challenging questions regarding the conditions that lead to the episodic energy release processes (Nitta & Hudson 2001; DeVore & Antiochos 2008; Archontis et al. 2014; Romano et al. 2015). In particular, it is not yet clear whether these events occur due to the continuous supply of free magnetic energy to the solar corona or because not all of the available free magnetic energy is released during a single flaring event. Emergence of new magnetic flux (Nitta & Hudson 2001) or photospheric shearing motions (Romano et al. 2015) have been observed during recurrent flares. However, quantitatively it is difficult to study the temporal evolution of the free magnetic energy of any AR due to the absence of any practical or direct method to measure the vector magnetic field in the coronal volume (Wiegelmann et al. 2014). Therefore, the spatial and temporal evolution of source region parameters which can be solely estimated from the photospheric magnetic field becomes important to probe the energy generation processes responsible for solar flares.

Hudson et al. (2008) were the first to quantitatively estimate the back reaction forces on the solar surface resulting from the implosion of the coronal magnetic field, which is required to release the energy during flares. They predicted that the photospheric magnetic fields should become more horizontal after the flare due to the act of the vertical Lorentz forces on the solar surface.

Fisher et al. (2012) introduced a practical method to calculate the net Lorentz force acting on the solar photosphere. Since then, it became one of the important nonpotential parameters to study the flare associated changes in the source region characteristics. Earlier studies revealed that large eruptive flares are associated with an abrupt downward change of the Lorentz force (Petrie & Sudol 2010; Petrie 2012). Comparing the magnitude of those changes associated with eruptive and confined flares, Sarkar & Srivastava (2018) reported that the change in Lorentz force is larger for eruptive flares. However, studies on the evolution of the photospheric magnetic field and the associated Lorentz force changes for the case of recurrent eruptive large flares have not been performed so far.

In this Letter, we study the evolution of the photospheric magnetic field and the associated net Lorentz force change during recurrent large flares which occurred in AR 11261 and AR 11283. Tracking the evolution of the net Lorentz force over

Table 1
Recurrent Flares Observed in AR 11261 and AR 11283

Active	Flares (*GOES*)					
Region	Date yyyy mm dd	Start Time (UT) hh:mm	Peak Time (UT) hh:mm	End Time (UT) hh:mm	Class	Location
AR 11261	2011 Aug 03	13:17	13:45	14:30	M6.0	N17W30
AR 11261	2011 Aug 04	03:41	03:45	03:57	M9.3	N16W38
AR 11283	2011 Sep 06	01:35	01:50	02:05	M5.3	N13W07
AR 11283	2011 Sep 06	22:12	22:20	22:24	X2.1	N14W18
AR 11283	2011 Sep 07	22:32	22:38	22:44	X1.8	N14W31

the period of all the recurrent flares under study, we address the following key questions.

- (i) Are the observed changes in net Lorentz force during the flare related to the linear momentum of the associated CME?
- (ii) Are there any prominent signatures related to the Lorentz force evolution which might reveal the restructuring of the magnetic field after the first flare and its associated CME? If so, these signatures might be indicative of rebuild-up of nonpotentiality of the coronal magnetic field and hence the imminent more powerful flare/CME.
- (iii) What causes the build-up of free magnetic energy between the successive flares?

2. Data Analysis

All the large recurrent M- and X-class flares that occurred in ARs 11261 (SOL2011-08-03T13:17 and SOL2011-08-04T03:41) and 11283 (SOL2011-09-06T01:35, SOL2011-09-06T22:12 and SOL2011-09-07T22:32) were well observed by the Atmospheric Imaging Assembly (AIA; Lemen et al. 2012) and the Helioseismic and Magnetic Imager (HMI; Schou et al. 2012) on board the *Solar Dynamics Observatory* (*SDO*; Pesnell et al. 2012). To study the evolution of the photospheric magnetic field associated with the recurrent flares, we have used the HMI vector magnetogram series from the version of Space weather HMI Active Region Patches (SHARP; Turmon et al. 2010) having a spatial resolution of 0.″5 and 12 minute temporal cadence.

As the errors in the vector magnetic field increase toward the limb, we have restricted our analysis to only those flares for which the flaring location of the AR was well within ±40° from the central meridian. Moreover, we focus on the recurrent flares that initiated in the same part of the polarity inversion line (PIL) of the AR and occurred within an interval of a day or less than that. This approach allows us to study the energy release and rebuild-up processes related to the recurrent flares by tracking the magnetic properties of a same flare productive part of an AR over a period of several days. Following the aforementioned criteria, we analyze the two recurrent M-class flares (SOL2011-08-03T13:17 and SOL2011-08-04T03:41) which occurred in AR 11261 during 2011 August 3 to 4 and three recurrent flares (SOL2011-09-06T01:35, SOL2011-09-06T22:12, and SOL2011-09-07T22:32) which occurred in AR 11283 during the period of 2011 September 5 to 8 (Table 1).

To calculate the net Lorentz force changes we have used the formulation introduced by Fisher et al. (2012). The change in the horizontal and radial component of the Lorentz force within a temporal window of δt is given as

$$\delta F_{\mathrm{r}} = \frac{1}{8\pi}\int_{A_{\mathrm{ph}}} (\delta B_{\mathrm{r}}{}^{2} - \delta B_{\mathrm{h}}{}^{2})\, dA \tag{1}$$

$$\delta F_{\mathrm{h}} = \frac{1}{4\pi}\int_{A_{\mathrm{ph}}} \delta(B_{\mathrm{h}} B_{\mathrm{r}})\, dA \tag{2}$$

where B_{h} and B_{r} are the horizontal and radial components of the magnetic field, F_{h} and F_{r} are the horizontal and radial components of the Lorentz force calculated over the volume of the AR, A_{ph} is the area of the photospheric domain containing the AR, and dA is the elementary surface area on the photosphere. Similar to Petrie (2012), we have reversed the signs in Equations (1) and (2) compared to Equations (9) and (10) of Fisher et al. (2012), as we are considering the forces acting on the photosphere from the above atmospheric volume instead of the equal and opposite forces acting on the above atmosphere from below.

As the flare related major changes in horizontal magnetic field and Lorentz forces are expected to occur close to the PIL (Wang 2006; Petrie & Sudol 2010; Petrie 2012; Sarkar & Srivastava 2018), we have selected subdomains (shown by the region enclosed by the green rectangular boxes in Figure 1) near the PIL on the flare productive part of each AR to carry out our analysis. As the recurrent flares studied in this paper occurred from the same part of the PIL, we are able to capture the evolution of the magnetic field over several days including the time of each flares within that same selected domain on the AR. In order to define the size, orientation, and location of the selected domains we examined the post-flare loops observed in the AIA 171 and 193 Å channels. Several studies have shown that the flare-reconnection process results in the simultaneous formation of a post-eruption arcade (PEA) and a flux rope above the PEA during solar eruptive events (Leamon et al. 2004; Longcope & Beveridge 2007; Qiu et al. 2007; Hu et al. 2014). Therefore in order to capture the magnetic imprints of the recurrent large eruptive flares on the solar photosphere, we have selected our region of interest in such a way so that the major post-flare arcade structures formed during each flare can be enclosed within that domain. The choice of such subdomains enables us to assume that the magnetic field on the side-boundaries enclosing the volume over those selected regions is largely invariant with time and the field strength on the top boundary is negligible as compared to that at the lower boundary on the photosphere. Therefore, only the photospheric magnetic field change contributes to the surface integrals as shown in Equations (1) and (2) to estimate the change in net Lorentz force acting on the photosphere from the above atmospheric volume.

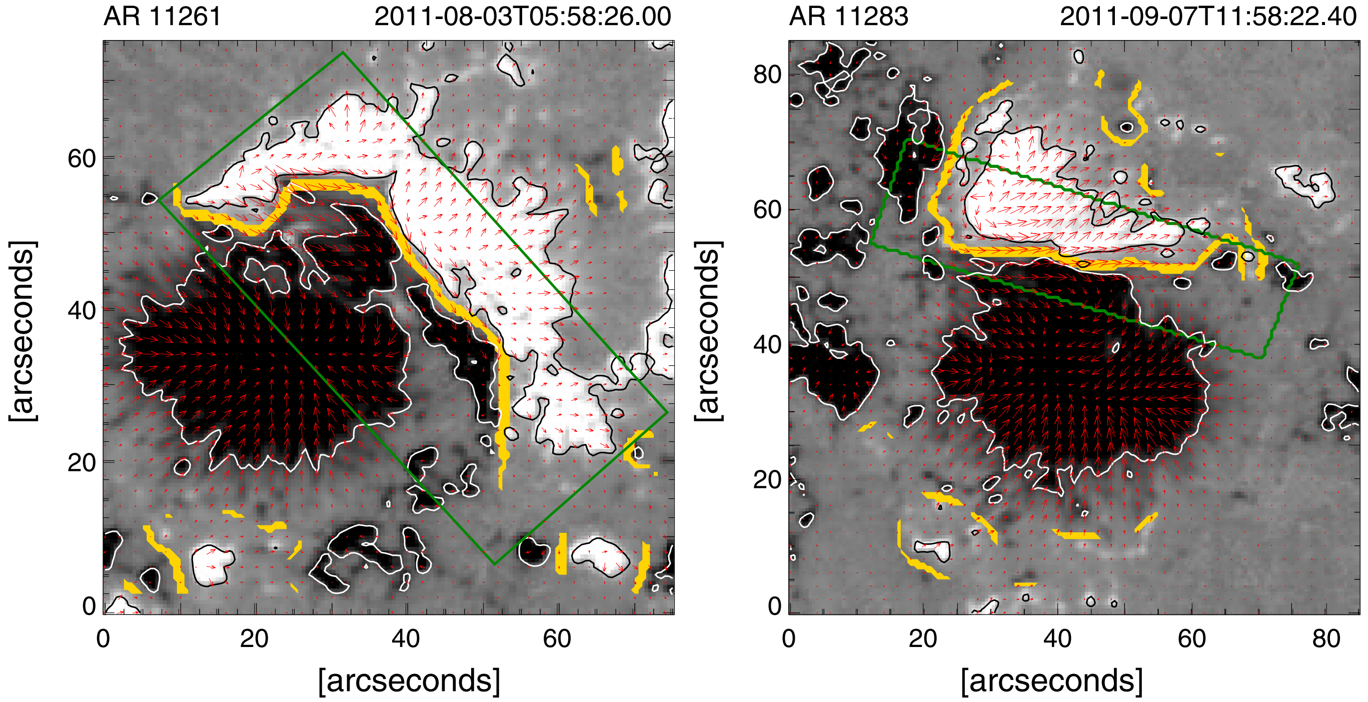

Figure 1. HMI vector magnetogram of AR 11261 (left panel) and AR 11283 (right panel). The radial component (B_r) of the magnetic field is shown in gray scale and the horizontal component (B_h) by red arrows, with saturation values ±500 G. The white/black solid line contours the region of negative/positive polarity of B_r having a magnitude greater than 500 G. The green rectangular boundary encloses the selected region within which all the calculations have been done. The yellow lines illustrate the polarity inversion line.

3. Result and Discussion

3.1. Abrupt Changes in Magnetic Field and Lorentz Force

Figure 2 depicts the abrupt changes in horizontal magnetic field and the radial component of net Lorentz forces calculated within the selected region of interest as shown in Figure 1. The distinct changes in the magnetic properties of AR 11261 and AR 11283 associated with the recurrent large M- and X-class flares are discussed as follows.

3.1.1. Magnetic Field Evolution in AR 11261

During the first M6.0 class flare (SOL2011-08-03T13:17) that occurred in AR 11261, the mean horizontal magnetic field increases approximately from 500 to 550 G and the associated net Lorentz force shows an abrupt downward change by approximately 2.8×10^{22} dyne. After the M6.0 class flare the mean horizontal magnetic field started to decrease and reached about 490 G prior to the M9.3 class flare (SOL2011-08-04T03:41). During the M9.3 class flare the mean horizontal magnetic field again approximately increased to 550 G. The associated change in net Lorentz force during this flare is about 5.1×10^{22} dyne which is almost two times larger than that associated with the previous M6.0 class flare.

In order to examine whether the kinematic properties of the associated CMEs are related to the flare induced Lorentz force changes or not, we obtain the true mass and the deprojected speed of each flare associated CME from Mishra et al. (2017). The two recurrent CMEs associated with the preceding M6.0 class and the following M9.3 class flares are hereinafter referred to as CME1 and CME2, respectively. Interestingly, CME2 was launched with a speed of $1700\,\mathrm{km\,s^{-1}}$, approximately 1.5 times higher than that of CME1 ($v = 1100\,\mathrm{km\,s^{-1}}$). The true masses of CME1 and CME2, estimated from the multiview of *STEREO-A* and *-B* coronagraph data, were 7.4×10^{12} kg and 10.2×10^{12} kg, respectively. Considering an error of $\pm 100\,\mathrm{km\,s^{-1}}$ in determining the CME speed (Mishra et al. 2017) and ±15% in estimating the CME mass (Bein et al. 2013; Mishra & Srivastava 2014), we derive the momentum of CME2 as $17 \times 10^{15} \pm 4 \times 10^{15}\,\mathrm{kg\,km\,s^{-1}}$, approximately twice the momentum of CME1 ($8 \times 10^{15} \pm 2 \times 10^{15}\,\mathrm{kg\,km\,s^{-1}}$). Therefore the magnitude of change in the net Lorentz force impulse during the two recurrent flares appears to be correlated with the associated CME momentum. This scenario is consistent with the flare related momentum balance condition where the Lorentz force impulse is believed to be proportional to the associated CME momentum (Fisher et al. 2012; Wang et al. 2012).

As the masses of the two CMEs were comparable, the successive Lorentz force impulse within a time window of approximately 14 hr from the same PIL of the AR with a larger change in magnitude during the following flare appears to be an important characteristic of the source AR in order to launch a high speed CME preceded by a comparatively slower one. This was an ideal condition for CME-CME interaction. Eventually, the two CMEs interacted at a distance of 145 solar radii (Mishra et al. 2017).

3.1.2. Magnetic Field Evolution in AR 11283

For all the three recurrent flares that occurred in AR 11283, the horizontal magnetic field and the net Lorentz force showed abrupt changes during each flare. It is noteworthy that the net Lorentz force increases substantially 2–4 hr prior to the occurrence of each flare, followed by a steep decrease of the same. The changes in net Lorentz force during the successive M5.3 (SOL2011-09-06T01:35), X2.1 (SOL2011-09-06T22:12), and X1.8-class (SOL2011-09-07T22:32) flares

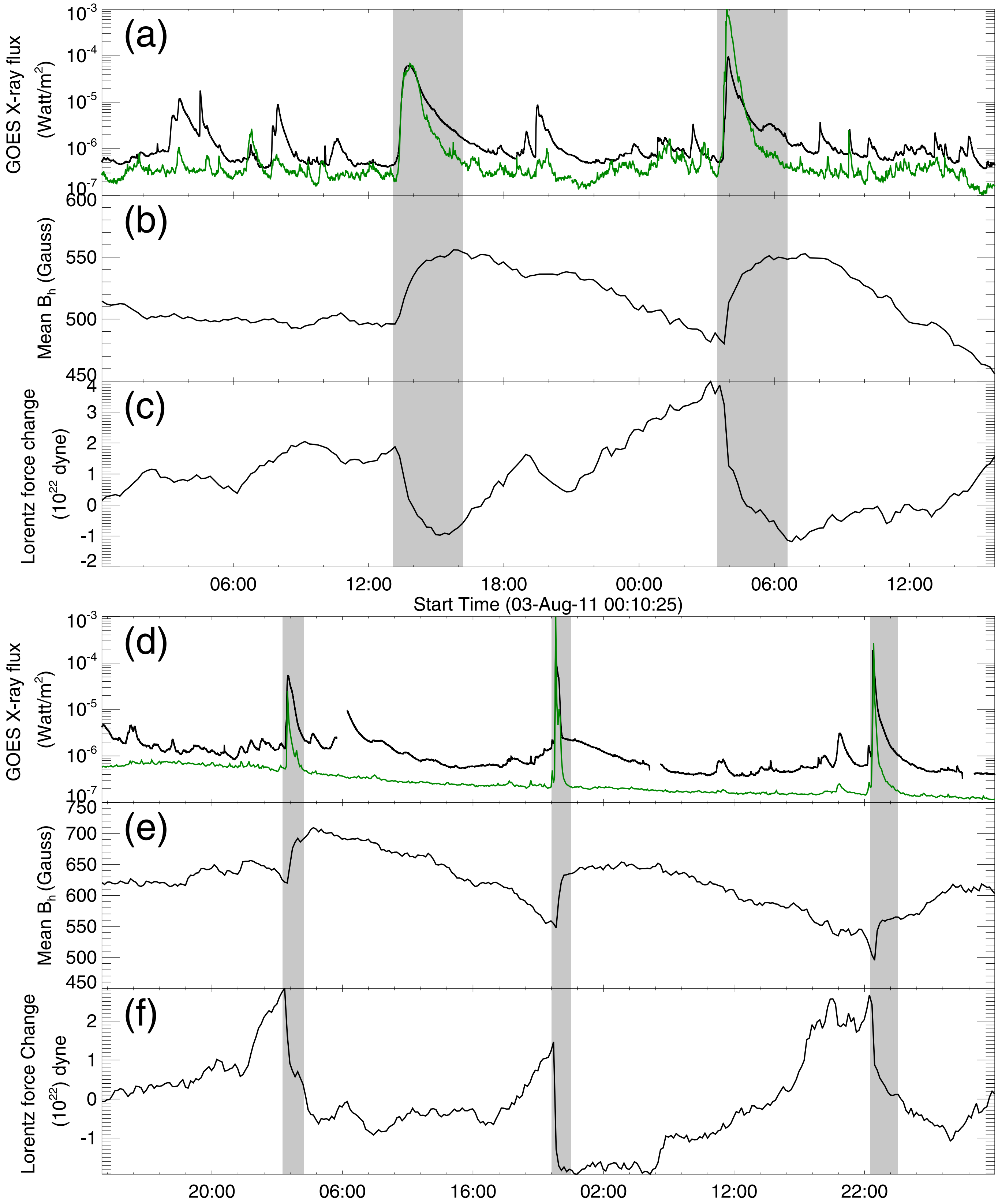

Figure 2. Temporal profile of the *GOES* 1–8 Å X-ray flux during the recurrent flares that occurred in AR 11261 (a) and AR 11283 (d). The solid green curves denote the temporal evolution of the brightening calculated within the field of view of the AR in the AIA 1600 Å channel. Evolution of the horizontal magnetic field ((b) and (e)) and changes in the radial component of the Lorentz force ((c) and (f)) within the selected regions (shown by rectangular boxes in Figure 1) of AR 11261 and AR 11283, respectively.

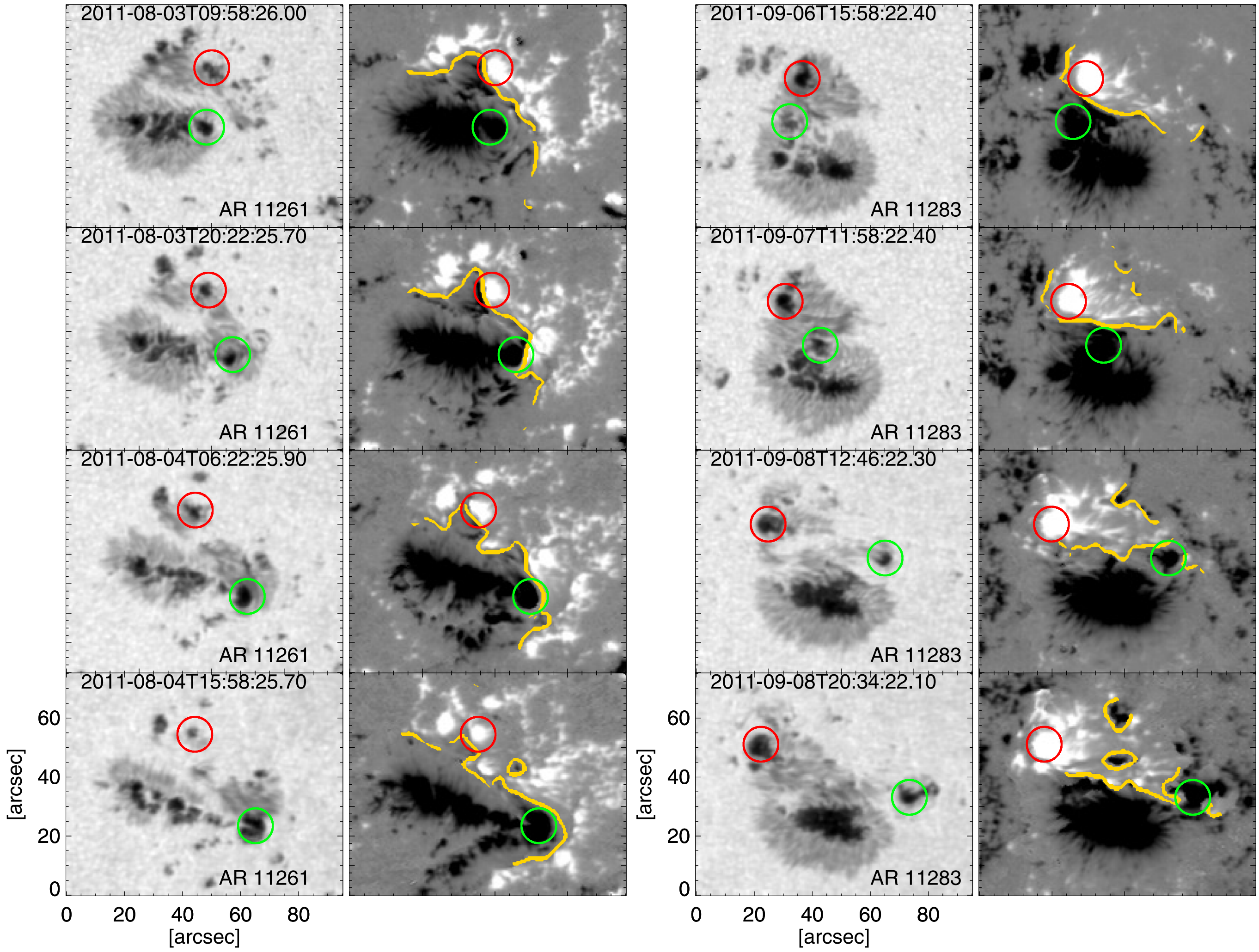

Figure 3. HMI continuum images of the flare productive part of AR 11261 (first column) and AR 11283 (third column). Different panels of each column show the temporal evolution of the sunspot group during the recurrent flares. The radial component of the HMI vector magnetic field of AR 11261 (second column) and AR 11283 (fourth column) within the same field of view as shown in the first and third columns respectively. Continuum images in each row of the first/third columns are cotemporal with the magnetic field maps shown in the same row of second/fourth column. The red and green circles depict the two prominent moving magnetic features of opposite polarities which show continuous antiparallel motion along the polarity inversion line denoted by the yellow solid lines.

were approximately 4×10^{22}, 3.5×10^{22}, and 3.5×10^{22} dyne respectively. All three flares were eruptive and the associated deprojected CME speeds were 640, 773, and 751 km s^{-1}, respectively, as reported in Soojeong Jang's Catalog (http://ccmc.gsfc.nasa.gov/requests/fileGeneration.php). For all three flares the magnitude of change in net Lorentz force were almost comparable and the associated CME speeds also do not differ too much. As the three associated CMEs were launched within an interval of a day and with approximately similar speed, there was no chance of interactions among them in the interplanetary space within 1 au. As the CDAW catalog (https://cdaw.gsfc.nasa.gov/CME_list/) reports poor mass estimation for the aforementioned CMEs, we do not compare the linear momentum of those CMEs with the associated change in net Lorentz force.

In strong events, flare induced artifacts in the magnetic field vectors may result in magnetic transients during the stepwise changes of the photospheric magnetic field (Sun et al. 2017). However, these magnetic transients as reported by Sun et al. (2017) are spatially localized in nature and temporally can be resolved within a timescale of ≈10 minutes. Moreover, the transient features do not show any permanent changes in the magnetic field evolution during the flares. The evolution of the horizontal magnetic field and the net Lorentz force as shown in Figure 2 are estimated within a large area on the photosphere using the 12 minute cadence vector magnetogram data. Therefore, within the time window of the stepwise changes in the horizontal magnetic field, there is no discontinuity found in the field evolution during the flares under this study as potentially occurring magnetic transients would be spatially and temporally averaged out. Hence, there are no flare related artifacts involved in the derivation of the net Lorentz force in this study.

3.2. Lorentz Force Rebuild-up in between the Successive Flares

After the abrupt downward change in net Lorentz force during each large flare that occurred in AR 11261 and AR 11283, the net Lorentz force started to rebuild-up in between the successive flares (see Figure 2). Starting from the magnitude of -1×10^{22} dyne after the M6.0 class, the change

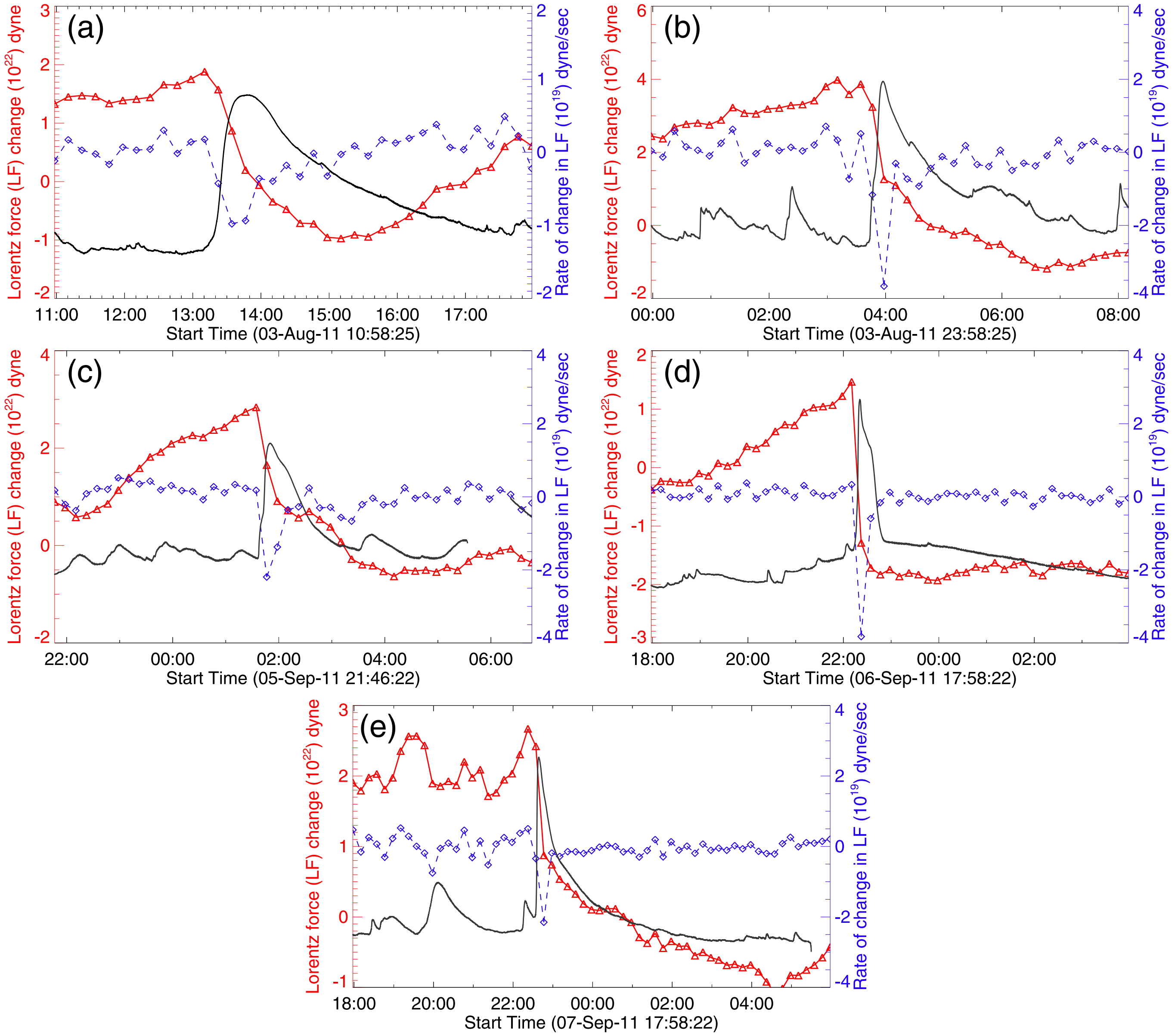

Figure 4. Relative evolution of *GOES* 1–8 Å X-ray flux (black solid lines) with that of the associated Lorentz force (red solid lines) during the recurrent flares under study. The blue dotted line denotes the rate of change in Lorentz force during the flares.

in net Lorentz force reached to a magnitude of 4×10^{22} dyne until the next M9.3 class flare occurred in AR 11261. Similarly in AR 11283, the net Lorentz force was rebuilt-up by approximately 2×10^{22} dyne in between the M5.3 and X2.1 class flares, and again rebuilt-up by approximately 4×10^{22} dyne before the X1.8-class flare. This rebuild-up of the Lorentz force reveals the restructuring of the magnetic field configuration in the vicinity of the PIL in order to increase the nonpotentiality of the coronal magnetic field which in turn relaxes by producing the next recurrent flare.

We tested the sensitivity of the obtained results on the size of the bounding boxes selected around the PIL. Increasing the bounding box (see Figure 1) from approx 20 to 40 Mm, the evolutionary pattern of the Lorentz force remains similar. However, integrating the Lorentz force density over the whole AR area dilutes the flare-associated changes in the estimated net Lorentz force profile.

The rebuild-up of net Lorentz force in between the recurrent flares could be the consequence of the continuous shearing motion along the PIL. Figure 3 shows the continuous shearing motion observed for the two prominent moving magnetic features (MMFs) of opposite magnetic polarities (indicated by the red and green circles). The antiparallel motions of these MMFs along the two sides of the PIL of each AR during the recurrent flares provide evidence for rebuild-up of nonpotential energy in between the successive flares. Therefore, the evolution of Lorentz force appears to be a clear indication of energy rebuild-up processes in order to produce successive flares from the same part of any AR.

Importantly, for the first time we have shown the evolution of a nonpotential parameter (net vertical Lorentz force change) that reveals the rebuild-up of nonpotentiality of the AR in between the successive large flares. Indeed, this is a significant finding and has important implications. In particular, the evolutionary pattern of the net vertical Lorentz force change can be used for forecasting the recurrent large eruptive flares from the same AR. Furthermore, the associated successive CMEs from the same AR, will in turn enhance their chance of being launched in the same direction. In this scenario, the following faster CME may interact with the preceding slower one in the corona or interplanetary space, which can significantly enhance their geoeffectiveness (Wang et al. 2003; Farrugia & Berdichevsky 2004; Farrugia et al. 2006; Lugaz & Farrugia 2014).

Currently available machine-learning algorithms for flare prediction use, among many other parameters, the evolution of Lorentz force integrated over the whole AR, which does not show a high skill score in the forecast verification metrics (Bobra & Couvidat 2015). However, the distinct changes in the vertical component of the Lorentz forces integrated near the PIL demonstrated in our study, could prove to be an important parameter to train and test the machine-learning algorithms in order to improve the current capability of flare-forecasting.

3.3. Relative Evolution of the GOES *X-Ray Flux with that of the Associated Lorentz Force During the Flares*

The temporal evolution of the *GOES* 1–8 Å X-ray flux and the associated change in Lorentz force shows that the Lorentz force starts to decrease at the start of the rising phase of the *GOES* flares (Figure 4). Most interestingly, the Lorentz force decreases with a pattern similar to the decay phase of the *GOES* X-ray flux during all the flares. Among all five flares (see Table 1), the decay phase of the X2.1 class flare (panel (d) of Figure 4) was significantly steeper than the other four flares. This reflects in the associated changes in Lorentz force. The Lorentz force also decreases sharply during that X2.1 class flare in comparison to the other flares. The derived rate of change in net Lorentz force associated with the X2.1 class flare is 3×10^{19} dyne s^{-1} (Figure 4), which is the highest among all the five flares studied in this work.

These results suggest that the change in Lorentz force is not only related to the phase of impulsive flare energy release, but takes place over a longer interval and follows a similar evolutionary pattern like the decay phase of the *GOES* soft X-ray flux. This could be associated with a slower structuring of the coronal magnetic field during the decay phase of the flaring events.

4. Conclusion

Studying the evolution of the photospheric magnetic field and the associated Lorentz force change during the recurrent large flares that occurred in AR 11261 and AR 11283, we find that the vertical component of Lorentz force undergoes abrupt downward changes during all the flares. This result is consistent with earlier studies (Wang 2006; Petrie & Sudol 2010; Petrie 2012; Sarkar & Srivastava 2018). The observed increase in horizontal magnetic field during each flare is in agreement with the conjecture given by Hudson et al. (2008), which suggests that the magnetic loops should undergo a sudden shrinkage or implosion due to the energy release processes during flares. This also supports the results obtained by Romano et al. (2015), which show a decrease in the dip angle after each large flare that occurred in AR 11283. Interestingly, the decrease in horizontal magnetic field in between the successive flares reported in our study, could be due to the storage of newly supplied energy that increases the coronal magnetic pressure, thereby stretching the magnetic loops upward as proposed by Hudson (2000).

Our study also reveals that the decrease in Lorentz force is not only related to the phase of impulsive flare energy release, but takes place over a longer interval that covers also the decay phase of the flaring events. The magnitude of change in net Lorentz forces reported in this work, appears to be correlated with the linear momentum of the associated CME. This scenario is consistent with the flare related momentum balance condition where the Lorentz force impulse is believed to be proportional to the associated CME momentum (Fisher et al. 2012; Wang et al. 2012).

It is noteworthy that the flare-associated momentum conservation is not only related to the bodily transfer of mass in the form of CMEs, but also includes the effects related to explosive chromospheric evaporation (Hudson et al. 2012). However, quantifying the momentum related to the chromospheric evaporation during the flares under this study is not possible, as this requires spectroscopic observations of both the hot upflowing and cool downflowing plasma. Such measurements are rarely available, due to the localized and dynamic nature of solar flares in contrast to the limited spatio-temporal coverage of spectrometers. However, comparing the values we obtain for the CME momentum, which is of the order of 10^{15} kg km s^{-1}, with the momentum related to chromospheric evaporation flows in large flares as reported in the literature, which is of the order of 10^{13}–10^{14} kg km s^{-1} (Zarro et al. 1988; Canfield et al. 1990; Hudson et al. 2012), we may conclude that the momentum changes related to the CME are the dominant contribution. Therefore, the correlation between the Lorentz force impulse and the CME momentum in the large recurrent eruptive flares reported in our study is valid as the effects of impulsive chromospheric evaporation are at least an order of magnitude smaller.

Most importantly, after the abrupt downward changes during each flare, the net Lorentz force significantly increases to a higher value than that was observed few hours before the flaring event, and only then the subsequent (recurrent) energetic flare occurred. This rebuild-up of net Lorentz force in between the successive flares suggests that the magnetic field configuration in the vicinity of the PIL is restructured in order to increase the nonpotentiality of the coronal magnetic field. Observations of the continuous shearing motions of the MMFs on the two sides of the PIL of each AR provide supporting evidence for rebuild-up of nonpotential energy.

Romano et al. (2015) have also reported the shearing motion along the PIL of AR 11283 during the recurrent large M- and X-class flares. They have attributed these photospheric horizontal motions as the possible cause of monotonic injection of magnetic helicity in the corona, which might have resulted in the episodic energy release processes, leading to the recurrent flares. However, the evolution of the horizontal magnetic field and the associated Lorentz force reported in our study, clearly indicates the energy rebuild-up processes in order to produce successive flares from the same part of the AR. Therefore, we conclude that the recurrent flares studied in this work occurred due to the newly supplied energy to the AR through the continuous shearing motions of photospheric magnetic field in between the successive flares.

We thank the referee for helpful comments that improved the quality of this manuscript. We acknowledge NASA/*SDO* and the AIA and HMI science teams for data support. A.M.V. acknowledges the Austrian Science Fund (FWF): P27292-N20. This work was supported by the Indo-Austrian joint research project No. INT/AUSTRIA/BMWF/P-05/2017 and OeAD project No. IN 03/2017.

ORCID iDs

Ranadeep Sarkar https://orcid.org/0000-0001-6457-5207
Nandita Srivastava https://orcid.org/0000-0002-0452-5838
Astrid M. Veronig https://orcid.org/0000-0003-2073-002X

References

Archontis, V., Hood, A. W., & Tsinganos, K. 2014, ApJL, 786, L21
Bein, B. M., Temmer, M., Vourlidas, A., Veronig, A. M., & Utz, D. 2013, ApJ, 768, 31
Bobra, M. G., & Couvidat, S. 2015, ApJ, 798, 135
Canfield, R. C., Zarro, D. M., Metcalf, T. R., & Lemen, J. R. 1990, ApJ, 348, 333
Daglis, I., Baker, D., Kappenman, J., Panasyuk, M., & Daly, E. 2004, SpWea, 2, S02004
DeVore, C. R., & Antiochos, S. K. 2008, ApJ, 680, 740
Falconer, D. A., Moore, R. L., & Gary, G. A. 2002, ApJ, 569, 1016
Farrugia, C., & Berdichevsky, D. 2004, AnGeo, 22, 3679
Farrugia, C. J., Jordanova, V. K., Thomsen, M. F., et al. 2006, JGRA, 111, A11104
Fisher, G. H., Bercik, D. J., Welsch, B. T., & Hudson, H. S. 2012, SoPh, 277, 59
Gosling, J. T. 1993, PhFlB, 5, 2638
Green, L. M., Török, T., Vršnak, B., Manchester, W., & Veronig, A. 2018, SSRv, 214, 46
Hu, Q., Qiu, J., Dasgupta, B., Khare, A., & Webb, G. M. 2014, ApJ, 793, 53
Hudson, H. S. 2000, ApJL, 531, L75
Hudson, H. S., Fisher, G. H., & Welsch, B. T. 2008, in ASP Conf. Ser. 383, Subsurface and Atmospheric Influences on Solar Activity, ed. R. Howe et al. (San Francisco, CA: ASP), 221
Hudson, H. S., Fletcher, L., Fisher, G. H., Abbett, W. P., & Russell, A. 2012, SoPh, 277, 77
Leamon, R. J., Canfield, R. C., Jones, S. L., et al. 2004, JGRA, 109, A05106
Lemen, J. R., Title, A. M., Akin, D. J., et al. 2012, SoPh, 275, 17
Longcope, D. W., & Beveridge, C. 2007, ApJ, 669, 621
Lugaz, N., & Farrugia, C. J. 2014, GeoRL, 41, 769
Mishra, W., & Srivastava, N. 2014, ApJ, 794, 64
Mishra, W., Wang, Y., Srivastava, N., & Shen, C. 2017, ApJS, 232, 5
Nitta, N. V., & Hudson, H. S. 2001, GeoRL, 28, 3801
Pesnell, W. D., Thompson, B. J., & Chamberlin, P. C. 2012, SoPh, 275, 3
Petrie, G. J. D. 2012, ApJ, 759, 50
Petrie, G. J. D., & Sudol, J. J. 2010, ApJ, 724, 1218
Qiu, J., Hu, Q., Howard, T. A., & Yurchyshyn, V. B. 2007, ApJ, 659, 758
Romano, P., Zuccarello, F., Guglielmino, S. L., et al. 2015, A&A, 582, A55
Sammis, I., Tang, F., & Zirin, H. 2000, ApJ, 540, 583
Sarkar, R., & Srivastava, N. 2018, SoPh, 293, 16
Schou, J., Scherrer, P. H., Bush, R. I., et al. 2012, SoPh, 275, 229
Siscoe, G. 2000, JASTP, 62, 1223
Sun, X., Hoeksema, J. T., Liu, Y., Kazachenko, M., & Chen, R. 2017, ApJ, 839, 67
Toriumi, S., & Wang, H. 2019, LRSP, 16, 3
Tschernitz, J., Veronig, A. M., Thalmann, J. K., Hinterreiter, J., & Pötzi, W. 2018, ApJ, 853, 41
Turmon, M., Jones, H. P., Malanushenko, O. V., & Pap, J. M. 2010, SoPh, 262, 277
Wang, H. 2006, ApJ, 649, 490
Wang, S., Liu, C., & Wang, H. 2012, ApJL, 757, L5
Wang, Y., & Zhang, J. 2008, ApJ, 680, 1516
Wang, Y. M., Ye, P. Z., & Wang, S. 2003, JGRA, 108, 1370
Wiegelmann, T., Thalmann, J. K., & Solanki, S. K. 2014, A&ARv, 22, 78
Zarro, D. M., Canfield, R. C., Strong, K. T., & Metcalf, T. R. 1988, ApJ, 324, 582
Zirin, H., & Liggett, M. A. 1987, SoPh, 113, 267

The Astrophysical Journal, 888:121 (12pp), 2020 January 10 https://doi.org/10.3847/1538-4357/ab5fd7

© 2020. The American Astronomical Society. All rights reserved.

An Observationally Constrained Analytical Model for Predicting the Magnetic Field Vectors of Interplanetary Coronal Mass Ejections at 1 au

Ranadeep Sarkar[1,2], Nat Gopalswamy[3], and Nandita Srivastava[1]
[1] Udaipur Solar Observatory, Physical Research Laboratory, Badi Road, Udaipur 313001, India; ranadeep@prl.res.in
[2] Discipline of Physics, Indian Institute of Technology, Gandhinagar 382355, India
[3] NASA Goddard Space Flight Center, Greenbelt, MD 20771, USA

Received 2019 July 17; revised 2019 December 4; accepted 2019 December 6; published 2020 January 16

Abstract

We report on an observationally constrained analytical model, the INterplanetary Flux ROpe Simulator (INFROS), for predicting the magnetic field vectors of coronal mass ejections (CMEs) in the interplanetary medium. The main architecture of INFROS involves using the near-Sun flux rope properties obtained from the observational parameters that are evolved through the model in order to estimate the magnetic field vectors of interplanetary CMEs (ICMEs) at any heliocentric distance. We have formulated a new approach in INFROS to incorporate the expanding nature and the time-varying axial magnetic field strength of the flux rope during its passage over the spacecraft. As a proof of concept, we present the case study of an Earth-impacting CME which occurred on 2013 April 11. Using the near-Sun properties of the CME flux rope, we have estimated the magnetic vectors of the ICME as intersected by the spacecraft at 1 au. The predicted magnetic field profiles of the ICME show good agreement with those observed by the in situ spacecraft. Importantly, the maximum strength (10.5 ± 2.5 nT) of the southward component of the magnetic field (Bz) obtained from the model prediction is in agreement with the observed value (11 nT). Although our model does not include the prediction of the ICME plasma parameters, as a first-order approximation, it shows promising results in forecasting of Bz in near real time, which is critical for predicting the severity of the associated geomagnetic storms. This could prove to be a simple space-weather forecasting tool compared to the time-consuming and computationally expensive MHD models.

Unified Astronomy Thesaurus concepts: Solar coronal mass ejections (310); Solar flares (1496); Space weather (2037)

1. Introduction

Coronal mass ejections (CMEs) are powerful expulsions of gigantic clouds of magnetized plasma that routinely erupt from the Sun and propagate out through the solar system. When such an eruption is directed toward Earth with high speed and its north–south magnetic field component (Bz) is directed toward the south, an intense magnetic storm occurs upon the impact of the CME on Earth's magnetosphere (Wilson 1987; Tsurutani et al. 1988; Gonzalez et al. 1999; Huttunen et al. 2005; Yurchyshyn et al. 2005; Gopalswamy et al. 2008). The storm can occur when the interplanetary flux rope (FR) and/or the sheath between the FR and the associated shock has southward Bz. Therefore, prior knowledge of the strength and orientation of the magnetic field embedded in the FR is required in order to forecast the severity of geomagnetic storms caused by CMEs.

Several modeling efforts have been made in order to predict Bz at 1 au (Odstrčil & Pizzo 1999; Shen et al. 2014; Savani et al. 2015; Jin et al. 2017; Kay & Gopalswamy 2017; Möstl et al. 2018). However, due to the complexity of the Sun–Earth system in a time-dependent heliospheric context, the semi-analytical and global MHD models are usually unable to reproduce the strength and orientation of the magnetic field vectors observed by the in situ spacecraft. The FR from Eruption Data (FRED) technique published recently can be used to obtain the magnetic properties of the near-Sun coronal FRs from the photospheric magnetic flux under post-eruption arcades (PEAs) and the geometric properties of the FR obtained from the fitting of white-light coronagraphic structures (Gopalswamy et al. 2018a, 2018b). In this work, we developed an analytical model, the INterplanetary Flux ROpe Simulator (INFROS), that utilizes FRED parameters as realistic inputs and evolves those parameters in real time to predict the magnetic field vectors of interplanetary coronal mass ejections (ICMEs) reaching Earth.

Apart from using realistic inputs, we formulated a new approach in our model to incorporate the expanding nature and the time-varying axial magnetic field strength of the FR during its passage over the spacecraft. In contrast to existing models (Savani et al. 2015; Kay & Gopalswamy 2017; Möstl et al. 2018), our approach is unique in that it does not involve any free parameters like the dimension, axial field strength, time of passage, and the speed of the ICME at 1 au. Therefore, INFROS is the first such model that uses realistic inputs to predict the magnetic field vectors of ICMEs without involving any free parameters.

In principle, INFROS can be used to estimate the magnetic field vectors of ICMEs at any heliocentric distance. Importantly, the prediction of magnetic field vectors of Earth-reaching ICMEs at 1 au is crucial for space-weather forecasting. Therefore, in this paper, we considered this heliocentric distance to be 1 au for explaining the development of the model.

This article is organized as follows. The observational reconstruction techniques of the near-Sun FR parameters are discussed in Section 2. In Section 3, we describe the model architecture developed to predict the ICME vector profiles at 1 au. We validate our model for a test case in Section 4. Finally, we summarize our results and discuss their implications for space-weather forecasting in Section 5.

2. Near-Sun Observations of FR Properties

We determine the geometric and magnetic properties of the near-Sun FRs using the FRED technique as described in this section.

2.1. Geometrical Properties

We determine the three-dimensional morphology and the propagation direction of CMEs by using the graduated cylindrical shell (GCS; Thernisien 2011) model. This model fits the geometric structure of CMEs as observed by white-light coronagraphs such as the Large Angle and Spectrometric Coronagraph (LASCO; Brueckner et al. 1995) on board the *Solar and Heliospheric Observatory* (*SOHO*; Domingo et al. 1995) mission and the Sun Earth Connection Coronal and Heliospheric Investigation (SECCHI; Howard et al. 2008) on board the *Solar Terrestrial Relations Observatory* (*STEREO*; Kaiser et al. 2008) mission. Using the GCS model, we obtain the propagation longitude (ϕ) and latitude (θ), half-angular width (β), aspect ratio (κ), tilt angle (γ) with respect to the solar equator, and the leading-edge height (h) of the CME FR.

The parameter κ constrains the rate of expansion of the CME FR under the assumption of self-similar expansion. Therefore, the cross-sectional radius (r) of the self-similarly expanding FR at any heliocentric distance R ($=h - r$) can be obtained using the relation $r = \kappa h/(1+\kappa)$. On the other hand, the length (L) of the FR can be estimated from the relation $L = 2\beta R$, where 2β is the separation angle between the two legs of the CME in radians.

2.2. Magnetic Properties

Observational approaches to determine the three magnetic parameters that completely define any force-free FR are discussed as follows.

2.2.1. Axial Field Strength (B_0)

Several studies have shown that the azimuthal (poloidal) flux of magnetic FRs formed due to reconnection is approximately equal to the low-coronal reconnection flux, which can be obtained from either the photospheric magnetic flux underlying the area swept out by the flare ribbons (Longcope et al. 2007; Qiu et al. 2007) or the magnetic flux underlying the PEAs (Gopalswamy et al. 2017). Combining the geometrical parameters of the FR obtained from the GCS fitting as discussed in Section 2.1 with the estimation of the reconnected magnetic flux, Gopalswamy et al. (2018b) introduced the FRED model which shows that the axial magnetic field strength of the FR can be determined using a constant alpha force-free FR model (Lundquist 1950). We thereby obtain the magnetic field strength (B_0) along the FR axis using the relation (Gopalswamy et al. 2018a, 2018b),

$$B_0 = \frac{\phi_p x_{01}}{Lr}, \tag{1}$$

where ϕ_p is the azimuthal magnetic flux taken as the reconnection flux, x_{01} (=2.4048) is the first zero of the Bessel function J_0, L is the length, and r is the cross-sectional radius of the FR.

2.2.2. Direction of the Axial Magnetic Field and the Sign of Helicity

In order to determine the direction of the axial magnetic field and the helicity sign (chirality) associated with the FR, we first apply the hemispheric helicity rule to the source active region of the CME as a first-order approximation (Pevtsov et al. 1995; Bothmer & Schwenn 1998). However, the statistical studies by Liu et al. (2014) show that the hemispheric rule is followed only in 60% of cases. Therefore, in order to confirm the chirality and axial orientation of the FRs, we use other signatures such as preflare sigmoidal structures (Rust & Kumar 1996), J-shaped flare ribbons (Janvier et al. 2014), coronal dimmings (Thompson et al. 2000; Webb et al. 2000; Gopalswamy et al. 2018c), coronal cells (Sheeley et al. 2013), or filament orientations (Hanaoka & Sakurai 2017). Analyzing the locations of the two core dimming regions or the two ends of the preflare sigmoidal structure, one can identify the locations of the two footpoints of the FR. Thereafter, the locations of the FR footpoints can be overlaid on the line-of-sight magnetogram to determine in which magnetic polarities the FR is rooted (Palmerio et al. 2017). Once the direction of the axial field is determined, one can confirm the helicity sign (chirality) from the positive and negative polarities that are divided by the neutral line (Bothmer & Schwenn 1998; Marubashi et al. 2015; Gopalswamy et al. 2018a).

CMEs may undergo rotation in the lower corona depending on the amount of sigmoidality or the skew present in the associated pre-eruptive FR structure (Lynch et al. 2009). Therefore, one can get a mismatch between the FR orientation determined from the on-disk observations and the tilt angle of the CME obtained from the GCS fitting. Moreover, considering an uncertainty of $\pm 20°$ in determining the on-disk axis orientation (Palmerio et al. 2018) and $\pm 10°$ in determining the GCS tilt angle (Thernisien et al. 2009), one can obtain a difference in the angles of up to $\pm 30°$ between the GCS tilt and the on-disk axis orientation, in the absence of any significant rotation of the associated CME. Therefore, in order to resolve the 180° ambiguity in determining the FR axis orientation from the GCS tilt, we consider the smallest angle ($<180°$) between the on-disk and the GCS axis orientation. In this way, we can determine the direction of the axial magnetic field of the CME observed in the coronagraphic field of view.

3. Modeling the Interplanetary FRs Using the Near-Sun Observations

We track the evolution of the near-Sun FR properties using the analytical model (INFROS) and estimate the magnetic field vectors of the associated interplanetary FRs known as magnetic clouds (MCs). Notably, MCs are a subset of ICMEs which show enhanced magnetic fields with a smooth rotation in the direction of field vectors and low proton temperature during its passage over the in situ spacecraft (Burlaga 1988). On the other hand, ICMEs which lack MC signatures in their in situ profile are known as noncloud ejecta. The internal magnetic field structure of those ICMEs does not resemble that of a magnetic FR. However, it is important to note that all ICMEs may have FR structures, but their in situ observations may lack that coherent magnetic structure depending on the path of the observing spacecraft (Gopalswamy 2006; Kim et al. 2013). Therefore, similar to the existing semianalytical and analytical models (Savani et al. 2015; Kay & Gopalswamy 2017; Möstl et al. 2018), INFROS is applicable for all ICMEs in general,

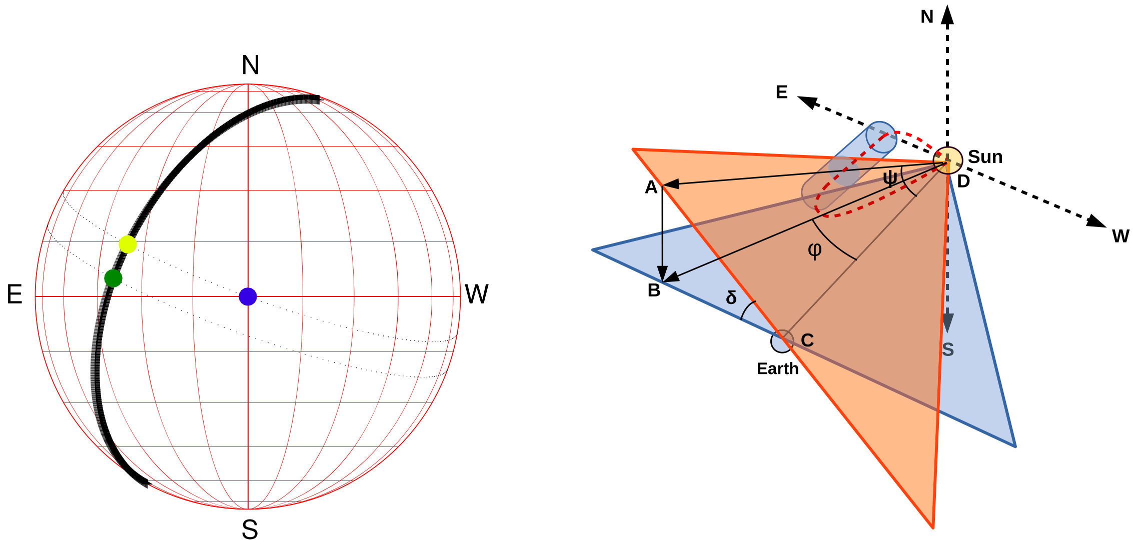

Figure 1. Left panel: the black solid line denotes the projected CME axis on the solar disk. Solar grids are shown in red with 15° intervals in both longitude and latitude. The projected location of Earth is indicated by the blue dot; the green dot marks the center of the CME axis. The yellow dot marks the location on the CME axis which is intersected by the black dotted line connecting the blue dot and perpendicular to the CME axis. Right panel: schematic picture of an MC propagating through the interplanetary space in between the Sun and Earth. The red dashed line indicates the axis of the MC. Locations of the Sun and Earth are indicated by the points D and C, respectively. The blue plane depicts the ecliptic plane, whereas the orange one is perpendicular to the MC axis and passes through the Sun–Earth line (CD). The MC axis is tilted by an angle γ with respect to the ecliptic plane. Therefore, the plane (orange) perpendicular to the MC axis makes an angle δ (=$90^o - \gamma$) with respect to the ecliptic plane (blue). The line connecting A and D lies on the orange plane and intersects the MC axis along the longitudinal direction ϕ (longitude of the yellow dot marked in the right panel) with respect to the Sun–Earth line. BD is the projection of line AD on the ecliptic plane (blue). The angle (ψ) between AD and CD denotes the separation angle between the MC axis and the Sun–Earth line.

but can be validated only for those ICME events which show MC signatures in their in situ profile.

As significant deflection and rotation of CMEs generally occur very close (less than $10R_S$) to the Sun (Lynch et al. 2009; Kay & Opher 2015), we assume that the propagation direction and the axis orientation of the CME obtained from the GCS fitting at approximately $10R_S$ are maintained throughout its evolution from the Sun to Earth. We also do not consider any CME–CME interaction in the interplanetary space, which may change the propagation trajectory of the CME. Assuming that the CMEs expand in a self-similar (Subramanian et al. 2014; Good et al. 2019; Vršnak et al. 2019) way during its interplanetary propagation, we estimate the geometrical parameters of the CME upon its arrival at 1 au. Using the conservation principle of the magnetic flux and helicity, we determine the magnetic properties of the FR when it is intersected by the spacecraft at 1 au. Finally, incorporating those estimated geometrical and magnetic parameters of the FR in a constant alpha force-free FR solution (Lundquist 1950), we estimate the expected magnetic vector profiles of Earth-impacting ICMEs. A detailed description of the INFROS model is as follows.

3.1. Estimating the Impact Distance

In order to estimate which part of the ICME will be intersected by the observing spacecraft at 1 au, it is important to first determine the impact distance (d) that is the closest distance between the MC axis and the location of the spacecraft. According to the geometry illustrated in Figure 1, we can write

$$\mathrm{BC} = R_{\mathrm{SE}} \times \tan\phi, \tag{2}$$

where R_{SE} is the distance between the Sun and Earth, and ϕ is the longitudinal direction of the line DA. As the plane perpendicular to the MC axis is tilted by an angle δ, we can further write

$$\mathrm{AC} = \frac{\mathrm{BC}}{\cos\delta} = R_{\mathrm{SE}} \times \frac{\tan\phi}{\cos\delta}. \tag{3}$$

Using the value of AC from Equation (3), we can obtain the minimum separation angle ψ between the axis of the MC and the Sun–Earth line from the following relation:

$$\tan\psi = \frac{\mathrm{AC}}{R_{\mathrm{SE}}} = \frac{\tan\phi}{\cos\delta}. \tag{4}$$

After determining the value of ψ, the impact distance (d) of the MC at any heliocentric distance (R) along the Sun–Earth line can be obtained from the following equation:

$$d = R \times \sin\psi = R \times \sin(\tan^{-1}\frac{\tan\phi}{\cos\delta}). \tag{5}$$

3.2. Cross-sectional Radius of the FR when the Spacecraft Just Encounters the Arrival of the MC

In order to infer the axial field strength of the MC from the conservation of magnetic flux, we need to estimate its cross-sectional area during its passage over the spacecraft. Figure 2 depicts a schematic picture of an MC cross section when the spacecraft just encounters its arrival. According to the geometry as illustrated in Figure 2, we can write

$$R_c \times \cos\psi + \sqrt{R_i^2 - R_c{}^2 \times \sin^2\psi} = R_{\mathrm{SE}}, \tag{6}$$

where R_C is the radial distance of the MC axis from the Sun center, ψ is the separation angle between the MC axis and the Sun–Earth line, and R_i is the radius of the cross section of the MC. Assuming that the CME has evolved self-similarly

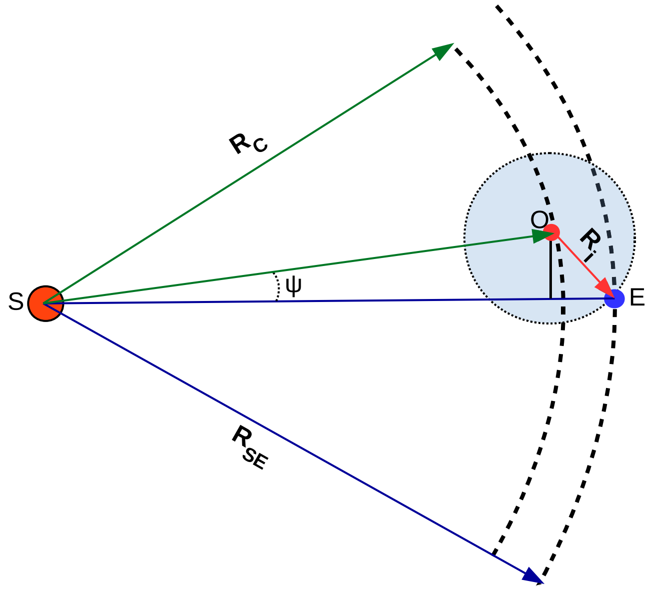

Figure 2. Schematic picture of the MC cross section on the plane (the orange plane as depicted in Figure 1) perpendicular to the MC axis. The MC axis is pointing out of the plane at point O. The angle ψ denotes the separation angle between the MC axis and the Sun–Earth line. R_C is the radial distance of the MC axis from the Sun center, and R_i is the radius of the cross section when the spacecraft just encounters the arrival of the MC.

between Sun and Earth, we can replace R_c in Equation (6) using the relation $R_i = \kappa R_c$, where κ is the aspect ratio of the CME FR obtained from the observations as discussed in Section 2.1. Thereby, we can estimate the initial radius of the FR cross section upon its arrival at Earth using the following equation:

$$R_i = \frac{\kappa \times R_{\rm SE}}{\cos\psi + \sqrt{\kappa^2 - \sin^2\psi}}. \tag{7}$$

For $\psi = 0$, Equation (7) reduces to Equation (8), which is the scenario when the spacecraft passes through the center of the FR cross section,

$$R_i = \frac{\kappa \times R_{\rm SE}}{1 + \kappa}. \tag{8}$$

3.3. Self-similar Approach to Incorporate the FR Expansion during Its Passage through the Spacecraft

Figure 3 depicts the spacecraft trajectory inside the MC assumed to expand isotropically with expansion speed $V_{\rm exp}$. The MC axis propagates with a speed $V_{\rm pro}$ along the direction depicted by the black arrows in Figure 3. Therefore, in the FR frame of reference, the spacecraft traverses from point A (lying on the front boundary of the MC) to point B (lying on the rear boundary of the MC) with speed $V_{\rm pro}$. If t_p is the travel time for the spacecraft to complete the path AB, we can write

$$\sqrt{R_i^2 - d^2} + \sqrt{R_f^2 - d^2} = v_{\rm pro} \times t_p, \tag{9}$$

where R_i and R_f are the cross-sectional radii of the front and rear boundaries of the MC, respectively, and "d" is the impact distance of the spacecraft from the MC axis. By the time (t_p) the spacecraft traversed the path AB, the cross-sectional radius of the MC has increased from R_i to R_f with expansion speed $V_{\rm pro}$. Therefore, we can write

$$R_f - R_i = v_{\rm exp} \times t_p. \tag{10}$$

Considering a general case, where the MC axis takes $t_{\rm travel}$ time to traverse a distance $R_{\rm tip}$ with a speed $v_{\rm pro}$, we can write

$$R_{\rm tip} = v_{\rm pro} \times t_{\rm travel}. \tag{11}$$

During the time $t_{\rm travel}$, as the cross-sectional area of the MC also expands with speed $v_{\rm exp}$, the final radius of the MC cross section after $t_{\rm travel}$ can be written as

$$R_{\rm cross} = v_{\rm exp} \times t_{\rm travel}. \tag{12}$$

Using the properties of self-similar expansion, $R_{\rm cross}$ and $R_{\rm tip}$ can be related as $R_{\rm cross} = \kappa R_{\rm tip}$. Therefore, using Equations (11) and (12), we can relate $v_{\rm pro}$ and $v_{\rm exp}$ through the following relation:

$$\frac{R_{\rm cross}}{R_{\rm tip}} = \frac{v_{\rm exp}}{v_{\rm pro}} = \kappa. \tag{13}$$

Using Equations (9), (10), and (13), we can write

$$\frac{R_f - R_i}{\sqrt{R_i^2 - d^2} + \sqrt{R_f^2 - d^2}} = \frac{v_{\rm exp}}{v_{\rm pro}} = \kappa. \tag{14}$$

In Equation (14), R_i, d, and κ are the known parameters. R_i is obtained from Equation (7), the impact distance "d" is obtained from Equation (5), and the value of κ is obtained from the observations as discussed in Section 2.1. Rewriting Equation (14), we get the following quadratic equation of R_f:

$$R_f^2 + b \times R_f + c = 0, \tag{15}$$

where

$$b = \frac{2 \times (R_i + \kappa \times \sqrt{R_i^2 - d^2})}{\kappa^2 - 1}$$
$$c = \frac{(R_i + \kappa \times \sqrt{R_i^2 - d^2})^2 - d^2 \times \kappa^2}{1 - \kappa^2}.$$

Therefore, solving Equation (15), we can estimate the final radius (R_f) of the expanding FR when the spacecraft encounters the rear boundary of the MC. After estimating R_i (initial radius of the MC front boundary), R_f (final radius of the MC rear boundary), and "d" (impact distance), we can estimate the path AB as depicted in Figure 3. In order to capture the full expansion profile of the MC, next we need to determine the cross-sectional radius of the expanding FR at any distance x traversed by the spacecraft throughout the path AB (Figure 3). Let us consider that at any time t ($0 \leqslant t \leqslant t_p$), the spacecraft traverses a distance x with a speed $v_{\rm pro}$ along AB in the frame of reference attached to the MC axis. Therefore, we can write

$$x = v_{\rm pro} \times t. \tag{16}$$

During the time t, the cross-sectional radius of the FR increases from R_i to R_t with a speed $v_{\rm exp}$. Therefore, we can write

$$R_t - R_i = v_{\rm exp} \times t. \tag{17}$$

Using Equations (14), (16), and (17), we can further write

$$\frac{R_t - R_i}{x} = \frac{v_{\rm exp}}{v_{\rm pro}} = \kappa. \tag{18}$$

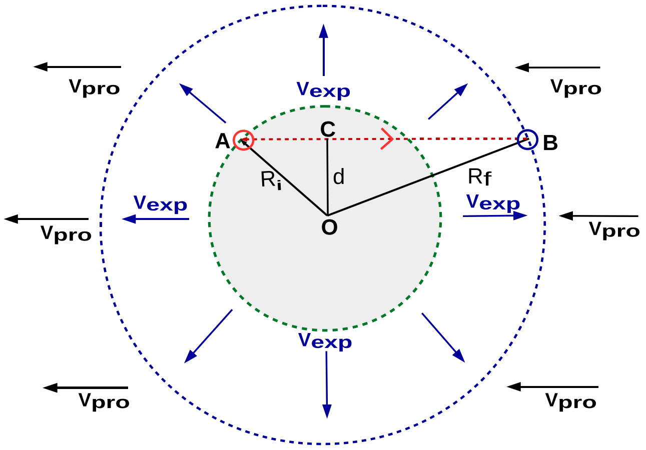

Figure 3. Schematic picture of the cross section of an expanding FR as it passes over the spacecraft with a propagation speed V_{pro} and expansion speed V_{exp}. The black arrows denote the direction of the MC propagation, whereas the blue arrows represent the isotropic expansion of the MC. The spacecraft intersects the MC at an impact distance "*d*" denoted by OC. The gray shaded region encircled by the green dashed line denotes the initial boundary of the FR with cross-sectional radius R_i when the spacecraft just encounters the arrival of the MC at point A marked by the red circle. The red dotted line illustrates the trajectory of the spacecraft from A to B inside the expanding MC. R_f is the final radius of the MC cross section encircled by the blue dashed line when the spacecraft encounters the end boundary of the MC.

Rewriting Equation (18), we get

$$R_t = R_i + \kappa \times x. \tag{19}$$

Therefore, at any distance x along the path AB (Figure 3), we can estimate the cross-sectional radius ($R_i \leqslant R_t \leqslant R_f$) of the expanding FR using Equation (19). It is noteworthy that we have started our formulation with the unknown parameters V_{exp}, V_{pro}, and t_p (see Equations (9) and 10) and finally arrived at Equations (15) and (18), which are independent of the aforementioned variables. This is the major advantage of this formulation as we have incorporated the FR expansion in such a way so as to get rid of the free or unknown parameters like the expansion speed (V_{exp}), propagation speed (V_{pro}), and time of passage (t_p) of the ICMEs at 1 au.

3.4. Estimating the Final Magnetic Field Profiles of the MC at 1 au Using a Cylindrical FR Solution

It is expected that the FR axial field strength (B_0) will decrease as the length ($L = \frac{2\beta}{\kappa}r$) and cross-sectional radius (r) of the FR will increase during its expansion and propagation throughout interplanetary space (see the expression of B_0 in Equation (1)). Assuming that the angular width (2β) of the CME remains constant throughout its propagation and the nature of expansion is self-similar, we can consider that $L \propto r$. Therefore, considering the conservation of magnetic flux (ϕ_p = constant), the axial magnetic field strength (B_0) of any FR having a cross-sectional radius r will follow the relation

$$B_0 \propto \frac{1}{r^2}. \tag{20}$$

Therefore, knowing the cross-sectional radius R_t ($R_i \leqslant R_t \leqslant R_f$) of the FR during its passage through the spacecraft using the Equation (19), we can estimate its axial field strength (B_t) at any time t ($0 \leqslant t \leqslant t_p$) using the following relation:

$$B_t = B_{0_{\text{CME}}} \times \frac{{r_{\text{CME}}}^2}{{R_t}^2}, \tag{21}$$

where r_{CME} is the cross-sectional radius, and $B_{0_{\text{CME}}}$ is the axial magnetic field strength of the near-Sun FR obtained from the observations as discussed in Section 2.

As the spacecraft intersects the MC along the path AB (see Figure 3), at any location (x) along AB, the magnetic field vectors of the FR can be obtained using a cylindrical FR solution (Lundquist 1950) in a local cylindrical coordinate (r, ϕ, z) attached to the MC axis. The magnetic vectors in the aforementioned (r, ϕ, z) coordinate system will be

$$B_r = 0, \tag{22}$$

$$B_\phi = H \times B_t \times J_1(\alpha r), \tag{23}$$

$$B_z = B_t \times J_0(\alpha r), \tag{24}$$

where $H = \pm 1$ is the handedness or sign of the helicity, which is the same as that of the near-Sun FRs according to the conservation of helicity rule, α is the constant force-free factor, and J_0 and J_1 are the Bessel functions of order 0 and 1, respectively. The boundary of the FR is located at the first zero of J_0, which leads to $\alpha = 2.41/R_t$ and R_t is therefore the radius of the FR. B_t and R_t evolve according to the relation described in Equations (21) and (19), respectively.

As we have assumed that after $10R_S$ the CME does not suffer any significant rotation and deflection, therefore the final elevation angle (θ) of the MC axis at 1 au should follow the tilt angle (δ) of the CME and the azimuthal angle of the MC should follow the propagation longitude (ϕ) of the CME obtained from the GCS fitting as discussed in Section 2.1. In order to get the final magnetic field vectors in the Geocentric Solar Ecliptic (GSE) coordinate system (Hapgood 1992), we first transform the B_r, B_θ, and B_ϕ from the local cylindrical coordinates (r, θ, z) to the local Cartesian coordinates (x', y', z') attached to the MC axis. Thereafter, knowing the azimuthal (ϕ) and elevation (θ) angles of the MC axis, we transform the magnetic vectors $B_{x'}$, $B_{y'}$, and $B_{z'}$ from the local Cartesian coordinates (x', y', z') to the GSE coordinate system (x, y, z). Thus, we get the predicted magnetic vectors B_x, B_y, and B_z of the ICME as detected by the spacecraft at 1 au.

4. INFROS Model Validation: A Test Case for the CME Event on 2013 April 11

As a proof of concept, we validate our model (INFROS) for an Earth-directed CME which erupted from the Sun on 2013 April 11 at around 06:50 UT. The CME was associated with an M6.6 class solar flare (Cohen et al. 2014; Lario et al. 2014; Vemareddy & Zhang 2014; Vemareddy & Mishra 2015; Joshi et al. 2017; Fulara et al. 2019) that occurred in the active region (AR) 11719. Its arrival at the L1 point was detected through the signature of shock arrival on 2013 April 13 at 22:54 UT, FR leading edge on 2013 April 14 at 17:00 UT and a trailing edge on 2013 April 15 at 19:30 UT. The smooth variation and rotation in its in situ magnetic field profile along with the low proton temperature hold the characteristic signatures of an MC (Burlaga 1988). Moreover, the CME did not exhibit any interaction with other CMEs and evolved as an isolated

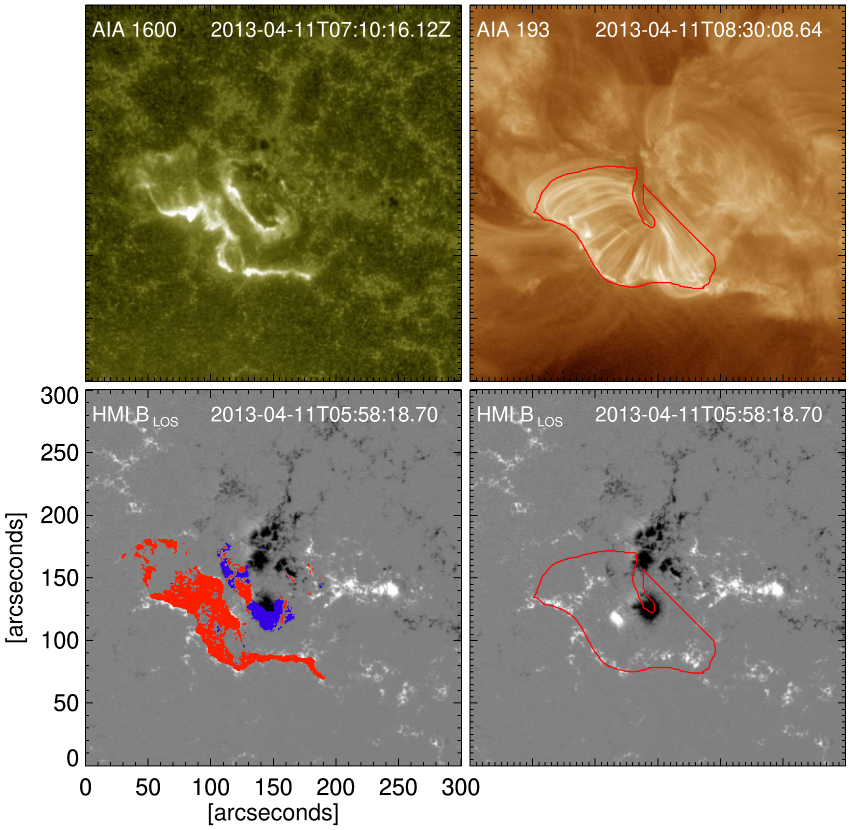
AIA 1600 2013-04-11T07:10:16.12Z
AIA 193 2013-04-11T08:30:08.64
HMI B LOS 2013-04-11T05:58:18.70
HMI B LOS 2013-04-11T05:58:18.70
300
250
200
150
100
50
0
[arcseconds]
0
50
100
150
200
250
300
[arcseconds]

Figure 4. Upper-left panel depicts the flare ribbon in AIA 1600 Å image. The red boundary line in the upper-right panel marks the post-eruption arcades (PEAs) in the AIA 193 Å image. Lower-left and lower-right panels illustrate the HMI line-of-sight magnetic field. The red and blue regions in the lower-right panel depict the cumulative flare ribbon area overlying the positive and negative magnetic fields, respectively. The red boundary in the lower-right panel is the overplotted PEA region.

magnetic structure from the Sun to Earth. Therefore, the basic assumptions made in our model hold good for this case study.

The evolution of the flare ribbons and the formation of PEAs associated with the M6.6 class flare (see Figure 4) were well observed by the Atmospheric Imaging Assembly (AIA; Lemen et al. 2012) and the Helioseismic and Magnetic Imager (HMI; Schou et al. 2012) on board the *Solar Dynamics Observatory* (Pesnell et al. 2012). Furthermore, the multivantage point observations from *STEREO-A*, *STEREO-B*, and LASCO were suitable to reconstruct the 3D morphology of the associated CME. Therefore, we are able to determine all the near-Sun FR properties of the CME in order to use those as realistic inputs for the INFROS model.

4.1. Model Inputs for the CME Event on 2013 April 11

4.1.1. Poloidal Flux Content of the FR

We calculate the flare-associated reconnection flux by applying both methods (Longcope et al. 2007; Qiu et al. 2007; Gopalswamy et al. 2017) as described in Section 2.2.1. The red and blue regions in the lower-left panel of Figure 4 show the cumulative flare ribbon area overlying the positive and negative polarities of the photospheric magnetic field, respectively. The average of the absolute values of the positive and negative magnetic fluxes underlying the cumulative flare ribbon area yields the value of the reconnection flux as 1.9×10^{21} Mx. Taking into account the formation height of the flare ribbons, we have incorporated a 20% correction (Qiu et al. 2007) in the estimation of the reconnection flux. The half of the total unsigned magnetic flux underlying the PEA (the region enclosed by the red boundary as shown in the upper-left and lower-left panels of Figure 4) yield the value of reconnection flux as 2.3×10^{21} Mx. In order to determine the magnetic properties of the associated CME, we equate the poloidal flux content of the FR to the average value (2.1×10^{21} Mx) of the reconnection fluxes obtained from the two aforementioned methods.

4.1.2. Direction of the Axial Magnetic Field and the Chirality of the FR

The source location of the M6.6 flare that occurred in AR 11719 was associated with a pre-eruptive sigmoidal structure (Vemareddy & Mishra 2015; Joshi et al. 2017). Panel (a) of Figure 5 shows the highly skewed preflare sigmoid observed in EUV images of the AIA passbands (94, 335 and 193 Å). The observed inverse S-shaped morphology of the sigmoidal structure (indicated by the red dashed line) has been overlaid on the HMI line-of-sight magnetogram (panel (b) of Figure 5), which reveals the left-handed chirality of the associated FR. This follows the hemispheric helicity rule (Bothmer & Schwenn 1998) as the source region of the CME was located in the northern solar hemisphere.

We identify the two boundaries as shown by the blue and green dashed lines in panel (a) of Figure 5, where the two ends of the bundle of sigmoidal field lines are rooted during the pre-eruptive phase. The two aforementioned boundaries are

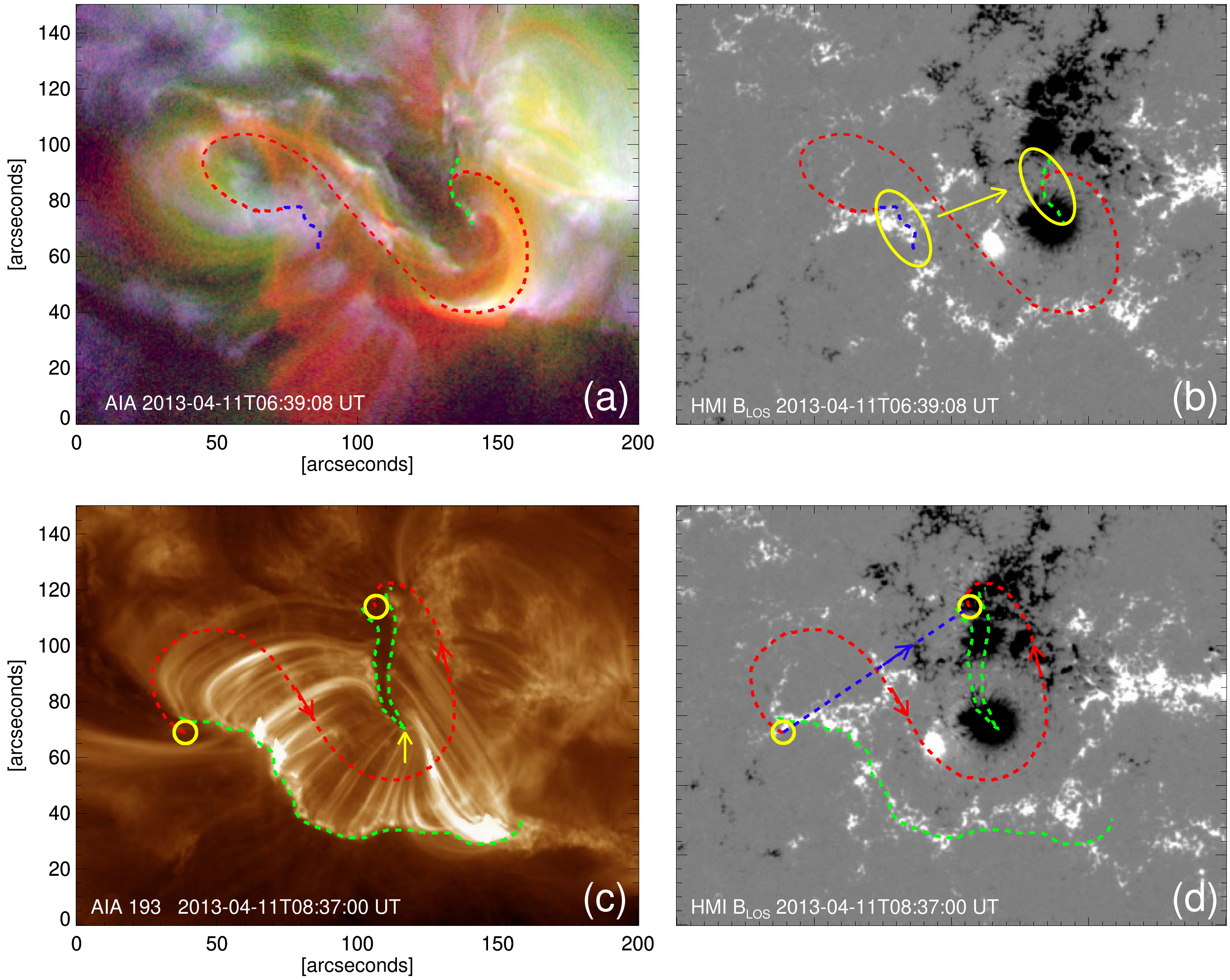
AIA 2013-04-11T06:39:08 UT
(a)
HMI B_{LOS} 2013-04-11T06:39:08 UT
(b)
AIA 193 2013-04-11T08:37:00 UT
(c)
HMI B_{LOS} 2013-04-11T08:37:00 UT
(d)
[arcseconds]
[arcseconds]
0
20
40
60
80
100
120
140
0
50
100
150
200

Figure 5. The preflare sigmoidal structure observed in the composite images constructed from the AIA 94 Å (red), 335 Å (green) and 193 Å (blue) passband observations (a). The associated HMI line-of-sight magnetic field plotted in gray scale within saturation values ±500 G (b). The red dashed line (plotted in panel (a)) that approximately resembles the sigmoidal structure has been overlaid on the HMI line-of-sight magnetic field in panel (b). The blue and green dashed lines in panel (a) approximately denote the boundaries where the two ends of the bundle of sigmoidal field lines are rooted. The same blue and green dashed lines are overlaid in panel (b). The post-eruption arcades (PEAs) observed in the AIA 193 Å passbands (c) and the associated HMI line-of-sight magnetic field (d). The green dashed lines in panel (c) mark the two side boundaries of the PEA and the same is overlaid in panel (d). The red dashed line is drawn along the approximate center of the two side boundaries of the PEA, connecting the two expected footpoint locations (shown by the yellow circles) of the erupting flux rope. The blue dashed line connecting the flux rope footpoints and the blue arrow in panel (d) indicates the northwest direction.

overlaid on the HMI line-of-sight magnetic field and the regions are marked by the yellow ellipses (see panel (b)). The simple connectivity (without considering any twist) between the two opposite magnetic polarities underlying the regions marked by the yellow ellipses suggests the northwest direction (as shown by the yellow arrow) as the axial orientation of the FR at higher heights in the corona (above $\approx 5\ R_S$). This is expected as the apex orientation of the left-handed FR should rotate in the counterclockwise direction to release the axial twist or writhe during its evolution in the lower corona below 5 R_S (Lynch et al. 2009).

In order to confirm the axial orientation of the FR, we further investigate the morphology of the associated PEA formed during the flare. Panel (c) of Figure 5 shows that the eastern part of the PEA channel is tilted toward the southwest direction and further bends toward the northwest direction at the location indicated by the yellow arrow, forming a nearly U-shaped morphology. This is certainly a complex morphology, which makes the event more complicated. Considering the apex orientation of the FR inferred only from the eastern part of the PEA channel, Palmerio et al. (2018) found a contradiction between the solar and 1 au Bz direction. However, we focused on the full U-shaped morphology of the PEA channel in this study. Considering the full extent of the PEAs allows us to analyze the FR structure beyond the sigmoidal pre-eruptive configuration and, therefore, to capture the complete evolution of the FR in the lower corona during the phase of sigmoid to arcade formation. According to the standard flare model in three dimensions (Shibata et al. 1995; Moore et al. 2001; Priest & Forbes 2002), the footpoints of the eruptive FRs are believed

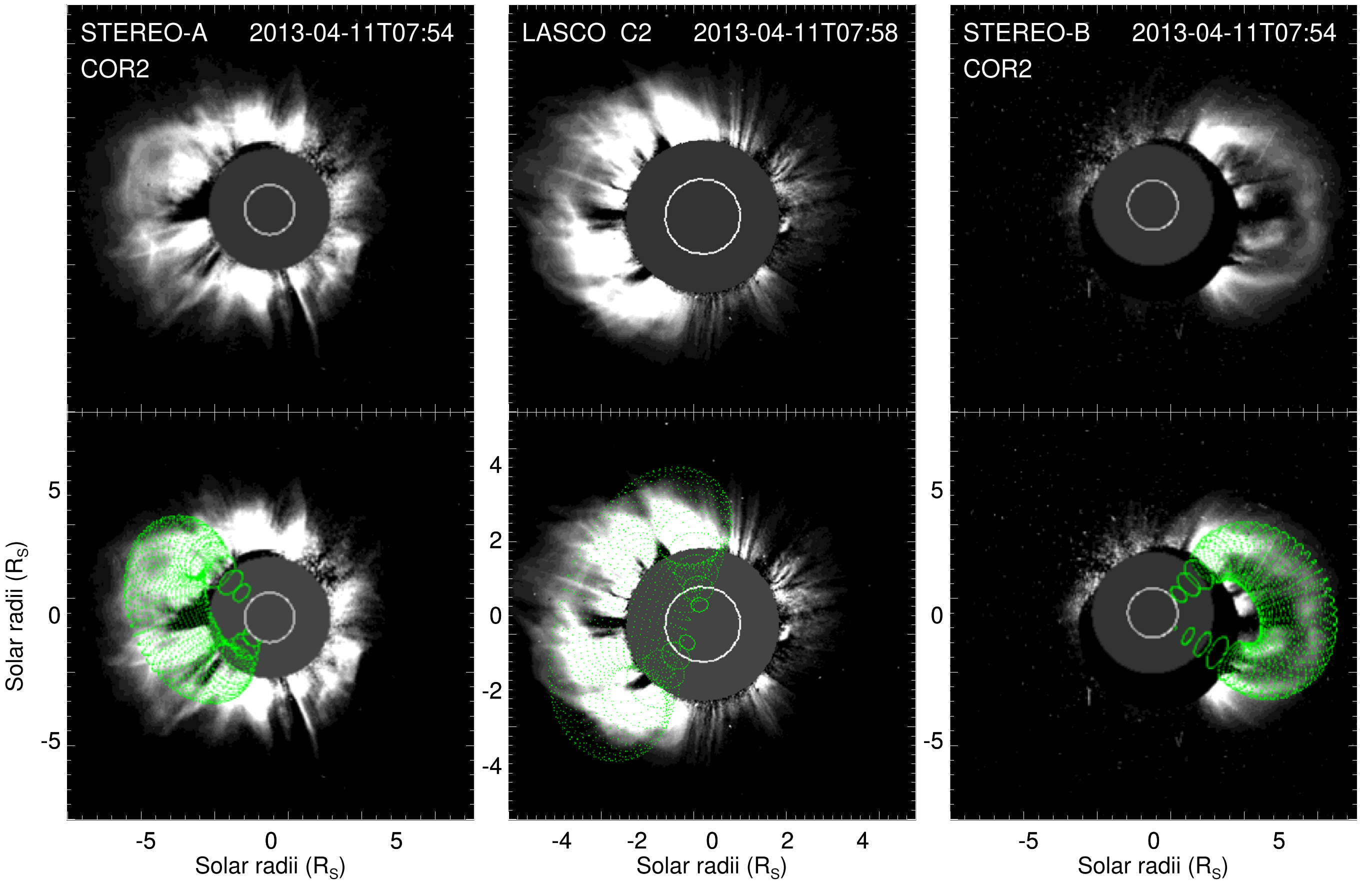

Figure 6. Top panels depict the CME morphology observed in COR2-A (top-left), LASCO C2 (top-middle), and COR2-B (top-right), respectively, at 07:54 UT on 2013 April 11. Bottom panels illustrate the overplot of the best-fitted wire frame (green dotted marks) of the FR using the GCS model.

to be located on either side of the two ends of the PEA channel. Therefore, considering the left-handed chirality, we mark the expected locations of the two footpoints of the FR as shown by the yellow circles at the two ends of the U-shaped PEA channel. The red dashed curve connecting the two yellow circles indicates the possible writhe presented in the FR during the formation phase. This is in agreement with the observed writhing motion of that FR during the eruptive phase as reported by Joshi et al. (2017). Therefore, due to the writhing motion, the FR would have relaxed the axial twist during its evolution in the lower corona, resulting in an orientation following the straight connectivity (shown by the blue dashed line in panel (d) of Figure 5) between the two footpoint locations. In such a scenario, the magnetic polarities underlying the two yellow circles clearly indicate that the axial orientation of the FR is directed toward the northwest.

From the GCS fitting (Figure 6) of the observed white-light morphology of the CME at $\approx 10R_S$, we estimate the tilt angle of the CME axis as 73° ± 10° with respect to the ecliptic plane. Minimizing the difference in angle between the GCS tilt and the axial direction (northwest) of the FR inferred from the on-disk observations, we obtain the axial magnetic field direction of the CME FR at $\approx 10R_S$ along 73° ± 10°, measured in the counterclockwise direction with respect to the solar equator. Assuming that no major rotation occurred after $10R_S$, we consider this axis orientation as the final orientation of the associated MC axis at 1 au.

4.1.3. Axial Field Strength of the FR

In order to estimate the axial field strength of the near-Sun FR, we first determine the geometrical parameters associated with it. The top panels of Figure 6 show the white-light morphology of the CME as observed in the base difference images obtained from *STEREO-A/B* and LASCO. The GCS fitting (bottom panels of Figure 6) to the multivantage point observations of the CME yields the aspect ratio (κ) and the half-angular width (β) of the CME as 0.22 and 26°, respectively. Therefore, the length ($L = 2\beta R$) of the associated FR at a radial distance (R) of $10R_S$ is estimated to be approximately $9R_S$. Using Equation (1), we obtain the axial field strength of the FR at $10R_S$ as 52 mG.

4.1.4. Propagation Direction of the CME

The GCS fitting (Figure 6) of CME morphology at $\approx 10R_S$ yields the propagation direction of the CME along S05E10. Taking into account an uncertainty of 10° in determining both the longitude and latitude of the propagation direction, we have performed the GCS fitting several times and found the propagation direction of the CME to lie within the range 0°–10° E and 5°–15° S. Using the range of values of the propagation direction and the tilt angle (73° ± 10°) of the CME as inputs, we estimate the impact distance of the CME magnetic axis at 1 au within the range 0–21 R_S.

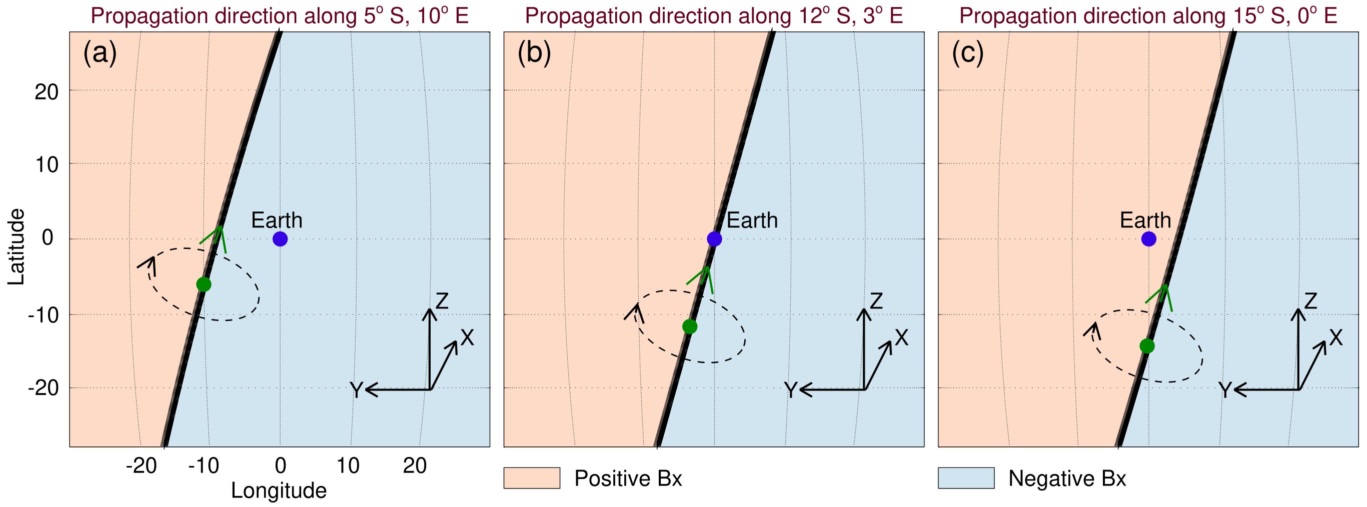
Propagation direction along 5° S, 10° E
Propagation direction along 12° S, 3° E
Propagation direction along 15° S, 0° E
(a)
(b)
(c)
Earth
Earth
Earth
Latitude
20
10
0
-10
-20
-20
-10
0
10
20
Longitude
Z
X
Y
Z
X
Y
Z
X
Y
Positive Bx
Negative Bx

Figure 7. Location of Earth (blue dots) with respect to the magnetic axis (black solid lines) of the CME projected on the solar disk. The green dots in each panel show the three different propagation directions of the CME. The black and green arrows denote the direction of poloidal and axial magnetic fields of the flux rope, respectively. Any virtual spacecraft that resides on the left/right side of the magnetic axis (denoted by the pink and blue shaded regions, respectively) will encounter the B_x component of the flux rope as positive/negative in the GSE coordinate system.

4.2. Sensitivity of the Estimated Magnetic Vectors to the Propagation Direction and Tilt Angle of the CME

We notice that the sign of the B_x component for the estimated magnetic vectors of the ICME as detected by any spacecraft aligned along the Sun–Earth line is very sensitive to the propagation direction of the CME. The three panels in Figure 7 depict the location of Earth (denoted by blue dots) with respect to the magnetic axis (denoted by black solid lines) of the CME propagating along three different directions which are within the error limits as estimated in Section 4.1.4. In each of the three panels, the Sun grids are shown within ±30° longitude and latitude where the projected location of Earth on the solar disk resides at 0° longitude and 0° latitude. Keeping the tilt angle as 73°, we project the magnetic axis of the CME on the solar disk as shown by the black solid lines in each panel. The green dots and arrows on the magnetic axis denote the propagation direction of the CME and the direction of the axial magnetic field of the associated FR, respectively. The arrows along the black dashed lines surrounding the CME magnetic axis depict the direction of the poloidal magnetic field according to the left-handed chirality of the associated FR.

Notably, at any projected location on the solar disk which lies on the left/right side of the CME axis, the direction of the poloidal magnetic field will be toward/outwards from the Sun. Accordingly, the sign of B_x will change at any location on either side of the magnetic axis, which we have shown by the pink and blue regions, where B_x possesses positive and negative values, respectively. Panel (a) in Figure 7 shows that the projected location of Earth lies on the region of negative B_x for the estimated direction (10° E, 5° S) and tilt (73° with respect to the ecliptic plane) of the MC axis as obtained from the GCS fitting. However, a small shift in the propagation direction from 10° E, 5° S to 3° E, 12° S results in a zero impact distance between the MC axis and the Sun–Earth line (see panel (b) in Figure 7) for which the estimated B_x component turns out to be zero. If we further shift the propagation direction of the MC axis from 3° E, 12° S to 0° E, 15° S within the error limits, the sign of B_x becomes positive as the location of Earth or any spacecraft aligned along the Sun–Earth line lies on the left side of the MC axis where the direction of the poloidal magnetic field is toward the Sun (see panel (b) in Figure 7). Therefore, our analysis shows that within the error limits of the propagation direction of the CME, B_x can have both positive and negative components in the estimated magnetic vectors of the ICME at 1 au.

It is noteworthy that the above-mentioned scenario is true for any tilt angle of the FR orientation where the propagation direction is very close to the Sun–Earth line. Interestingly, the sign or the direction of the variation (positive to negative or vice versa) of the estimated B_y and B_z components is not sensitive to small variations (±10°) in the propagation direction and tilt angle of the CME. Therefore, we expect less uncertainty in the prediction of the B_y and B_z components of the MC.

4.3. Model outputs

Using the near-Sun FR properties of the associated CME as described in Section 4.1, we estimate the magnetic vectors of the ICME as intersected by the spacecraft at 1 au. The curves shown by the black solid lines in Figure 8 depict the observed magnetic vectors of the ICME as detected by the *Wind* spacecraft (Ogilvie & Desch 1997). The red vertical lines denote the front and rear boundaries of the MC which we have estimated from the observed magnetic field and plasma parameters of the ICME.

Incorporating the uncertainties in the GCS parameters involved in the modeling, we generate all of the possible input data sets from the range of values of the input parameters, i.e., the propagation direction (0°–10°E, 5°–15° S), tilt angle (63°–83°), and aspect ratio (0.20–0.24) of the CME. Further, considering an error of 2×10^{20} Mx (standard deviation of the two values of reconnection flux obtained from the two different methods as discussed in Section 4.1.1) in determining the poloidal flux and ±0.02 in determining the CME aspect ratio, we get a 20% error in estimating the axial field strength ($B_{0_{\rm CME}}$) of the CME. This yields the estimated range of $B_{0_{\rm CME}}$ at $10R_s$ as 42–62 mG, with a mean value of 52 mG. This is consistent with the average value of the distribution of axial fields at $10R_S$

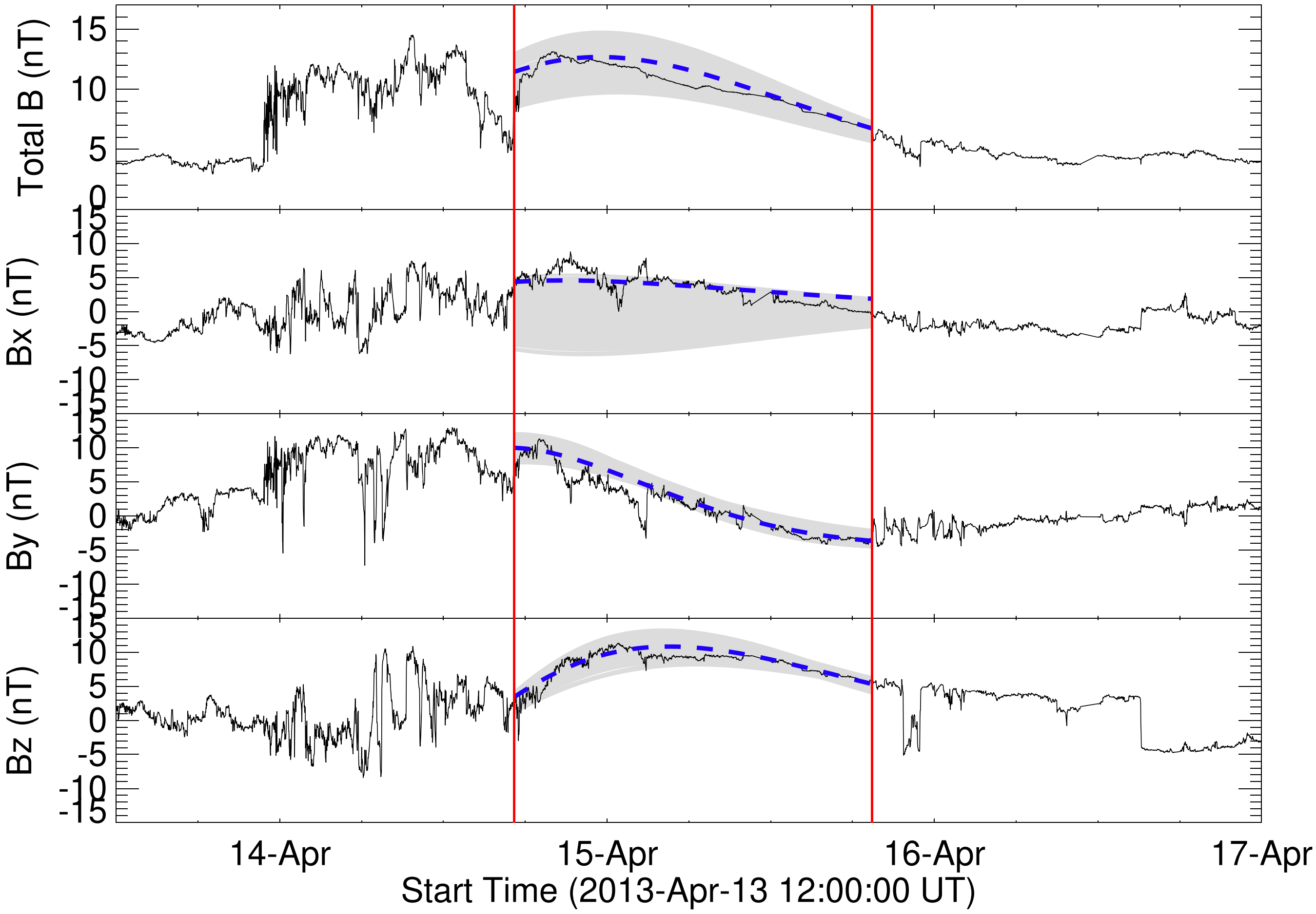

Figure 8. Magnetic vectors as detected by the *Wind* spacecraft for the 2013 April 14 ICME event. The two red vertical lines denote the magnetic cloud boundary. The blue dashed lines denote the predicted magnetic vectors obtained from the model which best match the observed magnetic profiles of the MC. The gray shaded regions denote the uncertainty in predicting the respective magnetic vectors.

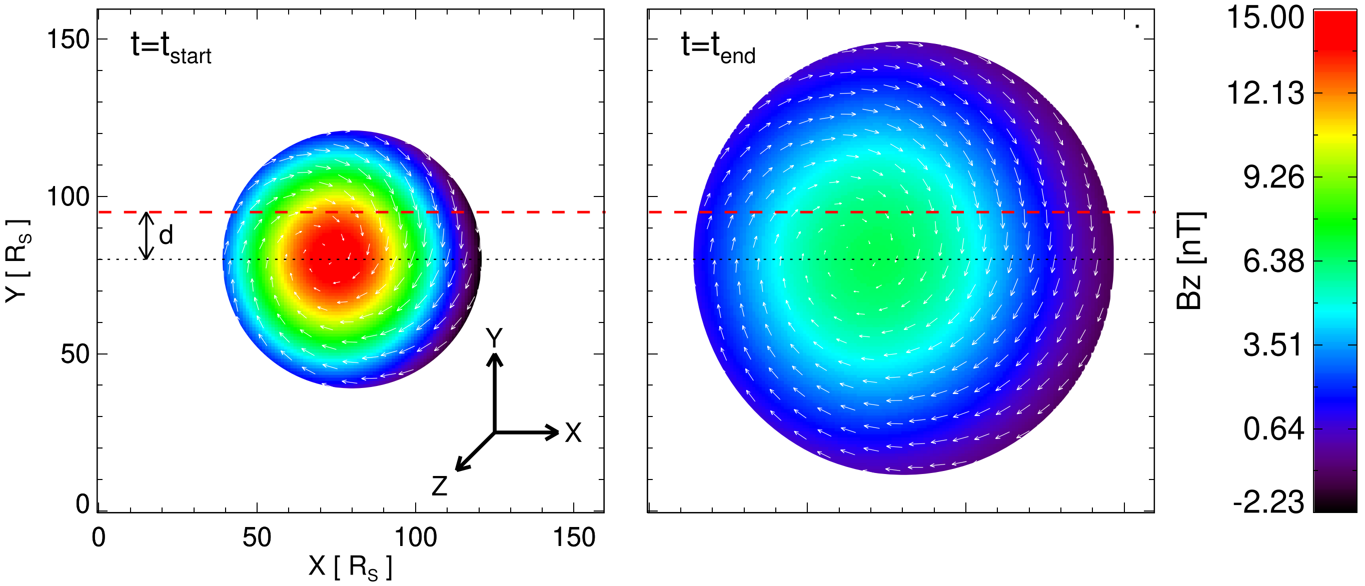

Figure 9. Left panel: cross section of the flux rope as viewed on the ecliptic plane when the spacecraft at 1 au just encounters the arrival of the magnetic cloud (MC). Right panel: cross section of the expanded flux rope when the spacecraft completes its passage through the magnetic cloud and reaches the rear boundary of the MC at 1 au. The color bar shows the strength of the southward component of the magnetic field in GSE coordinates, which is positive outwards the plane of the paper. The black dotted line passes through the axis of the flux rope. The white arrows mark the direction of the magnetic field component lying on the ecliptic plane inside the MC boundary. The red dashed line at a distance *d* (impact distance) from the black dotted line shows the spacecraft trajectory along which the MC intersects it at 1 au.

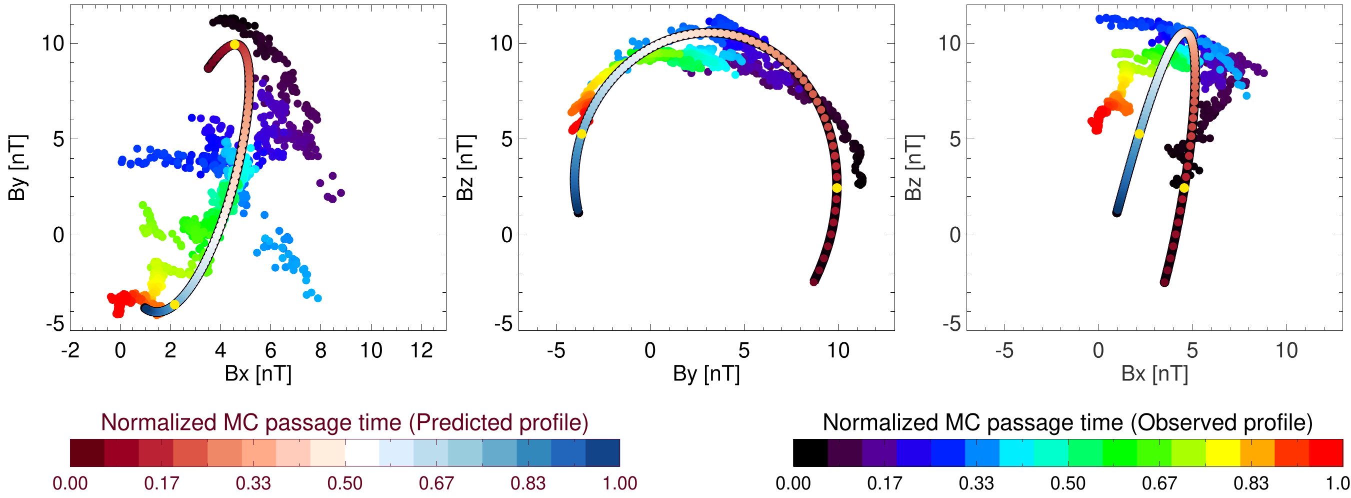

Figure 10. Hodogram plot of the magnetic field vectors within the MC for both observed and modeled data values. The yellow dots drawn over the plots for the modeled data values denote the data points that approximately match the front and rear boundaries of the observed MC.

(Gopalswamy et al. 2018b). Using these sets of input data, we run our model and generate synthetic magnetic profiles of the MC. Among these sets of predicted magnetic vectors, we find that the magnetic profiles (shown by the blue dashed lines in each panel of Figure 8) which best match the observed magnetic vectors of the MC can be obtained by using the propagation direction along 0° E, 15° S, the tilt angle as 73°, the aspect ratio as 0.22, and the axial field strength at $10R_s$ as 52 mG. For this set of input parameters, we show the spacecraft trajectory through the MC and the magnetic field profiles of the FR cross section when the spacecraft intersects the front and rear boundaries of the MC (Figure 9). The uncertainty in predicting the magnetic vectors as shown by the gray shaded region in each panel of Figure 8 is obtained by overplotting all sets of output magnetic profiles.

In order to overplot the modeled magnetic vectors within the temporal window of the observed MC, we identify the front and rear boundaries of the modeled MC from the hodogram analysis. Figure 10 shows the scattered plots among the magnetic field vectors within the MC for both observed and modeled data values. The yellow dots drawn over the plots for the modeled data values denote the data points that approximately match the front and rear boundaries of the observed MC. Therefore, we take the observed MC boundary as a reference boundary and overplot the data points of the modeled magnetic vectors that lie in between the two yellow dots.

Figure 8 shows that the predicted magnetic field profiles of the MC obtained from our model are in good agreement with those of the observed profiles as detected by the *Wind* spacecraft. In comparison to the B_y and B_z components, the larger uncertainty that arises in predicting the B_x component is due to its sensitivity toward the propagation direction of the CME, which we have discussed in Section 4.2. Nevertheless, the predicted profiles for the B_y and B_z components show good agreement with the observed profiles. The predicted strength of the B_z component has been found to be 10.5 ± 2.5 nT when the MC axis makes its closest approach to the spacecraft. This is in agreement with the maximum observed strength (11 nT) of the B_z component obtained from the in situ data. Therefore, our model successfully predicts both the strength and the general profile of the B_z component of the MC with good accuracy.

5. Conclusion

We presented an analytical model (INFROS) to predict the magnetic field vectors of ICMEs based on realistic inputs obtained from near-Sun observations. As a proof of concept, we validate our model for the 2013 April 11 CME event. The predicted magnetic field vectors of the ICME obtained from INFROS show good agreement with those observed by the *Wind* spacecraft at 1 au. This shows promising results in forecasting *Bz* in real time.

There are several key aspects in which INFROS appears to be superior than the existing semianalytical (Kay et al. 2017) and analytical (Savani et al. 2015) models. The analytical model proposed by Savani et al. (2015) does not incorporate the expanding nature of the ICME during its passage through the spacecraft, which yields an unrealistic symmetric profile of the total magnetic field strength of the ICME with time. Kay et al. (2017) included the expanding nature of ICMEs in their semianalytical model using the speed and duration of the passage of the ICME measured at 1 au as free parameters. However, the formulation developed in INFROS incorporates the FR expansion in such a way so as to get rid of the unknown parameters like the expansion speed (V_{exp}), propagation speed (V_{pro}), and time of passage (t_p) of the ICMEs at 1 au (see Section 3.3). Moreover, none of the existing models (Savani et al. 2015; Kay & Gopalswamy 2017; Möstl et al. 2018) were capable of predicting the time-varying axial field strength of the expanding FR embedded in ICMEs during its passage through the spacecraft. Therefore, it was not possible to forecast the strength of the southward component of the magnetic field (*Bz*) embedded in the ICMEs in order to predict the severity of the associated geomagnetic storms. It is worth noting that INFROS is capable of predicting the time-varying axial field strength and the expanding nature of the interplanetary FR without involving any free parameters, as all the input parameters are constrained either by the near-Sun observations or the inherent assumptions (self-similar expansion) made in the model. Therefore, the modeling approach proposed in this article turns out to be a promising space-weather forecasting tool where the magnetic field vectors of the ICMEs can be predicted well in advance using the near-Sun observations of CMEs.

In order to reduce the uncertainties involved in the model predictions, INFROS can be further constrained by the inputs obtained from the spacecraft orbiting at different heliocentric distances in between the Sun and Earth (e.g., *MESSENGER*, *VEX*, *Parker Solar Probe*, etc.). In a future study, we plan to validate this model for ICMEs detected by multiple spacecraft orbiting at different heliocentric distances, which will give better insight into the magnetic field variation from the Sun in the direction of the spacecraft.

We thank the referee for helpful comments that improved the quality of this manuscript. This work was performed at the NASA Goddard Space Flight Center under the aegis of the SCOSTEP Visiting Scholar program (R.S.). R.S. thanks SCOSTEP and NASA (via the Catholic University of America) for the financial support. N.G. was partly supported by NASA's Living with a Star program.

ORCID iDs

Ranadeep Sarkar https://orcid.org/0000-0001-6457-5207
Nat Gopalswamy https://orcid.org/0000-0001-5894-9954
Nandita Srivastava https://orcid.org/0000-0002-0452-5838

References

Bothmer, V., & Schwenn, R. 1998, AnGeo, 16, 1
Brueckner, G. E., Howard, R. A., Koomen, M. J., et al. 1995, SoPh, 162, 357
Burlaga, L. F. 1988, JGR, 93, 7217
Cohen, C. M. S., Mason, G. M., Mewaldt, R. A., & Wiedenbeck, M. E. 2014, ApJ, 793, 35
Domingo, V., Fleck, B., & Poland, A. I. 1995, SoPh, 162, 1
Fulara, A., Chandra, R., Chen, P. F., et al. 2019, SoPh, 294, 56
Gonzalez, W. D., Tsurutani, B. T., & Clúa de Gonzalez, A. L. 1999, SSRv, 88, 529
Good, S. W., Kilpua, E. K. J., LaMoury, A. T., et al. 2019, JGRA, 124, 4960
Gopalswamy, N. 2006, SSRv, 124, 145
Gopalswamy, N., Akiyama, S., Yashiro, S., Michalek, G., & Lepping, R. P. 2008, JASTP, 70, 245
Gopalswamy, N., Akiyama, S., Yashiro, S., & Xie, H. 2018a, in IAU Symp. 335, Space Weather of the Heliosphere: Processes and Forecasts, ed. C. Foullon & O. E. Malandraki (Cambridge: Cambridge Univ. Press), 258
Gopalswamy, N., Akiyama, S., Yashiro, S., & Xie, H. 2018b, JASTP, 180, 35
Gopalswamy, N., Mäkelä, P., Akiyama, S., et al. 2018c, JASTP, 179, 225
Gopalswamy, N., Yashiro, S., Akiyama, S., & Xie, H. 2017, SoPh, 292, 65
Hanaoka, Y., & Sakurai, T. 2017, ApJ, 851, 130
Hapgood, M. A. 1992, P&SS, 40, 711
Howard, R. A., Moses, J. D., Vourlidas, A., et al. 2008, SSRv, 136, 67
Huttunen, K. E. J., Schwenn, R., Bothmer, V., & Koskinen, H. E. J. 2005, AnGeo, 23, 625
Janvier, M., Aulanier, G., Bommier, V., et al. 2014, ApJ, 788, 60
Jin, M., Manchester, W. B., van der Holst, B., et al. 2017, ApJ, 834, 173
Joshi, B., Kushwaha, U., Veronig, A. M., et al. 2017, ApJ, 834, 42
Kaiser, M. L., Kucera, T. A., Davila, J. M., et al. 2008, SSRv, 136, 5
Kay, C., & Gopalswamy, N. 2017, JGRA, 122, 11810
Kay, C., Gopalswamy, N., Reinard, A., & Opher, M. 2017, ApJ, 835, 117
Kay, C., & Opher, M. 2015, ApJL, 811, L36
Kim, R.-S., Gopalswamy, N., Cho, K.-S., Moon, Y.-J., & Yashiro, S. 2013, SoPh, 284, 77
Lario, D., Raouafi, N. E., Kwon, R.-Y., et al. 2014, ApJ, 797, 8
Lemen, J. R., Title, A. M., Akin, D. J., et al. 2012, SoPh, 275, 17
Liu, Y., Hoeksema, J. T., Bobra, M., et al. 2014, ApJ, 785, 13
Longcope, D., Beveridge, C., Qiu, J., et al. 2007, SoPh, 244, 45
Lundquist, S. 1950, Ark Fys, 2, 361
Lynch, B. J., Antiochos, S. K., Li, Y., Luhmann, J. G., & DeVore, C. R. 2009, ApJ, 697, 1918
Marubashi, K., Akiyama, S., Yashiro, S., et al. 2015, SoPh, 290, 1371
Moore, R. L., Sterling, A. C., Hudson, H. S., & Lemen, J. R. 2001, ApJ, 552, 833
Möstl, C., Amerstorfer, T., Palmerio, E., et al. 2018, SpWea, 16, 216
Odstrčil, D., & Pizzo, V. J. 1999, JGR, 104, 483
Ogilvie, K., & Desch, M. 1997, AdSpR, 20, 559
Palmerio, E., Kilpua, E. K. J., James, A. W., et al. 2017, SoPh, 292, 39
Palmerio, E., Kilpua, E. K. J., Möstl, C., et al. 2018, SpWea, 16, 442
Pesnell, W. D., Thompson, B. J., & Chamberlin, P. C. 2012, SoPh, 275, 3
Pevtsov, A. A., Canfield, R. C., & Metcalf, T. R. 1995, ApJL, 440, L109
Priest, E. R., & Forbes, T. G. 2002, A&ARv, 10, 313
Qiu, J., Hu, Q., Howard, T. A., & Yurchyshyn, V. B. 2007, ApJ, 659, 758
Rust, D. M., & Kumar, A. 1996, ApJL, 464, L199
Savani, N. P., Vourlidas, A., Szabo, A., et al. 2015, SpWea, 13, 374
Schou, J., Scherrer, P. H., Bush, R. I., et al. 2012, SoPh, 275, 229
Sheeley, N. R., Jr., Martin, S. F., Panasenco, O., & Warren, H. P. 2013, ApJ, 772, 88
Shen, F., Shen, C., Zhang, J., et al. 2014, JGRA, 119, 7128
Shibata, K., Masuda, S., Shimojo, M., et al. 1995, ApJL, 451, L83
Subramanian, P., Arunbabu, K. P., Vourlidas, A., & Mauriya, A. 2014, ApJ, 790, 125
Thernisien, A. 2011, ApJS, 194, 33
Thernisien, A., Vourlidas, A., & Howard, R. A. 2009, SoPh, 256, 111
Thompson, B. J., Cliver, E. W., Nitta, N., Delannée, C., & Delaboudinière, J. P. 2000, GeoRL, 27, 1431
Tsurutani, B. T., Gonzalez, W. D., Tang, F., Akasofu, S. I., & Smith, E. J. 1988, JGR, 93, 8519
Vemareddy, P., & Mishra, W. 2015, ApJ, 814, 59
Vemareddy, P., & Zhang, J. 2014, ApJ, 797, 80
Vršnak, B., Amerstorfer, T., Dumbović, M., et al. 2019, ApJ, 877, 77
Webb, D. F., Cliver, E. W., Crooker, N. U., Cry, O. C. S., & Thompson, B. J. 2000, JGR, 105, 7491
Wilson, R. M. 1987, P&SS, 35, 329
Yurchyshyn, V., Yashiro, S., Abramenko, V., Wang, H., & Gopalswamy, N. 2005, ApJ, 619, 599